Enabling long cycle life lithium-ion capacitors through electrode-electrolyte interface optimization

by

Obinna Egwu Eleri

Thesis submitted in fulfilment of
the requirements for the degree of
PHILOSOPHIAE DOCTOR

(PhD)

University
of Stavanger

Faculty of Science and Technology

Department of Energy and Petroleum Technology

2024

Acknowledgements

My sincere gratitude goes to my supervisors, Dr Fengliu Lou and Professor Zhixin Yu, for their unwavering support, patience, advice and guidance throughout my master's thesis and now PhD. They devoted their time to directing and inspiring me in my academic and industrial aspirations.

My fellow Industrial PhD candidates at Beyonder AS, Frederik Huld and Zhang Yang, thank you for all the collaborations and fruitful discussions. The memory of going through the process together will forever be cherished. Likewise, my PhD colleagues and friends at UiS, Fawzi Chamssine, Georgio Semaan, Adijat Ogienagbon and Song Lu, and at NTNU, Philipp Schweigart, thank you for the insightful discussions, collaborations, and shared experiences.

My exceptional colleagues at Beyonder AS, Ana Maria, Julie, Rex, Trine, Nicholas, Rasim, Joachim, Yong, Vlad, Kingsley, etc., you all made every working day fun-filled. I am also grateful to the CEO/founder of Beyonder AS, Svein Kvernstuen, for offering me my first contract and the opportunity to be part of the team.

My wife, Siri Catherine, thank you for always being my number-one fan, supporting me, and being there in my most challenging moments. To my parents, thank you for instilling the qualities I have today and encouraging me throughout my life. Finally, my brothers, Enyinnia and Kelechi, and my sister, Elizabeth George, are the best support system anyone could ever wish for. Thank you for being so awesome.

<div align="right">

Obinna Egwu Eleri

September 2023, Stavanger.

</div>

...I can do all things through Christ who strengthens me...Philippians 4:13.

Abstract

Electrode-electrolyte interfaces in electrochemical cells represent critical boundaries between the electrode and electrolyte where most charge transfer or storage processes are initiated. Accordingly, the interface properties can influence the performance of electrochemical cells, affecting the capacity, energy and power density, electrode stability and cycle life. This is particularly significant in lithium-ion capacitors (LiC), a hybrid energy storage consisting of high surface area capacitive cathodes such as activated carbon (AC) from Supercapacitors (SC) and intercalation/alloying anodes such as graphite or hard carbon (HC) from Lithium-ion batteries (LiB) while using similar LiB electrolytes with large operating potential windows. However, the AC widely adopted as LiC cathode often possesses surface oxygenated functionalities and numerous defects from the extensive activation treatment to impact the high surface area. As a result, the AC electrode is enriched in active sites for accelerated electrolyte decomposition, which can cause rapid capacity fade and failure of such cells. Furthermore, the sensitive $LiPF_6$ salt widely adopted in LiB electrolyte formulations is prone to hydrolysis, which may inadvertently proceed upon contact with confined moisture in the AC pores. Degradation by-products, such as HF and PF_5, are formed, which may catalyse other component degradation and are detrimental to interfacial stability. Consequentially, the cycle life of the LiC is affected by these processes occurring on the AC and remains inferior compared to SC.

In the first part of this study, the capacity fade mechanism of the AC cathode in a LiC cell was investigated by a combination of electrochemical and post-mortem material characterisation techniques. First, the stability was probed using sustained floating voltage holds and intermittent electrochemical spectroscopy to examine the interfacial transformations during cycling. Then, the AC electrode surface was further examined ex-situ, utilising a variety of post-mortem characterisations after different durations of cycling to reveal changes in the surface area, defect level, and surface species with the capacity fade. Finally, the results showed that the capacity fade was caused by the

synergistic effect of electrolyte degradation and active material interface transformation by the deposited degradation products.

The second part examined the effect of electrolyte dielectric on the performance of the AC in symmetric cell configuration and in half cells with lithium counter electrodes. Electrolyte solutions with varying dielectrics were prepared and tested in the mentioned cellular configuration. High electrolyte dielectric was revealed to improve cycle life by delaying the PF_6^- anion degradation at the AC electrode surface. Furthermore, the increased electrolyte dielectric enhanced the oxidative stability of the PF_6^- anion through a sufficiently strengthened solvation shell. These properties enhanced the cycle life and decreased features associated with electrolyte degradation in the high-dielectric electrolyte.

The third part investigated the effect of electrolyte dielectric on the interfacial properties of the AC cathode and Hard carbon (HC) anode in a LiC full cell. Post-mortem characterisations and electrochemical impedance analysis were used to probe the AC and HC electrode interfaces. High electrolyte dielectric was revealed to be particularly beneficial for the AC cathode, with a three-fold decrease in interfacial impedance observed as the electrolyte dielectric was increased. Overall, increasing the electrolyte dielectric presents a method for extending the cycle life of AC LiC.

List publications

I. Lithium-ion capacitors: A review of strategies towards enhancing the performance of the activated carbon cathode.
O. E. Eleri, F. Lou, and Z. Yu.
Batteries, 2023, 9(11), 533.
DOI:10.3390/batteries9110533

II. Revealing mechanisms of activated carbon capacity fade in lithium-ion capacitors.
O. E. Eleri, F. Huld, J. Pires, W. M. Tucho, P. Schweigart, A. M. Svensson, F. Lou, and Z. Yu.
Electrochimica Acta, 2023, 453, 142359.
DOI: 10.1016/j.electacta.2023.142359

III. Enhanced activated carbon lithium-ion capacitor electrochemical stability through electrolyte dielectric optimisation
O. E. Eleri, J. Pires, F. T. Huld, S. Lu, P. Schweigart, A. M. Svensson, F. Lou, and Z. Yu.
Sustainable Energy & Fuels, 2023, 7(8), 1846-1854.
DOI: 10.1039/D3SE00122A

IV. Deciphering electrolyte dielectric extended electrochemical stability in lithium-ion capacitors.
O. E. Eleri, F. T. Huld, F. Lou, and Z. Yu.
Electrochimica Acta, 2023, 464, 142960.
DOI: 10.1016/j.electacta.2023.142960

This thesis is based on the above four papers.

Additional publications

V. Towards high-energy-density supercapacitors via less-defects activated carbon from sawdust.
O. E. Eleri, K. U. Azuatalam, M. W. Minde, A. M. Trindade, N. Muthuswamy, F. Lou, and Z. Yu.
Electrochimica Acta, 362, 137152.
DOI: 10.1016/j.electacta.2020.137152

VI. Characterisation Methods for Supercapacitors.
O. E. Eleri, F. Lou, and Z. Yu
Book chapter In Nanostructured Materials for Supercapacitors (pp. 101-128). Cham: Springer International Publishing.
DOI: 10.1007/978-3-030-99302-3_5

VII. On the Viability of Lithium bis(fluorosulfonyl) imide as Electrolyte Salt for use in Lithium-Ion Capacitors.
P. Schweigart, O. E. Eleri, I. Nylund, S. Y. Lai, F. Lou, and A. M. Svensson.
Batteries and Supercaps, 2023, e202300226.
DOI: 10.1002/batt.202300226

VIII. Sulfur-Decorated Ni− N− C Catalyst for Electrocatalytic CO_2 Reduction with Near 100% CO Selectivity.
S. Lu, Y. Zhang, M. F. Mady, O. E. Eleri, W. M. Tucho, M. Mazur, A. Li, F. L. Lou, M. Gu and Z. Yu.
ChemSusChem, 2022, 15, e202200870.
DOI: 10.1002/cssc.202200870

IX. Enabling Increased Delithiation Rates in Silicon-Based Anodes through Alloying with Phosphorus.

F. T. Huld, S. Y. Lai, W. M. Tucho, R. Batmaz, I. T. Jensen, S. Lu, <u>O. E. Eleri,</u> A. Y. Koposov, Z. Yu, and Lou, F.
ChemistrySelect, 2022, 7(42), e202202857.
DOI: 10.1002/slct.202202857

X.   Revealing Silicon's Delithiation Behaviour through Empirical Analysis of Galvanostatic Charge–Discharge Curves.
F. T. Huld, J. P. Mæhlen, C. Keller, S. Y. Lai, <u>O. E. Eleri,</u> A. Y. Koposov, Z. Yu and F. Lou.
Batteries, 2023, 9(5), 251.
DOI: 10.3390/batteries9050251

XI.   Nonaqueous Electrolytes for Lithium-Sulfur Batteries. Book chapter.
Z. Wang, <u>O. E. Eleri,</u> Z. Yu, and F. Lou.
Submitted.

XII.   New insights into the behaviour of commercial silicon electrode materials via empirical fitting of galvanostatic charge-discharge curves.
F. Huld, <u>O. E. Eleri</u>, Z. Yu and F. Lou.
ChemElectroChem, 2023, 10(12), e202300393.
DOI: 10.1002/celc.202300393

Conference presentations

I. <u>O. E. Eleri.</u> Revealing capacity fade mechanisms of activated carbon lithium-ion capacitors. *Oral* presentation at the International Workshop on "Advanced Characterization of Li-ion Batteries by Neutrons and X-rays". Trondheim, Norway, 20 -22 June, 2023.

II. <u>O. E. Eleri.</u> Examining electrode/electrolyte interface characteristics and failure mechanisms of activated carbon lithium-ion capacitors. *Oral* presentation at the University of Stavanger Battery Day. Stavanger, Norway, 2 May, 2023.

III. <u>O. E. Eleri,</u> J. Pires, F. Huld, S. Lu, Z. Yu, and F. Lou. Electrolyte stability on activated carbon lithium-ion capacitor cathodes: Influence of solvent type. *Poster* presentation at the World Conference on Carbon. London, the United Kingdom, 3-8 July, 2022.

Author contributions

The dissertation author performed all the experiments and data analysis and conducted the majority of the work except for the following:

- Scanning electron microscopy was performed by Wakshum Mekonnen Tucho at the Department of Mechanical, Structural Engineering and Material Science, University of Stavanger, Norway.

- X-ray photoelectron spectroscopy was performed at the Institute of Analytical Sciences and Physico-chemistry for Environment and Materials (IPREM), Pau, France, by Remi Dedryvere.

- Scanning electron microscopy and X-ray photoelectron spectroscopy were performed at the Norwegian University of Science and Technology NanoLab, by Philipp Schweigart and Verner Håkonsen.

List of abbreviations

Abbreviation	Definition
AC	Activated carbon
BET	Brunauer-Emmett-Teller
CE	Coulombic efficiency
CEI	Cathode electrolyte interface
CMC	Carboxymethyl cellulose
CPE	Constant phase element
CTAB	Cetyltrimethylammonium bromide
CV	Cyclic voltammetry
DEC	Diethyl carbonate
DMC	Dimethyl carbonate
DFT	Density functional theory
EC	Ethylene carbonate
EDX	Energy dispersive spectroscopy
EIS	Electrochemical impedance spectroscopy
EMC	Ethyl methyl carbonate
FVH	Floating voltage hold
GCD	Galvanostatic charge and discharge
GITT	Galvanostatic intermittent titration technique
HC	Hard carbon
HF	Hydrogen fluoride
ICE	Initial coulombic efficiency
LiB	Lithium-ion batteries
LiC	Lithium-ion capacitors
LFP	Lithium iron phosphate
LTO	Lithium titanate
NCM	Lithium nickel cobalt manganese oxides
NLDFT	Nonlocal Density functional theory
NMP	N-Methyl pyrrolidone
OCP	Open circuit potential

PAA	Polyacrylic acid
PAANa	Sodium polyacrylate
PM	Post-mortem
PPy	Polypyrrole
PTFE	Polytetrafluoroethylene
PVDF	Polyvinylidene difluoride
Rct	Charge transfer impedance
Rp	Passivation layer impedance
Rs	Bulk electrolyte resistance and active material/current collector contact resistance
SC	Supercapacitors
SBR	Styrene-butadiene rubber
SEI	Solid electrolyte interface
SEM	Scanning electron microscopy
TFB	1,3,5-trifluoro benzene
THF	Tetrahydrofuran
W	Warburg diffusion
WiSE	Water in salt electrolytes
XPS	X-ray photoelectron spectroscopy

Table of Contents

Table of Figures

List of Tables

1 Introduction

Attaining the global climate goal of reducing net CO_2 emissions is predominantly the driving force spurring the electrification of modern-day technologies and the transition from fossil fuel to renewable energy sources. Energy storage devices are expected to perform a leading role and must be continuously developed to sustain the energy, power and cycle life demanded by these electrified technologies. Among the energy storage devices, lithium-ion batteries (LiB) and supercapacitors (SC) are exceptional in satisfying the demands for high specific energy and specific power, respectively. However, due to the latency associated with chemical reactions, LiBs are unable to deliver high power and also suffer from a relatively lower cycle life as the charge transfer reactants are depleted [1, 2]. In contrast, SC operate based on a non-faradaic surface charge storage process of ion physisorption at the double layer; hence, they possess low specific energy but can deliver continuously beyond hundreds of thousandths of cycles [2, 3]. In 2011, a new hybrid energy storage device, named a lithium-ion capacitor (LiC), was developed by Amatucci et al. that incorporated cathodes and anodes adopted from SC and LiB, respectively, and similar LiB organic electrolytes that enabled operating at higher potential windows [4]. As a result, the LiC possessed superior specific energy than SC and specific power than LiB, without the underlying self-discharge problems of the former and with a longer cycle life than the latter [4-6].

The specific energy of LiC are up to 14 Wh/kg, which is significantly more than SC due to the high operating voltage limit (>3.5V) [7, 8]. Moreover, the specific power is typically around 10 kW/kg, significantly more than the capabilities of LiB [7, 8]. Hence, LiC are particularly suited for applications such as regenerative energy recovery during braking in automobiles and trains, grid voltage levelling, and support for other high energy systems during peak power shaving [9]. In general, they are excellent choices for applications requiring higher energy than SCs can deliver and higher power than LiB can sustain.

During the operation of LiC, electrolyte ions are adsorbed and desorbed on the capacitive cathode, while lithiation and de-lithiation through intercalation or alloying occur on the anode. Therefore, the charge storage mechanism of LiC is a hybrid process that requires meticulous optimisations to guarantee efficient performance. Optimising the active materials and electrode/electrolyte interfaces is necessary to ensure compatibility between the contrasting charge storage mechanisms at the cathode and anode.

1.1   *Electrode materials for LiC*

Since the positive performance attributes of LiC are a resultant effect of the hybrid device architecture, a meticulous selection of electrode materials is required to synergistically achieve the desired enhanced performance [6, 10, 11]. Several conventional SC electrode materials

have been employed as cathodes, which include materials such as activated carbon (AC), carbon nanotubes, carbon nanofibers, carbon aerogels, graphene, MXenes, and carbide-derived carbons due to their high surface area and favourable properties for surface charge storage. However, among these materials, AC has typically been the most widely adopted commercial cathode material due to its easily tuned properties, abundant precursors, and relative ease of process scalability in mass production. The favourable commercial potential has been demonstrated by several companies, such as Norit Carb, Beyonder, Jacobi, and Haycarb, who have implemented large-scale AC production facilities utilising precursors such as petroleum coke, sawdust, and coconut shells [12]. The flexibility of precursors has also been substantiated in several research publications, producing very high-quality AC from precursors such as Brewery wastes [13], Rice husks [14], Algae [15], Corncobs [16], Tobacco leaves [17] and Lignin [18] while revealing optimisation strategies for enhancing the AC performance.

Numerous advantages can therefore be derived from incorporating the AC as cathode material in LiC, especially concerning the valuation of biomass precursors which would have been otherwise been discarded as landfill materials.

As described in the device architecture, the AC must be combined with appropriate LiB battery-type anode materials, such as graphite, silicon, or hard carbon (HC), to realise the high specific energy. However, proper anode selection is critical for increased energy and power density. The

slower kinetics associated with the latency of chemical faradaic reactions in LiB anode materials is often a challenge regarding matching the AC's fast charge and discharge capabilities. Recently, HC has emerged as a suitable alternative, enabling higher power densities without the volume swelling and limited charge/discharge rates exhibited by other LiB anodes like graphite and Silicon. The beneficial properties of HC anodes arise from the nongraphitizable nature, and the random arrangement of graphene layers facilitates increased Li-ion intercalation capacity. However, HC electrodes are plagued by very low initial coulombic efficiencies (ICE) and accompanying high irreversible Li depletion from the electrolyte during solid electrolyte interface (SEI) film formation. These problems are associated with surface functionalities and the relatively higher surface area and microporosity of HC compared to typical intercalation anodes.

Nevertheless, the incorporation of a pre-lithiation step resolves this issue. Pre-lithiation entails pre-doping the LiC anode with Li to reduce the irreversible depletion of Li from the electrolyte in the cell during SEI formation. Pre-lithiation of the anode in LiC is vital because neither the AC nor HC electrodes possess additional Li sources besides the electrolytes. Hence, pre-lithiation is incorporated in the final full-cell assembly to ensure sufficient Li reservoirs while regulating the anode capacity and operating potential region. Additionally, pre-lithiation facilitates increased capacity of the AC, enabling Li adsorption below the open circuit potential (OCP).

1.2 Electrolytes for LiC

LiB electrolytes are adopted in LiC to guarantee the synergetic performance attributes gained from the SC cathode and LiB anode. These electrolytes are mostly nonaqueous and endowed with high operating potential windows that ensure enhanced energy density. Although other promising candidates such as aqueous electrolytes, water in salt electrolytes (WiSE) and ionic liquid electrolytes exist, they are limited by narrow operating potential windows and operating temperature ranges due to high viscosities. Hence, nonaqueous electrolytes consisting of the corresponding Li-salt (LiPF$_6$, LiFSI, LiTFSI, LiBF$_4$) dissolved in carbonate solvents are usually the preferred alternatives.

1.3 Evaluation of AC for LiC

The primary parameters considered during the evaluation of AC for LiC are the charge storage capacity, measured as capacity/capacitance, the stable operating potential window, and the long-term cycling stability. These parameters significantly determine the energy, power, and cycle life of the LiC incorporating the AC. Compared to battery-type anode materials, the capacity of the AC is minimal due to the dependence on available surface area and pores for ion physisorption during charge storage. Moreover, the LiC capacity determined by the relation $1/C_{\mathrm{LIC}} = 1/C_{\mathrm{anode}} + 1/C_{\mathrm{cathode}},$ is affected by the AC's low capacity; hence, to further enhance the LiC performance, the AC specific capacity must

be improved. Likewise, the energy density of the LiC, a function of the capacitance and square of the operating potential window, is also impacted by the AC. This is attributed to the often-accompanying surface oxygen functionalities and defects introduced during activation that are responsible for catalysing electrolyte decomposition at high operating potentials. Therefore, improving the performance of the AC cathode is imperative for enhanced LiC performance. Other parameters, such as leakage currents/self-discharge and electrochemical stability, are equally important. The electrochemical stability, in particular, can affect the cycle life of the LiC, especially considering the dual combination of high surface area and accompanying surface oxygen functionalities. A published review of recent strategies for improving the performance of the AC cathode written by the dissertation author is presented in Chapter 2.

The cycle life of the AC is often characterized by conducting millions of galvanostatic charge and discharge cycles, whereby the ability to deliver high power using fast charge and discharge rates is tested. The cell capacitance and equivalent series resistance is monitored consistently during cycling until the end-of-life criteria is reached (typically 80% capacity retention or a 100% increase in ESR). This process is time-consuming and may require several months or years to completely evaluate the chosen AC. Moreover, the time spent at the upper vertex potential is not sufficient and may not give a true representation of the stability at such upper vertex potentials. An alternative method considered in the evaluation of the stability of AC is the floating voltage

hold (FVH) method. This method consists of subjecting the device to a constant voltage hold at a particular voltage (typically the upper vertex potential or above the stability limits) for a specified duration and measuring the capacitance by conducting GCD cycles periodically as a function of time. Using the FVH method ensures that the stability of the AC electrode is sufficiently tested with appropriate durations at the upper vertex potential. Consequently, the stability can be determined using the same end-of-life criteria within a shorter time than the millions of cycles required for the GCD method [19].

1.4   Degradation mechanisms of LiC and characterization methods

The contrasting charge storage processes of LiC also imply differing degradation mechanisms at both electrodes, consisting of degradation characteristics from SC and typical failure mechanisms of the LiB anodes. Concerning the LiB anodes, the failure mechanisms have widely been investigated and can be summarised by mechanical instabilities associated with volume changes, unfavourable growth of the solid electrolyte interface (SEI), diminished lithium inventory, lithium plating and SEI instability [20, 21]. On the AC cathode, the failure mechanisms have commonly been reported in SCs utilising the organic electrolyte $TEABF_4$ in propylene carbonate (PC) or acetonitrile (AC) and are associated with unfavourable physical changes in the electrode-electrolyte interface characteristics [22, 23]. Moreover, the failure mechanisms of the AC differ according to the electrolyte choice,

whereby the stability limits of the electrolyte and compatibility with the electrode influence surface oxidation and reduction processes at the boundaries of the operating potential window. Electrolyte degradation products from the chosen electrolyte may affect the AC electrode and cell in distinct ways.

Nevertheless, the common observable features following the degradation of the electrolyte on the AC surface are the modification of the surface chemistry of the AC, severe gas evolutions, and generation of insoluble redox products that may precipitate on the AC surface and diminish the active surface area for charge storage.

Regarding LiC and the corresponding LiB electrolyte, the AC cathode performance is uniquely affected by the surface passivating nature of the carbonate solvents used in LiB electrolyte formulations. Meanwhile, the widely adopted $LiPF_6$ salt is sensitive to moisture and prone to hydrolyses that produce HF, which is detrimental to electrode interface stability. These reactions may subsequently occur upon contact with confined moistures often present in the AC pores following their exposure to ambient atmosphere/electrode fabrication processes and are often difficult to remove under intensive drying. Moreover, undesirable redox reactions are likely initiated between the Li-ion-containing electrolyte and surface oxygen functionalities that inadvertently accompany the AC after the activation process [24]. Consequently, electrolyte degradation at the AC surface is inevitable, alongside current collector corrosion, severe gas generation, active material delamination

from current collectors and loss of effective surface area for charge storage. These factors contribute to the observable decrease in capacitance/capacity, increased resistance, decreased operating potential window and cycle life of the AC.

Several methods, such as surface hydrophobisation, defect reduction, surface coating using atomic layer deposition of ZnO, and heteroatom doping, have been proposed to alleviate electrolyte degradation on the surface of the AC [25-28]. However, understanding the degradation processes and time-resolved transformation of the electrode-electrolyte interface is fundamental to identifying mitigation measures and improvement techniques to enhance the cycle life. Moreover, the proposed alleviation methods should encompass strategies which are easier to incorporate industrially without being process-intensive and requiring complex steps.

After evaluating the cycle life, the degradation mechanisms can be characterised using a combination of non-destructive or destructive techniques. Non-destructive methods such as electrochemical impedance spectroscopy (EIS) reveal information about the changes in the interfacial properties of the electrode while providing a time-resolved characterisation of the capacitance, resistance, and reaction processes as a function of ageing time. Destructive techniques, on the other hand, reveal physical changes on the electrode surfaces after a post-mortem examination. Changes to the electrode surface morphology, surface chemical species, graphitisation degree, crystallinity, surface area and

pores could be obtained using analytical equipment such as Scanning electron microscopy (SEM), Transmission electron microscopy (TEM), X-ray photoelectron spectroscopy (XPS), Raman spectroscopy, X-ray diffraction studies and Nitrogen physisorption analysis. A holistic characterisation of the electrode/electrolyte interface using non-destructive and destructive techniques can complement identifying degradation processes that coincide with physical changes. For example, a decrease in capacitance observed during ageing using non-destructive methods can be correctly attributed to loss of active surface area when accompanied by post-mortem electrode characterisation with Nitrogen physisorption.

Investigating the degradation processes is, hence, beneficial for understanding the underlying failure mechanisms, proposing mitigation methods, and ultimately improving the performance and cycle life of the LiC.

1.5   Objectives and scope of the study

The main objective of this thesis is to understand the interactions between the AC electrode and Li-ion electrolyte and how these interactions can affect the performance and, consequently, the cycle life of LiC. An in-depth knowledge of such interactions and degradation mechanisms at the electrode/electrolyte interface will complement the strategies outlined to improve the performance.

A review of different strategies adopted to improve the performance of the AC when used in LiC is presented in **Chapter 2**. This review is adapted from **Paper I**. Despite the numerous studies, a gap exists in understanding the electrolyte decomposition mechanisms and how this can be decreased on the AC electrode. Understanding such mechanisms is vital to improving the performance of the AC and further extending the cycle life of LiC to match that of SC without sacrificing power or energy density.

The experimental section in **Chapter 3** presents the methodology employed in this study. Different electrolyte formulations were prepared by mixing the denoted ratios of salt and solvents. However, only $LiPF_6$ salt was used, as electrolytes with LiFSI salt were plagued by severe corrosion of the stainless-steel coin cell parts. Moreover, $LiPF_6$ is very sensitive to hydrolysis and degradation, while the carbonate solvents are renowned for their electrode surface passivating abilities. These attributes can significantly affect the electrode/electrolyte interface formed on the AC and, consequently, the performance.

The results and discussions section in this study is divided into three sub-sections, summarized from **Papers II, III,** and **IV**, and presented in **Chapter 4**. In **Paper II**, the capacity fade mechanisms of the AC in a typical LiB electrolyte were investigated using a combination of electrochemical and material characterization techniques. These techniques were employed in probing the AC at various stages and

understanding the transformations at the electrolyte/electrolyte interface in relation to the capacity fade.

After revealing electrolyte decomposition on the high surface area and oxygen functionality-rich AC as a major cause of capacity fade, numerous active material modification techniques were identified in the literature, which can mitigate electrolyte decomposition on the AC electrode. However, such techniques are often complex, and expensive and present challenges regarding upscaling. **Papers III** and **IV** demonstrated a facile method of improving the electrochemical stability by optimizing the electrolyte dielectric. The stability of electrolyte formulations with varying dielectric was compared in AC/Li Half cells, AC/AC symmetric cells and AC/ Pre lithiated HC full cells. The various electrode/electrolyte interfaces formed in electrolyte solutions with varying dielectrics were probed using a combination of EIS and post-mortem electrode characterizations to understand the mechanism underlying the improved electrochemical stability. The different interfaces and mechanisms underlying the improved electrochemical stability are further discussed. Finally, concluding remarks and aspects for future work are presented in **Chapter 5**.

2 Literature review

This chapter presents a review of LiC, focussing on strategies towards enhancing the performance of the AC cathode. The review is a partial reproduction of **Paper I**, attached as appendix A.

2.1 Strategies towards achieving high-performance LiC (Paper I)

As mentioned, achieving high-performance LiC requires a critical focus on the AC cathode to increase the capacity, operating potential window and electrochemical stability. The performance of the AC in LiC can be improved by different strategies categorized under material, electrode, electrolyte and cell design optimization techniques.

2.1.1 Material optimization

AC is synthesised by subjecting a carbon precursor to a controlled heating procedure in the presence of physical and/or chemical activation agents [29-31]. The nature of the activating agent determines the classification of the activation process, broadly categorised into physical activation, chemical activation, or a combination of the two. Excellent reviews exist on producing activated carbon from various biomass sources using the earlier methods [32-34]. The activation process aims to impact a high surface area of tailored pores with dimensions suited to the electrolyte moieties to be adsorbed. Parameters such as precursor

type, activation temperature, activation time and activating agent concentration are varied during the activation process to optimise the resulting AC's surface area and pore size distribution [17]. The surface area and pore size distribution of the AC correlate with the adsorption capacity for electrolyte moieties, given the double layer phenomena, where the obtainable capacitance *C (F)* is determined from the equation $C = \varepsilon(A/d)$ [35, 36]. The constant ε represents the product of the electric constant and relative permittivity, *A* represents the area of the plates, and *d* represents the distance between the plates. Therefore, the amount of charge stored can be converted to capacity (mAh) by multiplying the capacitance obtained by the potential window. This section will discuss strategies for improving the AC's performance enabled by different material optimization techniques.

2.1.1.1 Activation process optimization

AC cathodes, by virtue of the surface charge storage phenomenon, require a high surface area with pores consisting of micropores (< 2nm) for adsorption of electrolyte ions, mesopores (2-50 nm) to facilitate ion diffusion and accessibility to the micropores, and macropores (> 50nm) to serve as electrolyte reservoirs and to enhance ion diffusion to the mesopores and micropores. However, these characteristics necessitated the continuous search for optimum activation procedures, initially focused on increasing the surface area and optimizing the pore size distribution. As a result, high specific surface areas of up to 3000 m^2 g^{-1} have been achieved using various activation methods, including KOH

chemical activation, combined KOH-KCl chemical activation, H_3PO_4 chemical activation and $ZnCl_2$ with excellent reviews on the different mechanisms of the activation agents [30-33, 37, 38]. These high surface area AC have yielded specific capacitance values up to 160 F g^{-1} within the operating potential window of 0-2.7 V in organic electrolytes. However, it was noticed that further increases in the surface area do not translate into higher specific capacitance [39]. Furthermore, the extensive activation treatments broaden the pore size distribution, leading to the abundance of ineffective pores that are smaller than the de-solvated electrolyte ion and only contribute to the high surface area. Besides, the existing micropores may widen into mesopores due to the intensive gasification of the carbon matrix. Consequentially, low electrode densities often accompany very high specific surface area AC and may result in poor volumetric performance. Concerning the electrolyte, the high porosity would necessitate increased electrolyte volume in the cells, which may impact the energy density due to the increased weight [5]. Further, the high surface area may also serve as an active site for accelerated electrolyte decomposition, decreasing the cycle life. Khomenko et al. [40] compared the cycle life of two ACs cycled in organic electrolytes. It was revealed that the AC with the highest surface area had the highest capacity fade. Although a high surface area is required for adsorption, carefully controlled activation procedures are necessary to modulate the surface area and create pores with diameters similar to the electrolyte ions. AC with pores of similar diameters to the electrolyte ions has reportedly increased capacitance

[41]. The discovery that ions could access pores smaller than the solvated ion size further underscores the need for activation process optimization [42]. Likewise, controlled mesoporosity formation and tailored microporosity could facilitate increased volumetric performance through enhanced electrode densities.

Several modified activation techniques have recently yielded ACs with superior gravimetric and volumetric electrochemical performance beyond the typical physical or chemical activation procedure with steam or singular chemical agents. Eleri et al. [25] used a non-destructive activation method to synthesise high-performance AC from sawdust with reduced defects, high surface area, increased microporosity and high electrode density with optimised mesoporosity. The non-destructive activation method incorporated an Al additive in a modified KOH chemical activation method, acting as an oxygen scavenger to reduce the oxides' extensive gasification of the carbon matrix. The modified activation procedure ensured that exfoliation due to potassium intercalation into the carbon matrix was the dominant activation method, creating more micropores and reducing gasification-induced mesoporosity. Zheng et al. [43] incorporated a surfactant-modified KOH activation process in synthesising in-situ nitrogen-doped activated porous carbons with controlled pore size, which could function as a dual anode and cathode material in a 4.5 V LiC. The AC was obtained from the carbonisation of polypyrrole (PPy) prepared with a surfactant, cetyltrimethylammonium bromide (CTAB), and subsequent KOH activation of the carbonised material. The surfactant-modified KOH

activation process influenced the pore size distribution of the carbon by creating mesopores in the spaces occupied by the decomposed surfactant and controlling the porosity formation. Specific capacities reaching 80 mAh g^{-1} at 0.1 A g^{-1} in the potential window 2-4.5 V were achieved using this material in the half-cell configuration with 1M $LIPF_6$ EC:DEC (1:1) vol% electrolyte. On the contrary, the AC synthesised without the surfactant possessed a higher surface area (2528.0 m^2 g^{-1} compared to 1894.9 m^2 g^{-1}) but poor electrochemical performance due to hindered ion diffusion, nonuniform pore size distribution and ineffective micropores. Again, this further underscores the need for optimised pore size distributions, in contrast with solely achieving high surface area through extensive activation.

2.1.1.2 Functionalization and Doping

The nature of chemical functionalities at the surface and doped elements within the carbon matrix can influence the electrochemical performance of AC. Surface functionalities could be inherited from the precursor material or deliberately introduced during the activation or post-treatment activation procedures. As a result, benefits such as enhanced conductivity, improved wettability, and increased active sites for pseudocapacitive Li^+ storage can be achieved [44]. This section discusses the effect of heteroatoms such as N, B, O, F, S and P on the AC's performance in nonaqueous electrolytes.

Nitrogen

Nitrogen functionalisation has particularly been popular due to improved charge carrier transport caused by increased contributions of p- electrons to the Π system, following the positive synergy between the N atom and carbon lattice [44-46]. This, therefore, enables an increased sorption capacity towards the anion when combined with appropriate pore size distributions [47, 48]. The electron-donating abilities induced by nitrogen functionalization create additional electroactive sites, thereby improving the doped AC's electrochemical reactivity, surface polarity, electrical conductivity and wettability [49]. Li et al. [50] synthesised nitrogen-doped AC from corn cobs with a very high surface area of up to 2900 m^2 g^{-1}. The nitrogen-doped AC exhibited an initial specific capacity of 129 mAh g^{-1} at 0.4 A g^{-1} in the half-cell configuration, using an organic electrolyte and operating potential window of 2-4.5 V.

Boron

Boron functionalization is another method of increasing the electrochemical reactivity of the AC by modifying the carbon electronic structure. Functionalization with boron increases the density of charge carriers in the carbon matrix after the substitution and improves the electronic conductivity due to the p-type characteristics [51]. Jiang et al. [52] reported on the effect of dual doping of boron and nitrogen on the performance of LiC in organic electrolytes. Doping with boron enabled a widened operating potential window of up to 4.8 V and improved electrode conductivities and electrochemical performance.

Oxygen

Surface oxygen functionalities on the AC present a dilemma regarding irreversible or reversible redox reactions with the nonaqueous electrolytes commonly used in LiC. Liu et al. [27] reported that oxygen functionalization facilitated improved capacitance in AC electrodes used in LiC. Commercial ACs were functionalized by ammonium persulphate and sulphuric acid treatment. The functionalized AC displayed superior capacities of 78 mAh g^{-1} when tested in half cells with a Lithium counter electrode and an organic electrolyte 1M LiTFMS/diglyme. The authors proposed that the improved performance was caused by reversible pseudocapacitive reactions between Li$^+$ ions and C=O functional groups introduced after the functionalization treatment. However, the functionalized AC displayed a lower capacity retention during continuous cycling than the pristine AC. This behaviour was further attributed to detrimental irreversible redox processes, which may have contributed to lower cyclic stabilities. A related study by Li et al.[53], using similar ammonium persulphate and sulphuric acid functionalization of a commercial AC revealed that oxygen functionalities improved the performance of the functionalized carbon in the aqueous 6M KOH electrolyte and not the organic electrolyte 1M Et$_4$NBF$_4$/PC. Therefore, the beneficial effect of oxygen functionalities concerning nonaqueous electrolytes may be restricted to AC electrodes cycled in electrolytes with Li$^+$ ions as the adsorbed/desorbed species during charge storage.

Fluorine

Fluorine functionalisation has been reported to facilitate improved affinity for organic electrolyte ions on the AC surface [54]. Doping with fluorine amplifies the electroactive sites and impacts some electronegativity onto the carbon surface. Zhou et al. [54] synthesized fluorine-doped AC that achieved a high specific capacitance of 168 F g^{-1} using an organic electrolyte and symmetric cell configuration. The improved performance with high fluorine content was caused by the synergy between increased surface area and favourable surface chemistry. Density functional theory (DFT) calculations showed that the affinity for the TEA$^+$ ions was increased with Fluorine doping compared to the pristine material.

Phosphorous

The electron-donating ability and large covalent radius of phosphorous make it an attractive heteroatom for doping carbon matrices. Phosphorous doping has been reported to facilitate improved performance through enhanced pseudocapacitive reactions and improved electronic conductivity caused by the electron-donating ability of phosphorous [55, 56]. In addition, the much larger covalent radius of phosphorus (107 ± 3 pm) compared to carbon (73 ± 1 pm) creates defects on the carbon surface after doping [57]. These defects may serve as active sites where charges are concentrated, facilitating charge transfer reactions [56].

Sulphur

Sulphur functionalization on the AC surface induces electron delocalization of carbon backbones, thereby creating more electroactive sites that increase wettability and improve conductivity. The electron delocalization occurs due to the overlap between a lone electron pair on the p-orbital in sulphur and the Π orbital of the sp^2 hybridized sites in the AC. Sulphur-containing materials, like thioglycolic acid and thiourea, have been used as dopants to impact sulphur functionalities in carbon matrixes. Thangavel et al. [58] obtained a specific capacitance of 252 F g^{-1} at 0.5 A g^{-1} in a sodium ion capacitor after nitrogen and sulphur codoping of the cathode with thiourea. The improved performance was attributed to the enhanced synergetic effect of the dual heteroatom elements. The sulphur heteroatoms enhanced the space utilization and promoted the electrosorption of the electrolyte ions, while the nitrogen enabled increased electron transport and rapid ion transport kinetics inside the pores [58-60].

2.1.1.3 Precursor optimization

Precursor materials can affect the final properties of the produced AC. Parameters such as the carbon content, organic and inorganic matter %, heteroatoms, precursor carbon structure, and the interactions between the precursor carbon matrix and activation agent would determine the qualities of the synthesised AC [31]. AC produced from naturally occurring precursors, such as biomass materials, often retains the inherent structure of the biomass material. The activation process

typically occurs via crosslinking, dehydration, exfoliation, or gasification of the precursor matrix, depending on the type of activation agent [61]. These processes are broadly summarized by the reduction of the oxygen content of the precursor through the removal of volatiles, moisture, and some of the precursor's carbon content as the pores are being created. The precursor's carbon, oxygen, and volatile matter content can therefore affect the efficacy of the activation process [31]. The activation agent is often more attracted to the oxygen radicals of the precursor, thereby increasing the activation intensity and reducing the activation duration needed to achieve particular burn-off rates. Precursor materials with high volatile content, such as biomass-based materials, often possess higher surface areas than synthetic materials (e.g. organic polymers) [31, 62]. Although the removal of volatiles during the carbonization/pyrolysis process is strongly related to the activation temperature, the macrostructure and nature of crosslinks between the precursor crystallites can affect the diffusion of the activation agent, which in turn dictates the porosity formation [63]. Precursors containing crystallite structures with several aromatic layers are reportedly more difficult to activate due to stronger covalent bonds among the carbon atoms in the layers [64]. In contrast, precursors containing carbon atoms with unsaturated bonds (mainly at the edge) are considerably more reactive and easily activated [64].

Some precursor materials can also undergo self-activation without the need for activation agents. The absence of activation agents can enable controlled porosity generation in the AC with well-distributed pores.

Klezyk et al. [17] synthesized AC from tobacco leaves and stem wastes without any activation agent. The synthesized AC had narrow pore size distribution and excellent electrochemical performance in both aqueous and organic electrolytes. The success of the self-activation could be linked to the presence of well-distributed alkalis in the precursor on the atomic scale. Moreover, the evolved gases during the carbonization treatment can simultaneously participate in the activation process during the carbonization step.

Therefore, self-activating precursors present a facile approach towards achieving narrow pore distribution due to the atomically dispersed nature of the alkali metals and the absence of external activation agents that may contribute to uncontrollable gasification rates. Similar self-activating abilities have been demonstrated by seaweed and proposed to occur in biomass precursors that contain naturally embedded elements such as Na, K, Ca and Mg [65]. Synthetic materials such as polyvinylidene chloride have also demonstrated excellent self-activating properties, achieving high-performance AC without an additional activation step [66].

Atomically dispersed elements in precursors have also aided the activation process by serving as templates during porosity formation. Xue et al. [14] reported on the templating behaviour exhibited by Silica present in rice husk precursors during the synthesis of AC. The silica nanoparticles were selectively leached using NaOH and KOH treatment before activation. A detailed study was conducted on the effectiveness

of silica embedded in the rice husk and on the surface. Nanoparticle silica embedded in the rice rusk was revealed to favour porosity formation through templating and synergetic effect with alkali activators that ensured more active sites during activation. In contrast, the silica present at the surface reduced the efficiency of the activation agent, and the produced AC had decreased porosity and templating effect. Niu et al. [67] reported on the self-activating effect of hydroxyapatite found in animal bones, which enabled the synthesis of high-performance cathodes (109 mAh g^{-1} at 0.1A g^{-1} in the potential window 2.0-4.5 V) after a simple pyrolysis step.

2.1.2 Electrode optimization

After synthesising the active material, the electrode is the next critical step influencing performance. During the electrode fabrication, the AC powder is mixed with selected binders, ensuring good adhesion between the particles and the current collector. Moreover, the electrode can be fabricated with a dissolving solvent to aid the dispersion of the particles, binder, and additive composites often introduced to optimise the performance. This section discusses the influence of parameters such as binders and hybrid composites consisting of carbon materials or high-capacity bi-functional cathodes on the performance of the AC.

2.1.2.1 Bi-functional hybrid composites

Despite the advances in the activation process discussed previously, the capacity of AC remains limited compared to intercalation-type battery

cathodes like lithium iron phosphate (LFP) (170 mAh g^{-1}). Recently, researchers have implemented composite mixtures of AC with conventional battery-type materials as bi-functional hybrid cathodes to increase the capacity and energy density of the LiC cathode. Benefits such as increased cathode composite conductivity, improved rate performance, and enhanced power and energy densities were obtained when these hybrid composite electrodes were integrated into the LiC architecture. Shellikeri et al. [68] investigated the performance of an AC/LFP (80/20)wt% bi-functional cathode paired with a pre-lithiated HC anode in the fabrication of LiC. A capacity retention of 76% after 20,000 cycles was obtained using the hybrid cathode, in contrast with 47% obtained by pure LFP after a similar duration. The LFP and AC synergistically enhanced the energy and power density of the LiC, compared to using singular AC or LFP as cathode materials. Furthermore, the beneficial effect of the hybrid cathode was more noticeable at high C-rates, where the FePO$_4$ (FP) phase plagued by low conductivity cannot be discharged entirely due to increased concentration gradient from Li salt deficiency. The AC in the composite delayed the overpotential of the LFP, improved the conductivities of the FP phase and enhanced the Li-ion transport at high current densities. Granados-Moreno et al. [69] adopted a similar bifunctional blend of AC/LFP, using a 60wt% AC and 40wt% LFP composite. This composite blend achieved specific capacities of 102 mAh g^{-1} at 0.25 A g^{-1} and 80 mAh g^{-1} at 30 A g^{-1}. A similar work using AC/LFP composites by Bockenfeld et al. [70] further highlighted the positive synergy between

the AC and LFP. Diluting the LFP with the AC yielded higher specific capacity than pure LFP at high c-rates. The authors attributed the improvement to the favourable ratio of Li-ions in the electrolyte within the pores and in the active material when the LFP was mixed with the AC. Moreover, the AC/LFP composites had improved conductivities and favourable morphology (the LFP particles, which were smaller and less porous, occupied the spaces between the AC particles, enabling adequate contact between the two active materials). Sun et al. [71] investigated the effect of different ratios of $LiNi_{0.5}Co_{0.2}Mn_{0.3}O_2$ powders (NCM) blended with the AC as bifunctional cathodes for LiC. A 25 wt% NCM content was determined as the optimum blend, which yielded higher specific capacity than the pure AC (60.5 vs 38.6 mAh g^{-1}) in the potential window 2.5-4.1 V. Moreover, this blend enabled a 35% increase in the volumetric energy density without sacrificing the power density or cycle life compared to the pure AC cathode.

2.1.2.2 Hybrid composite with other carbon materials

To achieve sufficient surface area and porosity in the synthesized AC, the precursors are often subjected to harsh gasification conductions in the activation process, distorting the carbon structure and producing disjointed pores. Pores of varying dimensions are often created without sufficient interconnectivity when activation methods that do not include templating for tailored micropore formation are used. The presence of randomly created pores with insufficient interconnectivity can result in

poor conductivity of the AC and inaccessibility of electrolyte ions into the pores. Besides, while aiming to further increase the surface area, the existing micropores may collapse into mesopores and macropores from over-activation, consequentially reducing the electrode density and volumetric performance. Therefore, hybrid compositing with other carbon materials has been explored to increase the conductivity of the AC electrode and electrode density and improve the volumetric performance. Commonly incorporated carbon materials include carbon black, carbon nanotubes, carbon nanofibres and carbon nano onions.

2.1.2.3 Binder optimization

Binders perform an essential role in the electrode fabrication and proper functioning of electrodes for LiC. They serve as the holding agent, securing the active materials while providing a conductive pathway for ionic species. Appropriate selection of binders can influence the AC electrode's mechanical strength, electrode stability, self-discharge, and ionic and electrical conductivity. Typical binders used in AC electrode fabrication include polyvinylidene difluoride (PVDF), carboxymethyl cellulose/styrene-butadiene rubber (CMC)/SBR, polytetrafluoroethylene (PTFE), polyacrylic acid (PAA) and sodium alginate. The impact of these binders on the performance of AC has been investigated by several authors. Chen et al. [72] compared the performance of AC fabricated using three binders AC/PTFE, AC/PVDF, and AC/CMC/SBR, using the organic electrolyte 1M $TEABF_4$ in PC and symmetric supercapacitor configuration. It was revealed that CMC/SBR possessed the best

wettability and lowest contact angle in the electrolyte. The fluoropolymers, PTFE and PVDF, had lower wettabilities due to high surface energies. Furthermore, nitrogen physisorption analysis of the AC powder and AC electrode with the different binders revealed decreased porosity and surface area due to the binders. The lowest surface area was obtained from the PVDF binder, while the CMC/SBR had only a minor decrease. These microstructural differences influenced the rate performance and interfacial impedance, especially at high charge and discharge rates, with the CMC/SBR exhibiting superior performance compared to the rest. Moreover, the CMC/SBR had the lowest self-discharge among the binders, attributed to the ease of mass transport within the macropores/mesopores favouring homogenously adsorbed ions during charging. The homogeneously charged surface reduced the self-discharge caused by ion redistribution in the electrode. Tran et al. [73] investigated the influence of the binders PTFE, PVDF, PAA, Alginate and PAANa (Sodium polyacrylate) on the performance and cycle life of AC electrodes used in LiC. The exceptional performance of the green alginate was highlighted. Stress relaxation tests conducted during the investigation of the rheological properties revealed that the alginate-based slurry remained stable, whereas the PVDF/NMP slurry viscosity decreased with time. Changes in slurry viscosity are significant problems encountered while upscaling electrode slurry formulations. Hence, alginate-based binders are advantageous over typical PVDF/NMP slurries. Additionally, the water-based nature eliminates the

need to adapt special process operating conditions, such as those required for PVDF while using NMP solvent.

2.1.3 Electrolyte optimization

Electrolytes are indispensable components in energy storage devices. Electrolytes enable the operation of energy storage devices by performing diverse roles, such as facilitating ion transfer between cathodes and anodes, stabilising electrode surfaces, and promoting improved electrochemical stability and device performance [74, 75]. The electrolytes used in LiC consist of a salt of the corresponding lithium ion dissolved in a solvent or often solvent combinations, with or without additives. These electrolyte constituents are optimised to influence the conductivity, viscosity, density, operating potential window and operating temperature tolerance. Factors such as the ion transport between the cathode and anode, cathode and anode interfacial stability, device cycle life, energy and power density are hence affected by the nature of the electrolyte.

2.1.3.1 Electrolyte solvents

Electrolyte solvents dissolve the electrolyte salt to enable dissociation into mobile conducting ions enclosed by a solvation shell. The nature of the dissolving solvent affects the electrolyte classification, which could be aqueous or nonaqueous, Ionic liquids or solid-state electrolytes without any dissolving liquid solvent. The latter two are not widely applied in LiC due to the rigorous preparation conditions, high costs for

the ionic liquids, and poor conductivities of the solid-state polymer electrolytes at low temperatures. Meanwhile, the aqueous electrolytes are limited by the decomposition potential of water at 1.2 V, which restricts the operating potential window. Even though very high conductivities and high capacitances can be obtained using such electrolytes, the resulting energy density remains constrained due to the low operating potential windows. Nonaqueous electrolytes, on the other hand, yield lower capacitance from the bulkier solvated ions dimensions but higher energy densities due to the wider operating potential window. Hence, the solvent choice can significantly affect the performance of the device.

Among the nonaqueous electrolytes, carbonate solvent-based electrolytes are widely adopted in LiC due to the ability to operate at higher maximum potentials $> 4V$, compared to conventional supercapacitor solvents such as acetonitrile (~2.7V). The latter solvent is unstable at potentials below 0.5V vs Li but possesses higher conductivities and superior low-temperature performance than the former. However, the ion-solvent interactions can influence the AC's rate performance, especially at high c-rates. Carbonate solvents, such as EC, possess significantly larger dipole moments and bind more strongly to the Li cation than acetonitrile. Therefore, the strong coordination of EC to the Li impacts difficulty in the desolvation process by the surrounding electric field. This can interfere with the specific capacitance at high c-rates, since the optimum pore size for maximum power density is affected. The pore size of the AC must accommodate the dimensions of

the solvated ion and allow for free diffusion of charges without affecting the double layer. Decaux et al. [76] investigated the influence of these two solvents on the performance of AC electrodes. It was revealed that larger pore dimensions in the range of 1.1-1.3 nm are needed to achieve increased capacity when using carbonate solvents. On the contrary, the easily de-solvated acetonitrile solvent required smaller pore dimensions (0.7-0.8 nm) to achieve the maximum specific capacitance.

The choice of solvent can also promote ion adsorption on the AC surface by optimising the initial electrode potential. Ho Lee et al. [77] reported on the tetrahydrofuran (THF)-facilitated improvement of the AC capacity. The authors showed that adding THF to the electrolyte (1M LiBF$_4$ in EC:DEC(3:7) vol%) resulted in a shift in the electrolyte electrostatic potential, increased ionic mobility and easier adsorption of BF$_4^-$ anion on the AC electrode surface. Ho Lee et al.[78] also reported on the enhanced rate performance of an AC/Li LiC achieved via the addition of 1,3,5-trifluoro benzene (TFB) in the electrolyte (1M LiBF$_4$ in EC:DEC(3:7) vol%).

2.1.3.2 Electrolyte salts

Several salts have been investigated with different degrees of dissociating ability, capacity and conductivities in carbonate solvent blends. Among the Li-salts, LiPF$_6$, LiTFSI, LiFSI, LiCF$_3$SO$_3$, LiClO4, and LiBF$_4$ are some notable mentions that have been explored. Amatucci et al. [4], emphasized the importance of optimizing the electrolyte salt capacity and molecular weight in LiC. The electrolyte salts LiPF$_6$,

50

$LiCF_3SO_3$, $LiClO_4$, and $LiBF_4$ were revealed to possess capacities of 176, 272, 252 and 286 mAh g^{-1}, respectively. Moreover, using electrolyte salts with high molecular weights could decrease the energy density of the LiC. Furthermore, the anions, in particular, influence the obtainable capacity of the AC electrode. The variation in electrochemical performance of the AC electrode using different lithium salts in the electrolyte can also be correlated with the dimensions of the de-solvated anions. Kato et al. [79] examined the influence of Li-salts with various anions on AC/LTO LiC performance. As expected, the Li-salt with the largest de-solvated anions dimensions had the lowest capacities. However, $LiBF_4$, with the smallest de-solvated anion dimensions, did not possess the largest specific capacity. The authors emphasized that the discrepancies were due to the lower conductivities of the $LiBF_4$ electrolyte, which was attributed to the lower dissociation constant observed for the BF_4^- anion compared to the others. Therefore, further demonstrates the importance of selecting appropriate electrolyte salts with de-solvated anion dimensions suited to the AC pores and an optimum balance in conductivities.

Having observed the relationship between the de-solvated anion dimensions and the capacity of the AC, researchers have implemented dual anion salts to maximize the available capacity through the adsorption of ions of various dimensions. In a notable work, Zhang et al. [80] investigated the electrochemical performance of electrolyte salt blends consisting of NEt_4BF_4 and $LiPF_6$ dissolved in singular PC or EC:DMC(1:1), compared to singular $LiPF_6$ or $LiBF_4$. $LiBF_4$ exhibited

inferior performance, having had the highest equivalent series resistance and lowest conductivity, necessitating the substitution with NEt_4BF_4. It was interesting to observe that the capacitance of the electrolyte blend (NEt_4BF_4 and $LiPF_6$) was higher than the singular $LiPF_6$ at low current densities. However, at high current densities, the contrary occurred. This may have been caused by increased competition between the dual anions at the AC pore entrance, creating a sieving effect and consequentially slightly lower capacities than singular $LiPF_6$. Moreover, the solvation shell contributed by the dissolving solvent also affected the performance and electrochemical stability.

The various alkali metal salts (derivatives of Li, Na and K) possess different stabilities and distinct electrochemical performances when used as electrolyte salts with the same AC and organic solvents. Stpie et al. [81] investigated the electrochemical behaviour of AC when exposed to different electrolytes based on Li, Na and K salts containing the anions (PF_6, FSI and TFSI) while dissolved in similar solvents. It was revealed that electrolytes based on the K-salts exhibited superior performances: higher ionic conductivity and faster ion diffusion within the AC micropores. Moreover, the larger K cation and "softer" character compared to Li facilitated lower interactions with the electrolyte decomposition active sites on the AC and displayed lower desolvation energies. Meanwhile, the strong acidic nature of Li and binding energy to the solvent caused the increased presence of solvents in the AC pores, where most decomposition reactions occur. The ease of desolvation of

the K cation reduces the amount of solvent in the pores; hence, solvent decomposition occurs mainly at the external surface.

2.1.4 Cell design

The hybrid nature of LiC necessitates meticulous design to counter the in-balances of the capacitive AC cathode and the energy-dense intercalation type anode. These in-balances are due to the sluggish kinetics of the anode, in contrast with the rapid charge storage by ion physisorption occurring on the AC cathode. Consequentially, inadequate cell design can present issues such as unutilized potential windows, electrode potential encroachment into unsafe electrolyte decomposition regions, poor cycle life, limited energy, and power density. The following section discusses recent cell design strategies to improve the performance of the AC.

2.1.4.1 Capacity balancing

Capacity balancing is a fundamental step required for the optimum performance of LiC due to the mismatch between the capacities of the AC cathode and the significantly larger anode material. High-power symmetric SC utilises a 1:1 direct cathode: anode balance, which guarantees high power along with the rapid physisorption kinetics of the AC material [82, 83]. However, if such ratios are utilized in LiC, for example, using the AC cathode (specific capacity < 60 mAh g^{-1}) and the HC anode (specific capacity > 360 mAh g^{-1}), the AC capacity would be completely charged before the anode. Moreover, the energy density is

reduced since the anode potential is underutilised and may swing towards unstable regions where electrolyte degradation is accelerated [84].

It has been demonstrated in several works that a cathode: anode mass ratio >4 is required to achieve very high energy densities in LiC [10, 85]. Using such high mass ratios enables complete utilisation of the anode capacity since an equal charge balance can be achieved between the AC cathode and the battery-type anode, improving the device capacity and energy density. Dsoke et al. [85] explicitly highlight the effect of electrode mass ratio on the performance of AC/ lithium titanate (LTO) LiC. The authors compared the performance of LiC of different electrode mass ratios, beginning from the classically balanced mass ratio of 4.17:1 derived from the experimentally obtained AC electrode capacity of 38.36 mAh g^{-1} and LTO electrode capacity of 160 mAh g^{-1}. Therefore, the AC electrode thickness was increased up to 4.17 times the initial mass while the LTO mass was kept constant. As the AC/LTO mass ratio increased, the energy density increased while the capacity retention decreased. It is worth noting that the cycle life of LiC with very high energy densities deteriorates faster when such high mass ratios are utilised to achieve similar capacities as the LiB counterparts. Moreover, the overall energy density of the cell is also significantly reduced after accounting for the weight of active materials, which are mostly subjected to weight and thickness constraints. Thus, demonstrating the significance of capacity balancing during cell design.

2.1.4.2 Operating potential window regulation

The operating potential window influences the AC's capacity, electrode stability, achievable energy, and power density. Operating beyond stable limits can lead to encroachment into regions where electrolyte decomposition may be accelerated at the upper or lower vertex potentials. Furthermore, the anodes deliver distinct electrochemical performances depending on the chosen region in the potential window [86]. Therefore, investigating the operating potential window of the AC and selecting appropriate regions on the anode where kinetics mismatch can be alleviated is necessary. Jin et al. [86] demonstrated a practical matching approach for selecting appropriate potential regions during the design and fabrication of an AC/HC LiC. The authors first determined the appropriate operating potential regions of the HC anode using a combination of galvanostatic charge and discharge analysis (GCD), galvanostatic intermittent titration technique (GITT) and electrochemical impedance spectroscopy (EIS) conducted at different potentials to observe the corresponding distinct electrochemical processes. After evaluating the appropriate region, the HC anode was pre-lithiated to enable operation within the chosen region, and matched with the appropriate mass balance to the AC cathode and working potential. Incorporating these processes improved the energy density, power density and cycle life.

Several operating potential limits for the AC cathodes have been utilized in various research, ranging from 1.5-4.6 V. Increasing the operating potential window enhances the capacity until a trade-off at these limits

where further increased potential does not correspond to increased capacity. Moreover, electrolyte decomposition is accelerated at these limits and accompanied by severe passivation of the AC electrode surface by electrolyte decomposition products. Furthermore, the cycling stability is also affected by faradaic processes, the magnitude of which may vary based on the chosen potential window. Zhang et al. [87] investigated the capacity retention of AC/HC LiC cycled in different potential windows: 2.0–4.0 V and 2.2-3.8 V. The capacity retention was 73.8% after 80 000 cycles in the former and 94.5% of the initial value after 200 000 cycles in the latter. Hence, this demonstrates the need to select appropriate upper and lower cut-off potentials. The critical selection of safe operating potential windows depends on the evaluation method, an objective widely explored by various researchers [19, 88]. Sun et al. [89] reported on a method for determining the operating potential of the AC cathode without the influence of the anode. The authors established that the stable potential limits can be obtained using the energy efficiency and the criterion that the second derivative of the S value plotted against the vertex potential, $d^2S/dU^2 < 0.05$. The operating potential limit of the AC in their study was determined to be from 2.2–3.9 V. However, these operating potential limits depend on the nature of the electrolyte (organic solvent and salt) and operating temperature. Other parameters such as the presence of oxygenated functional groups on the AC surface, binder type (CMC/SBR vs PTFE) and aluminium current collector (etched vs carbon coated) can significantly influence the operating potential window of the AC. Compared to the alternatives,

superior stabilities are obtained using coated collectors and PTFE binders [89].

Although the region below 1.5 V is generally avoided, Dsoke [90] investigated processes occurring when the AC was cycled in the region below 1.5 V and revealed distinct relationships between the potential limit, capacity and cycling stability. It was observed that 1.0 V represented a critical limit where the performance was severely impacted if the AC was cycled using this lower limit. However, changing the lower limit to 0.5 V, the AC capacity increased without a corresponding increase in the resistance and or negatively impacted cycling stability. Moreover, at further lower potential limits (0.2, 0.1 and 0.005 V), the capacity of the AC increased, but the cycling stability was affected.

2.1.4.3 Pre-lithiation

In contrast with the battery counterparts, LiC possess no Li source other than the Li ions in the electrolyte. However, during the initial cycling process, the formation of SEI on the anode and cathode can rapidly deplete the already limited Li ions in the cell. Therefore, a pre-lithiation step is necessary to increase the availability of Li ions for charge storage. Furthermore, the pre-lithiation also mitigates against Li depletion after the SEI formation on the anodes, resulting in enhanced cycling performance without changes in materials or device structure [91]. Moreover, sufficient Li ions allow the AC cathode to operate at a widened potential window through the adsorption of Li below the OCP and anion above the OCP. As a result, the capacity of the AC cathode is

increased, and the resulting energy density for the LiC is enhanced. Pre-lithiation also facilitates safe anode utilisation within the typical electrolyte decomposition limits < 0.8 V by forming an initial SEI with the excess metal ions.

Pre-lithiation is commonly achieved using various electrochemical or direct contact pre-lithiation techniques [91, 92]. Central to each method is a sacrificial Li source where cations migrate from and to the anode either under the influence of an externally applied electrochemical driving force or by internal or external short-circuiting after direct contact. The pre-lithiation step could also be conducted as a pre-assembly procedure, where the anode is pre-cycled with the Li source and the potential is regulated to the desired pre-lithiation degree before disassembly and reassembly of the final full cell with the intended cathode. In this case, two cell assembly steps are needed, which may complicate assembly line procedures in full-scale manufacturing and present additional contamination risks. Moreover, the direct contact method is usually conducted with the corresponding pure Li metal as the Li source. Consequently, the direct contact method is often uncontrollable, with a nonuniform degree of pre-lithiation since the strategy relies on direct contact between the Li metal and anode with no external controlling force. Besides, the risk of thermal runways, fire hazards and other issues associated with handling the highly reactive pure metal is significant and may pose serious concerns during large-scale assembly.

In response to the above concerns, a new pre-lithiation technique was developed, which involves incorporating inorganic or organic sacrificial compounds containing the Li cations as an alternative to using the highly reactive pure metal during pre-lithiation [92-94]. These sacrificial compounds are composited in the AC cathode during the electrode fabrication. The selection of sacrificial cathode pre-lithiation additives is based on the ability to irreversibly de-lithiate in the working potential window of the cathode and exhibit high volumetric or gravimetric capacities while remaining electrochemically, chemically and thermally stable under electrode processing conditions and after the de-lithiation. Examples of such additives include Li_2MoO_3 [95], Li_5FeO_4 [96], Li_2DHBN [97], Li_3N [98], $Li_2C_4O_4$ [94] and $Li_2C_4O_6$.

Park et al. [95, 96] used Li_2MoO_3 and Li_5FeO_4 as sacrificial pre-lithiation additives mixed with the AC electrode during fabrication. However, the oxidation of these materials occurs at high potentials (4.7 V), which are in regions where electrolyte oxidation is prominent, and the AC surface can easily be passivated, at the detriment of the surface charge storage capacity. Moreover, there is a remnant inactive mass in the cell, which subsequently decreases the specific energy of the LiC. The sacrificial salts, therefore, show more promise because they produce no residues after de-lithiation. The listed ternary salts only produce N_2 and CO_2 gas, which can be removed during the formation step. This is particularly important when using capacitive materials since any residue after the de-lithiation can block the pores or contribute to inactive masses in the cell. Arnaiz et al. [94] demonstrated an effective pre-lithiation strategy using

59

$Li_2C_4O_4$ as sacrificial pre-lithiation additives mixed with the AC cathode and paired with a HC anode. It was revealed in this work that the pre-lithiation process did not affect the performance of the AC. On the contrary, the rate performance of the recovered AC after the de-lithiation of the $Li_2C_4O_4$ agent was superior to the AC without the pre-lithiation. Post-mortem electrode examinations revealed void spaces in the AC after the pre-lithiation, attributed to the oxidation of $Li_2C_4O_4$ in the electrode. The electrode further exhibited microstructural changes, evidenced by the creation of additional meso and macroporosity in the AC. These microstructural changes on the AC electrode were beneficial for improved electrolyte accessibility and superior rate performance.

Some sacrificial pre-lithiation additives can serve as dual-functioning additives, pre-lithiating the anode while increasing the capacitance of the AC through pseudocapacitance. Zhang [99] demonstrated the use of Li-rich Li_2CuO_2 as a cathode pre-lithiation additive during the fabrication of AC/graphite LiC. The AC/Li_2CuO_2 cathode composite was revealed to behave as a pure capacitor when cycled between 2.8-4.2 V, yielding similar capacitance and capacity as the AC/Li half-cell. However, when the operating potential window was changed to 2.0-4.0 V, the remnant Li_2CuO_2, after irreversible de-lithiation in the first cycle (342 mAh g^{-1}), provided extra capacitance through pseudocapacitive behaviour (increased from 150 F g^{-1} to 189 F g^{-1}).

3   Experimental

3.1   Materials

Commercial activated carbon (YEC-8B) was purchased from Fuzhou Yihuan Carbon Co., Ltd. Lithium hexafluorophosphate (LiPF$_6$) (purity 99.94%), lithium chips, Ethylene carbonate (EC) (purity 99.9%), Ethyl methyl carbonate (EMC) (purity 99.9%), dimethyl carbonate (DMC) (purity 99.9%), and polytetrafluoroethylene (PTFE) (60 wt.%) were purchased from Sigma Aldrich. Electrolyte formulations used in this study were prepared in a moisture and oxygen-free glove box. Karl Fishers' titration was performed on all solvents and electrolytes, and their water content was determined to be less than 25 ppm. The different electrolytes/solvent combinations are summarised in Table 1. 1 M LiPF$_6$ salt concentration was used in all electrolytes.

Table 1: Composition of prepared electrolytes

Denotation	Salt	EC vol%	DMC vol%	EMC vol%
EC:DMC (3:7)	1M LiPF$_6$	30	70	-
EC:DMC (1:1)	1M LiPF$_6$	50	50	-
EC:DMC (7:3)	1M LiPF$_6$	70	30	-
EC:EMC (3:7)	1M LiPF$_6$	30	-	70
EC:EMC (1:1)	1M LiPF$_6$	50	-	50
EC:EMC (7:3)	1M LiPF$_6$	70	-	30

3.2   Electrode fabrication

Self-standing electrodes were assembled by mixing 92 wt.% AC powder and 8 wt.% PTFE binder into a dough, and roll pressed at 80 °C. The self-standing electrode was laminated at 160 °C onto a double-sided carbon-coated Al current collector with a hot rolling press (MTI-Corp). 15 mm discs were punched from the laminated electrode, weighed, and dried overnight in a vacuum oven at 140 °C. The active material thickness and loading were 100 µm and 5.7 mg cm^{-2}, respectively. Single-side coated commercial HC electrodes with an active material loading of 2.7 mg cm^{-2} were obtained from Beyonder AS and used without further treatment. Electrode discs of 15 mm and 16 mm were punched from the AC and HC electrode sheets, respectively, and dried overnight in a vacuum oven at 140 °C or 120 °C. After drying, the electrode discs were transferred to the glove box, where the cell assembly was performed.

3.3   Cell assembly

Half cells incorporating AC as the working electrode, lithium metal as the counter/reference electrode, symmetric cells (AC/AC), and AC/ Pre-lithiated HC full cells were assembled in the glove box using CR2032 type coin cells (Hohsen). Cellulose TF4030 (19 mm Ø) was used as the separator, and 100 µl of the prepared electrolyte was added to each cell.

In **paper IV**, the pre-lithiation of the HC was performed using HC/Li metal half cells. The pre-lithiation procedure was as follows: the cell was charged and discharged between 1.5-0.01 V for three cycles at 25 mA g^{-1}, upon which it was stopped at the last discharge with a targeted pre-lithiation capacity of 250 mAh g^{-1}. After the pre-lithiation, the cells were disassembled using a custom coin cell de-crimper (Holsen), and the electrodes were carefully extracted for full cell assembly.

3.4   Electrochemical analysis

3.4.1   Cyclic voltammetry

Cyclic voltammetry (CV) was conducted using an Autolab PGSTAT302N potentiostat from Metrohm. The operating potential window was determined in the half cells via progressive increase from OCP of the cell to 4.7 V with increments of 0.1 V. Three cycles were obtained at each potential window, using a scan rate of 0.5 mV s^{-1}.

3.4.2   Galvanostatic charge and discharge (GCD)

GCD analysis was performed using a Neware BTS8-5V10mA battery tester. The cells were cycled within the determined stable operating potential windows from CV, using current densities ranging from 1–1000 mA g^{-1}.

In **Paper II and III**, the assembled cells were subjected to galvanostatic charge and discharge (GCD) cycling at different current densities (0.1C

for 3 cycles, 0.5 C for 3 cycles, 1C, 2C, 5C, 10C, 20 C, 1C and 10C for 5 cycles; 1C = 42.6 mAh g^{-1}) in the potential range 3.0–4.2 V.

3.4.3 Floating voltage hold (FVH) stability test

The floating voltage ageing protocol consisted of a FVH at 4.2 V for 10 h with five consecutive capacity checks before and after each floating sequence to monitor the capacity fade. This procedure was repeated in a loop until the end-of-life criteria (80% capacity retention) was attained. The voltage drop was obtained intermittently from the fifth discharge cycle after each floating duration.

In **Paper III**, the FVH stability test on the symmetric cells were conducted using similar procedures as above, but this time with an FVH hold at 2.5 V.

In **Paper IV**, three formation cycles at 4.26 mA g^{-1} were conducted on fresh cells in the potential window 3-4.2 V, after which five GCD capacity check cycles at 213 mA g^{-1} (based on the mass of the AC) were conducted before and after every 10 h FVH at 4.2 V.

3.4.4 Electrochemical impedance spectroscopy (EIS)

EIS measurements were obtained using an Autolab PGSTAT302N potentiostat from Metrohm at OCP with an applied potential of 5 mV in

the frequency range of 100 kHz to 0.01 Hz. The EIS spectra were fitted using the *impedance.py* package in PYTHON.

In **Paper II**, EIS was acquired after every cumulative 100 h of floating on the cycled cells until 80% capacity retention, and periodically afterwards until 0% capacity retention.

In **Paper III**, EIS was acquired before and after the floating voltage stability tests using symmetric cells assembled with the different electrolytes.

In **Paper IV**, EIS was acquired from the AC/HC pre-lithiated full cells before and after cycling with the different electrolytes. The cycled full cells were subsequently disassembled and reassembled into symmetric AC/AC or HC/HC cells for further EIS analysis.

3.5   Sample characterisation

Cell disassembly was done in the Argon glovebox to examine the AC and HC electrode at different conditions. The cells were de-crimped using a custom-type CR2032 de-crimper (Hohsen). Electrodes for post-mortem analysis were extracted from disassembled coin cells in the glove box, rinsed with DMC to remove excess electrolytes and dried under vacuum before characterisation. Sample exposure to the ambient atmosphere was minimised as much as possible.

3.5.1 Nitrogen physisorption

Nitrogen physisorption analysis was performed using a Tristar II micromeritics surface and pore volume analyser. Prior to measurements, samples were degassed under vacuum using a Micromeritics VacPrep 061 for 24 h at 80 ºC while ensuring limited exposure to the ambient atmosphere during handling. The physisorption isotherms were acquired across a pressure range of $0.0002 < P/Po < 1$. The total pore volume was obtained using the quantity of gas adsorbed at relative pressures of 0.99. The specific surface area and pore size distributions were determined using the Brunauer-Emmett-Teller (BET) and Nonlocal Density functional theory (NLDFT) methods.

3.5.2 Scanning electron microscopy

Surface morphology was examined using Supra 35VP (ZEISS) field emission gun scanning electron microscope (FEG-SEM). The samples were adhered to a carbon tape without any coating during the examination. Energy dispersive spectroscopy (EDX) analysis was acquired using a JEM-2100 plus (JEOL) electron microscope at 200 kV coupled with the SEM.

3.5.3 Raman spectroscopy

Raman spectra were obtained using a Renishaw InVia Qontor Raman Microscope. The spectra were acquired using a 532 nm laser wavelength, x20 objective lens, exposure time of 20 s and 3 accumulations.

3.5.4 X-ray photoelectron spectroscopy

XPS data were collected with a Thermo Scientific ESCALAB 250 spectrometer, using a focused monochromatised Al Kα radiation ($h\nu$ = 1486.6 eV). The pressure was maintained at 10^{-8} mBar, and charge neutralisation was applied. The analysed area of the samples was an ellipse with a dimension of 450x900 µm. The XPS introduction chamber was directly connected to an argon glovebox to protect the sample from contact with air and moisture during the transfer. Spectra deconvolution and peak fitting were performed using Origin software and Gaussian peak fits.

4   Results and discussion

4.1   *Revealing mechanisms of activated carbon capacity fade (Paper II)*

In this paper, the capacity fade mechanisms of the AC were investigated by electrochemical and post-mortem characterisation at different stages.

4.1.1   *Electrochemical analysis*

The capacity retention during the floating voltage is presented in Figure 1, while the rate performance and respective charge/discharge curves at different C-rates are displayed in Appendix B, Figure S1 in Supporting Information (SI). The AC electrode endured up to 950 h of floating voltage prior to reaching 80 % capacity retention and approximately 1900 h before reaching 0% capacity retention. The aging profile could be divided into three phases (denoted by the dashed lines) based on the distinct features and slope of the capacity retention profile. The exact position of the phases was determined by fitting the data to straight lines with varying slopes and marking the intersection of the lines. The phases corresponded to the capacity retention profile with three distinct features. Phase one is characterised by an initial increase in capacity, followed by a stable period which can be fitted to a horizontal straight line. After 350 h, the capacity retention decreases very slowly up to 750 h. The third phase is characterised by accelerated capacity fade in a steep slope until 0% capacity retention at 1900 h.

68
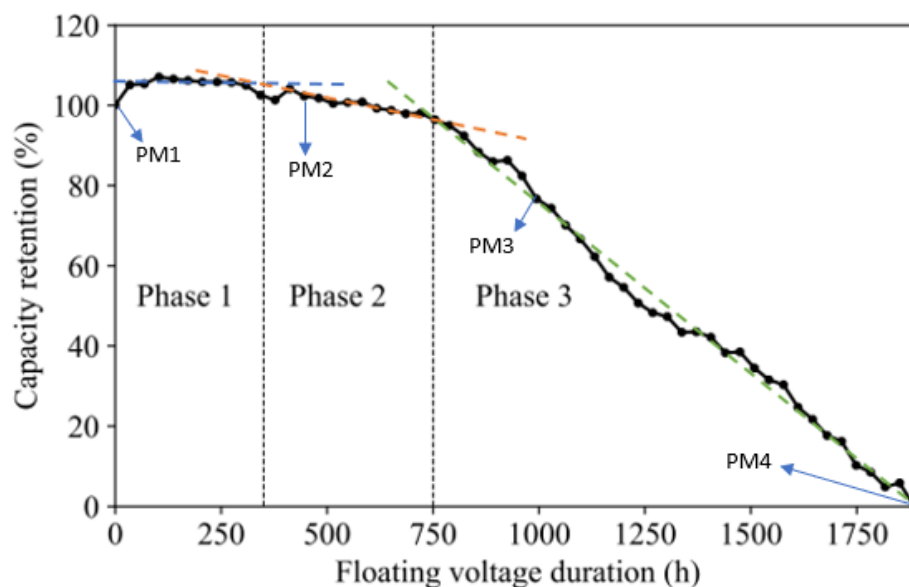
Figure 1: Capacity retention during the floating voltage stability test; three distinct phases of capacity fade were identified. The arrows mark the FVH time points when the samples were obtained.

Samples for the post-mortem (PM) analysis were obtained at the respective positions denoted by PM in Figure 1 to reveal the changes in the AC electrode surface. These points coincided with the state of the AC at different phases and was correlated with the capacity fade. The AC electrode after 450 h of FVH was without any visible capacity fade but was also studied to disclose possible surface transformations in phase two. The results from the post-mortem characterisations are presented in section 4.1.2. All the characterised samples are summarised in Table 2.

Table 2: Denotations and descriptions of the samples

Denotations	Descriptions
AC powder	Dried AC powder
AC electrode	Dried AC electrode
Blank electrode	AC electrode immersed in electrolyte (uncycled)
0 h of FVH	AC electrode after GCD cycles but 0 h of FVH (cell at 100% capacity retention)
450 h of FVH	AC electrode after 450 h of FVH (cell at near 100% capacity retention)
950 h of FVH	AC electrode after 950 h of FVH (cell at 80% capacity retention)
1900 h of FVH	AC electrode after 1900 h of FVH (cell at 0% capacity retention)

The floating voltage stability test was complemented by EIS to reveal changes at the active material/electrolyte interfaces in relation to the state of capacity retention of the cell. The EIS spectra were acquired before floating (0 h) and after every 100 h of floating until 950 h when the cell was at 80% capacity retention, and periodically until 1900 h when the cell was at 0% capacity retention. The obtained EIS spectra are presented in Figure 2a.
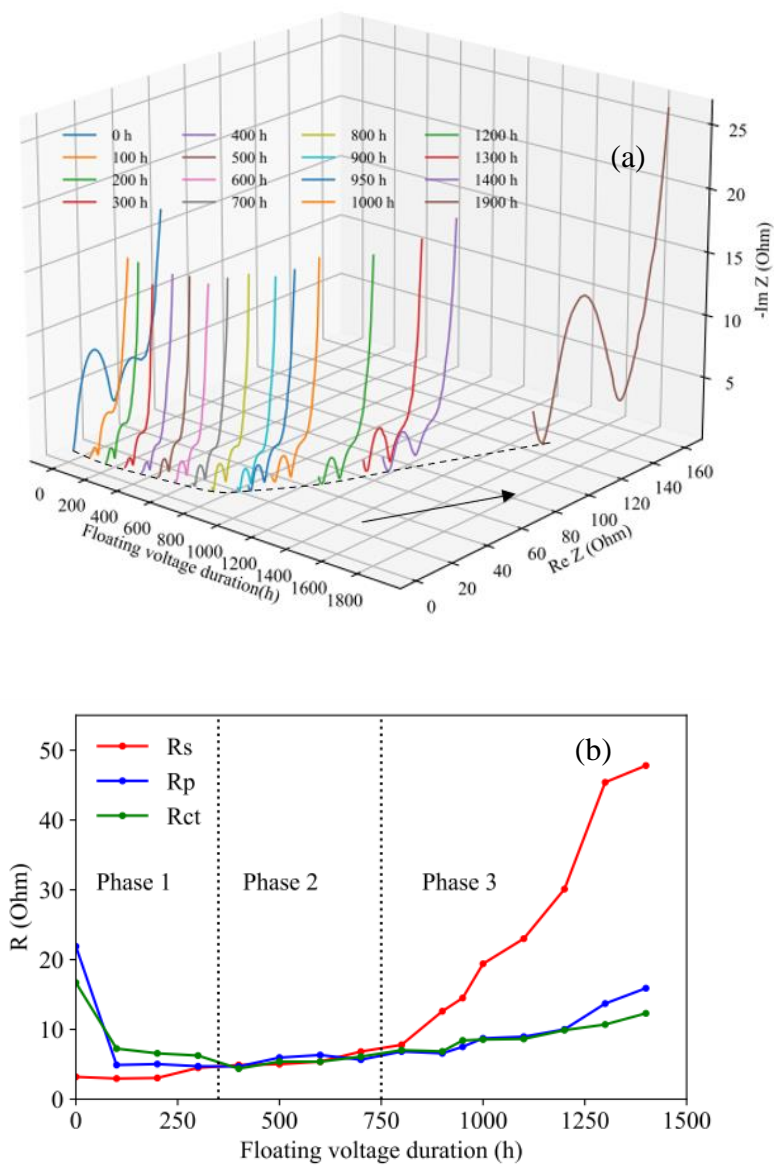
Figure 2 (a) 3D EIS spectra after different durations of floating; (b) Resistance parameters (Rs, Rp, Rct) after fitting.

The spectra were characterised by two semi circles at the high to medium frequency regions associated with the passivation layer impedance (Rp) and charge transfer impedance (Rct), a 45-degree sloping line at low frequencies attributed to Warburg diffusion (W) impedance, and a vertical straight line representing the capacitance (C). As the floating progressed, the spectra were gradually transformed at the high frequency region with the appearance of a conspicuous negatively sloped inverted line. The length and slope of this feature increased as the duration of aging progressed. The origin of this feature was ambiguous and could be due to a capacitive behaviour/artefact, which might have originated from the increasing active material and contact resistance usually obtained at high frequencies. To simplify the discussion, Rs was assigned to represent the bulk electrolyte resistance and active material/current collector contact resistance, which was the point at high frequency when the inverted sloping line intercepted with the real axis. The impedance spectra were fitted with similar circuits as reported in literature [10, 100]. The evolution of the resistance Rs, Rp and Rct obtained from the fitting as the floating time progressed are presented in Figure 2b. The deconvoluted R-CPE loops are illustrated in Appendix B, Figure S2 in SI, while the values of the fitting parameters are summarised in Appendix B, Table S1.

In Figure 2b, Rs remained relatively constant in phase one as the floating voltage progressed, which implied that the bulk solution resistance and contact resistances were not altered in this phase and hence did not affect the capacity. On the contrary, Rp and Rct were 22 Ohm and 17 ohms

before the floating but decreased significantly to around 5 ohms at the end of phase one. The trend for Rp and Rct in phase one suggests a reformation of the passivating deposits at the electrode interfaces owing to electrochemical activation and improved accessibility of electrolyte ions at the surface [100]. The electrochemical activation may have opened more pores on the AC surface for adsorption of the PF_6^- anions during the floating voltage charge, which resulted in the slight capacity increase. In phase two, the increase in Rs signalled electrolyte decomposition and accumulation of degradation products that coincided with a steady decrease in capacity. Meanwhile, the relatively stable Rp and Rct suggested that the initially formed passivating deposits remained unchanged. However, the overlayed R-CPE loops in Figure S2b and e, indicated some slight increase in Rp and Rct, which implied some transformation of the passivating deposits and increased charge transfer resistance. Therefore, the capacity fade in phase two could have been instigated by reduced accessibility of electrolyte moieties into the electrode surface, together with the effect of diminished PF_6^- anions for charge storage following the electrolyte decomposition.

In phase three, the capacity retention progressively decreased with a 45-degree slope line to near zero. On the contrary, the Rs value began to rise in a 45-degree trend, which inferred that electrolyte resistance/electrolyte degradation and accumulation of degradation products was substantially accelerated in this phase. Also, Rp and Rct increased significantly to 16 ohm and 12 ohm after 1400 h of floating, which was almost 3 times the value at the end of phase one. In contrast, the Rs increased to 47.8 Ohm

after 1400 h, which was almost 10 times greater than the value at the end of phase one. This further implied that the electrolyte could have been substantially decomposed after 750 h, while the growth of the inverted vertical sloping peak at high frequencies (Figure 2a) suggested that the artefact was strongly related to the electrochemical aging of the cell since it considerably increased towards the end of life.

The initial deterioration up to 80% capacity retention (950 h) could have been dominated by transformation of the AC electrode surface by the degradation products and gradual reduction of PF_6^- anions. Nevertheless, the contribution of the lithium counter electrode cannot be ignored, because the rapidly expanded Rp in phase three could be attributed to the deposition of irregular aggregates of dead lithium and pulverisation of the initial formed surface passivating film on the lithium counter electrode [101]. More active sites might have been created upon which electrolyte degradation was accelerated as indicated by the exponential increase in Rs. Hence, electrolyte starvation in phase three may have significantly contributed to the capacity fade in this phase.

4.1.2 Degradation mechanism

The results from the electrochemical analysis using combined floating voltage and intermittent EIS analysis suggested transformations of the electrode surfaces as the capacity fade progressed. In this section, different characterisation techniques are employed to reveal the nature

of the surface changes and deposits on the electrodes at different stages, which contributed to the capacity fade.
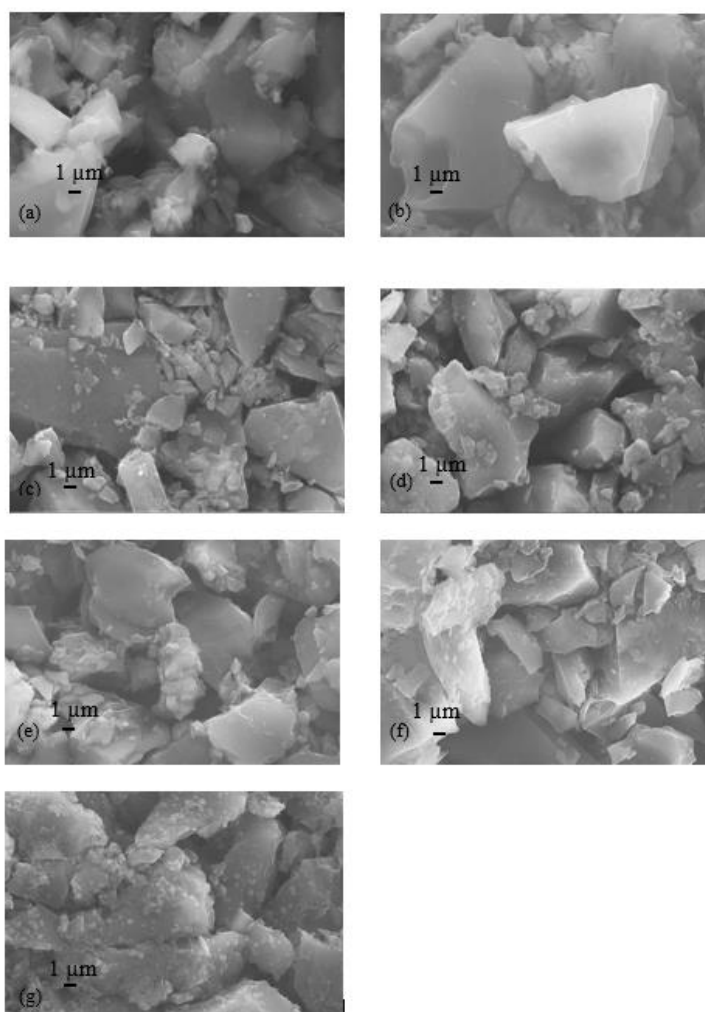
Figure 3: SEM images of the (a) AC powder, (b) AC electrode, (c) Blank electrode, AC electrode at (d) 0 h of FVH, (e) 450 h of FVH, (f) 950 h of FVH, and (g) 1900 h of FVH. All images were taken at 10 000X magnification.

75

SEM was used to probe the changes in surface morphology of the AC. From Figure 3a and b, one can distinguish the effect of the PTFE binder as reflected by the fused and compacted nature of dry electrode, in contrast with the isolated grains of the AC powder. The compacted nature indicated a reduced surface area of the AC electrode when compared to the AC powder due to the PTFE binder penetration in the pores. Moreover, some aggregates of passivating deposited species were observed in the SEM image of the blank electrode (Figure 3c). Therefore, by immersing the AC electrode in the electrolyte, though without cycling, the passivating deposits may have covered some of the available surface area or occupied the pores. The passivating deposits are likely formed from reactions between the electrolyte species and oxygen functionalities on the surface of the AC electrode [81, 102, 103].

The electrode at 0 h of FVH had undergone few GCD cycles but exhibited similar passivating deposits at the surface (Figure 3d). However, the edges of the AC grains appeared to be etched, possibly from electrochemical activation due to the cycling [80]. As cycling progressed towards phase two (450 h of FVH) and three (950 h of FVH), the passivating deposits increased due to substantial deposition of insoluble electrolyte degradation products (Figure 3e and f). Therefore, the capacity fade could be related to the loss of surface area and pores for ion adsorption.

At 1900 h of FVH (Figure 3g) with 0 % capacity retention, the AC electrode surface was completely covered by the aggregated

decomposition products and appeared to be of a fused nature. In addition, some new spherical deposits were observed. EDX analysis of these spherical spots (Appendix B, Figure S3) revealed that they were predominantly composed of carbon (69%), oxygen (8%), fluorine (20%) and phosphorus (2%), which are elemental constituents of the electrolyte and electrolyte degradation products.

Nitrogen physisorption analysis was used in probing the pore property transformation at different stages. The physisorption isotherms (Figure 4a) display type I/IV characteristic according to the IUPAC classification, with predominantly micropores and some mesopores in the AC powder. The incorporation of the PTFE binder reduced the surface area and pore volume by around 20 % and 7 % (Figure 4b). The reductions occurred mostly in the micropores where some of the PTFE binder was absorbed, while the slight reduction in the mesopores was due to compaction during the electrode fabrication process. The appearance of a hysteresis loop upon contact with the electrolyte (blank electrode) and further growth upon electrochemical cycling (0 h of FVH), inferred that the pore structure of the AC electrode was indeed modified by the electrochemical process.
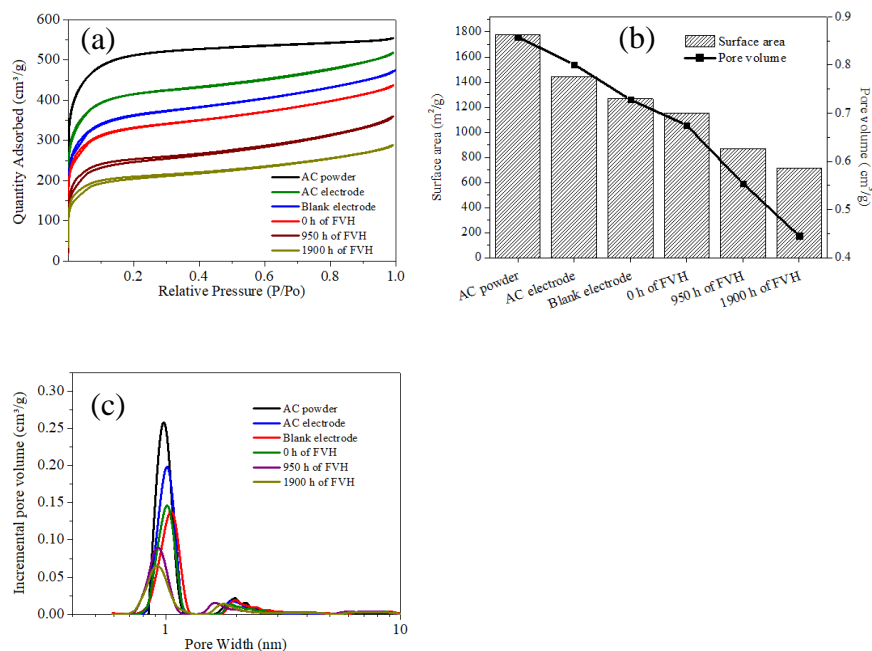
Figure 4 (a) Nitrogen adsorption and desorption isotherms, (b) BET Surface area and pore volume, (c) Pore size distributions of AC powder and different AC electrodes

Further reductions in surface area and pore volume were observed as the AC electrode (Blank electrode) was contacted with the electrolyte. The reductions are in accordance with the observed passivating deposits in SEM study. The AC electrode at 0 h of FVH had a remarkable increase in micropores compared to the blank electrode, although the total surface area and pore volume decreased. Therefore, the electrochemical activation process increased the micropores for charge storage and was responsible for the increased capacity retention beyond 100 % in phase one [80, 104-106]. The electrochemical activation may have opened pores that were blocked by the passivating deposits, although the

decrease in total surface area and pore volume may be related to slight electrolyte degradation after the few GCD cycles. At 950 h of FVH, the surface area and pore volume decreased further, which inferred that electrolyte decomposition continued. The approximately 20 % capacity loss was commensurate with the reduction in micropore volume after comparing the cumulative volume of micropores of the electrode (0.3491 cm^3 g^{-1}) with the initial volume at 0 h of floating (0.4662 cm^3 g^{-1}). This was expected, since the micropores were predominantly where ion adsorption and charge storage occurred. Moreover, the isotherm at 950 h of FVH was slightly modified, with a more pronounced hysteresis loop occurring within relative pressure of 0-0.4, in contrast with the barely visible hysteresis loop at 0 h of FVH. Hence, the pores were also modified by possible reactions with electrolyte degradation products such as HF and PF$_5$ that could erode active material and passivating deposits [107, 108]. Furthermore, at 950 h of FVH, the electrode further broadened the pore size distribution, with the presence of larger micropores around 1.4-1.6 nm and smaller micropores < 0.8 nm.

It was interesting to observe that the AC electrode at 1900 h of FVH still retained around 40-50 % of the original surface area and pore volume. Thus, the failure in phase three could be certainly ascribed to the loss of ionic species from accelerated electrolyte degradation caused by electrode structural integrity alteration and eventual pulverisation.

XPS was used to study the surface species evolution at different stages. The C1s spectra of the AC powder revealed the presence of six peaks at

binding energies of 283.7, 284.2, 284.9, 285.5, 286.8 and 288.9 eV, corresponding to sp (C≡C), AC (C=C), CH_x (C-C), C-OH, C-O and C=O surface groups (Figure 5a). The C=C peak was characteristic of AC due to the abundant sp^2 like species and is correlated to the activation temperature [109]. The elemental composition of the AC powder was determined to be carbon (97.7 %) and oxygen (2.3 %). The C1s spectra of the AC electrode (Figure 5b) revealed similar peaks as the AC powder but with a new peak at 291.9 eV, corresponding to the CF_2 group from the PTFE binder. The oxygenated functionalities on AC are responsible for electrolyte degradation and the passivating deposits observed at the surface of the blank electrode (Figure 3c) [81, 102, 103].
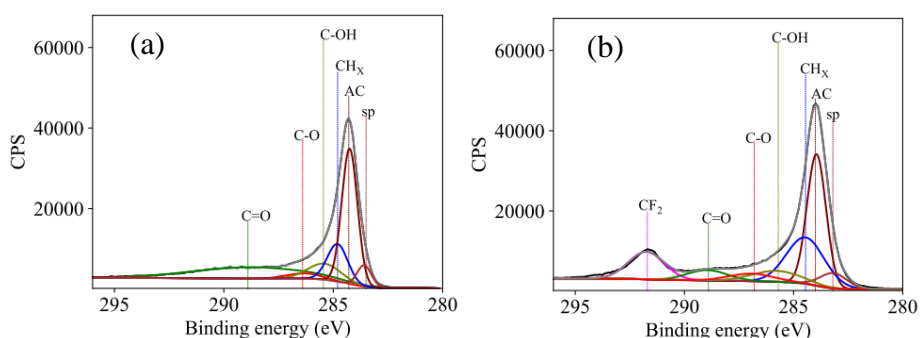
Figure 5: Deconvoluted C1s spectra of (a)AC powder, (b) AC electrode.

The deconvoluted C1s, F1s and P2p spectra of electrodes after contact with the electrolyte are presented in Figure 6. The C1s spectra of the blank electrode (Figure 6a) showed peaks at 284.2, 286.5, 288.2, 290.1 and 291.9 eV, assigned to the C=C, C-O, C=O, CO_3 and CF_2 groups. The

disappearance of the sp peak indicate that some carbon species were reacted. It is also interesting to see that the asymmetric conducting carbon shape was modified, and the PTFE intensity was increased in comparison to the C1s spectra of the AC electrode (Figure 5b). The increased CF_2 intensity suggests that contact with the electrolyte exposed more PTFE at the surface after reacting with the oxygenated carbon species on the AC electrode. In the P2p spectra, $Li_xPO_yF_z$ and polyphosphates were identified at 133.7 and 135.5 eV, while LiF, $Li_xPO_yF_z$ and CF_2 species were identified at 685.1, 686.4 and 689.1 eV in the F1s spectra. These species together with the oxygenated carbon species are the products of $LiPF_6$ and the carbonate solvent decomposition after nucleophilic attack by surface oxygen species and moisture in the pores. Moreover, the LiF species could also come from the ion paired $LiPF_6$. LiF and PF_5 are the equilibrium decomposition products of ion paired $LiPF_6$, which is commonly present in incompletely dissociated $LiPF_6$ [107, 110, 111]. PF_5 is also responsible for inducing solvent degradation and other parasitic reactions that may form HF, which is detrimental to active material and interfacial stability [107, 110, 111].
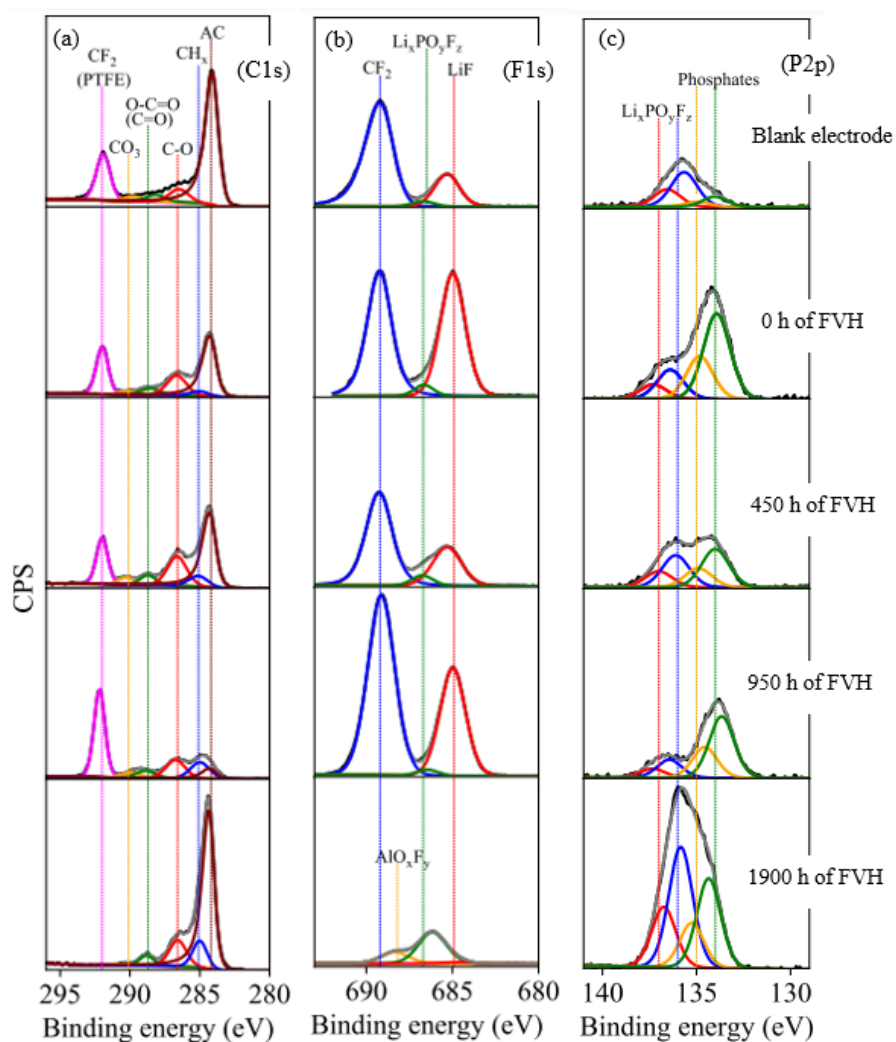
Figure 6: Deconvoluted XPS spectra showing the (a) C1s, (b) P2p, and (c) F1s peaks of the AC electrode at different stages of FVH after contact with the electrolyte.

The diminished AC peak in the C1s spectra for the electrode at 0 h of FVH (Figure 6a) and the increase of the PTFE peak and oxygenated

carbons are ascribed to surface passivation and continued electrolyte salt and carbonate solvent decomposition. Furthermore, the F1s and P2p spectra of the electrode at 0 h of FVH (Figure 6b and c) showed increased intensities of LiF and phosphate species, confirming enhanced electrolyte degradation after the few GCD cycles. This correlates with the reduced surface area from the nitrogen physisorption analysis.

The C1s spectra of the electrodes after 450 h of FVH and at 950 h of FVH exhibited similar oxygenated carbon species. The further diminished AC peak signified intense surface coverage of the electrode, while the increased CF_2 band suggested exposed/exfoliated binder after surface restructuring. The P2p and F1s spectra showed increased presence of phosphates, $Li_xPO_yF_z$ and LiF, with the latter being the dominant specie. Thus, the capacity fade observed in phase three was caused by enhanced anion decomposition. This was in combination with restricted access of the already depleted ionic moieties to the pores of the AC electrode with decreased pore volumes.

At 1900 h of FVH, it was interesting to see that the intensity of AC was significantly increased, in comparison with the electrode after 950 h of FVH. We speculate that this may be related to the spherical amorphous specie observed in SEM (Figure 3g) or caused by AC electrode pulverisation from possible binder degradation. Moreover, the disappearance of the CF_2 band at 1900 h of FVH suggested that either the AC electrode surface was completely covered by this newly deposited amorphous carbon, or the PTFE binder reacted with adsorbed

lithium on the surface of the electrode. Although PTFE is known to be very stable and unreactive, it could be reduced upon contact with lithium to form an amorphous carbon specie and LiF, as shown below [112]:

$$-(-CF_2-)_n- + 2n\ Li \longrightarrow n\ C\ (amorphous) + 2n\ LiF$$
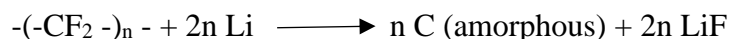
The presence of AlO_xF_y species in the F1s spectra at 1900 h of FVH (Figure 6b) supports fluorinated attack of the current collector, which could indicate the pulverisation of the AC electrode. Meanwhile, the increased $Li_xPO_yF_z$ and phosphates species signify total salt degradation at 1900 h of FVH (Figure 6c).

Raman spectroscopy was conducted to investigate changes in graphitic order and defects during floating. The spectra were deconvoluted using origin software and exhibited five peaks as illustrated in Figure 7a. The two prominent peaks at around 1350 and 1580 cm^{-1} are the characteristic D and G bands. The latter is attributed to the in-plane vibrations of sp^2 hybridised carbon, while the former is attributed to out of plane vibrations arising from structural defects and multiphases in the carbon structure [113]. The D_1 band at 1179 cm^{-1} is assigned to impurities in the graphitic lattice, while the D_2 band at 1493 cm^{-1} corresponds to the stacking defects in the graphene layer [113] and the presence of sp^2 amorphous carbon [114]. The D_3 band at 1653 cm^{-1} is assigned to disorder in the surface graphene layers [113, 115, 116].
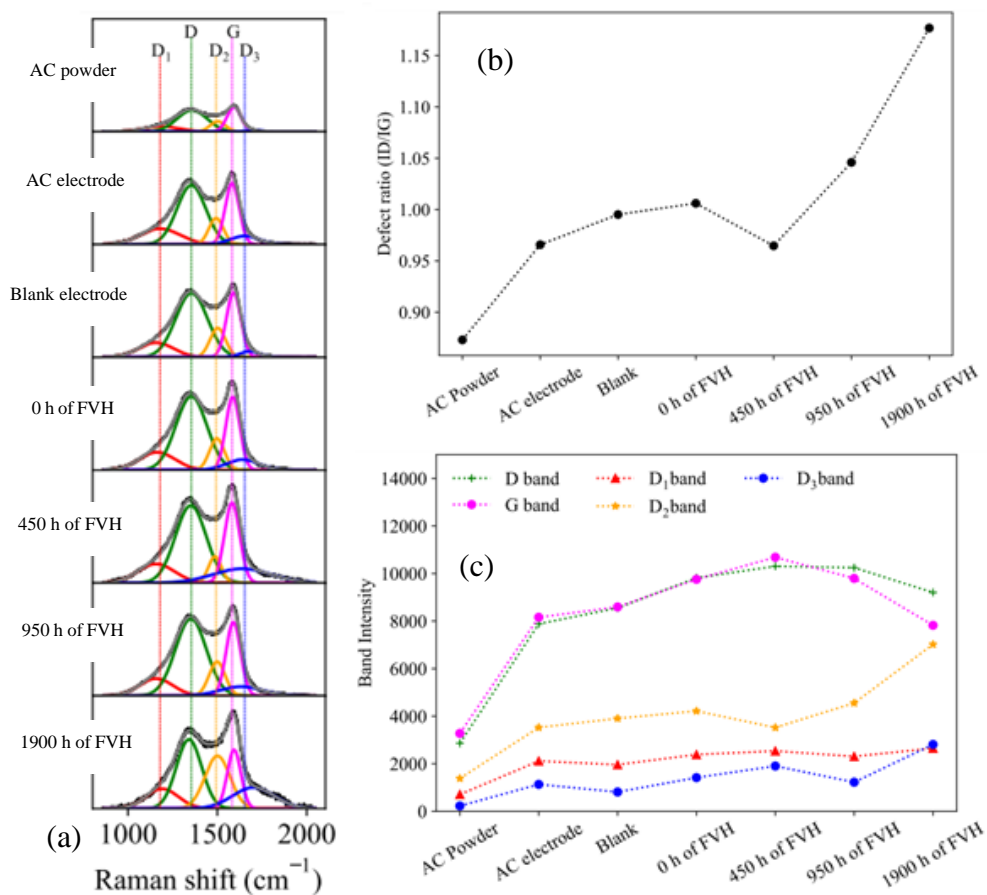
Figure 7: (a) Deconvoluted Raman spectra, (b) Defect ratio, and (c) Comparison of band intensities of the activated carbon electrode at different stages. The I_d/I_g ratio was calculated from the intensity of the D and G bands.

The defect ratio was calculated from the intensities of the D and G band (Figure 7b). The defect level increased as the AC powder was transformed to the AC electrode and subjected to electrochemical

cycling. The defects originated from PTFE addition and deposits of electrolyte degradation products at the AC surface. Moreover, the decrease in the defect ratio after 450 h of FVH was caused by increased graphitisation as evidenced by the band intensities (Figure 7c). The band intensities in Figure 7c showed that the D and G band increased in a continuous trend until the plateau at 450 h of FVH. Beyond this point, increased D_2 bands were responsible for the increased defects since the other defective bands (D_1 and D_3) remained relatively the same.

At 950 h of FVH, the defect ratio increased again and reached maximum after 1900 h of FVH. Hence, increased defects also contributed to the capacity fade. The increased defect level is synonymous with increased electrode resistance and reduced particle to particle conductivity [117]. Moreover, the continuously increasing D_2 band at 950 h and 1900 h of FVH meant that the stacking defects in the graphitised carbon structure was significant. Besides, it might also be related to the increased presence of sp^2 carbons formed after electrochemical oxidisation of the AC electrode by electrolyte species or binder exfoliation and electrode pulverisation discussed earlier.

4.2 Enhanced activated carbon lithium-ion capacitor electrochemical stability through electrolyte dielectric optimisation (Paper III)

In this paper, the electrolyte dielectric was found to affect the electrochemical stability of the AC in half cells with Lithium counter electrodes and symmetric AC/AC full cells. Therefore, electrolytes with high dielectric possessed superior stabilities due to delayed PF_6^- degradation.

Dielectric constants of solvent mixtures influence several properties of the electrolyte such as ionic conductivity, solvation ability, ion dissociation, ionic mobility, electrochemical stability, chemical equilibrium of ionic moieties, reaction rates and mechanism [118]. The dielectric constant of EC, DMC and EMC is 90.03, 3.107 and 2.9, respectively [118-120]. For binary solvent mixtures, the resulting dielectric constants for EC:DMC(3:7), EC:DMC(1:1) and EC:DMC(7:3) are 18.1, 32.8, and 50 respectively, which follow an increasing trend with increased EC% in the solvent mixture [118, 119, 121]. The EC:EMC mixtures have similar dielectric constants as the EC:DMC mixtures due to the comparable molecular structure and dielectric constants of singular DMC and EMC.

4.2.1   Nitrogen physisorption study

Nitrogen physisorption analysis of the AC powder (Appendix C, Figure S1a in the Supporting Information) revealed type I/IV isotherm according to IUPAC classification, suggesting some degree of mesoporosity alongside high microporosity. The BET surface area and pore volume are 1773 m^2 g^{-1} and 0.84 cm^3 g^{-1}, respectively. Pore size distribution analysis confirms that the AC had large volume of micropores (Appendix C, Figure S1b), which are suitable for adsorption of solvated and de-solvated electrolyte ions. The mesoporosity is beneficial to facilitate electrolyte transport and accessibility to the micropores.

4.2.2   Operating potential window

CV was conducted using AC/Li half cells to determine the stable operating potential window above the open circuit potential (OCP). The voltammograms at various potential windows for EC:DMC(3:7), EC:DMC(1:1) and EC:DMC(7:3) are presented in Figure 8. The voltammograms of EC:EMC electrolytes showed similar results as the EC:DMC and are presented in Appendix C, Figure S2. Therefore, the EC:DMC electrolytes would be discussed. All the voltammograms exhibited rectangular box like shapes which is characteristic of voltammograms from AC based electrochemical double layer capacitors and signifies reversible adsorption and desorption of PF_6^- anions as the charge storage mechanism when scanning above the OCP [24, 80]. The

electrolytes exhibited similar maximum operating potential of 4.2 V, in accordance with an earlier study [122]. Above 4.2 V, a pronounced increase in faradaic current was observed, implying electrolyte decomposition. However, remarkable differences were observed at higher potentials, whereby the magnitude of the peak current decreased as the EC ratio was increased in the electrolytes. This feature is attributed to the formation of a protective surface passivation layer on the electrodes that prevents further electrolyte decomposition. The passivation film is formed from the decomposition of solvents contained in the solvation sheath of the ions, after surpassing the limits of the LUMO and HUMO of the electrodes [123]. In electrolytes with EC/Li coordination >3, the bulk of the solvation sheath is dominated by EC, although some participation of the DMC molecules has been reported [124]. However, EC retains the bulk of the solvation sheath at very high EC% in binary mixtures, and this further influences the nature of the protective passivation layer formed on the electrode surface. Passivation films formed in electrolytes with high EC% offer effective protection against continuous solvent co-intercalation in the graphene layers and decomposition on the AC surface [123, 125, 126].
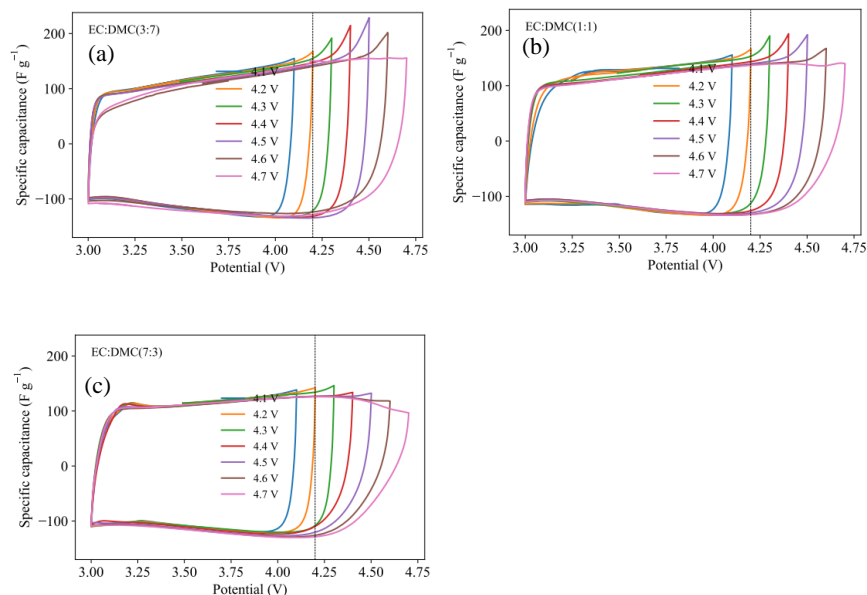
Figure 8: Cyclic voltammograms for (a) EC:DMC(3:7), (b) EC:DMC(1:1), and (c) EC:DMC(7:3). The dotted line indicates the maximum operating potential.

Moreover, the de-solvation energy increases with EC% and consequently affects ion diffusion through the passivation film, since both de-solvated and solvated ions take part in charge storage. This is reflected in the capacitance obtained because the de-solvation becomes the rate-limiting step during charge storage [124]. Electrolytes with EC:DMC ratios of 3:7 and 1:1 displayed similar specific capacitance around 140 F g^{-1} at the determined operating potential window. While EC:DMC(7:3) had lower capacitance of 114 F g^{-1} due to high de-solvation energy and possible solution diffusion hinderance.

4.2.3 Rate performance

Rate performance of the electrolytes was studied via GCD analysis at various current densities in the stable operating potential window determined from CV (3-4.2V). The charge and discharge profile at various C-rates for EC:DMC (3:7), EC:DMC(1:1) and EC:DMC(7:3) are shown in Figure 9a-c, while for the EC:EMC electrolytes are presented in Appendix C, Figure S3. The rate performance of the electrolytes is compared in Figure 9d. The current densities 42.6, 85.2, 213, 426 and 852 mA g^{-1} correspond to discharge durations of approximately 60, 30, 12, 6 and 3 minutes, respectively. The electrolytes displayed somewhat similar specific capacities within 39-45 mAh g^{-1}, though marginally higher capacities were obtained for EC:DMC(1:1). This is explained by a favourable compromise between conductivity and viscosity. Meanwhile, the EC:DMC/EMC(7:3) electrolytes had the lowest capacities due to high de-solvation energy and increased viscosity that could impact ionic mobility and diffusional resistance, especially at high discharge rates.
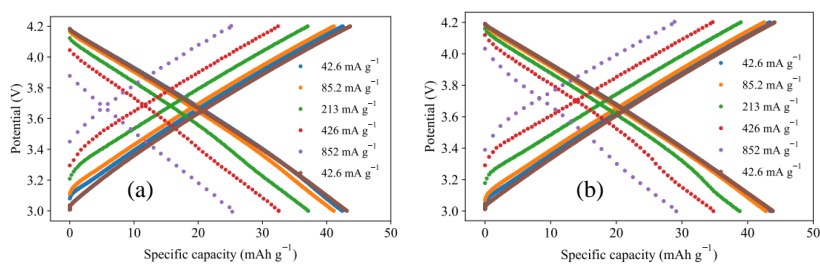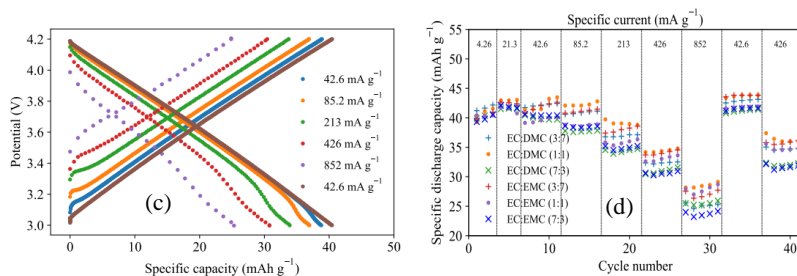
Figure 9: Charge and discharge capacity plots at different C-rates for (a) EC:DMC (3:7), (b) EC:DMC(1:1), and (c) EC:DMC(1:1); (d) Rate performance of the different electrolytes.

4.2.4 Electrochemical stability

The influence of EC and the electrolyte dielectric on the cycling stability was investigated using sustained floating voltage hold (FVH) at the maximum upper vertex potential (4.2 V) determined from CV. Implementing the floating voltage protocol ensured that the anion stability in particular, was tested under severe conditions of sustained voltage holds at 4.2 V. This is in contrast with the usual galvanostatic cycling where thousands-millions of cycles are needed to evaluate active material cycling stability, but not enough time is spent at the maximum potential where most of the degradation occurs. The results from the floating voltage stability tests using AC/Li half cells are presented in Figure 10.

Figure 10a revealed improved electrochemical stability with increased EC% and conversely the electrolyte dielectric. The electrolytes EC:DMC/EMC(3:7) retained 80% of their capacity even after 750 h of

floating voltage, while EC:DMC/EMC(1:1) endured up to 950 h of floating voltage prior to 80% capacity retention. EC:DMC/EMC(7:3) on the other hand, displayed more impressive stability with up to 1000 h of floating voltage duration at 80 % capacity retention. The ohmic drop during the floating test (Figure 10b) showed that the 7:3 electrolytes had higher initial internal resistances than the other solvent combinations, which was most likely due to the higher viscosities. However, as cycling progressed, the increase in the internal resistance for the 3:7 electrolytes is more severe than for the 1:1 and 7:3 electrolytes. The increased internal resistance is possibly related to electrolyte degradation at the active material surface. Therefore, the electrochemical stability was improved with increased EC ratio. The improved stability is further demonstrated by the charge and discharge plots of EC:DMC(3:7), EC:DMC(1:1) and EC: DMC (7:3) after different durations of FVH (0, 200, 500, 750 and 950 h) (Figure 10c-e). Specifically, at 750 and 950 h, EC:DMC(3:7) had specific capacities of 31 and 21.7 mAh g^{-1}, while EC:DMC(1:1) had specific capacities of 37 and 29 mAh g^{-1} after the same duration. EC:DMC(7:3) had lower initial capacities at 0 h of FVH, and specific capacities of 28 and 26 mAh g^{-1} after the same duration. Although the initial specific capacity of EC:DMC(7:3) was the lowest among the EC:DMC solvents, it retained 80 % of the capacity for the longest duration of FVH. The charge and discharge plots of the EC:EMC electrolytes after different durations of floating are presented in Appendix C, Figures S4 and show similar trend.
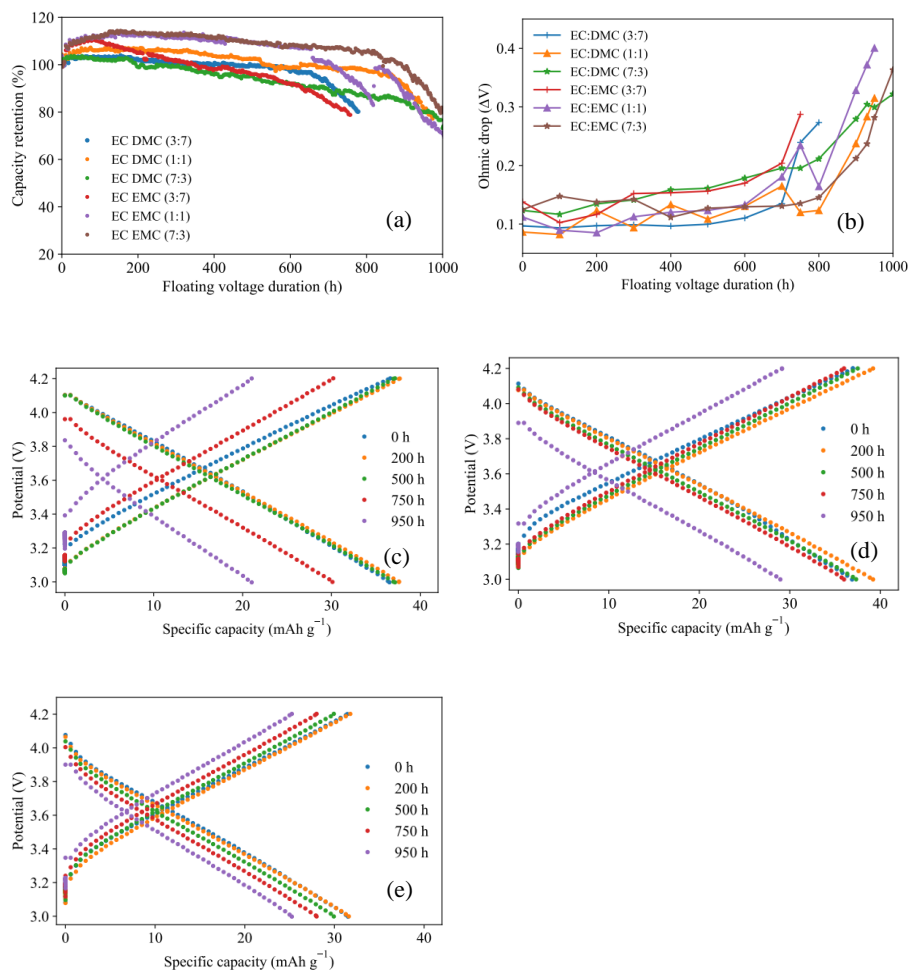
Figure 10: (a) Floating voltage stability tests, and (b) Ohmic drop of the different electrolytes; Charge and discharge plots after different durations of FVH for (c) EC:DMC(3:7), (d) EC:DMC(1:1), and (e) EC:DMC(7:3).

Furthermore, the slope of the capacity plots of EC:DMC(3:7) (Figure 10c) deviated as the floating voltage duration prolonged, especially after 750 h. For EC:DMC(1:1) and EC:DMC(7:3), the slope remained relatively unchanged until 950 h (Figure 10d and e). The linear slope in

the charge discharge profile of capacitive electrodes is indicative of double layer charging occurring from adsorption and desorption of ionic species with change in applied potential. The specific capacitance was calculated by multiplying the current by the inverse of the slope and mass of the AC electrode. It decreased in EC:DMC(3:7) to 112 and 90.3 F g^{-1} after 750 and 950 h of FVH, respectively. On the contrary, the specific capacitance was 120 and 117 F g^{-1} after 750 and 950 h for EC:DMC(1:1). The specific capacitance of EC:DMC(7:3) remained constant at 100 F g^{-1} even after 750 and 950 h of FVH. These results suggest that the electrolytes had distinctive behaviour at the AC surface.

4.2.5 Post-mortem characterisation

Post-mortem SEM images of the electrode surface morphology and electrode cross section from EC:DMC(3:7) and EC:DMC(1:1) after 950 h of FVH are shown in Figure 11. Notably, the surface of the electrode from EC:DMC(3:7) appeared to be severely covered by deposits of the electrolyte degradation products (Figure 11a), in contrast with less coverage of EC:DMC(1:1) (Figure 11d). Similar severe coverage was also observed in the electrode cross-section (Figure 11b and c) for EC:DMC (3:7), and to a less extent for EC:DMC(1:1) (Figure 11e and f).
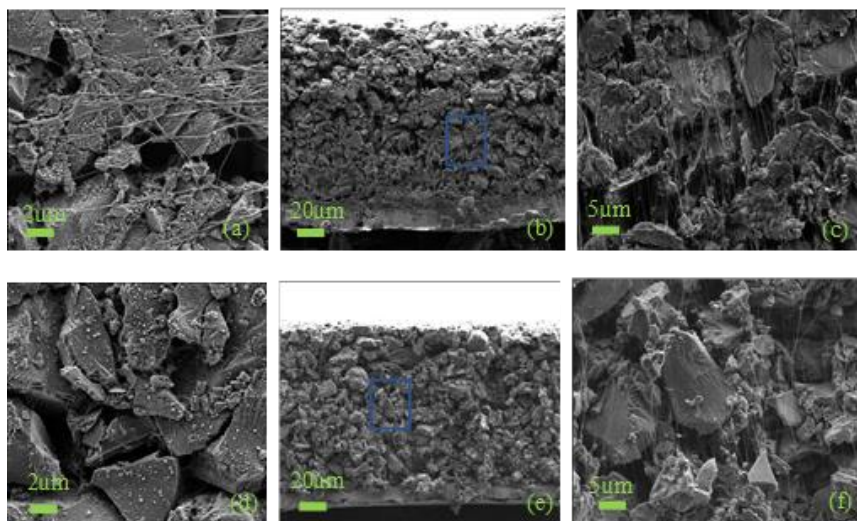
Figure 11: Post-mortem SEM after 950 h of FVH from EC:DMC(3:7) (a) electrode surface, (b) cross-section, (c) the highlighted rectangle in the cross-section image; from EC:DMC(1:1) (d) electrode surface, (e) cross-section, (f) the highlighted rectangle in the cross-section image

The extracted electrodes from EC:DMC(3:7) and EC:DMC(1:1) were further characterised using nitrogen physisorption analysis to investigate the pore properties. The isotherms display type I/IV characteristics, with a prominent hysteresis loop stretching from relative pressure from 0.005 to 0.3 (Figure 12a). We compared the pore properties of the extracted electrodes after cycling with the pristine AC electrode, which had surface area of 1443 m^2 g^{-1} and pore volume of 0.801 cm^3 g^{-1}.

The surface area and pore volume decreased to 679 m^2 g^{-1} and 0.469 cm^3 g^{-1} in EC:DMC(3:7), and 868 m^2 g^{-1} and 0.554 cm^3 g^{-1} for EC:DMC(1:1) (Figure 12b). Therefore, larger amount of electrolyte decomposition

products may have been deposited on the surface of the EC:DMC(3:7) electrode, which resulted in lower capacity after 950 h in comparison to EC:DMC(1:1). Furthermore, the pore size distribution (Figure 12c) showed that the major loss in porosity occurred in the micropores, which was expected due to charge storage by ion adsorption in the micropores. The EC solvent that constitutes the bulk of the solvation shell is decomposed in the micropores through reactions with confined moisture and oxygenated functionalities [80, 125]. Hence, the volume of micropores is expected to decrease significantly from surface passivation by the degradation products. It was interesting to see that the microporous region was broadened compared to the uncycled AC electrode, consistent with electrochemical activation phenomena. Electrochemical activation phenomenon has been previously reported by several studies [80, 104-106, 127]. It is explained by the irreversible increase in capacitance of a carbon material after the application of a potential beyond the critical value for activation. It has been demonstrated that the increase in capacitance is due to the increased surface area and widened pore size distribution after creation of new pores. Our observations are consistent with earlier studies, explaining the increased capacity during the floating voltage stability test. Furthermore, Figure 12c revealed that the mesopore volumes were also reduced, although with a lower magnitude than the micropores. This may have resulted in increased ion diffusion resistance.
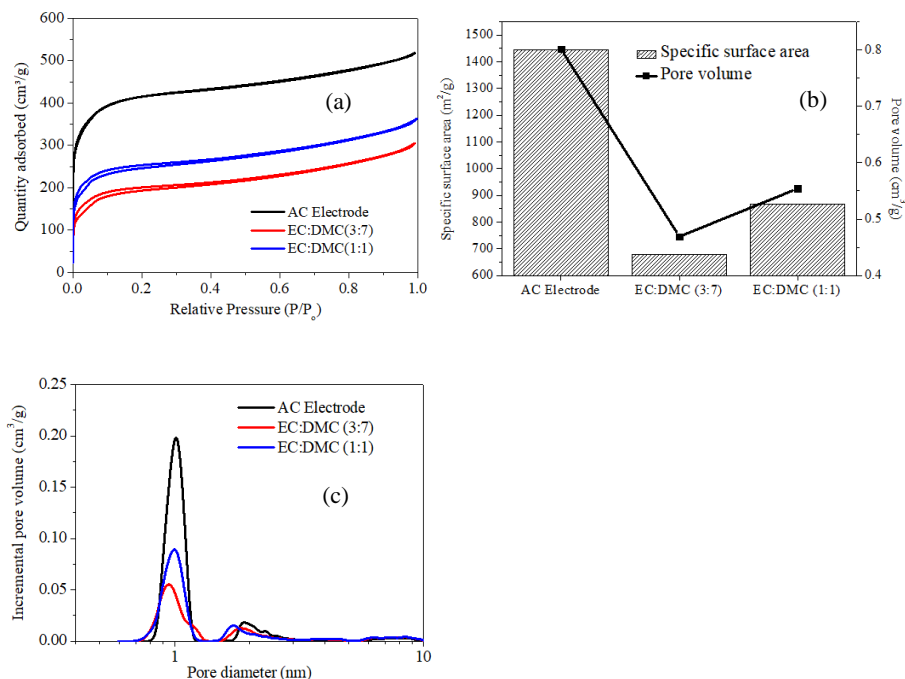
Figure 12: Pore property comparison of the pristine AC electrode, and electrodes extracted from EC:DMC(3:7) and EC:DMC(1:1), (a) nitrogen adsorption/desorption isotherm, (b) surface area and pore volume, (c) pore size distribution.

The electrodes were also characterised by XPS to identify the surface passivating species. The diminished AC peak at binding energies of 284.2 eV in the C1s spectra (Figure 13a) corroborated the SEM results and demonstrated that EC:DMC(3:7) electrode had more passivating deposits on the surface. Other peaks were identified in both electrodes at binding energies of 285.0, 286.2, 288.5, 290.3 and 291.7 eV and corresponded to the presence of CHx, C-O, O-C-O, CO3 and CF_2 from the polytetrafluoroethylene (PTFE) binder. Hence, the occurrence of

oxygenated carbon species from the carbonate solvent decomposition is confirmed.
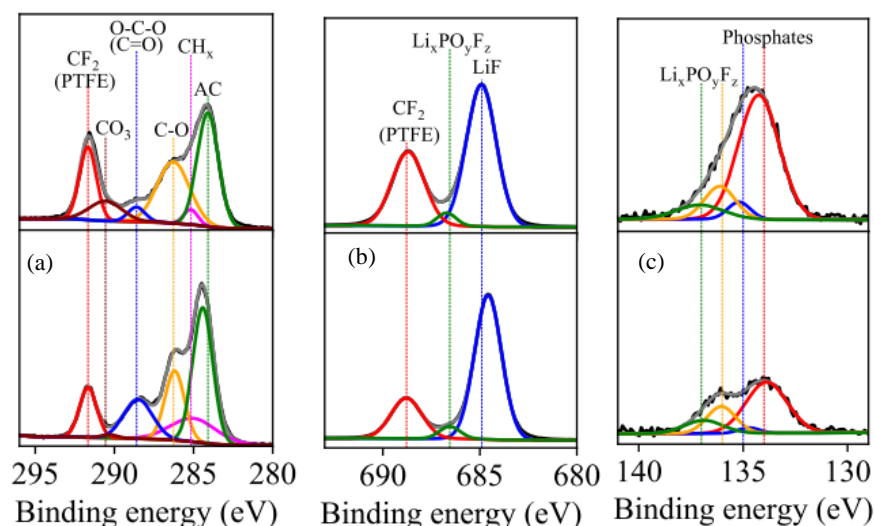
Figure 13: Comparison of (a) C1s XPS spectra, (b) F1s XPS spectra and (c) P2p XPS spectra; Top and bottom spectra represent EC:DMC(3:7) and EC:DMC(1:1), respectively.

The F1s spectra had peaks at 684.9, 686.7 and 689 eV (Figure 13b), corresponding to LiF, $Li_xPO_yF_z$ and CF_2 species. However, there is a slight increase in CF_2 for EC:DMC(3:7). It is possible that some exfoliation of the PTFE binder may have occurred during the FVH. Moreover, the P2p spectra (Figure 13c) showed more intense presence of phosphate species from anion decomposition at 134.2 and 135.2 eV in EC:DMC(3:7), together with the presence of $Li_xPO_yF_z$ at 136.1 and 137 eV from $LiPF_6$ decomposition. Thus, the electrolyte stability and anionic resistance to oxidation in the AC/Li half cells was enhanced by increased EC% and accordingly, the electrolyte dielectric.

Similar improved cyclic stability with increased EC% has been reported by Li et al. using lithium metal anodes [128]. EC stabilised the lithium metal anode through the alteration of the Li^+ solvation structure and improved electrode/electrolyte interfacial properties. The stabilised solid electrolyte interface (SEI) mitigates further electrolyte decomposition with increased EC% [128, 129]. However, as demonstrated by the post-mortem characterisation, EC also has an effect on the AC cathode. To eliminate the influence of the lithium counter electrode, we conducted similar floating voltage stability tests using symmetric AC/AC cells.

4.2.6 Symmetric cell stability test

The capacity retention from the floating voltage stability test at 2.5 V for the AC/AC symmetric cells is presented in Figure 14a, while the capacitance at various FVH duration is compared for EC:DMC(3:7), EC:DMC(1:1) and EC:DMC(7:3) in Figure 14b-d.

The floating voltage hold duration prior to the 80% capacity retention was 150, 300 and 350 h for EC:DMC(3:7), EC:DMC(1:1) and EC:DMC (7:3), respectively. The lower durations of floating voltage hold achieved in the symmetric cells in comparison with the AC/Li half cells are due to the wider operating potential window 0-2.5 V in the symmetric cells and possible concurrent electrolyte decomposition occurring on the AC anode and cathode. The improved stability with increased electrolyte dielectric is further demonstrated by the specific capacitance obtained at different durations of floating voltage (Figure 14b-d). After 400 h,

100

EC:DMC(3:7), EC:DMC(1:1) and EC:DMC(7:3) had specific capacitance of 70, 93 and 104 F g^{-1} respectively. Furthermore, the EIS measurements obtained on pristine cells (Figure 14e) showed that EC:DMC(3:7) had the highest particle to particle and current collector contact resistance, which is derived from the diameter of the semi-circle at high frequencies [130]. EC:DMC(7:3) with high viscosity had the highest diffusion impedance, indicated by the deviation of the vertical slope line from linearity at low frequencies. The EIS spectra after 400 h of FVH (Figure 14f) further demonstrated that EC:DMC (3:7) had the highest resistance, attributed to increased deposits of electrolyte degradation products at surface. Moreover, the intermediate resistance of EC:DMC(7:3) suggests that the electrode surfaces are distinctively affected by the electrolyte dielectric, especially at the anodes, even though it had superior capacity retention.
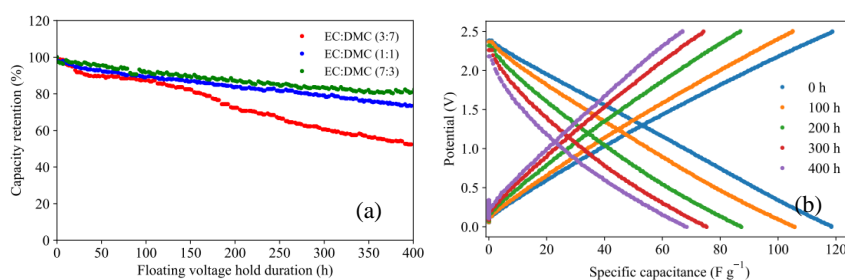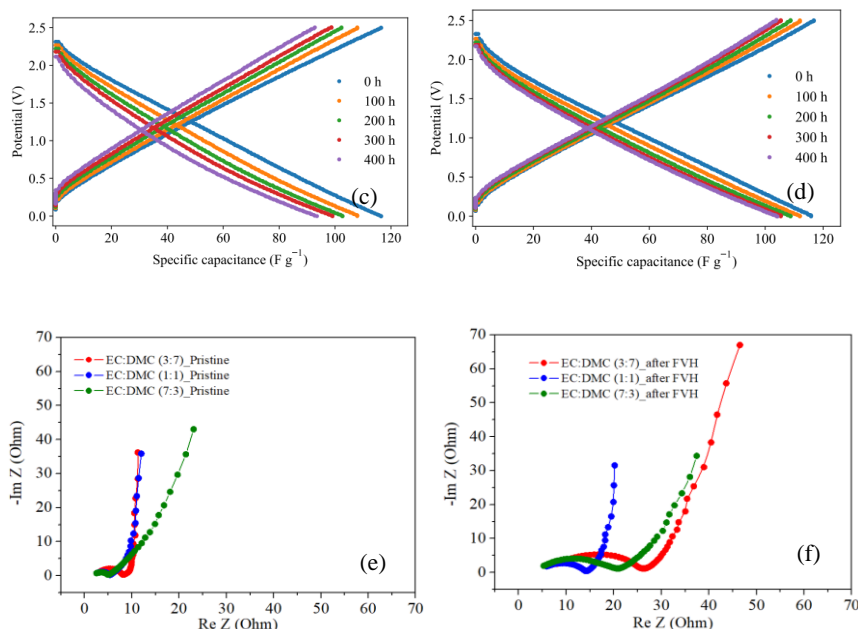
Figure 14: (a) Capacity retention of EC:DMC (3:7), EC:DMC (1:1) and EC:DMC (7:3) during floating voltage holds at 2.5V; Charge and discharge plots after different durations of floating voltage for (b) EC:DMC(3:7), (c) EC:DMC(1:1), and (d) EC:DMC(7:3); EIS obtained from (e) pristine assembled cells before the floating test, and (f) cycled cells after 400 h of floating.

4.2.7 Electrolyte degradation mechanism

The capacity fade mechanism in all cell configurations was due to electrolyte decomposition on the surface of the AC electrode. The electrochemical stability is improved with increased EC% in the electrolyte mixture. Two degradation mechanisms could be proposed. First, the degradation of EC:DMC (3:7) electrolyte could be from the presence of ion-paired LiPF$_6$, due to the insufficient dielectric for

complete salt dissociation. Ion-paired $LiPF_6$ readily undergoes equilibrium decomposition into LiF and PF_5 [107, 111, 131], while the latter could catalyse other component degradation such as ring opening of the EC, formation of other polymerised species, and CO_2 gas [132, 133]. Therefore, by increasing EC% in the solvent mixture, the dielectric is increased, and conversely, the amount of ion pairing and PF_5 formation is reduced. Secondly, the strength of the solvation sheath and surrounding anion dielectric influence the oxidative stability and delay the degradation of the PF_6^- anion. The floating voltage polarises the electrode at the maximum potentials whereby high energy at the double layer (Inner Helmholtz plane) would accelerate cell degradation. If the dielectric in the double layer of the cathode is increased, the anions are sufficiently insulated by the solvation sheath and good charge separation is achieved. Thus, the solvated anion can withstand prolonged durations of floating voltage and the eventual degradation is delayed. However, DFT calculations have disclosed that the oxidation and reduction potential of solvents are not significantly affected when the dielectric constant is extended beyond 40 [118]. In this work, EC:DMC (7:3) and EC:DMC (1:1) have dielectric constants of 50 and 32.8, and the stability of the former was only marginally improved, consistent with DFT simulations. Moreover, the high dielectric solvents often have high viscosities, which impede the transport processes when considering solvent mixtures and free energy of solvation. DFT studies by Borodin et al. [110] have further demonstrated that the anion oxidative stability was enhanced when the solvent dielectric in the vicinity of the anion was

increased, especially at the cathodes and upon exposure to higher polarisation energies. The anion and carbonate solvent degradation pathway occurred via fluorine abstraction from the PF_6^- anion, hydrogen abstraction from the carbonate solvent and HF formation.

4.3   Deciphering electrolyte dielectric extended electrochemical stability in activated carbon/hard carbon lithium-ion capacitors (Paper IV)

In this paper, the effect of the electrolyte dielectric was demonstrated in LiC full cells using AC as the cathode and pre-lithiated HC as anode. The interfaces formed on both electrodes were probed in relation to the electrolyte dielectric using EIS and postmortem characterization techniques.

4.3.1   GCD Analysis

The GCD analysis of the AC-HC full cells was conducted in the operating potential window 3-4.2 V [134]. In this potential window, the PF_6^- is the adsorbed/desorbed specie on the AC electrode surface during charge/discharge. At the same time, Li^+ cations are intercalated/deintercalated in the HC electrode concurrently. Figures 15a, b and c show the 1st three charge and discharge cycles at 4.26 mA g^{-1} obtained with the different electrolytes. Despite the pre-lithiation of the HC electrodes, all the electrolytes exhibit an initial coulombic efficiency (ICE) loss in the first cycle (Figure 15a), attributed to CEI/SEI film formation on the AC and HC. The amount of CEI/SEI formed on the electrodes can be determined by the ICE, which gives a measure of the electrolyte ions trapped irreversibly in the CEI/SEI [135, 136].

However, the CE loss is higher for EC:DMC(3:7) than for the other electrolytes, as summarised in Table 3. The higher CE obtained with increased EC% and electrolyte dielectric suggests that a thinner passivation film is formed, which suppress further electrolyte degradation and consumption of active ionic species for charge storage. Low initial CE is a challenge encountered with HC anodes, for which losses of up to 20% of the initial capacity are expected due to SEI formation [137]. However, the pre-lithiation step enables the pre-SEI formation on the HC anode and reduces the capacity loss after full cell assembly. Therefore, the ICE loss may be related to the AC electrode, which possesses a high surface area and abundant oxygen surface functionalities [138]. Despite the high ICE of EC:DMC(7:3), the specific capacity is expectedly the lowest among the electrolytes due to the high viscosity.
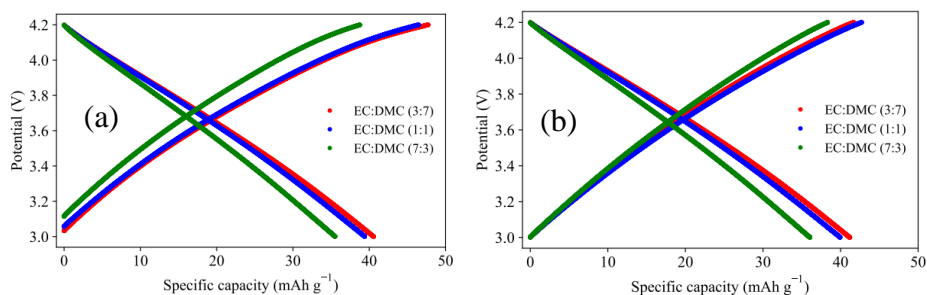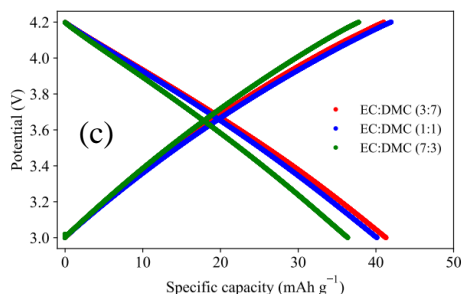
Figure 15: Charge and discharge profile of the different electrolytes at 4.26 mA g^{-1} (a) 1st cycle, (b) 2nd cycle, and (c) 3rd cycle.

Table 3: CE comparison of the electrolytes after the first three cycles

Electrolyte	1st cycle (%)	2nd cycle (%)	3rd cycle (%)
EC:DMC(3:7)	84.19	90.74	92.61
EC:DMC(1:1)	84.89	93.64	95.66
EC:DMC(7:3)	91.65	94.05	96.25

4.3.2 Stability test

Figure 16a shows the capacity retention profile during the FVH stability test. After 900 h of FVH, EC:DMC(7:3) had the highest capacity retention of nearly 96%. On the other hand, EC:DMC(1:1) and EC:DMC(3:7) had a capacity retention of 90%. The charge and discharge capacity plots of the electrolytes after different durations of FVH are presented in Figure 16b-d. The excellent capacity retention of EC:DMC(7:3) is demonstrated in Figure 16d, where no significant

change was observed. On the other hand, EC:DMC(1:1) and EC:DMC(3:7) exhibit slight deviations due to possible electrolyte decomposition and loss of ionic species for charge storage (Figure 16b and c). The results from the floating voltage stability tests correspond with the previous study, where the effect of the electrolyte dielectric on AC electrochemical stability was examined in AC/Li half cells and AC/AC symmetric cells [134]. However, in this case, only marginal differences exist between the capacity retention of EC:DMC(3:7) and EC:DMC(1:1). Though, high EC% and electrolyte dielectric remain beneficial for enhanced electrochemical stability.
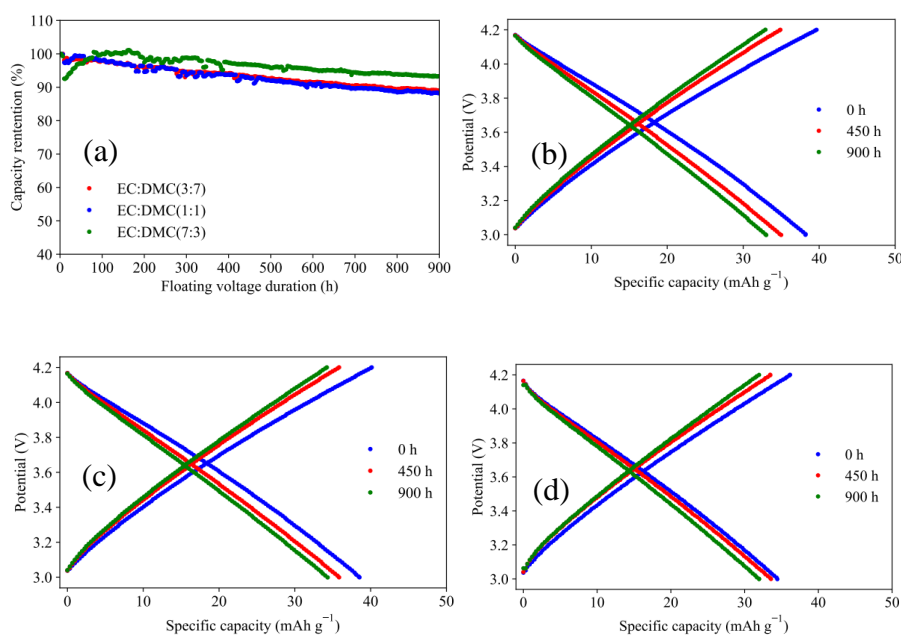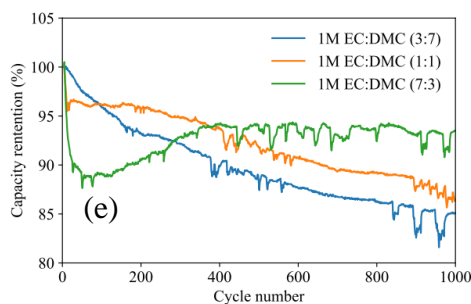
Figure 16: (a) Capacity retention during floating voltage stability tests; Charge and discharge profile after different durations of floating voltage for (b) EC:DMC(3:7), (c) EC:DMC (1:1), and (d) EC:DMC(7:3); (e) Capacity retention during GCD cycling in the potential window 3-4.6 V at 213 mA g^{-1}.

Since EC:DMC(1:1) and EC:DMC(3:7) barely showed any differences in capacity retention in the potential window 3-4.2 V, the upper vertex potential was extended to 4.6 V to further investigate the stability at stringent conditions. The same cells were retested in the potential window 3-4.6 V after reconditioning by three cycles of charge and discharge at 4.26 mA g^{-1}. GCD cycling was implemented instead of the previous FVH to prevent rapid electrolyte decomposition when the cells are subjected to sustained voltage holds at 4.6 V. The capacity retention during the GCD cycling is presented in Figure 16e. Again, the superior stability of EC:DMC(7:3) is demonstrated, with 95% capacity retention after 1000 cycles. Moreover, there is a clear distinction between the capacity retentions of EC:DMC(1:1) and EC:DMC(3:7), with the former having a capacity retention of 88% and the latter 84% after the same duration.

4.3.3 EIS analysis

After the GCD analysis, EIS measurements were acquired from the cells and compared with the uncycled full cells to understand the mechanisms underlying the capacity fade. The EIS spectra from the uncycled cells display two prominent semi-circles: a small semi-circle at high-mid frequencies and a larger semi-circle deconvoluted into two additional semi-circles (Figure 17a). The EIS spectra were deconvoluted using the Gaussian process distribution of relaxation time (GP-DRT) model to determine the number of processes and their assignment to individual electrodes [139]. Appendix D, Figure S1 in the Supporting Information (SI) shows the DRT analysis of EC:DMC(3:7) in different cell chemistries to separately match the peaks. Based on the peak positions and time constants, the three semi-circles in the uncycled AC-HC full cell EIS spectra are assigned to the active material and current collector contact resistance of AC and HC (predominantly AC), the resistance of the passivation layer formed on the electrodes (predominantly HC), and the charge transfer resistance, respectively [140, 141]. The near 45-degree vertical sloping line at low frequencies is associated with the electrolyte Warburg diffusion coefficient (W).
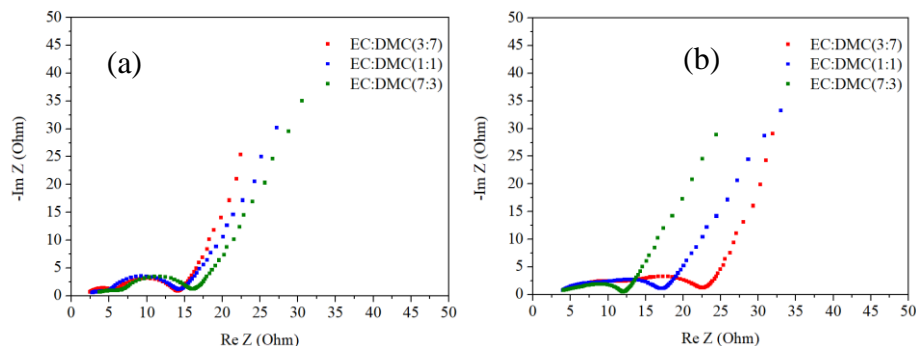
Figure 17: EIS spectra obtained from different electrolytes (a) Uncycled AC-HC full cells, and (b) Cycled AC-HC full cells. EIS was acquired at open circuit potential (OCP) 3.06 V +/- 0.05V.

The equivalent circuit used in the fitting is given by *R0-p(C1,R1)-p(CPE2,R2)-p(C3,R3)-W1-C4* [140]. Where *R0* represents the ohmic resistance (combined bulk electrolyte and active material resistance); *C1* and *R1* represent the capacitance, and active material/current collector contact resistance of the AC and HC electrode; *CPE2* and *R2* represent the capacitance and SEI resistance of the HC electrode; *C3* and *R3* represent the capacitance and charge transfer resistance; and *C4* the capacitance of the device. The constant phase element (CPE) was introduced to account for surface roughness and heterogeneity of the SEI layer. Fitting without this element yielded significant errors and unsatisfactory results. However, using the respective circuits described and supported by the DRT analysis, x^2 values less than 10^{-4} were obtained. The obtained paraments after fitting are summarised in Table 4. For illustration purposes, different EIS spectra for EC:DMC(3:7) and their corresponding fitting are presented in Appendix D, Figure S1.

Table 4: Parameters of the uncycled AC-HC full cell spectra after fitting.

Electrolyte	R0	C1	R1	CPE2_0	CPE2_1	R2	C3	R3	W1	C4
	(Ohm)	(F)	(Ohm)	(Ohm^{-1}s^a)		(Ohm)	(F)	(Ohm)	Ohm s$^{-0.5}$	(F)
EC:DMC(3:7)	1.81	0.00042	4.56	0.00721	0.345	7.64	0.000007	1.58	1.20	0.930
EC:DMC(1:1)	1.70	0.00186	2.74	0.00011	0.481	4.25	0.000310	4.75	3.27	0.950
EC:DMC(7:3)	2.97	0.00161	2.63	0.00039	0.563	4.64	0.000480	4.94	3.62	0.771

The *R1* values obtained from EC:DMC(3:7), EC:DMC(1:1) and EC:DMC(7:3) follow a decreasing trend as the electrolyte dielectric increases. The smaller *C1* value obtained in EC:DMC(3:7) indicates that the surface area is reduced to a large extent by the passivation film formed in this electrolyte compared to the others. The same trend of decreasing resistance with increased electrolyte dielectric was displayed for the *R2* values. Thus, the initial passivation layer impedance is more resistive in the AC and HC electrode with EC:DMC(3:7). It was interesting to see that *R3* increased proportionally with the electrolyte dielectric, in agreement with previous studies [124, 125]. Therefore, the charge transfer resistance increases with the electrolyte dielectric due to higher desolvation energies at the HC anode interface [124, 125]. Moreover, the largest *W* was obtained for EC:DMC(7:3), which can be attributed to the higher viscosity associated with increased EC%.

After the GCD cycling, the EIS spectra appeared to be depressed with a decreased imaginary impedance (Figure 17b), which signified a reformed passivation layer at the electrode surfaces. The total cell impedance of EC:DMC(3:7) and EC:DMC(1:1) determined from the

intercept on the real axis increased compared to the uncycled cells. However, the opposite trend is observed for EC:DMC(7:3). This was contrary to the expected growth in real impedance after cycling. Moreover, the two distinct semi-circles observed in the pristine cells are absent in the cycled cells. Instead, the semi-circles appear to be merged, further supporting significant electrode surface transformation after cycling. The spectra were fitted with the same equivalent circuit described previously. The obtained parameters after cycling are summarised in Table 5.

Table 5: Parameters of the cycled AC-HC full cell EIS spectra after fitting

Electrolyte	R0	C1	R1	CPE2_0	CPE2_1	R2	C3	R3	W1	C4
	(Ohm)	(F)	(Ohm)	$(Ohm^{-1}s^a)$		(Ohm)	(F)	(Ohm)	Ohm s$^{-0.5}$	(F)
EC:DMC(3:7)	3.20	0.000510	3.84	0.00060	0.477	12.8	0.00045	2.26	2.39	0.826
EC:DMC(1:1)	3.32	0.000232	2.21	0.00018	0.648	6.97	0.00078	3.57	3.89	0.867
EC:DMC(7:3)	2.63	0.000480	1.88	0.00054	0.557	5.28	0.00078	2.46	2.57	0.937

From the cycled cells EIS spectra fit, *R0* is increased in EC:DMC(3:7) and EC:DMC(1:1), consistent with increased electrolyte and active material resistance in the electrolytes. On the contrary, EC:DMC(7:3) exhibits a slightly decreased *R0*, signifying only marginal decomposition of the electrolyte, but the decreased *W* may imply decreased electrolyte viscosity after cycling. Interestingly, *R1* decreased in all electrolytes while *R2* increased, although EC:DMC(3:7) had the highest value. EC:DMC(3:7) further exhibited a slight increase in *R3*, whereas the other electrolytes exhibited a decrease. This trend suggests a marginally

113

increased charge transfer resistance in EC:DMC(3:7) as the capacity fade progressed. Meanwhile, the decreased charge transfer resistance of EC:DMC(1:1) and EC:DMC(7:3) may indicate that cycling induces significant reformations of the native passivation layer and electrode interfaces.

The full cell EIS analysis results indicate that EC:DMC(3:7) had the highest total resistance among the electrolytes, possibly due to increased electrolyte degradation and active material and surface passivation layer transformation. However, the interpretations of the resistance parameters to individual electrodes require further validation, given that the EIS measurement is obtained simultaneously across the various AC and HC interfaces, and the resistance parameters contain contributions from both electrodes [142].

To determine the transformations of the individual electrodes after cycling in relation to the electrolyte dielectric, symmetric cells were constructed from the cycled AC-HC full cells and subjected to EIS analysis. Two corresponding AC-AC and HC-HC electrodes were extracted and reassembled into symmetric cells with a new separator and electrolyte. Figures 18a and b show the spectra from the reassembled AC-AC and HC-HC symmetric cells. The EIS spectra of the symmetric cells were divided by two to account for the impedance of the single electrode.
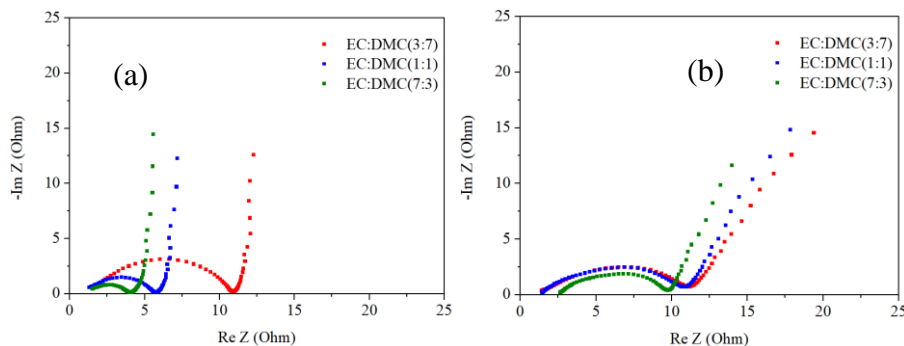
Figure 18: EIS spectra for the reassembled (a) AC-AC, and (b) HC-HC symmetric cells.

Figure 18a shows that the AC-AC spectra display characteristics associated with symmetric AC cells. The semi-circle at high to mid-frequency corresponds to the particle-particle/particle-to-current collector contact resistance (R_p). The vertical line at low frequencies represents the double-layer capacitance. The spectra were fitted using similar equivalent circuits as Köps et al.[143]. The circuit consists of a resistor R_{el} representing the electrolyte solution resistance, an *Rp/CPE* loop representing the particle-to-particle/particle-to-current collector interface, a Warburg element W, and a capacitor C connected in series.

The *Rp* values after the fitting were 9.45, 4.85 and 3.37 Ohm for EC:DMC(3:7), EC:DMC(1:1) and EC:DMC(7:3), respectively. The symmetric AC-AC impedance results correspond with the *R1* values in the cycled full-cell EIS analysis. Hence, validating our initial assumption that *R1* is related to the AC. The values are slightly higher due to the disassembly and reassembly processes, which may introduce minor increases in the resistance. Furthermore, the increased electrolyte

dielectric remarkably decreases the resistance of the AC electrode by a factor of three, implying decreased electrolyte decomposition products at the AC surface. Therefore, it confirms that the high electrolyte dielectric is beneficial for enhanced AC stability. Deposited electrolyte degradation products reduce the accessible surface area of the AC electrode and increase the resistance [138].

For the reassembled HC-HC symmetric cells (Figure 4b), the semi-circle at high-mid frequencies is associated with the passivation layer and charge transfer impedance, while the vertical sloping line at low frequencies corresponds to the Warburg diffusion. It has been reported that the primary failure mechanism of graphite and HC anodes is due to the growth of the SEI and the loss of cyclable lithium ions [144]. Fitting the impedance spectra was challenging due to significant errors in some parameters. Hence, we directly compared the diameter of the semi-circle as a relative comparison of the total resistance due to the passivation layer and charge transfer. It turned out that the HC-HC anodes from EC:DMC(7:3) again present the smallest total resistance (~7.5 Ohm), attributed to a less resistive SEI or degradation products. Meanwhile, the resistance of EC:DMC(1:1) and EC:DMC(3:7) are similar at ~9 Ohms. The total resistance values in the HC-HC symmetric cells correspond with the sum of *R2* and *R3* obtained from the cycled AC-HC full cells and follow a decreasing trend with the increase of the electrolyte dielectric. Therefore, increased electrolyte dielectric is also beneficial for enhanced cycling stability of the HC anode, though to a less extent than the AC electrode.

4.3.4 Post-mortem electrode analysis

Post-mortem electrode examinations were then conducted on the cycled electrodes to reveal the constituents at the surface. The SEM images obtained from the AC and HC electrodes are presented in Figure 19. The SEM images show features of deposits of electrolyte degradation products on the cycled electrodes, which are absent in the uncycled reference electrode for both the AC and HC. The deposits on the surface of the cycled AC electrode (Figure 19c, e and g) resembled aggregates, with varying degrees of visible binder among the samples. The cross-sectional SEM images in Appendix D, Figure S2 further confirm increased binder visibility in EC:DMC(3:7), which may be attributed to the AC electrode bulk and binder restructuring from exfoliation. We conjecture that the exfoliation may be linked to PF_6^- intercalation within the graphitic layers, which reportedly reduces as the PF_6^- anion is increasingly solvated [145]. This explains the reduced binder visibility in EC:DMC(1:1) and EC:DMC(7:3). Moreover, EC:DMC (3:7) had the highest surface deposits covering the AC grains. However, the aggregated deposits were reduced on the AC electrode surface as the electrolyte dielectric was increased, with EC:DMC(7:3) having less deposits at the surface. This is consistent with the EIS measurements (Figure 18a). Therefore, the high resistance of EC:DMC(3:7) could be related to increased deposits of electrolyte degradation products at the AC surface and increased active material resistance caused by electrode transformations after exfoliation.

117
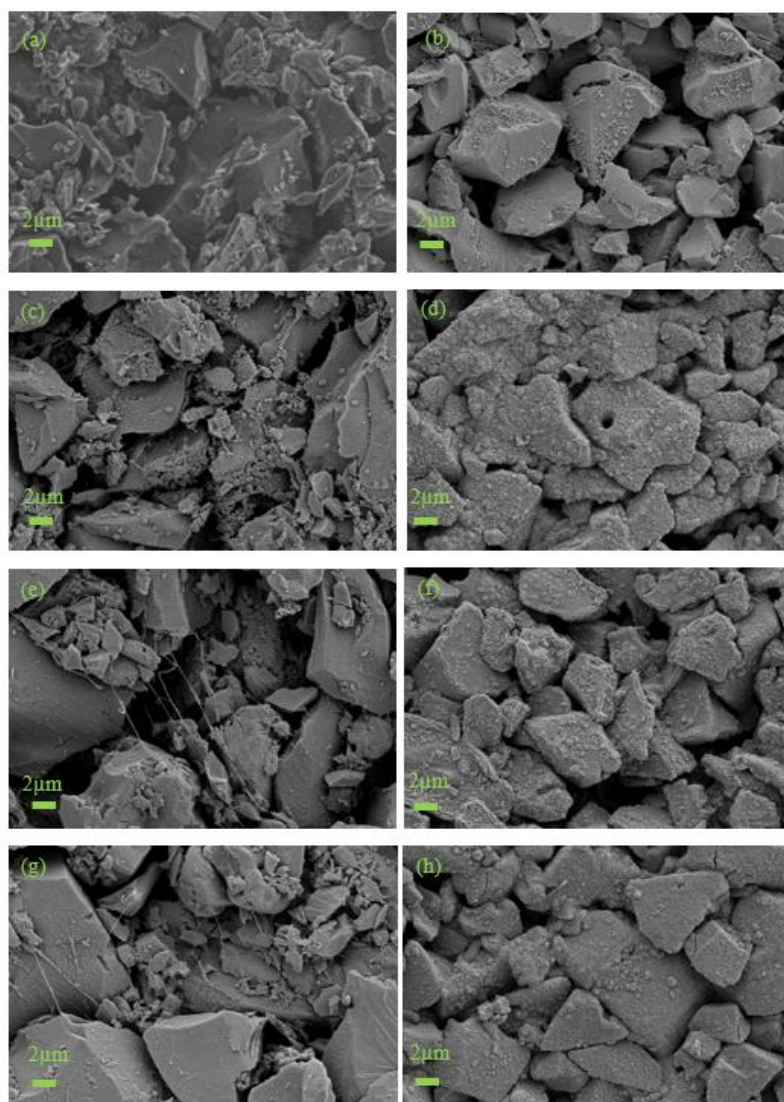
Figure 19: SEM micrographs of (a, b) the reference AC and HC electrode; (c, d) cycled AC and HC electrode from EC:DMC(3:7); (e, f) cycled AC and HC electrode from EC:DMC(1:1); (g, h) cycled AC and HC electrodes from EC:DMC(7:3).

For the cycled HC electrodes (Figure 19d, f and h), a layer with increased SEI formation is observed. However, the surface of EC:DMC(7:3) appeared relatively smoother than EC:DMC(1:1) and EC:DMC(3:7), with the latter showing the roughest and highest magnitude of deposits (Appendix D, Figure S3). Again, this is consistent with the HC-HC symmetric cell EIS analysis (Figure 18b), corroborating a greater extent of electrolyte decomposition with lower EC%.
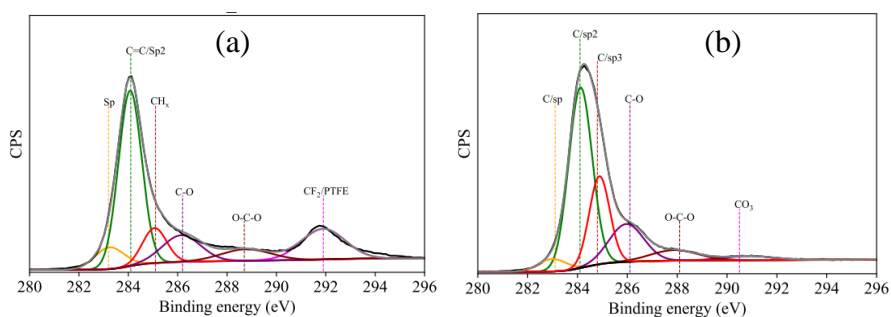
Figure 20: C1s XPS spectra of the uncycled (a) AC, (b) HC electrode.

The nature of surface passivating species on the AC and HC electrodes was probed using XPS. The C1s XPS spectra of the reference AC and HC electrodes are presented in Figures 20a and b. The C1s spectra of the uncycled AC electrode display six peaks at binding energies of 283.5, 284.1, 284.7, 286.1, 288.1 and 291.7, corresponding to the presence of sp (C≡C), sp2 (C=C), sp3 (C-C), C-O, O-C-O groups and CF_2 from the PTFE binder [138, 146]. The relative elemental composition of the AC surface is 69 % carbon, 5% oxygen and 26% fluorine. For the uncycled HC electrode, the peaks are present at binding energies of 283.1, 284.1, 284.8, 286.1, 288.1 and 290.5 eV, corresponding to sp (C≡C), sp2

(C=C), sp3 (C-C), C-O, O-C-O and CO_3 groups. The different oxygenated carbon environments of the AC and HC electrodes are possible contributors to the low ICE after reactions with the electrolyte [147]. The uncycled HC electrode surface presents 86% carbon and 14% oxygen.

Table 6: Relative concentrations of the C, O, F, P and Li on the surface of the cycled AC cathode in different electrolytes.

Elements	C%	O%	F%	P%	L%
Reference	69	5	26		
EC:DMC(3:7)	44	10	40	1	5
EC:DMC(1:1)	45	10	39	1	4
EC:DMC(7:3)	45	10	40	1	4
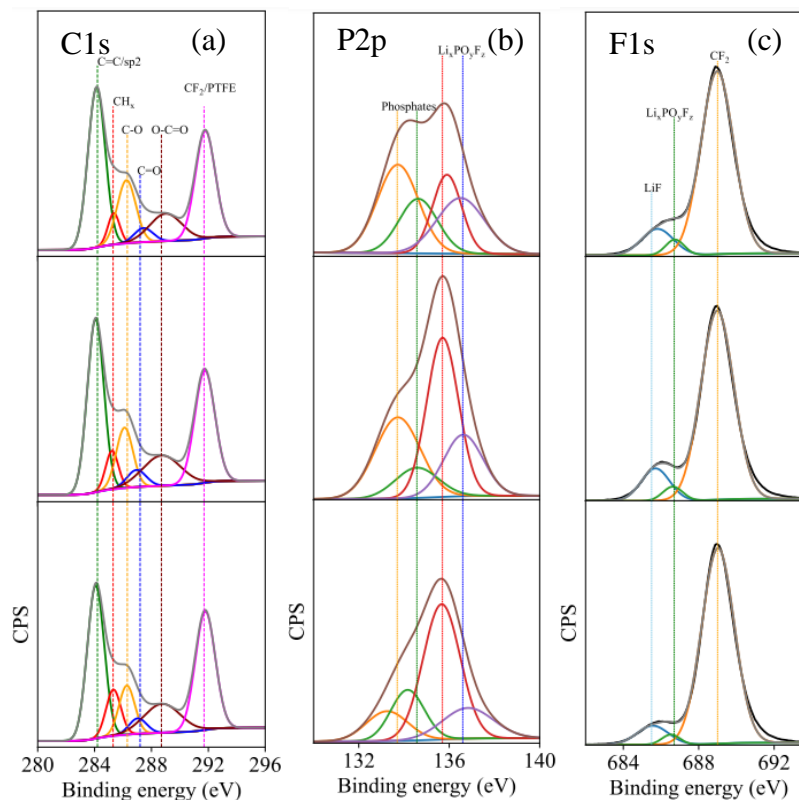
Figure 21: Deconvoluted XPS spectra of the cycled AC electrode (a) C1s, (b) P2p, and (c) F1s. Top EC:DMC(3:7), middle EC:DMC(1:1), and bottom EC:DMC(7:3).

The C1s, P2p and F1s spectra of the cycled AC electrodes from EC:DMC (3:7), EC:DMC(1:1) and EC:DMC (7:3) are compared in Figure 21, while the relative elemental composition is presented in Table 6. Notably, the C1s spectra of the cycled AC electrodes display six peaks at binding energies of 284.2, 285.3, 286.3, 287.2, 288.7 and 291.7 eV, corresponding to sp^2 (C=C), CH_x, C-O, C=O, O-C-O and CF_2 groups arising from the PTFE binder (Figure 21a) [138, 146]. The disappearance

of the sp (C≡C) peak suggests that some carbon species were reacted or may be covered by the passivating layer. Moreover, the decreased C% and increased O% are evidence of passivation of the surface of the AC electrode and marginal CEI formation. However, the CEI is somewhat limited, as revealed by the SEM images, which do not resemble the clear layer of SEI formed on the HC anode. Nevertheless, the composition of the surface species in the C1s spectra resembles typical CEI products (lithium alkyl carbonates) found on cathodes cycled in carbonate solvents [148]. However, these products arise from ring-opening reactions of EC with PF_5 (from PF_6 or ion-paired $LiPF_6$ decomposition). Therefore, the diminished C-O content in the CEI of EC:DMC(1:1) and EC:DMC(7:3) suggests less carbonate solvent decomposition, possibly related to sufficiently solvated PF_6^- and delayed PF_6^- degradation at the surface [149].

In the P2p spectra, phosphates and $Li_xPO_yF_z$ species are identified at binding energies of 133.7, 134.57, 135.7 and 136.6 eV. These products are associated with the PF_6^- anion decomposition and remnant salts on the AC surface. This is more apparent on the AC electrode from EC:DMC(3:7), suggesting more PF_6^- decomposition products.

In the F1s spectra, LiF, $Li_xPO_yF_z$ and CF_2 were identified at binding energies of 685.5, 686.7 and 689 eV. However, the immense presence of CF_2 peak from the PTFE binder diminishes the LiF peak and may be ascribed to more binder exposure at the surface as cycling progresses. Moreover, a slightly reduced ratio of LiF to CF_2 binder was observed for

EC:DMC(7:3), in comparison with EC:DMC(3:7). This further supports that there is less PF_6^- degradation products at the AC surface with increased EC%. Increased phosphate species and LiF on the AC surface correlate with the capacity fade and are attributed to more passivating species with the capacity fade [138].

The C1s spectra of the cycled HC electrodes display a clearer trend (Figure 22a). In EC:DMC(3:7), six peaks are identified at binding energies of 283.8, 284.8, 285.5, 286.3, 288.7 and 290.1 eV, corresponding to LiCx/spC, sp2 (C=C), CHx, C-O, C=O, O-C=O and CO_3 species [146, 150, 151]. In EC:DMC(1:1) and EC:DMC(7:3), the CH_x peak is absent, and the intensity of the LiCx/ spC peak is low.
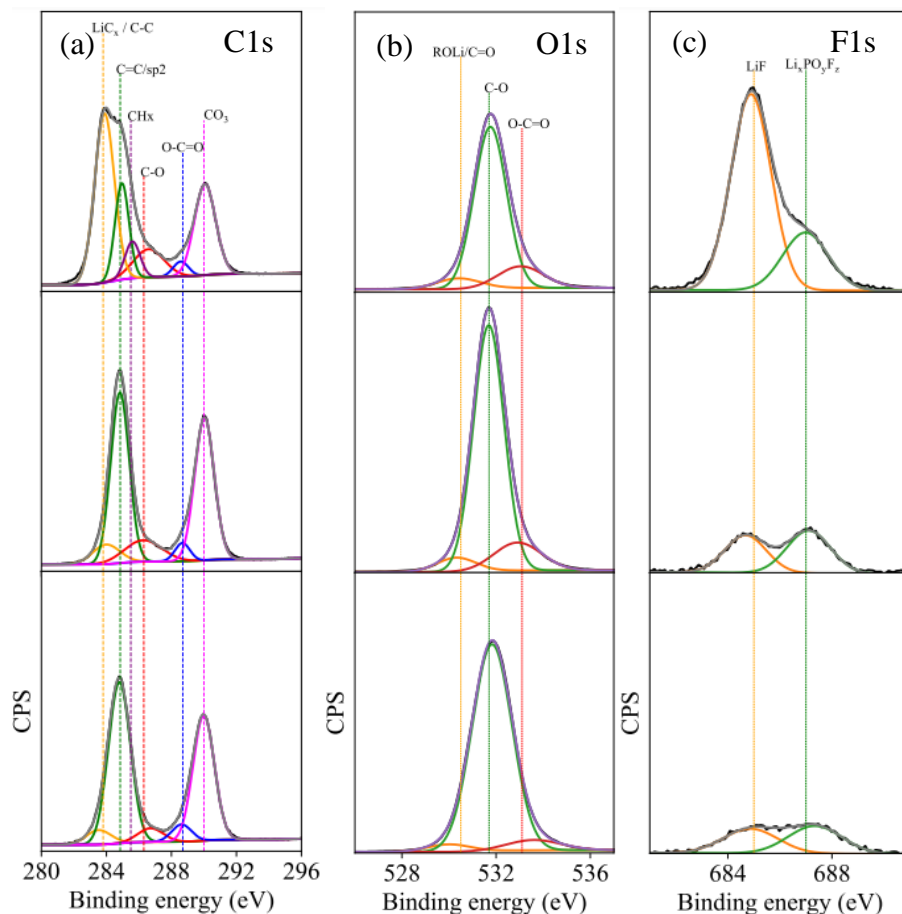
Figure 22: Deconvoluted XPS spectra of the cycled HC electrode (a) C1s, (b) O1s, and (c) F1s. Top EC:DMC(3:7), middle EC:DMC(1:1), and bottom EC:DMC(7:3).

The disappearance of the CH_x peak in EC:DMC(1:1) and EC:DMC (7:3) may be related to less linear carbonate in the solvation shell and dominance of EC-derived SEI products at the HC electrode surface [151]. Additionally, the $C-O/OCH_3$ peak at binding energies of 287.1 eV is ascribed to DMC derived SEI products and decreases with the DMC% in the electrolyte [150]. The $O-C=O$ and CO_3 peaks at 288.7 and 290.1

eV are ascribed to -CH_2OCO_2 and Li_2CO_3, derived from EC [150, 151]. Therefore, in EC:DMC(3:7), more DMC derived products are present, while in EC:DMC(1:1) and EC:DMC(7:3), more EC derived products are present. However, the SEI with more Li_2CO_3 is more stable than the DMC derived SEI, given the decreased intensity of the LiCx peak. The presence of the LiCx peak may indicate broken SEI at the surface. Hence the electrode in EC:DMC(3:7) possesses an unstable SEI, which does not effectively protect against further electrolyte degradation. This is additionally confirmed by the elemental composition in Table 7, which shows more F% in EC:DMC(3:7) from $LiPF_6$ decomposition. The smoother surface of EC:DMC(1:1) and EC:DMC(7:3) may therefore indicate uniform SEI coverage at the surface, in contrast with the rough and otherwise broken SEI of EC:DMC(3:7) (Figure 19d, f and h).

Table 7: Relative concentrations of C, O, F, P and Li on the surface of the cycled HC anode in different electrolytes.

Elements	C%	O%	F%	P%	L%
Reference	86	14			
EC:DMC(3:7)	38	31	4	1	25
EC:DMC(1:1)	31	39	2		28
EC:DMC(7:3)	31	39	2		28

The O1s spectra revealed three peaks at binding energies of 530.5, 531.7 and 533.1 eV, corresponding to ROLi/CO, C-O and O-C=O (Figure 22b) [150]. In the F1s spectra (Figure 22c), LiF and $Li_xPO_yF_z$ species are

125

present at binding energies of 685 and 687 eV. However, the intensity of LiF species is the highest in EC:DMC(3:7), which might be the cause of the high impedance. Furthermore, it has been reported that degradation products from the cathode can migrate to the anode and get deposited [152]. Therefore, the increased LiF presence in EC:DMC(3:7) could also be related to ion-paired $LiPF_6$ and PF_6^- decomposition at the cathode.

The XPS results have thus revealed that the HC anode surface in EC:DMC(3:7) is likely enriched in LiF and LiCx/spC peak, compared to the other electrolytes. The presence of the latter suggested SEI attack since these peaks are supposed to be covered by the native passivation films. Although LiF is mostly a favourable SEI component due to its impressive stability, our results have shown that this alone does not translate to improved stabilities. Specifically, the increased LiF intensity and polyphosphates would result from PF_6^- degradation. PF_6^- degradation has been linked to the incomplete dissociation of $LiPF_6$, which depends on the solvating ability/electrolyte dielectric of the solvents [107]. Low solvating ability/electrolyte dielectric in EC:DMC(3:7) would lead to increased ion-paired $LiPF_6$ and propensity for dissociation into LiF and PF_5. While PF_5 may react with moisture in the AC pores and oxygen radicals at the surface, producing HF and POF_3. POF_3 could further react with DMC to produce POF_2OCH_3 and polyphosphates, which may also react with PF_5, to generate more POF_2OCH_3 in a continuous destructive cycle [153]. POF_3 can also catalyse further ring-opening reactions of the EC, thereby depleting EC and resulting in capacity fade.

126

Moreover, electrodes with well-formed SEIs are also prone to HF and PF_5 attacks. The former is responsible for SEI thickening, where Li_2CO_3 is converted to LiF and leads to more SEI formation [154]. This corroborates the XPS results for the HC anode, with EC:DMC(3:7) having the lowest intensity of Li_2CO_3 and the highest intensity of LiF. Therefore, the lower dielectric solvents are more prone to electrolyte degradation. High electrolyte dielectric is beneficial for enhanced stability, which is particularly suited for applications requiring high-powered devices with long cycle life.

5. Conclusions and future work

5.1. Conclusions

Changes to the electrode-electrolyte interfacial properties significantly affect the cycle life of LiC, especially arising from the AC cathode with already limited capacity. The causes of capacity fade have been investigated in this thesis, using a combination of EIS acquired intermittently during floating voltage ageing and post-mortem electrode surface characterisation of the AC. The ageing profile consisted of three distinct phases as characterised by the change in the slope of the capacity retention profile. These phases corresponded with a modified passivation layer on the electrode surface and accelerated electrolyte degradation. The characteristics of the AC electrode-electrolyte interface were further examined after different durations of cycling. Post-mortem analysis revealed a progressive decrease in the surface area corresponding to the capacity fade and identified anion degradation products on the surface that blocked the surface area. Therefore, the capacity fade was caused by an unfavourably modified electrode-electrolyte interface and anion decomposition that depleted the active species for charge storage.

After revealing the degradation mechanisms, a method of enhancing the cycle life by delaying the anion degradation was found. This method involved optimising the electrolyte dielectric and enabling a conducive electrode-electrolyte interface. Electrolyte solutions with increased dielectric and, conversely, EC% possessed superior electrochemical

1 stabilities. This was confirmed in different cell configurations consisting

2 of AC/AC symmetric cells, AC/Li Half cells and AC/ Pre-lithiated HC

3 full cells. The enhanced cycle life with increased dielectric was enabled

4 by improved anion oxidative stabilities in the double-layer region due to

5 sufficient solvation and insulating dielectric. Consequently, the

6 degradation of the anion during polarization at high voltages was

7 minimized, and the associated degradation products were relatively

8 decreased.

9 Furthermore, the effect of the electrolyte dielectric was more prominent

10 on the AC electrode. A three-fold decrease in the impedance after cycling

11 was observed on the AC electrode cycled with the high dielectric

12 electrolyte. Therefore, increased electrolyte dielectric resulted in

13 enhanced cycle life of the LiC through favourable electrode-electrolyte

14 interface characteristics and decreased anion degradation at the AC

15 electrode surface.

16 Optimizing the AC electrode-electrolyte interface and utilizing some of

17 the reviewed strategies towards improving the performance of the AC,

18 can help realise high performance AC LiC, with extended cycle life and

19 performance beyond SC.

20 ## 5.2 Future work

21 The electrochemical performance (cycle life, specific energy and power)

22 of LiC requires continuous improvement from a holistic perspective

23 without limitations to specific device components. Although the AC

129

1 cathode remains a limiting factor toward achieving higher capacities and

2 improved energy density, several approaches can potentially resolve this

3 issue and consequentially enhance the performance of the LiC.

4 • Beginning from the cycle life, a continued investigation into the

5 relationship between the electrolyte solvent properties and

6 cycling stability is needed. The search for more high-dielectric

7 solvents beyond EC (due to the very high viscosity) and

8 corresponding low-viscosity solvents beyond EMC and DMC are

9 vital to realise further the benefits of improved anion stability in

10 LiC accrued from using high-dielectric solvents. Since the high

11 dielectric solvents typically have higher viscosities, mixed

12 electrolyte solvent blends with very low viscosities can mitigate

13 the increased ion diffusion resistance caused by the high EC%.

14 Examples of interesting solvents include partially fluorinated

15 ethers and localized high-concentration electrolytes consisting of

16 conventional high-concentration electrolytes mixed with a

17 diluent. These types of electrolytes have yielded promising

18 results with high-voltage cathodes and lithium metal anodes due

19 to the improved CEI/SEI film properties.

20 • Understanding the influence of chemical cross-talk species

21 originating from the use of CEI/SEI film-forming additives in

22 LiC electrolytes. These additives are deliberately introduced to

23 optimize the electrode/electrolyte interface properties. However,

24 the influence of these species on the AC surface remains a

25 mystery. Specifically, questions such as whether the AC charge

1 storage mechanism can be influenced by these additives and to
2 what degree electrolyte decomposition can be abated on the AC
3 surface due to the formation of a passivation film.

4 Beyond the electrolyte, these techniques on the cathode active material
5 level can further improve the performance of LiC

6 • Optimization of the activation process of AC through the use of
7   nanoscale atomically dispersed synthetic precursors containing
8   alkali metals. This approach is adapted from the self-activating
9   biomass precursors. Using such synthetic precursors and
10   controlled percentages of the dispersed alkali metals will enable
11   the production of high-quality AC with controlled pore size
12   distribution and high purity. Hence, redundant pores are
13   eliminated, while the volumetric performance is likewise
14   improved due to maximized electrode density.

15 • The development of hybrid amorphous-graphitized AC presents
16   another approach for enhancing the capacity. However, a good
17   balance between graphitized and amorphous species is needed to
18   improve the capacity without affecting the rate performance. The
19   implementation of this technique will enable a hybrid charge
20   storage mechanism consisting of shallow intercalation and the
21   typical ion adsorption/desorption in the AC pores.

Reference

[1] B. Babu, P. Simon, A. Balducci, Fast charging materials for high power applications, Advanced Energy Materials 10(29) (2020) 2001128.

[2] P. Simon, Y. Gogotsi, B. Dunn, Where do batteries end and supercapacitors begin?, Science 343(6176) (2014) 1210-1211.

[3] P. Simon, Y. Gogotsi, Materials for electrochemical capacitors, Nature Materials 7 (2008) 845.

[4] G.G. Amatucci, F. Badway, A. Du Pasquier, T. Zheng, An asymmetric hybrid nonaqueous energy storage cell, Journal of the Electrochemical Society 148(8) (2001) A930.

[5] B. Li, J. Zheng, H. Zhang, L. Jin, D. Yang, H. Lv, C. Shen, A. Shellikeri, Y. Zheng, R. Gong, Electrode materials, electrolytes, and challenges in nonaqueous lithium-ion capacitors, Advanced Materials 30(17) (2018) 1705670.

[6] P.H. Smith, T.N. Tran, T.L. Jiang, J. Chung, Lithium-ion capacitors: Electrochemical performance and thermal behavior, Journal of power sources 243 (2013) 982-992.

[7] M. Soltani, S.H. Beheshti, A comprehensive review of lithium ion capacitor: development, modelling, thermal management and applications, Journal of Energy Storage 34 (2021) 102019.

[8] J. Micro, JM Energy's Lithium Ion Capacitor: the Hybrid Energy Storage Advantage, Thin film users group: Alternative Energy Symposium, 2009.

[9] J. Ding, W. Hu, E. Paek, D. Mitlin, Review of hybrid ion capacitors: from aqueous to lithium to sodium, Chemical reviews 118(14) (2018) 6457-6498.

[10] Z. Shi, J. Zhang, J. Wang, J. Shi, C. Wang, Effect of the capacity design of activated carbon cathode on the electrochemical performance of lithium-ion capacitors, Electrochimica Acta 153 (2015) 476-483.

[11] S.R. Sivakkumar, A. Pandolfo, Evaluation of lithium-ion capacitors assembled with pre-lithiated graphite anode and activated carbon cathode, Electrochimica Acta 65 (2012) 280-287.

[12] O.E. Eleri, F. Lou, Z. Yu, Lithium-Ion Capacitors: A Review of Strategies toward Enhancing the Performance of the Activated Carbon Cathode, Batteries 9(11) (2023) 533.

[13] S.D. Magar, C. Leibing, J.L. Gómez-Urbano, R. Cid, D. Carriazo, A. Balducci, Brewery waste derived activated carbon for high performance electrochemical capacitors and lithium-ion capacitors, Electrochimica Acta 446 (2023) 142104.

[14] B. Xue, L. Jin, Z. Chen, Y. Zhu, Z. Wang, X. Liu, X. Wang, The template effect of silica in rice husk for efficient synthesis of the activated carbon based electrode material, Journal of Alloys and Compounds 789 (2019) 777-784.

[15] B. Zhu, B. Liu, C. Qu, H. Zhang, W. Guo, Z. Liang, F. Chen, R. Zou, Tailoring biomass-derived carbon for high-performance supercapacitors from controllably cultivated algae microspheres, Journal of Materials Chemistry A 6(4) (2018) 1523-1530.

[16] C. Falco, J.M. Sieben, N. Brun, M. Sevilla, T. Van der Mauelen, E. Morallón, D. Cazorla-Amorós, M.M. Titirici, Hydrothermal carbons from hemicellulose-derived aqueous hydrolysis products as electrode materials for supercapacitors, ChemSusChem 6(2) (2013) 374-382.

[17] P. Kleszyk, P. Ratajczak, P. Skowron, J. Jagiello, Q. Abbas, E. Frąckowiak, F. Béguin, Carbons with narrow pore size distribution prepared by simultaneous carbonization and self-activation of tobacco stems and their application to supercapacitors, Carbon 81 (2015) 148-157.

[18] Y. Tong, J. Yang, J. Li, Z. Cong, L. Wei, M. Liu, S. Zhai, K. Wang, Q. An, Lignin-derived electrode materials for supercapacitor applications: progress and perspectives, Journal of Materials Chemistry A (2023).

[19] D. Weingarth, A. Foelske-Schmitz, R. Kötz, Cycle versus voltage hold–Which is the better stability test for electrochemical double layer capacitors?, Journal of Power Sources 225 (2013) 84-88.

[20] M. Kabir, D.E. Demirocak, Degradation mechanisms in Li-ion batteries: a state-of-the-art review, International Journal of Energy Research 41(14) (2017) 1963-1986.

[21] A. Sarkar, I.C. Nlebedim, P. Shrotriya, Performance degradation due to anodic failure mechanisms in lithium-ion batteries, Journal of Power Sources 502 (2021) 229145.

[22] P. Azaïs, L. Duclaux, P. Florian, D. Massiot, M.-A. Lillo-Rodenas, A. Linares-Solano, J.-P. Peres, C. Jehoulet, F. Béguin, Causes of supercapacitors ageing in organic electrolyte, Journal of power sources 171(2) (2007) 1046-1053.

[23] P. Ruch, D. Cericola, A. Foelske, R. Kötz, A. Wokaun, A comparison of the aging of electrochemical double layer capacitors with acetonitrile and propylene carbonate-based electrolytes at elevated voltages, Electrochimica Acta 55(7) (2010) 2352-2357.

[24] S.S. Zhang, Effect of surface oxygen functionalities on capacitance of activated carbon in non-aqueous electrolyte, Journal of Solid State Electrochemistry 21(7) (2017) 2029-2036.

[25] O.E. Eleri, K.U. Azuatalam, M.W. Minde, A.M. Trindade, N. Muthuswamy, F. Lou, Z. Yu, Towards high-energy-density supercapacitors via less-defects activated carbon from sawdust, Electrochimica Acta 362 (2020) 137152.

[26] C. Wu, F. Zhang, X. Xiao, J. Chen, J. Sun, D. Gandla, Y. Ein-Eli, D.Q. Tan, Enhanced Electrochemical Performance of Supercapacitors via Atomic Layer Deposition of ZnO on the Activated Carbon Electrode Material, Molecules 26(14) (2021) 4188.

[27] C. Liu, B.B. Koyyalamudi, L. Li, S. Emani, C. Wang, L.L. Shaw, Improved capacitive energy storage via surface functionalization of activated carbon as cathodes for lithium ion capacitors, Carbon 109 (2016) 163-172.

[28] B. Fang, L. Binder, Enhanced surface hydrophobisation for improved performance of carbon aerogel electrochemical capacitor, Electrochimica acta 52(24) (2007) 6916-6921.

[29] P. Carrott, M.R. Carrott, Lignin–from natural adsorbent to activated carbon: a review, Bioresource technology 98(12) (2007) 2301-2312.

[30] P. González-García, Activated carbon from lignocellulosics precursors: A review of the synthesis methods, characterization techniques and applications, Renewable and Sustainable Energy Reviews 82 (2018) 1393-1414.

[31] M.A. Yahya, Z. Al-Qodah, C.Z. Ngah, Agricultural bio-waste materials as potential sustainable precursors used for activated carbon production: A review, Renewable and sustainable energy reviews 46 (2015) 218-235.

[32] M. Danish, T. Ahmad, A review on utilization of wood biomass as a sustainable precursor for activated carbon production and application, Renewable and Sustainable Energy Reviews 87 (2018) 1-21.

[33] A.M. Abioye, F.N. Ani, Recent development in the production of activated carbon electrodes from agricultural waste biomass for

supercapacitors: a review, Renewable and sustainable energy reviews 52 (2015) 1282-1293.

[34] N.A. Rashidi, S. Yusup, A review on recent technological advancement in the activated carbon production from oil palm wastes, Chemical Engineering Journal 314 (2017) 277-290.

[35] B.E. Conway, Electrochemical supercapacitors: scientific fundamentals and technological applications, Springer Science & Business Media2013.

[36] H.v. Helmholtz, Ueber einige Gesetze der Vertheilung elektrischer Ströme in körperlichen Leitern, mit Anwendung auf die thierisch-elektrischen Versuche (Schluss.), Annalen der Physik 165(7) (1853) 353-377.

[37] Y. Gao, Q. Yue, B. Gao, A. Li, Insight into activated carbon from different kinds of chemical activating agents: A review, Sci Total Environ 746 (2020) 141094.

[38] K. Ukanwa, K. Patchigolla, R. Sakrabani, E. Anthony, S. Mandavgane, A Review of Chemicals to Produce Activated Carbon from Agricultural Waste Biomass, Sustainability 11(22) (2019).

[39] O. Barbieri, M. Hahn, A. Herzog, R. Kötz, Capacitance limits of high surface area activated carbons for double layer capacitors, Carbon 43(6) (2005) 1303-1310.

[40] V. Khomenko, E. Raymundo-Piñero, F. Béguin, High-energy density graphite/AC capacitor in organic electrolyte, Journal of Power Sources 177(2) (2008) 643-651.

[41] G. Salitra, A. Soffer, L. Eliad, Y. Cohen, D. Aurbach, Carbon electrodes for double-layer capacitors I. Relations between ion and pore dimensions, Journal of the Electrochemical Society 147(7) (2000) 2486.

[42] M. Salanne, B. Rotenberg, K. Naoi, K. Kaneko, P.-L. Taberna, C.P. Grey, B. Dunn, P. Simon, Efficient storage mechanisms for building better supercapacitors, Nature Energy 1(6) (2016) 1-10.

[43] W. Zheng, Z. Li, G. Han, Q. Zhao, G. Lu, X. Hu, J. Sun, R. Wang, C. Xu, Nitrogen-doped activated porous carbon for 4.5 V lithium-ion capacitor with high energy and power density, Journal of Energy Storage 47 (2022) 103675.

[44] G. Li, Z. Yang, Z. Yin, H. Guo, Z. Wang, G. Yan, Y. Liu, L. Li, J. Wang, Non-aqueous dual-carbon lithium-ion capacitors: a review, Journal of Materials Chemistry A 7(26) (2019) 15541-15563.

[45] D.P. Dubal, O. Ayyad, V. Ruiz, P. Gomez-Romero, Hybrid energy storage: the merging of battery and supercapacitor chemistries, Chemical Society Reviews 44(7) (2015) 1777-1790.

[46] S. Li, J. Chen, M. Cui, G. Cai, J. Wang, P. Cui, X. Gong, P.S. Lee, A High-Performance Lithium-Ion Capacitor Based on 2D Nanosheet Materials, Small 13(6) (2017) 1602893.

[47] K. Laszlo, E. Tombacz, K. Josepovits, Effect of activation on the surface chemistry of carbons from polymer precursors, Carbon 39(8) (2001) 1217-1228.

[48] G. Lota, B. Grzyb, H. Machnikowska, J. Machnikowski, E. Frackowiak, Effect of nitrogen in carbon electrode on the supercapacitor performance, Chemical Physics Letters 404(1-3) (2005) 53-58.

[49] L. Lyu, K.-d. Seong, D. Ko, J. Choi, C. Lee, T. Hwang, Y. Cho, X. Jin, W. Zhang, H. Pang, Recent development of biomass-derived carbons and composites as electrode materials for supercapacitors, Materials Chemistry Frontiers 3(12) (2019) 2543-2570.

[50] B. Li, F. Dai, Q. Xiao, L. Yang, J. Shen, C. Zhang, M. Cai, Nitrogen-doped activated carbon for a high energy hybrid supercapacitor, Energy & Environmental Science 9(1) (2016) 102-106.

[51] L. Ci, L. Song, C. Jin, D. Jariwala, D. Wu, Y. Li, A. Srivastava, Z. Wang, K. Storr, L. Balicas, Atomic layers of hybridized boron nitride and graphene domains, Nature materials 9(5) (2010) 430-435.

[52] H. Jiang, D. Shi, X. Sun, S. Wang, Y. Li, B. Chang, B. Zhang, Y. Shao, Y. Wu, X. Hao, Boron carbonitride lithium-ion capacitors with an electrostatically expanded operating voltage window, ACS Applied Materials & Interfaces 12(42) (2020) 47425-47434.

[53] X.-r. Li, Y.-h. Jiang, P.-z. Wang, Y. Mo, Z.-j. Li, R.-j. Yu, Y.-t. Du, X.-r. Zhang, Y. Chen, Effect of the oxygen functional groups of activated carbon on its electrochemical performance for supercapacitors, New Carbon Materials 35(3) (2020) 232-243.

[54] H. Zhou, Y. Peng, H.B. Wu, F. Sun, H. Yu, F. Liu, Q. Xu, Y. Lu, Fluorine-rich nanoporous carbon with enhanced surface affinity in organic electrolyte for high-performance supercapacitors, Nano energy 21 (2016) 80-89.

[55] Y. Gao, Z. Yang, Y. Wang, X. Wang, Boosting capacitive storage of cathode for lithium-ion capacitors: Combining pore structure with P-doping, Electrochimica Acta 368 (2021) 137646.

[56] X. Hu, M. Fan, Y. Zhu, Q. Zhu, Q. Song, Z. Dong, Biomass-derived phosphorus-doped carbon materials as efficient metal-free catalysts for selective aerobic oxidation of alcohols, Green Chemistry 21(19) (2019) 5274-5283.

[57] Z.-L. Jiang, H. Sun, W.-K. Shi, J.-Y. Cheng, J.-Y. Hu, H.-L. Guo, M.-Y. Gao, H. Zhou, S.-G. Sun, P-Doped Hive-like Carbon Derived from Pinecone Biomass as Efficient Catalyst for Li–O2 Battery, ACS Sustainable Chemistry & Engineering 7(16) (2019) 14161-14169.

[58] R. Thangavel, A.G. Kannan, R. Ponraj, V. Thangavel, D.-W. Kim, Y.-S. Lee, Nitrogen-and sulfur-enriched porous carbon from waste watermelon seeds for high-energy, high-temperature green ultracapacitors, Journal of Materials Chemistry A 6(36) (2018) 17751-17762.

[59] G. Xu, J. Han, B. Ding, P. Nie, J. Pan, H. Dou, H. Li, X. Zhang, Biomass-derived porous carbon materials with sulfur and nitrogen dual-doping for energy storage, Green chemistry 17(3) (2015) 1668-1674.

[60] Y. Ren, J. Zhang, Q. Xu, Z. Chen, D. Yang, B. Wang, Z. Jiang, Biomass-derived three-dimensional porous N-doped carbonaceous aerogel for efficient supercapacitor electrodes, Rsc Advances 4(45) (2014) 23412-23419.

[61] M. Molina-Sabio, F. Rodrıguez-Reinoso, Role of chemical activation in the development of carbon porosity, Colloids and Surfaces A: Physicochemical and Engineering Aspects 241(1-3) (2004) 15-25.

[62] A.C. Lua, F.Y. Lau, J. Guo, Influence of pyrolysis conditions on pore development of oil-palm-shell activated carbons, Journal of analytical and applied pyrolysis 76(1-2) (2006) 96-102.

[63] A. Bóta, K. László, L.G. Nagy, T. Copitzky, Comparative study of active carbons from different precursors, Langmuir 13(24) (1997) 6502-6509.

[64] C.-y. Guo, C.-y. Wang, Effects of microstructure of precursors on characteristics of pitch based activated carbons, Microporous and mesoporous materials 102(1-3) (2007) 337-340.

[65] E. Raymundo-Piñero, M. Cadek, F. Béguin, Tuning carbon materials for supercapacitors by direct pyrolysis of seaweeds, Advanced Functional Materials 19(7) (2009) 1032-1039.

[66] M. Endo, Y. Kim, K. Ishii, T. Inoue, T. Nomura, N. Miyashita, M. Dresselhaus, Heat-treatment retention time dependence of

polyvinylidenechloride-based carbons on their application to electric double-layer capacitors, Journal of materials research 18(3) (2003) 693-701.

[67] J. Niu, R. Shao, M. Liu, J. Liang, Z. Zhang, M. Dou, Y. Huang, F. Wang, Porous carbon electrodes with battery-capacitive storage features for high performance Li-ion capacitors, Energy Storage Materials 12 (2018) 145-152.

[68] A. Shellikeri, S. Yturriaga, J. Zheng, W. Cao, M. Hagen, J. Read, T. Jow, J. Zheng, Hybrid lithium-ion capacitor with LiFePO4/AC composite cathode–long term cycle life study, rate effect and charge sharing analysis, Journal of Power Sources 392 (2018) 285-295.

[69] M. Granados-Moreno, G. Moreno-Fernández, R. Mysyk, D. Carriazo, A high-energy hybrid lithium-ion capacitor enabled by a mixed capacitive-battery storage LiFePO 4–AC cathode and a SnP 2 O 7–rGO anode, Sustainable Energy & Fuels 7(4) (2023) 965-976.

[70] N. Böckenfeld, T. Placke, M. Winter, S. Passerini, A. Balducci, The influence of activated carbon on the performance of lithium iron phosphate based electrodes, Electrochimica Acta 76 (2012) 130-136.

[71] X. Sun, X. Zhang, H. Zhang, N. Xu, K. Wang, Y. Ma, High performance lithium-ion hybrid capacitors with pre-lithiated hard carbon anodes and bifunctional cathode electrodes, Journal of Power Sources 270 (2014) 318-325.

[72] C.-C. Chen, J. Patra, F.-M. Wang, J.-Y. Lin, Q.-F. Dong, Y.-S. Su, J.-K. Chang, Binder-controlled pore size distribution of carbon electrodes to mitigate self-discharge of supercapacitors, Carbon (2023).

[73] H.Y. Tran, M. Wohlfahrt-Mehrens, S. Dsoke, Influence of the binder nature on the performance and cycle life of activated carbon electrodes in electrolytes containing Li-salt, Journal of Power Sources 342 (2017) 301-312.

[74] T.R. Jow, K. Xu, O. Borodin, M. Ue, Electrolytes for lithium and lithium-ion batteries, Springer2014.

[75] C. Zhong, Y. Deng, W. Hu, J. Qiao, L. Zhang, J. Zhang, A review of electrolyte materials and compositions for electrochemical supercapacitors, Chemical Society Reviews 44(21) (2015) 7484-7539.

[76] C. Decaux, C.M. Ghimbeu, M. Dahbi, M. Anouti, D. Lemordant, F. Béguin, C. Vix-Guterl, E. Raymundo-Pinero, Influence of electrolyte

ion–solvent interactions on the performances of supercapacitors porous carbon electrodes, Journal of Power sources 263 (2014) 130-140.

[77] C. ho Lee, C. Jung, Enhancement of Li+ ions mobility on activated carbon electrode for lithium ion capacitor, Electrochimica Acta 232 (2017) 596-600.

[78] C. ho Lee, F. Xu, C. Jung, Influence of the electrolyte distribution near the micropores of the activated carbon (AC) electrode on high rate performance of high voltage capacitors, Electrochimica Acta 131 (2014) 240-244.

[79] K. Kato, M.-T.F. Rodrigues, G. Babu, P.M. Ajayan, Revealing anion chemistry above 3V in Li-ion capacitors, Electrochimica Acta 324 (2019) 134871.

[80] T. Zhang, B. Fuchs, M. Secchiaroli, M. Wohlfahrt-Mehrens, S. Dsoke, Electrochemical behavior and stability of a commercial activated carbon in various organic electrolyte combinations containing Li-salts, Electrochimica Acta 218 (2016) 163-173.

[81] D. Stępień, Z. Zhao, S. Dsoke, Shift to post-li-ion capacitors: Electrochemical behavior of activated carbon electrodes in li-, na-and k-salt containing organic electrolytes, Journal of The Electrochemical Society 165(11) (2018) A2807.

[82] X.Y. Shan, Y. Wang, D.W. Wang, F. Li, H.M. Cheng, Armoring graphene cathodes for high-rate and long-life lithium ion supercapacitors, Advanced Energy Materials 6(6) (2016) 1502064.

[83] D. Han, Z. Weng, P. Li, Y. Tao, C. Cui, L. Zhang, W. Lin, Y. Gao, D. Kong, Q.-H. Yang, Electrode thickness matching for achieving high-volumetric-performance lithium-ion capacitors, Energy Storage Materials 18 (2019) 133-138.

[84] H. Qin, H. Chao, M. Zhang, Y. Huang, H. Liu, J. Cheng, L. Cao, Q. Xu, L. Guan, X. Teng, Precious potential regulation of carbon cathode enabling high-performance lithium-ion capacitors, Carbon 180 (2021) 110-117.

[85] S. Dsoke, B. Fuchs, E. Gucciardi, M. Wohlfahrt-Mehrens, The importance of the electrode mass ratio in a Li-ion capacitor based on activated carbon and Li4Ti5O12, Journal of Power Sources 282 (2015) 385-393.

[86] L. Jin, X. Guo, C. Shen, N. Qin, J. Zheng, Q. Wu, C. Zhang, J.P. Zheng, A universal matching approach for high power-density and high

cycling-stability lithium ion capacitor, Journal of Power Sources 441 (2019) 227211.

[87] X. Zhang, X. Zhang, X. Sun, Y. An, S. Song, C. Li, K. Wang, F. Su, C.-M. Chen, F. Liu, Electrochemical impedance spectroscopy study of lithium-ion capacitors: Modeling and capacity fading mechanism, Journal of Power Sources 488 (2021) 229454.

[88] D. Weingarth, H. Noh, A. Foelske-Schmitz, A. Wokaun, R. Kötz, A reliable determination method of stability limits for electrochemical double layer capacitors, Electrochimica Acta 103 (2013) 119-124.

[89] X. Sun, X. Zhang, K. Wang, Y. An, X. Zhang, C. Li, Y. Ma, Determination strategy of stable electrochemical operating voltage window for practical lithium-ion capacitors, Electrochimica Acta 428 (2022) 140972.

[90] S. Dsoke, Expanding the Cathodic Potential Window of Activated Carbon Electrodes in a Lithium-Salt Containing Electrolyte, Batteries & Supercaps 1(6) (2018) 215-222.

[91] Z. Huang, Z. Deng, Y. Zhong, M. Xu, S. Li, X. Liu, Y. Zhou, K. Huang, Y. Shen, Y. Huang, Progress and challenges of prelithiation technology for lithium-ion battery, Carbon Energy 4(6) (2022) 1107-1132.

[92] F. Holtstiege, P. Bärmann, R. Nölle, M. Winter, T. Placke, Pre-Lithiation Strategies for Rechargeable Energy Storage Technologies: Concepts, Promises and Challenges, Batteries 4(1) (2018).

[93] W.M. Dose, C.S. Johnson, Cathode pre-lithiation/sodiation for next-generation batteries, Current Opinion in Electrochemistry 31 (2022) 100827.

[94] M. Arnaiz, D. Shanmukaraj, D. Carriazo, D. Bhattacharjya, A. Villaverde, M. Armand, J. Ajuria, A transversal low-cost pre-metallation strategy enabling ultrafast and stable metal ion capacitor technologies, Energy & Environmental Science 13(8) (2020) 2441-2449.

[95] M.-S. Park, Y.-G. Lim, J.-H. Kim, Y.-J. Kim, J. Cho, J.-S. Kim, A novel lithium-doping approach for an advanced lithium ion capacitor, Adv. Energy Mater 1(6) (2011) 1002-1006.

[96] M.S. Park, Y.G. Lim, S.M. Hwang, J.H. Kim, J.S. Kim, S.X. Dou, J. Cho, Y.J. Kim, Scalable integration of Li5FeO4 towards robust, high-performance lithium-ion hybrid capacitors, ChemSusChem 7(11) (2014) 3138-3144.

[97] P. Jeżowski, O. Crosnier, E. Deunf, P. Poizot, F. Béguin, T. Brousse, Safe and recyclable lithium-ion capacitors using sacrificial organic lithium salt, Nature materials 17(2) (2018) 167-173.

[98] C. Sun, X. Zhang, C. Li, K. Wang, X. Sun, Y. Ma, High-efficiency sacrificial prelithiation of lithium-ion capacitors with superior energy-storage performance, Energy Storage Materials 24 (2020) 160-166.

[99] S.S. Zhang, Eliminating pre-lithiation step for making high energy density hybrid Li-ion capacitor, Journal of Power Sources 343 (2017) 322-328.

[100] X. Sun, X. Zhang, W. Liu, K. Wang, C. Li, Z. Li, Y. Ma, Electrochemical performances and capacity fading behaviors of activated carbon/hard carbon lithium ion capacitor, Electrochimica Acta 235 (2017) 158-166.

[101] K. Guo, S. Qi, H. Wang, J. Huang, M. Wu, Y. Yang, X. Li, Y. Ren, J. Ma, High-Voltage Electrolyte Chemistry for Lithium Batteries, Small Science 2(5) (2022) 2100107.

[102] C. Tran, J. Kafle, X.-Q. Yang, D. Qu, Increased discharge capacity of a Li-air activated carbon cathode produced by preventing carbon surface passivation, Carbon 49(4) (2011) 1266-1271.

[103] F. Béguin, V. Presser, A. Balducci, E. Frackowiak, Carbons and electrolytes for advanced supercapacitors, Advanced materials 26(14) (2014) 2219-2251.

[104] M.M. Hantel, T. Kaspar, R. Nesper, A. Wokaun, R. Kötz, Partially reduced graphite oxide for supercapacitor electrodes: Effect of graphene layer spacing and huge specific capacitance, Electrochemistry communications 13(1) (2011) 90-92.

[105] S. Mitani, S.-I. Lee, K. Saito, S.-H. Yoon, Y. Korai, I. Mochida, Activation of coal tar derived needle coke with K2CO3 into an active carbon of low surface area and its performance as unique electrode of electric double-layer capacitor, Carbon 43(14) (2005) 2960-2967.

[106] T. Aida, I. Murayama, K. Yamada, M. Morita, High-energy-density hybrid electrochemical capacitor using graphitizable carbon activated with KOH for positive electrode, Journal of Power Sources 166(2) (2007) 462-470.

[107] J.G. Han, K. Kim, Y. Lee, N.S. Choi, Scavenging materials to stabilize LiPF6-containing carbonate-based electrolytes for Li-ion batteries, Advanced Materials 31(20) (2019) 1804822.

[108] J. Kim, J.G. Lee, H.-s. Kim, T.J. Lee, H. Park, J.H. Ryu, S.M. Oh, Thermal degradation of solid electrolyte interphase (SEI) layers by phosphorus pentafluoride (PF5) attack, Journal of The Electrochemical Society 164(12) (2017) A2418.

[109] A. Lazzarini, A. Piovano, R. Pellegrini, G. Leofanti, G. Agostini, S. Rudić, M.R. Chierotti, R. Gobetto, A. Battiato, G. Spoto, A comprehensive approach to investigate the structural and surface properties of activated carbons and related Pd-based catalysts, Catalysis Science & Technology 6(13) (2016) 4910-4922.

[110] O. Borodin, W. Behl, T.R. Jow, Oxidative stability and initial decomposition reactions of carbonate, sulfone, and alkyl phosphate-based electrolytes, The Journal of Physical Chemistry C 117(17) (2013) 8661-8682.

[111] D.M. Seo, O. Borodin, S.-D. Han, Q. Ly, P.D. Boyle, W.A. Henderson, Electrolyte solvation and ionic association, Journal of The Electrochemical Society 159(5) (2012) A553.

[112] G. Li, R. Xue, L. Chen, The influence of polytetrafluorethylene reduction on the capacity loss of the carbon anode for lithium ion batteries, Solid State Ionics 90(1-4) (1996) 221-225.

[113] W. Chen, X. Zhou, S. Shi, N. Thiphuong, M. Chen, Synergistical enhancement of the electrochemical properties of lignin-based activated carbon using NH 3· H 2 O dielectric barrier discharge plasma, RSC advances 7(12) (2017) 7392-7400.

[114] T. Jawhari, A. Roid, J. Casado, Raman spectroscopic characterization of some commercially available carbon black materials, Carbon 33(11) (1995) 1561-1565.

[115] A. Sadezky, H. Muckenhuber, H. Grothe, R. Niessner, U. Pöschl, Raman microspectroscopy of soot and related carbonaceous materials: Spectral analysis and structural information, Carbon 43(8) (2005) 1731-1742.

[116] M.A.d. Amaral, J.T. Matsushima, M.C. Rezende, E.S. Gonçalves, J.S. Marcuzzo, M.R. Baldan, Production and characterization of activated carbon fiber from textile PAN fiber, Journal of Aerospace Technology and Management 9 (2017) 423-430.

[117] P.T. Araujo, M. Terrones, M.S. Dresselhaus, Defects and impurities in graphene-like materials, Materials Today 15(3) (2012) 98-109.

[118] D.S. Hall, J. Self, J. Dahn, Dielectric constants for quantum chemistry and Li-ion batteries: solvent blends of ethylene carbonate and ethyl methyl carbonate, The Journal of Physical Chemistry C 119(39) (2015) 22322-22330.

[119] R. Naejus, D. Lemordant, R. Coudert, P. Willmann, Excess thermodynamic properties of binary mixtures containing linear or cyclic carbonates as solvents at the temperatures 298.15 K and 315.15 K, The Journal of Chemical Thermodynamics 29(12) (1997) 1503-1515.

[120] A.B. McEwen, S.F. McDevitt, V.R. Koch, Nonaqueous electrolytes for electrochemical capacitors: imidazolium cations and inorganic fluorides with organic carbonates, Journal of The Electrochemical Society 144(4) (1997) L84.

[121] I.N. Daniels, Z. Wang, B.B. Laird, Dielectric properties of organic solvents in an electric field, The Journal of Physical Chemistry C 121(2) (2017) 1025-1031.

[122] T. Panja, J. Ajuria, N. Díez, D. Bhattacharjya, E. Goikolea, D. Carriazo, Fabrication of high-performance dual carbon Li-ion hybrid capacitor: mass balancing approach to improve the energy-power density and cycle life, Scientific reports 10(1) (2020) 1-11.

[123] K. Xu, Nonaqueous liquid electrolytes for lithium-based rechargeable batteries, Chemical reviews 104(10) (2004) 4303-4418.

[124] K. Xu, "Charge-transfer" process at graphite/electrolyte interface and the solvation sheath structure of Li+ in nonaqueous electrolytes, Journal of The Electrochemical Society 154(3) (2007) A162.

[125] K. Xu, Y. Lam, S.S. Zhang, T.R. Jow, T.B. Curtis, Solvation sheath of Li+ in nonaqueous electrolytes and its implication of graphite/electrolyte interface chemistry, The Journal of Physical Chemistry C 111(20) (2007) 7411-7421.

[126] C. Bommier, R. Xu, W. Wang, X. Wang, D. Wen, J. Lu, X. Ji, Self-activation of cellulose: A new preparation methodology for activated carbon electrodes in electrochemical capacitors, Nano Energy 13 (2015) 709-717.

[127] P. Ruch, M. Hahn, D. Cericola, A. Menzel, R. Kötz, A. Wokaun, A dilatometric and small-angle X-ray scattering study of the electrochemical activation of mesophase pitch-derived carbon in non-aqueous electrolyte solution, Carbon 48(7) (2010) 1880-1888.

[128] Q. Li, Z. Cao, W. Wahyudi, G. Liu, G.-T. Park, L. Cavallo, T.D. Anthopoulos, L. Wang, Y.-K. Sun, H.N. Alshareef, Unraveling the new role of an ethylene carbonate solvation shell in rechargeable metal ion batteries, ACS Energy Letters 6(1) (2020) 69-78.

[129] S.-K. Jeong, M. Inaba, T. Abe, Z. Ogumi, Surface film formation on graphite negative electrode in lithium-ion batteries: AFM study in an ethylene carbonate-based solution, Journal of The Electrochemical Society 148(9) (2001) A989.

[130] Z. Ding, V. Trouillet, S. Dsoke, Are functional groups beneficial or harmful on the electrochemical performance of activated carbon electrodes?, Journal of The Electrochemical Society 166(6) (2019) A1004.

[131] D.M. Seo, S. Reininger, M. Kutcher, K. Redmond, W.B. Euler, B.L. Lucht, Role of mixed solvation and ion pairing in the solution structure of lithium ion battery electrolytes, The Journal of Physical Chemistry C 119(25) (2015) 14038-14046.

[132] C.L. Campion, W. Li, W.B. Euler, B.L. Lucht, B. Ravdel, J.F. DiCarlo, R. Gitzendanner, K. Abraham, Suppression of toxic compounds produced in the decomposition of lithium-ion battery electrolytes, Electrochemical and Solid-State Letters 7(7) (2004) A194.

[133] S.E. Sloop, J.B. Kerr, K. Kinoshita, The role of Li-ion battery electrolyte reactivity in performance decline and self-discharge, Journal of power sources 119 (2003) 330-337.

[134] O.E. Eleri, J. Pires, F.T. Huld, S. Lu, P. Schweigart, A.M. Svensson, F. Lou, Z. Yu, Enhanced activated carbon lithium-ion capacitor electrochemical stability through electrolyte dielectric optimisation, Sustainable Energy & Fuels (2023).

[135] Y. Rangom, R.R. Gaddam, T.T. Duignan, X. Zhao, Improvement of hard carbon electrode performance by manipulating SEI formation at high charging rates, ACS applied materials & interfaces 11(38) (2019) 34796-34804.

[136] X. Zhang, C. Fan, S. Han, Improving the initial Coulombic efficiency of hard carbon-based anode for rechargeable batteries with high energy density, Journal of Materials Science 52 (2017) 10418-10430.

[137] X. Li, X. Sun, X. Hu, F. Fan, S. Cai, C. Zheng, G.D. Stucky, Review on comprehending and enhancing the initial Coulombic

efficiency of anode materials in lithium-ion/sodium-ion batteries, Nano Energy 77 (2020) 105143.

[138] O.E. Eleri, F. Huld, J. Pires, W.M. Tucho, P. Schweigart, A.M. Svensson, F. Lou, Z. Yu, Revealing mechanisms of activated carbon capacity fade in lithium-ion capacitors, Electrochimica Acta 453 (2023) 142359.

[139] J. Liu, F. Ciucci, The Gaussian process distribution of relaxation times: A machine learning tool for the analysis and prediction of electrochemical impedance spectroscopy data, Electrochimica Acta 331 (2020) 135316.

[140] J.P. Schmidt, T. Chrobak, M. Ender, J. Illig, D. Klotz, E. Ivers-Tiffée, Studies on LiFePO4 as cathode material using impedance spectroscopy, Journal of Power Sources 196(12) (2011) 5342-5348.

[141] W. Cao, M. Greenleaf, Y. Li, D. Adams, M. Hagen, T. Doung, J. Zheng, The effect of lithium loadings on anode to the voltage drop during charge and discharge of Li-ion capacitors, Journal of Power Sources 280 (2015) 600-605.

[142] M. Gaberšček, Understanding Li-based battery materials via electrochemical impedance spectroscopy, Nature Communications 12(1) (2021) 6513.

[143] L. Köps, P. Ruschhaupt, C. Guhrenz, P. Schlee, S. Pohlmann, A. Varzi, S. Passerini, A. Balducci, Development of a high-energy electrical double-layer capacitor demonstrator with 5000 F in an industrial cell format, Journal of Power Sources 571 (2023) 233016.

[144] S. Frisco, A. Kumar, J.F. Whitacre, S. Litster, Understanding Li-ion battery anode degradation and pore morphological changes through nano-resolution X-ray computed tomography, Journal of The Electrochemical Society 163(13) (2016) A2636.

[145] H. Wang, M. Yoshio, Suppression of PF 6− intercalation into graphite by small amounts of ethylene carbonate in activated carbon/graphite capacitors, Chemical communications 46(9) (2010) 1544-1546.

[146] M. Smith, L. Scudiero, J. Espinal, J.-S. McEwen, M. Garcia-Perez, Improving the deconvolution and interpretation of XPS spectra from chars by ab initio calculations, Carbon 110 (2016) 155-171.

[147] R. Lundström, N. Gogoi, X. Hou, E.J. Berg, Competing Ethylene Carbonate Reactions on Carbon Electrode in Li-Ion Batteries, Journal of The Electrochemical Society 170(4) (2023) 040516.

[148] H. Jia, L. Zou, P. Gao, X. Cao, W. Zhao, Y. He, M.H. Engelhard, S.D. Burton, H. Wang, X. Ren, High-performance silicon anodes enabled by nonflammable localized high-concentration electrolytes, Advanced Energy Materials 9(31) (2019) 1900784.

[149] Z. Piao, P. Xiao, R. Luo, J. Ma, R. Gao, C. Li, J. Tan, K. Yu, G. Zhou, H.M. Cheng, Constructing a Stable Interface Layer by Tailoring Solvation Chemistry in Carbonate Electrolytes for High-Performance Lithium-Metal Batteries, Advanced Materials 34(8) (2022) 2108400.

[150] Z.-Y. Wu, Y.-Q. Lu, J.-T. Li, S. Zanna, A. Seyeux, L. Huang, S.-G. Sun, P. Marcus, J. Światowska, Influence of Carbonate Solvents on Solid Electrolyte Interphase Composition over Si Electrodes Monitored by In Situ and Ex Situ Spectroscopies, ACS omega 6(41) (2021) 27335-27350.

[151] P. Verma, P. Maire, P. Novák, A review of the features and analyses of the solid electrolyte interphase in Li-ion batteries, Electrochimica Acta 55(22) (2010) 6332-6341.

[152] O.C. Harris, S.E. Lee, C. Lees, M. Tang, mechanisms and consequences of chemical cross-talk in advanced Li-ion batteries, Journal of Physics: Energy 2(3) (2020) 032002.

[153] S. Wilken, M. Treskow, J. Scheers, P. Johansson, P. Jacobsson, Initial stages of thermal decomposition of LiPF 6-based lithium ion battery electrolytes by detailed Raman and NMR spectroscopy, Rsc Advances 3(37) (2013) 16359-16364.

[154] A. Andersson, K. Edström, Chemical composition and morphology of the elevated temperature SEI on graphite, Journal of the Electrochemical Society 148(10) (2001) A1100.

Appendices

Appendices

Appendix A - Paper I and supplementary information

Lithium-ion capacitors: A review of strategies towards enhancing the performance of the activated carbon cathode

O. E. Eleri, F. Lou, and Z. Yu

Batteries, 2023, 9(11), 533.

DOI: 3390/batteries9110533

Review

Lithium-Ion Capacitors: A Review of Strategies toward Enhancing the Performance of the Activated Carbon Cathode

Obinna Egwu Eleri [1,2], **Fengliu Lou** [2,*] **and Zhixin Yu** [1,*]

[1] Department of Energy and Petroleum Engineering, University of Stavanger, 4036 Stavanger, Norway; obinna@beyonder.no

[2] Beyonder AS, Stokkamyrveien 30, 4313 Sandnes, Norway

[*] Correspondence: fengliu@beyonder.no (F.L.); zhixin.yu@uis.no (Z.Y.)

Abstract: Lithium-ion capacitors (LiC) are promising hybrid devices bridging the gap between batteries and supercapacitors by offering simultaneous high specific power and specific energy. However, an indispensable critical component in LiC is the capacitive cathode for high power. Activated carbon (AC) is typically the cathode material due to its low cost, abundant raw material for production, sustainability, easily tunable properties, and scalability. However, compared to conventional battery-type cathodes, the low capacity of AC remains a limiting factor for improving the specific energy of LiC to match the battery counterparts. This review discusses recent approaches for achieving high-performance LiC, focusing on the AC cathode. The strategies are discussed with respect to active material property modifications, electrodes, electrolytes, and cell design techniques which have improved the AC's capacity/capacitance, operating potential window, and electrochemical stability. Potential strategies and pathways for improved performance of the AC are pinpointed.

Keywords: activated carbon; lithium-ion capacitors; high energy density; high power density and long cycle life

1. Introduction

The global transition toward clean and sustainable energy sources has accelerated the electrification of modern-day technologies, particularly in automotive and uninterruptible power supply where fossil fuel energy sources have previously dominated. Energy storage devices, such as lithium-ion batteries (LiB) and supercapacitors (SC), are vital to achieving this rapid transition but are limited by the former's low specific power and the latter's low specific energy [1,2]. However, a breakthrough in 2011 by Amatucci et al. led to the development of a hybrid energy storage device identified as a lithium-ion capacitor (LiC), which combines electrodes from SC and lithium-ion batteries (LiB) as the cathodes and anodes, respectively, while using similar battery-type electrolytes with wide operating potential windows [3]. Therefore, the LiC possessed higher energy density than SC and higher power density than LiB without the self-discharge problems of the former and with a longer cycle life than the latter [3–5].

The demand for lithium has experienced an exponential increase due to the continued electrification of modern society and global population growth. The lithium supply risk has thus necessitated the research and adoption of alternative metals such as sodium, potassium, and aluminum, which can utilize similar mechanisms and reduce the lithium dependence [6,7]. Hence, some of these alternatives will also be discussed in this work, and the strategies outlined can be applied interchangeably.

Conventional SC electrodes incorporated in LiC facilitate high-power densities due to their surface charge storage phenomena [5,8,9]. However, activated carbon (AC) remains the most commercially feasible large-scale alternative compared to other capacitive

cathodes such as graphene, carbon aerogels, carbon nanotubes, and nanofibers due to the complexity associated with incorporating such exquisite cathodes in mass production. On the contrary, AC is favored by the relative ease of fabrication, availability of raw materials, and process scalability. For example, several companies, such as Haycarb, Beyonder, Jacobi, and Norit Carb, have successfully manufactured AC from precursors such as coconut shells, sawdust, and petroleum coke in continuous commercial processes. In addition, other precursors such as algae [10], brewery wastes [11], corncobs [12], tobacco leaves [13], rice husk [14], and lignin [15] have been used to produce high-quality AC in lab-scale research with optimization strategies to synthesize AC from diverse biomass wastes while achieving excellent performance.

AC produced from brewery wastes possessed a surface area of 3600 m^2/g, pore volumes of 1.8 cm^3/g, and textural features of visible cavities and open channels inherited from the precursor [11]. The high surface area and accessible pores enabled superior rate performance with minor capacity fade even after a 40-fold increase in the scan rate. The AC produced from the activation of corn cob hydrolysis products is characterized by extensive microporosities with surface areas up to 2300 m^2/g, pore volumes of 0.93 cm^3/g, and minimal mesoporosity [12]. Using a two-step activation procedure involving hydrothermal carbonization and subsequent activation, the microstructure of the AC transforms from micrometer-sized spherical particles of varying dimensions to macrometer-sized monolith fragments possessing extensive microporosity. Algae, as a precursor, yields AC with inherent nitrogen doping which can be controlled by optimizing the proteinous nutrients during algae cultivation. However, the porosity of the formed AC is affected by excessive residual metal content which hinders the activation intensity while the inherent nitrogen-doped functionalities are unstable during pyrolysis. Rice husk and tobacco leaves possess inherent silica and atomically dispersed alkali metals, respectively [13,14]. The inherent silica in rice husk enables templated pore creation of beneficial micropores with a narrow pore size distribution while the dispersed alkali metals in tobacco facilitate self-activation by simple carbonization without using externally introduced activation agents. Therefore, the nature of the precursor can significantly influence the properties of the synthesized AC, as will be discussed extensively in Section 2.4.

The renewed focus on sustainable energy storage solutions has spurred interest in carbon-based energy storage devices such as AC/hard carbon (HC) LiC manufactured from sustainable biomass precursors without transition metals. The use of AC as a cathode material is beneficial for achieving sustainable and economical high-powered energy storage devices. For example, wastes and processing by-products such as sawdust and coconut shells, which would have been burnt or deposited in landfills, can be converted into valuable electrode materials for high-power energy storage devices.

When evaluating AC for LiC, the primary parameters considered are its ability to store charge (capacity/capacitance), operating potential range, and electrochemical stability over time. These properties affect the energy, power, and electrochemical stability of the resulting LiC. However, given the non-faradaic surface charge storage phenomena, the AC cathode possesses significantly lower capacity than the faradaic battery-type anode materials incorporated in LiC. Moreover, since the capacity of the LiC is determined by the relation $1/C_{LIC} = 1/C_{anode} + 1/C_{cathode}$, increasing the capacity of the AC becomes vital toward increasing the overall capacity of the LiC. The energy density of LiC is also proportional to the capacitance and square of the operating potential window. Wide operating potential windows can facilitate increased energy density but the electrochemical stability of the electrode at the AC surface can limit the performance. Therefore, to improve the performance of LiC, it is necessary to focus on improving the capacity and electrochemical stability of the AC cathode.

Previously, Dubey et al. [16] reviewed various AC synthesis strategies that yielded favorable morphologies for increased power and energy density. Zou et al. [17] reviewed the application of carbon materials in LiCs. However, only a limited section was devoted to the cathode. Han et al. [18] conducted a comprehensive review of material design

strategies and the performance of different cathode and anode material pairs in LiCs. Dos Reis et al. [19] reviewed the application of biomass produced via different synthesis methods in energy storage devices and the effects of their properties on performance. In most of these works, limited attention was devoted to the AC cathode compared to the anode counterparts. Furthermore, in the few reviews highlighting the cathode, the discussion has predominantly been the review of various material synthesis strategies. Here, we discuss strategies regarding the recent progress in material synthesis, electrode, electrolyte, and cell design which have enhanced the performance of the AC cathode incorporated into the LiCs. A schematic of the approach is displayed in Figure 1.
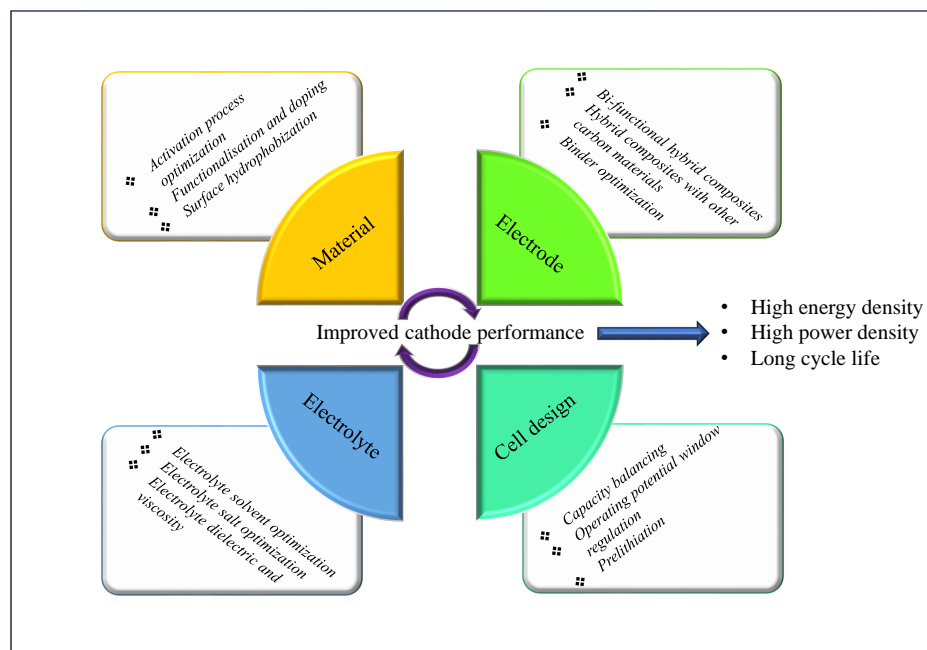
Figure 1. Schematic illustrating strategies toward improved performance of the AC cathode.

By not only focusing on the material design, this review provides a broad perspective on enabling the efficient integration of AC in LiC through favorable synergies with other components. The application of these highlighted techniques during the design and fabrication of LiC will facilitate enhanced performance while mitigating potential issues associated with the AC cathode. In the concluding aspect, further areas requiring attention and future research are highlighted.

2. Material Optimization

AC is synthesized by subjecting a carbon precursor to a controlled heating procedure in the presence of physical or/and chemical activation agents [20–22]. The nature of the activating agent determines the classification of the activation process, broadly categorized into physical activation, chemical activation, or a combination of the two. Excellent reviews exist on producing AC from various biomass sources using physical or chemical activation processes [23–25]. The activation process aims to produce high surface area materials with tailored pores with dimensions suited to the electrolyte moieties to be adsorbed. Parameters such as the precursor type, activation temperature, activation time, and activating agent concentration are varied during the activation process to optimize the resulting AC's surface area and pore size distribution [13]. The surface area and pore size distribution of the AC correlate with the adsorption capacity for electrolyte moieties given the double layer phenomena, where the obtainable capacitance *C (F)* is determined from the equation $C = \varepsilon(A/d)$ [26,27]. The constant ε represents the product of the electric constant and relative permittivity, *A* represents the area of the plates, and *d* represents the distance between the plates. Therefore, the amount of charge stored can be converted to capacity

(mAh) by multiplying the capacitance obtained by the potential window. This section will discuss strategies for improving AC's performance enabled by different material optimization techniques.

2.1. Activation Process Optimization

AC cathodes, by virtue of the surface charge storage phenomenon, require a high surface area with pores consisting of micropores (<2 nm) for adsorption of electrolyte ions, mesopores (2–50 nm) to facilitate ion diffusion and accessibility to the micropores, and macropores (>50 nm) to serve as electrolyte reservoirs and to enhance ion diffusion to the mesopores and micropores. However, these characteristics necessitated the continuous search for optimum activation procedures initially focused on increasing the surface area and optimizing the pore size distribution. As a result, high specific surface areas of up to 3000 $m^2\ g^{-1}$ were achieved using various chemical activation methods, including KOH activation, combined KOH-KCl activation, H_3PO_4 activation, and $ZnCl_2$. Some excellent reviews on the different mechanisms of the activation agents have been published [21–24,28,29]. These high surface area ACs have yielded specific capacitances of up to 160 F g^{-1} within the operating potential window of 0–2.7 V in organic electrolytes. However, it was noticed that further increases in surface area do not translate into higher specific capacitance [30]. Furthermore, the extensive activation treatments broaden the pore size distribution, leading to the abundance of ineffective pores that are smaller than the de-solvated electrolyte ion. Moreover, the existing micropores may widen into mesopores due to the intensive gasification of the carbon matrix. The extensive activation also reduces the carbon content in the matrix as numerous mesopores and macropores are created, reducing the density of the AC. This also affects the electrical conductivity due to a large interparticle gap within the carbon structure and a disconnect within the electronic structure. Consequently, low electrode densities often accompany very high specific surface area AC and may result in poor volumetric performance.

Concerning the electrolyte, the high porosity would necessitate increased electrolyte volume in the cells, which may impact the energy density due to the increased weight [4]. Furthermore, the high surface area may also serve as an active site for accelerated electrolyte decomposition, decreasing the cycle life. Khomenko et al. [31] compared the cycle life of two ACs cycled in organic electrolytes. Figure 2a shows the cycling stability tests of two different ACs: Maxsorb and Super 50 with surface areas of 3487 and 1402 $m^2\ g^{-1}$ cycled at different upper cut-offs, respectively.
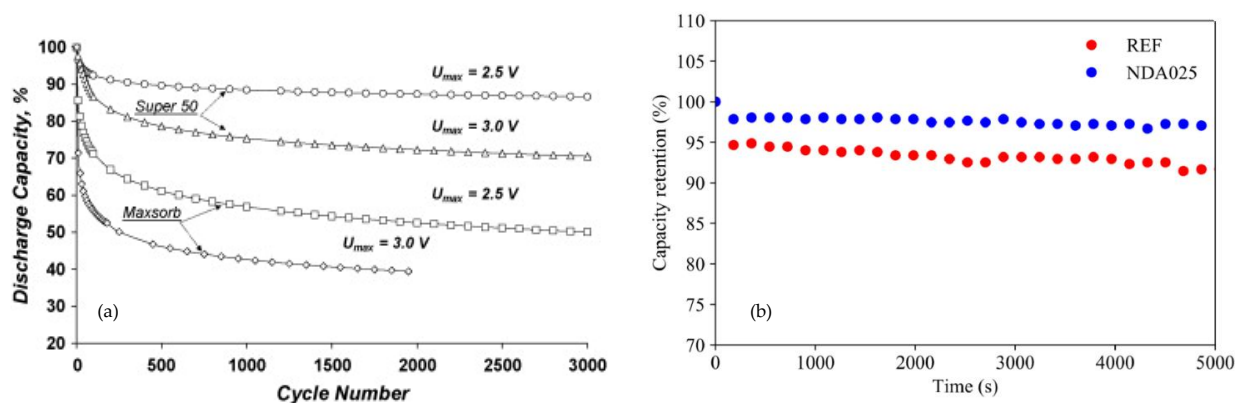
Figure 2. (**a**) Cycle life comparison of Super 50 and Maxsorb using 1 M Et_4NBF_4 in acetonitrile. The cells are cycled with different cut-off voltages (U_{max}) at a current density of 650 mA g^{-1}. Reprinted from [31], copyright (2008), with permission from Elsevier. (**b**) Cycle life comparison of AC produced by a modified activation method (NDA025) and the reference sample (REF) using 1 M $TEABF_4$ in PC. Retrieved from [32], copyright (2020), with permission from Elsevier.

The results in Figure 2a revealed that the AC with the highest surface area had the highest capacity fade. Although a high surface area is required for adsorption, carefully controlled activation procedures are necessary to modulate the surface area and create pores with diameters similar to the electrolyte ions. An AC with pores of similar diameters to the electrolyte ions was reported to have increased capacitance [33]. The discovery that ions could access pores smaller than the solvated ion size further underscores the need for the activation of process optimization [34]. Likewise, controlled mesoporosity formation and tailored microporosity could facilitate increased volumetric performance through enhanced electrode densities.

Several activation techniques have recently yielded ACs with superior gravimetric and volumetric electrochemical performance beyond the typical physical or chemical activation procedure with steam or singular chemical agents. Eleri et al. [32] used a non-destructive activation method to synthesize high-performance AC from sawdust with reduced defects, high surface area, increased microporosity, and high electrode density with optimized mesoporosity. The non-destructive activation (NDA) method incorporated an Al additive in KOH chemical activation acting as an oxygen scavenger to reduce the oxides' extensive gasification of the carbon matrix. The modified activation procedure ensured that exfoliation due to potassium intercalation into the carbon matrix was the dominant mechanism, creating more micropores and reducing gasification-induced mesoporosity. The NDA carbon also exhibited superior performance in the cycling stability test than the reference sample as shown in Figure 2b. The improved performance can be attributed to reduced defective sites on the NDA carbon which are active sites upon which electrolyte degradation is accelerated compared to the reference sample. Zheng et al. [35] incorporated a surfactant-modified KOH activation process in synthesizing in situ nitrogen-doped activated porous carbons with a controlled pore size, which could function as dual anode and cathode materials in a 4.5 V LiC. The porous carbon was obtained from the carbonization of polypyrrole (PPy) prepared with the surfactant cetyltrimethylammonium bromide (CTAB) and subsequent KOH activation of the carbonized material. The surfactant-modified KOH activation process influenced the pore size distribution of the carbon by creating mesopores in the spaces occupied by the decomposed surfactant and controlling the porosity formation. Specific capacities reaching 80 mAh g^{-1} at 0.1 A g^{-1} in the potential window 2–4.5 V were achieved using this material in the half-cell configuration with 1M LiPF$_6$ EC:DEC (1:1) vol% electrolyte. On the contrary, the AC synthesized without the surfactant possessed a higher surface area (2528.0 m^2 g^{-1} compared to 1894.9 m^2 g^{-1}) but poor electrochemical performance due to hindered ion diffusion, nonuniform pore size distribution, and ineffective micropores. Again, this further amplifies the need for optimized pore size distributions in contrast with solely achieving high surface area through extensive activation.

AC is structurally classified as an amorphous disordered material that relies on ion adsorption/desorption as the charge storage mechanism. However, it has been demonstrated that introducing some degree of ordered structures through partial graphitization while maintaining sufficient porosity can also increase the capacity of the AC by enabling intercalation within the ordered structure. Sun et al. [36] synthesized an ordered–disordered hybrid AC cathode as opposed to the typical disordered AC. The ordered–disordered hybrid AC was produced by simultaneous nitrogen doping, in situ graphitization, and subsequent activation of a Ni and Zn citrate composite prepared using a one-step solvothermal route. A schematic of the activation procedure is shown in Figure 3a.

The graphitization degree was controlled by modifying the ratio of the incorporated Zn and Ni elements. The latter two were subsequently removed by acid leaching after the activation process. High-resolution transition electron microscopy (HR-TEM) images of the produced AC showing the ordered structure surrounded by an amorphous phase are presented in Figure 3b–d. The ordered–disordered AC enabled dual charge storage mechanisms through anion intercalation and the typical adsorption and desorption, realizing a specific capacity of 130 mAh g^{-1} in the potential window 2–4.6 V. The assembled LiC had an energy density of 23.5 Wh kg^{-1} at a power density of 40.6 W kg^{-1}. Moreover, the

presence of the ordered structure also decreased the self-discharge while the porous and amorphous nature alleviated the volume swelling commonly encountered in ordered carbon. Cho et al. [37] also developed similar ordered–disordered carbon, named as partially graphitic carbon, which combined shallow intercalation and double-layer adsorption as the charge storage mechanism.
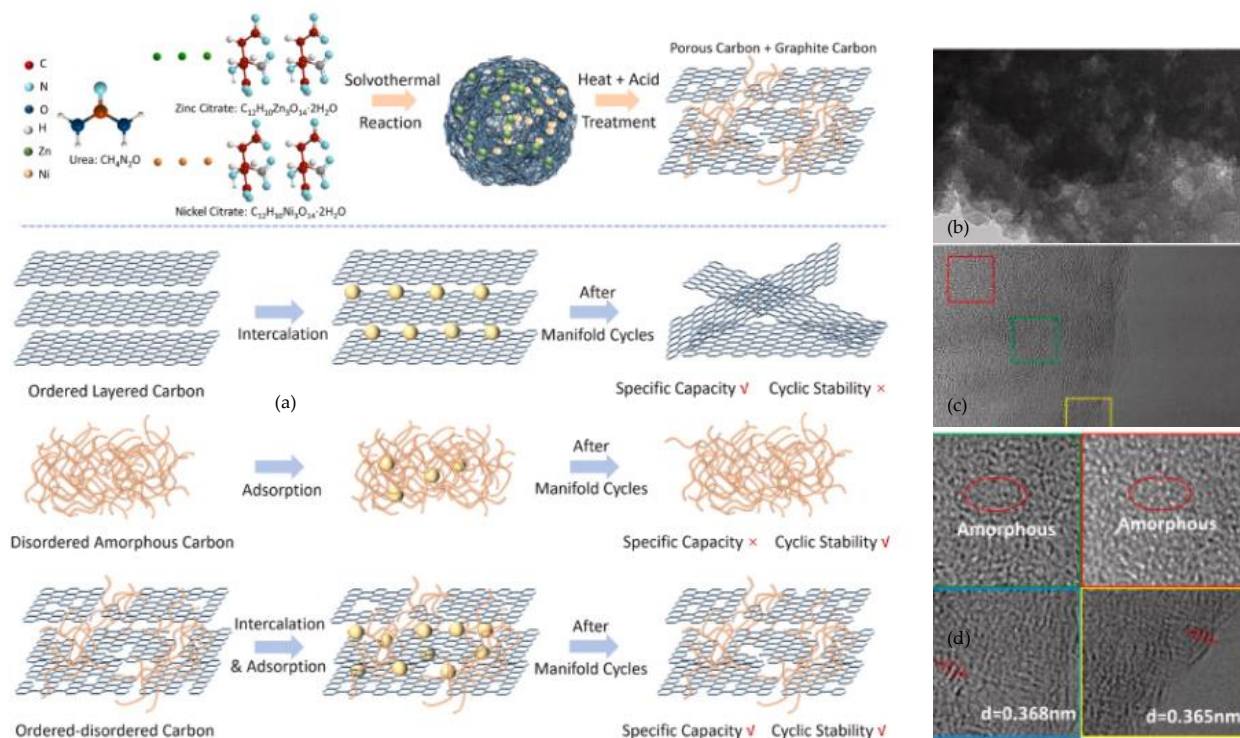
Figure 3. (**a**) Schematic of the preparation procedure. (**b**–**d**) High-resolution transition electron microscopy (HR-TEM) images of the prepared ordered–disordered carbon. Reprinted from [36], copyright (2022) with permission from Elsevier.

In a notable work, Jain et al. [38] reported on the synthesis of a high specific surface area and mesoporosity-rich AC that achieved a specific capacity of 70 mAh g^{-1} in the potential window of 2.0–4.0 V using the electrolyte 1M LiPF$_6$ in EC:DMC (1:1). The AC was produced using a modified ZnCl$_2$ activation method. The precursor material was pretreated with H$_2$O$_2$ and then hydrothermally carbonized in an autoclave. The carbonized material was impregnated with ZnCl$_2$ and a processing agent benzene tetracarboxylic acid (BTA) before drying and subsequent activation. The pre-treatment step with H$_2$O$_2$ enhanced the mesoporosity and the oxygenated surface functionalities onto the carbonized material while the processing agent BTA enabled increased mesopore surface area during activation. Furthermore, the introduced surface functionalities improved the efficacy of the ZnCl$_2$ activation agent by promoting nucleophilic attraction of the Zn^{2+} to the free electron pairs of the oxygen atoms, thereby ensuring greater access to the precursor surface and facilitating dehydration of the biomass material in the activation step.

2.2. Functionalization and Doping

The nature of chemical functionalities at the surface and doped elements within the carbon matrix can influence the electrochemical performance of AC. Surface functionalities could be inherited from the precursor material or deliberately introduced during the activation or post-treatment activation procedures. As a result, benefits such as enhanced conductivity, improved wettability, and increased active sites for pseudocapacitive Li$^+$ storage can be obtained [39]. This section discusses the effect of heteroatoms such as N, B, O, F, S, and P on the AC's performance in nonaqueous electrolytes.

2.2.1. Nitrogen

Nitrogen functionalization has been particularly popular due to improved charge carrier transport caused by increased contributions of p- electrons to the Π system following the positive synergy between the N atom and carbon lattice [39–41]. This therefore enables an increased sorption capacity toward the anion when combined with appropriate pore size distributions [42,43]. The electron-donating abilities induced by nitrogen functionalization create additional electroactive sites, thereby improving the AC's electrochemical reactivity, surface polarity, electrical conductivity, and wettability [44]. Li et al. [45] synthesized nitrogen-doped AC from corn cobs with a very high surface area of up to 2900 m^2 g^{-1}. The nitrogen-doped AC exhibited an initial specific capacity of 129 mAh g^{-1} at 0.4 A g^{-1} in the half-cell configuration using an organic electrolyte and operating potential window of 2–4.5 V. Yang et al. [46] synthesized nitrogen-doped porous carbons using urea as nitrogen dopant and glucose as a precursor. The nitrogen-doped porous carbon realized a specific capacity of 62 mAh g^{-1} in the potential window 3–4.6 V compared to 38 mAh g^{-1} obtained from a commercial AC at similar conditions. Furthermore, specific energies of 83.25 W h kg^{-1} at a 25 kW kg^{-1} power density were achieved using the nitrogen-doped porous carbon as the cathode and MnO-graphene composite as the anode. The impressive performance was attributed to the well-developed interconnected pore structure and active N-sites in the AC that facilitated capacitive and redox reactions during charge storage. Lota et al. [43] investigated the influence of nitrogen content in AC samples on the performance of capacitor systems using aqueous and organic electrolytes. A clear correlation between increased capacities and nitrogen content was obtained in aqueous media. However, in the organic media, increased nitrogen content resulted in a capacitance increase only when matched with appropriate pore size distribution.
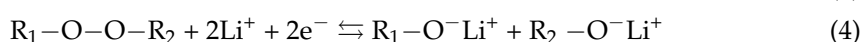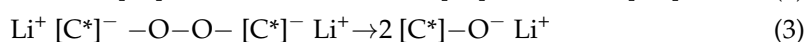
2.2.2. Boron

Boron functionalization is another method of increasing the electrochemical reactivity of the AC by modifying the carbon electronic structure. Functionalization with boron increases the density of charge carriers in the carbon matrix after the substitution and improves the electronic conductivity due to the p-type characteristics [47]. Since boron atoms possess one electron deficient in the valence layer and are less electronegative than carbon, the presence of boron (an electron acceptor) in the carbon matrix induces a shift in the fermi level to the conducting band, thereby modifying the carbon electronic structure and improving properties related to the electrochemical efficiency and chemical reactivity [48–50]. Furthermore, the crystallinity of the carbon structure is improved and the oxidation rate of the matrix is lower due to the decreased electroactive sites for oxygen chemisorption [49–52]. Boron functionalization and the consequent formation of borates on the carbon structure also reportedly induce pseudocapacitive charge storage on the carbon surface [51] together with the improved electrical conductivity of the electrode that enhances the high-rate performance.

Jiang et al. [53] reported the effect of dual doping of boron and nitrogen on the performance of LiC in organic electrolytes. Doping with boron enabled a widened operating potential window of up to 4.8 V and improved electrode conductivities and electrochemical performance. Furthermore, the presence of boron atoms on the cathode promoted the adsorption of PF_6 anions, as revealed by DFT calculations of the adsorption energy. The boron-doped cathode possessed lower adsorption energy compared to the undoped alternative. Therefore, the electropositive boron atoms created a net positive charge on the electrode and, in that way, reinforced the ability of the electrode to lose electrons while facilitating the intense attraction of the PF_6 anion. Consequentially, incorporating the boron-doped cathode in the LiC architecture delivered a specific energy of 200 Wh kg^{-1} at 239.9 W kg^{-1} with a capacity retention of 80% after 7000 cycles. Zhu et al. [54] obtained a high capacity of 190.2 mAh g^{-1} after dual boron–nitrogen doping of a zinc ion capacitor cathode. The dual doping strategy increased anion adsorption and chemical interactions with Zn^{2+} at the electrode/electrolyte interface.

2.2.3. Oxygen

Surface oxygen functionalities present a dilemma for AC regarding irreversible or reversible redox reactions with the nonaqueous electrolytes commonly used in LiC. Liu et al. [55] reported that oxygen functionalization facilitated improved capacitance in AC electrodes used in LiC. Commercial ACs were functionalized by ammonium persulfate and sulfuric acid treatment. The functionalized AC displayed superior capacities of 78 mAh g^{-1} when tested in half cells with a lithium counter electrode and an organic electrolyte of 1 M LiTFMS/diglyme. The authors proposed that the improved performance was caused by reversible pseudocapacitive reactions between Li$^+$ ions and C=O functional groups introduced after the functionalization treatment. However, the functionalized AC displayed lower capacity retention during continuous cycling than the pristine AC. This behavior was further attributed to detrimental irreversible redox processes which may have contributed to lower cyclic stability. Moreover, these redox processes were assumed to be finite and occurred during a transition period in the first few cycles, beyond which stable cycling was attained. A related study by Li et al. [56] also using ammonium persulfate and sulfuric acid functionalization of a commercial AC, revealed that oxygen functionalities improved the performance in the aqueous 6 M KOH electrolyte but not the organic electrolyte 1M Et$_4$NBF$_4$/PC, as shown in Figure 4a. Therefore, the beneficial effect of oxygen functionalities concerning nonaqueous electrolytes may be restricted to AC electrodes cycled in electrolytes with Li$^+$ ions as the adsorbed/desorbed species during charge storage. This was further demonstrated by Zhang et al. [57] who used the electrolyte 1 M LiPF$_6$ in EC:EMC (3:7). The effect of surface oxygen functionalities of the AC was investigated in lithium half cells and symmetric AC/AC cells. It was interesting to observe the positive pseudocapacitive impact of oxygen functionalities arising from faradaic reactions with Li$^+$ ions. The charge and discharge potential profile of the AC electrode with 4.26 wt.% oxygen was examined in the three-electrode configuration. Figure 4b,c shows the potential profiles in the first cycle sweep obtained from different electrolytes. Three regions are identified which correspond to incremental capacity by adsorption/desorption in I, combined adsorption/desorption and pseudocapacitance in II, and irreversible oxidation/reduction in the electrolyte solvent in III.

The Initial reactions between the surface oxygen functionalities and electrolyte moieties affect the initial coulombic efficiency, capacitance retention, potential profile, and subsequent formation of soluble redox products such as organic and hydrogen peroxides. These redox products can shuttle between the positive and negative electrodes due to their strong coordinating ability to Li$^+$. Furthermore, changes in the electrolyte solubility arising from the continued accumulation of such redox products may cause the precipitation of insoluble deposits (lithium salts) at the AC surface, thereby blocking the pores and accessible surface area and reducing the capacity of the AC. The irreversible reactions can be identified by the deviation of the charge and discharge profile from the expected linear lines due to the reversible double-layer adsorption and desorption of electrolyte ions. Nevertheless, the potential profile of the AC gradually reverts to a linear shape upon continued cycling due to the depletion of the irreversible surface oxygen functionalities and the formation of a protective solid electrolyte interface layer. Pseudocapacitive reactions with surface oxygen functionalities of the AC are proposed to occur via the following reactions (1)–(4) [57]:

$$\text{On the positive electrode: } 2[\text{C*}]-\text{OH}-2e^- \leftrightarrows [\text{C*}]-\text{O}-\text{O}-[\text{C*}] + 2\text{H}^+ \qquad (1)$$

$$\text{On the negative electrode: } 2[\text{C*}]=\text{O}+2\text{Li}^+ +2e^- \leftrightarrows \text{Li}^+[\text{C*}]^- -\text{O}-\text{O}-[\text{C*}]^- \text{Li}^+ \qquad (2)$$

$$\text{Li}^+[\text{C*}]^- -\text{O}-\text{O}-[\text{C*}]^- \text{Li}^+ \rightarrow 2[\text{C*}]-\text{O}^- \text{Li}^+ \qquad (3)$$

$$\text{R}_1-\text{O}-\text{O}-\text{R}_2 + 2\text{Li}^+ + 2e^- \leftrightarrows \text{R}_1-\text{O}^-\text{Li}^+ + \text{R}_2 -\text{O}^-\text{Li}^+ \qquad (4)$$
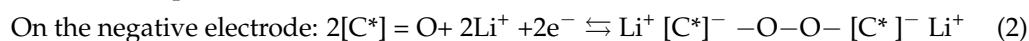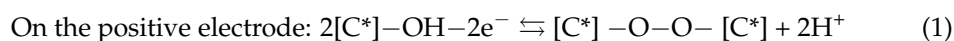
where [C*] represents the sp^2 carbon situated at the edges of the graphene moieties capable of delocalizing the charge. Equations (1) and (2) are reversible processes responsible for the pseudocapacitance through reactions of the surface oxygen bonded to the graphene moieties capable of delocalizing charge. However, Equation (3) expresses the irreversible

formation of an insoluble lithium salt which is terminated by the reaction described in Equation (4). The expression $R_1-O-O-R_2$ represents probable soluble redox species such as organic peroxides and hydrogen peroxide, where R_1 and R_2 are organic functional groups inherent to the AC's surface chemistry. Therefore, Equations (3) and (4) postulate the irreversible reactions responsible for the low initial coulombic efficiency in the first and subsequent cycles prior to depletion of the surface functionalities.
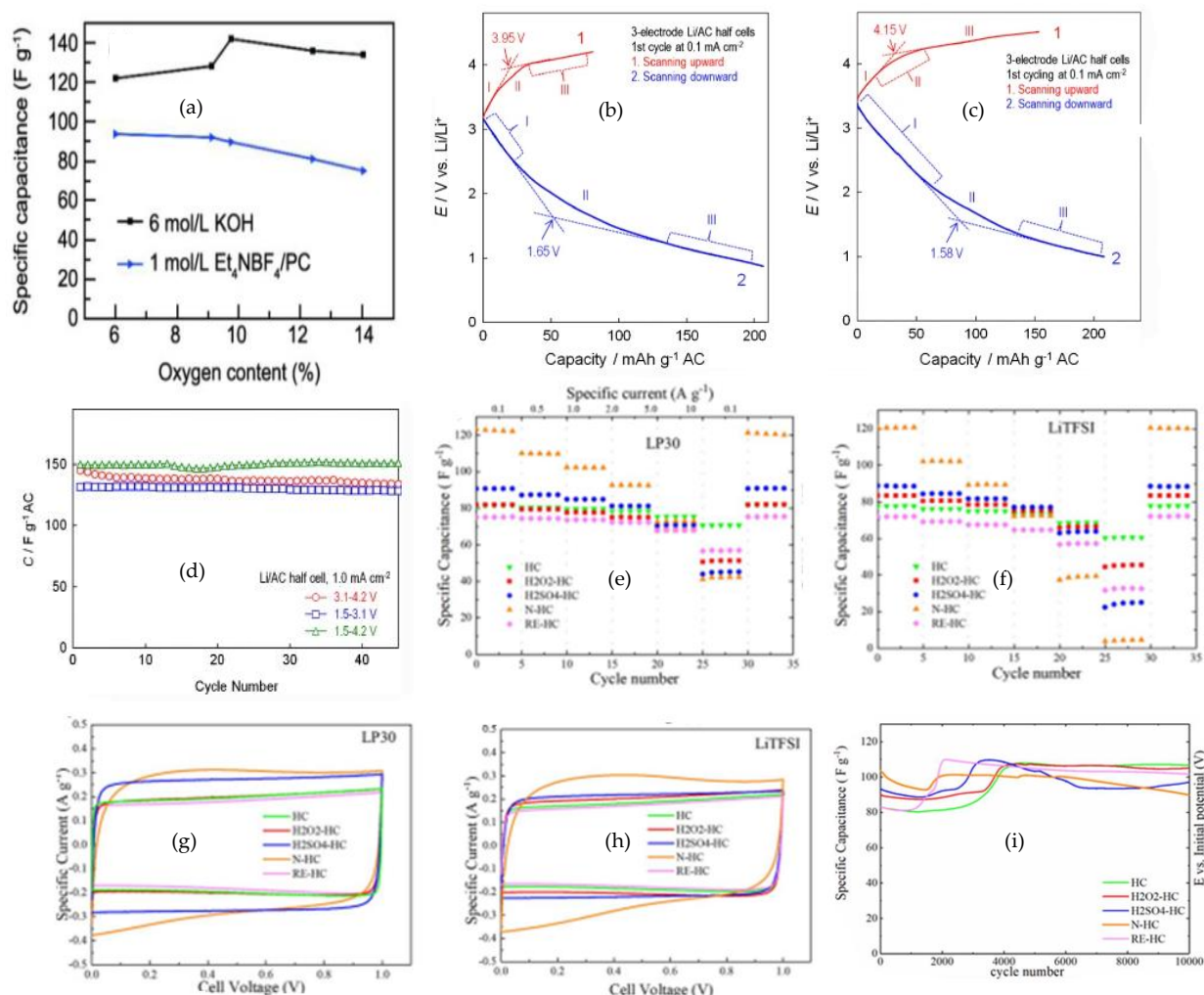
Figure 4. (**a**) Effect of oxygen content on cycle life in organic and aqueous electrolytes, reprinted from [56], copyright (2020), with permission from Elsevier. First cycle charge and discharge profile of fresh AC electrodes using three-electrode cell configuration with a lithium reference electrode in (**b**) 1M LiPF$_6$ in EC/DMC (3:7) electrolyte and (**c**) 1M TBABF$_4$ in EC/DMC (3:7) electrolyte. (**d**) Comparison of cycle life at different potential windows, reprinted from [57], copyright (2017), with permission from Springer. Effect of various surface functionalities on the performance of the AC in (**e**) LP30 and (**f**) LiTFSI electrolytes. Cyclic voltammetry obtained using (**g**) LP30 and (**h**) LiTFSi electrolyte. (**i**) Effect of surface functionalities on the cycle life, reprinted from [58] (CC-BY).

To confirm the existence of the reversible pseudocapacitive phenomena, three potential windows were examined that encompassed PF$_6$ adsorption and desorption (3.1–4.2 V) above the open circuit potential (OCP), Li adsorption and desorption below the OCP (1.5–3.1 V), and combined PF$_6$ and lithium adsorption/desorption (1.5–4.2 V), as presented in Figure 4d. From Figure 4d, expectedly, the widest potential window (1.5–4.2 V) exhibited the largest capacitance of 150 F g^{-1}. On the other hand, the potential window (3.1–4.2 V) had a slightly increased initial capacitance than 1.5–3.1 V but later stabilized to similar values. Since the AC specific capacitance by double layer adsorption and desorption

is independent of the potential window, the increased capacitance using 1.5–4.2 V can undoubtedly be attributed to reversible pseudocapacitance through equations 1 and 2. Therefore, oxygen functionalities have been demonstrated to be beneficial by facilitating capacitance increase through pseudocapacitance [57].

Ding et al. [58] further validated the existence of pseudocapacitive reactions with oxygen functionalities that could influence the capacitance of AC cycled in nonaqueous electrolytes of lithium salts. In this work, a commercial AC was functionalized by deliberate treatment with nitric acid, sulfuric acid, hydrogen peroxide, and di-functionalized via heat treatment under hydrogen/argon gas. Figure 4e,f shows the results from the electrochemical testing of these samples in 1M $LiPF_6$ in EC:DMC(1:1) (LP30) and 1M LiTFSI in EC:DMC(1:1) (LiTFSI) electrolytes. The beneficial effects of surface oxygen functionalities were again demonstrated by an increase in the AC-specific capacitance through pseudocapacitance. All the functionalized AC had a lower surface area than the di-functionalized AC due to the oxidation treatment. However, despite the higher surface area of the di-functionalized AC, the functionalized AC had much higher specific capacitance even with the lower surface area. Furthermore, the nitric acid-treated AC had the highest capacitance and C=O groups among the functionalized samples. The effect of surface functionalities was also noted in the investigated electrolyte stability windows, as shown in Figure 4g,h. The di-functionalized AC had the narrowest electrolyte stability window due to the higher number of reactive sites caused by the hydrogen reduction treatment. Among the functionalized samples, the nitric acid-treated AC had the narrowest electrolyte stability window, which can be related to the C=O groups at the surface. Therefore, functionalization can increase the specific capacitance through reversible pseudocapacitance but may also impact the electrolyte stability window. Meanwhile, the absence of stabilized functional groups at the surface following reductive treatment would create highly reactive sites that can accelerate electrolyte decomposition and reduce the electrolyte stability window. This work further confirmed that the pseudocapacitive behavior was related to Li^+ ions and that the respective anions do not partake in the pseudocapacitive reactions [58]. Additionally, intermediate surface oxidation with the optimum oxygen functionalities can ensure increased capacitance through pseudocapacitance without negatively impacting the cycle life. Nevertheless, the specific content or nature of oxygenated surface functionalities that can facilitate pseudocapacitance without affecting long-term cyclability through irreversible faradaic reactions remains a question to be answered. The results from the cycling stability test conducted on these samples are presented in Figure 4i. During the cycling stability tests, the H_2O_2-treated AC had the highest capacitance retention rate which was superior to the pristine AC or difunctionalized AC. Meanwhile, the nitric acid-treated AC with more C=O functionalities had the lowest capacity retention rate during the long-term cycling.

2.2.4. Fluorine

Fluorine functionalization has been reported to facilitate improved affinity for organic electrolyte ions on the AC surface [59]. Doping with fluorine amplifies the electroactive sites and impacts some electronegativity onto the carbon surface. Zhou et al. [59] synthesized fluorine-doped AC that achieved a high specific capacitance of 168 F g^{-1} using an organic electrolyte 1M tetraethylammonium tetrafluoroborate in propylene carbonate (1M TEA BF_4 in PC) and symmetric cell configuration. The improved performance with high fluorine content was caused by the synergy between increased surface area and favorable surface chemistry. DFT calculations showed that the affinity for the TEA^+ ions was increased with fluorine doping compared to the pristine material. However, the existence of pseudocapacitive contributions of fluorine is yet to be confirmed.

2.2.5. Phosphorous

The electron-donating ability and large covalent radius of phosphorous make it an attractive heteroatom for doping carbon matrices. Phosphorous doping was reported to facilitate improved performance through enhanced pseudocapacitive reactions and improved

electronic conductivity caused by the electron-donating ability of phosphorous [60,61]. In addition, the much larger covalent radius of phosphorus (107 ± 3 pm) compared to carbon (73 ± 1 pm) creates defects on the carbon surface after doping [62]. These defects may serve as active sites where charges are concentrated, facilitating charge transfer reactions [61]. Furthermore, phosphorous doping expands the interlayer spacing of the carbon lattice due to the larger atomic radius than the carbon matrix, thereby favoring more adsorption of sodium or lithium ions [63,64]. Gao et al. [60] synthesized AC from starch, using phytic acid as an activation agent and phosphorous dopant. The AC displayed a high specific capacity of 81.7 mAh g^{-1} at 0.05 A g^{-1} and good rate capability in the potential window 2–4 V in Li half cells using 1M LiPF$_6$ in EC:DMC:EMC (1:1:1) electrolyte. The high capacity achieved was attributed to the combined effect of pseudocapacitance and electrochemical double-layer capacitance from the synergy between the appropriate pore size distribution and high phosphorous content.

2.2.6. Sulfur

Sulfur functionalization on the AC surface induces electron delocalization of carbon backbones, thereby creating more electroactive sites that increase wettability and improve conductivity. The electron delocalization occurs due to the overlap between an electron pair on the p-orbital in sulfur and the Π orbital of the sp^2 hybridized sites in the AC. Sulfur-containing materials, like thioglycolic acid and thiourea, can be used as dopants to impact sulfur functionalities in carbon matrixes. Thangavel et al. [65] obtained a specific capacitance of 252 F g^{-1} at 0.5 A g^{-1} in a sodium ion capacitor after nitrogen and sulfur codoping of the cathode with thiourea. The improved performance was attributed to the enhanced synergetic effect of the dual heteroatom elements. The sulfur heteroatoms enhanced the space utilization and promoted the electrosorption of the electrolyte ions while nitrogen enabled increased electron transport and rapid ion transport kinetics inside the pores [65–67].

Different heteroatoms have been reviewed in the previous section, highlighting the improved AC performance through enhanced space utilization, decreased adsorption potentials, or pseudocapacitance during charge storage. Heteroatoms such as oxygen, phosphorus, nitrogen, and boron have reportedly exhibited increased capacitance through pseudocapacitance, although to varying degrees. Moreover, the positive pseudocapacitive effect is mainly observed while using aqueous electrolytes. However, pseudocapacitance has also been reported in organic electrolytes, particularly when matched with appropriate pore size dimensions. A capacitance increase is often accompanied by decreased cycling stability for heteroatoms like oxygen. On the contrary, nitrogen, boron, and phosphorus exhibit pseudocapacitance without the accompanying loss in cycling stability. The pseudocapacitive effects of fluorine and sulfur remain unconfirmed, but they are beneficial for enhancing space utilization, improving surface chemistry, and promoting the electrosorption of electrolyte ions.

In summary, heteroatom doping in the carbon matrix can improve the performance of the AC through various means. However, further studies are needed to compare the efficacy of heteroatom doping in organic electrolyte systems, in particular, using Li-ion or other alkali metal ion salt that can exhibit peculiar pseudocapacitive behaviors with surface functionalities.

2.3. Surface Hydrophobization

The interactions between the electrolyte solvent and active material surface can influence the performance of the electrochemical energy storage devices. The wettability can affect the surface area utilization and accessibility to the pores. Poor wettability can result in high internal resistance and lower capacitance despite the capacitive material possessing sufficient surface area and pores [68–71]. Hence, increasing the wettability is an efficient technique to improve the performance of the AC. Wei et al. [71] demonstrated a unique approach to increasing the wettability of active materials in organic electrolytes

through surface modification with a surfactant (sodium oleate). The surfactant enabled the attachment of non-polar organic functional groups to the AC surface, thereby increasing the surface hydrophobicity and affinity to the organic solvent. The modified material consequentially displayed improved capacitance, reduced internal resistance, and higher energy and powder densities than the unmodified material. Similarly, improved performance through surface modifications using Vinyltrimethoxysilane surfactant has also been reported [70,72]. Surface modifiers containing the silane functional group with only a methyl and alkoxy group bonded to the silicon atom can effectively facilitate increased hydrophobicity at the surface. Nevertheless, the surface modification process can reduce the AC's surface area and limit accessibility to the pores if the grafted surface modifiers possess too large a molecular size.

2.4. Precursor Optimization

Precursor materials can affect the final properties of the produced AC. Parameters such as the carbon content, organic and inorganic matter content, heteroatoms, precursor carbon structure, and the interactions between the precursor carbon matrix and activation agent would determine the qualities of the synthesized activated carbon [22]. AC produced from naturally occurring precursors, such as biomass materials, often retain the inherent structure of the original biomass material. The activation process typically occurs via crosslinking, dehydration, exfoliation, or gasification of the precursor matrix depending on the type of activation agent [73]. These processes are broadly summarized by the reduction in the oxygen content of the precursor through the removal of volatiles and moisture as well as some of the precursor's carbon content as the pores are being created. The precursor's carbon, oxygen, and volatile matter content can therefore affect the efficacy of the activation process [22]. The activation agent is often more attracted to the oxygen radicals of the precursor, thereby increasing the activation intensity and reducing the activation duration needed for achieving particular burn-off rates. Precursor materials with high volatile content, such as biomass-based materials, often possess higher surface areas than synthetic materials (e.g., organic polymers) [22,74]. Although the removal of volatiles during the carbonization/pyrolysis process is strongly related to the activation temperature, the macrostructure and nature of crosslinks between the precursor crystallites can affect the diffusion of the activation agent, which in turn dictates the porosity formation [75]. Precursors containing crystallite structures with several aromatic layers are reportedly more difficult to activate due to stronger covalent bonds among the carbon atoms in the layers [76]. In contrast, precursors containing carbon atoms with unsaturated bonds (mainly at the edge) are considerably more reactive and easily activated [76].

Comparing biomass-based precursors and others such as petroleum coke, residues, and synthetic organic polymers, the former possesses relatively higher ash content and inorganic impurities from fertilizers and nutrients absorbed from the soil. The latter is somewhat purer with low inorganic contents and often results in AC with higher yields due to the increased carbon content. However, high ash content and mineral impurities are detrimental to the performance of the AC. Their presence in the AC can lead to high self-discharge and poor electrochemical cycling stability, attributed to parasitic reactions between the metals and electrolytes [77]. Moreover, the high ash content in the precursor can reduce the effect of the activation agent, thereby hindering pore formation and necessitating high concentrations of the activation agent to achieve the desired activation degree [78].

The precursor can also influence the surface chemical functionalities and heteroatoms present in the AC. Several biomass precursors possess heteroatoms, such as nitrogen, sulfur, and the typical carbon, hydrogen, and oxygen, as elemental constituents. Li et al. [79] synthesized high-performance N-doped AC (8 wt.% N) with a hierarchical porous structure from eggshells (possessing 12–15 wt.% N) by simple carbonization without any doping agent. Naturally N-doped AC has also been synthesized from silk fibroins [80,81], fish scales [82], and prawn shells [83]. Biomass protein precursors, such as broad beans and

chicken bones, contain sulfur and can produce sulfur-doped AC [66,84]. Fruit seeds and pulps are excellent natural phosphorous dopants [85].

Some precursor materials can also undergo self-activation without the need for activation agents. The absence of activation agents can enable controlled porosity generation in the AC with well-distributed pores. Klezyk et al. [13] synthesized AC from tobacco leaves and stem wastes without any activation agent. The synthesized AC had a narrow pore size distribution and excellent electrochemical performance in both aqueous and organic electrolytes. The success of the self-activation could be linked to the presence of well-distributed alkalis in the precursor on the atomic scale. Moreover, the evolved gases during the carbonization treatment can simultaneously participate in the activation process during the carbonization step. Therefore, self-activating precursors present a facile approach toward achieving narrow pore distribution due to the atomically dispersed nature of the alkali metals and the absence of external activation agents that may contribute to uncontrollable gasification rates. Similar self-activating abilities have been demonstrated by seaweed and proposed to occur in biomass precursors that contain naturally embedded elements such as Na, K, Ca, and Mg [86]. Synthetic materials such as polyvinylidene chloride have also demonstrated excellent self-activating properties, achieving high-performance AC without an additional activation step [87].

Atomically dispersed elements in precursors have also aided the activation process by serving as templates during porosity formation. Xue et al. [14] reported that the templating behavior exhibited by silica present in rice husk precursors during the synthesis of AC. The silica nanoparticles were selectively leached using NaOH and KOH treatment before activation. A detailed study was conducted on the effectiveness of silica embedded in the rice husk and on the surface. Nanoparticle silica embedded in the rice rusk was revealed to favor porosity formation through a templating and synergetic effect with alkali activators that ensured more active sites during activation. In contrast, the silica present at the surface reduced the efficiency of the activation agent and the produced AC had decreased porosity and a decreased templating effect. Niu et al. [88] reported the self-activating effect of hydroxyapatite found in animal bones which enabled the synthesis of high-performance cathodes (109 mAh g^{-1} at 0.1 A g^{-1} in the potential window 2.0–4.5 V) after a simple pyrolysis step.

In summary, the precursor's nature can affect AC's quality. Other notable works synthesizing high-quality AC from different precursors are summarized in the following. Quian et al. [89] synthesized high-performance AC from petroleum asphalt using potassium bicarbonate as an activation agent. The AC had a specific capacity of 92 mAh g^{-1} at 0.1 A g^{-1} in the operating potential window 2.0–4.5 V using the electrolyte 1 M LiPF$_6$ in EC:DMC:EMC(1:1:1) vol%. Yang et al. [90] synthesized AC from corn cobs using sulfuric acid as an activation agent. The obtained AC possessed a specific capacitance of 251 F g^{-1} at 0.3 A g^{-1} in the operating potential window 2.0–4.5 V while using the electrolyte 1 M LiPF$_6$ in EC:DMC(1:1). Sennu et al. [91] synthesized AC from Prosopis juliflora using the typical KOH activation at 900 °C. The produced AC had in situ heteroatoms from the precursor (N, S, and Ca) which enabled a specific capacity of 98 mAh g^{-1} at 0.1 A g^{-1} in the operating potential window 2.0–4.0 V.

3. Electrode Optimization

After synthesizing the active material, the electrode is the next critical step influencing performance. During electrode fabrication, the AC powder is mixed with selected binders, ensuring good adhesion between the particles and the current collector. Moreover, the electrode can be fabricated with a dissolving solvent to aid the dispersion of the particles, binder, and additive composites which are often introduced to optimize the performance. This section discusses the influence of parameters such as binders and hybrid composites consisting of carbon materials or high-capacity bi-functional cathodes on the performance of the AC.

3.1. Bi-Functional Hybrid Composites

Despite the advances in the activation process discussed previously, the capacity of AC remains limited compared to intercalation-type battery cathodes like lithium iron phosphate (LFP) (160 mAh g^{-1}). Recently, researchers have implemented composite mixtures of AC with conventional battery-type materials as bi-functional hybrid cathodes to increase the capacity and energy density of the LiC cathode. Benefits such as increased cathode composite conductivity, improved rate performance, enhanced power, and energy density were obtained when these hybrid composite electrodes were integrated into the LiC architecture. Chen et al. [92] used a hybrid cathode mixture consisting of AC and LiNi$_{0.6}$Co$_{0.2}$Mn$_{0.2}$O$_2$ (NCM) and HC as the anode to achieve simultaneous higher power and energy density than the conventional NCM/HC battery at high C-rates. The improved energy and power density of the hybrid cathode were ascribed to the properties of the AC, such as mesoporosity, surface area, and enhanced electrode conductivity. The mesopores served as electrolyte reservoirs facilitating fast lithium diffusion while the high surface area contributed to the increased capacity through double-layer charging. However, optimizing the AC content in the electrode was essential to achieving such improved capacity. Shellikeri et al. [93] investigated the performance of an AC/LFP (80/20) wt.% bi-functional cathode paired with a pre-lithiated HC anode in the fabrication of LiC. SEM images obtained from the hybrid cathode are presented in Figure 5a. The AC occupied the spaces between the LFP particles which promoted faster kinetics during charge and discharge at high c-rates. Three-electrode cell measurements probed the individual capacity profiles of the electrodes, as presented in Figure 5b. The cathode exhibited a dual charge storage mechanism, with the capacity contribution in zone a (2.2–3.45 V) and c (3.45–3.8 V) due to the AC while zone c with the plateau at 3.45 V is from the LFP. Cycling stability tests conducted on the hybrid cathode are presented in Figure 5c.
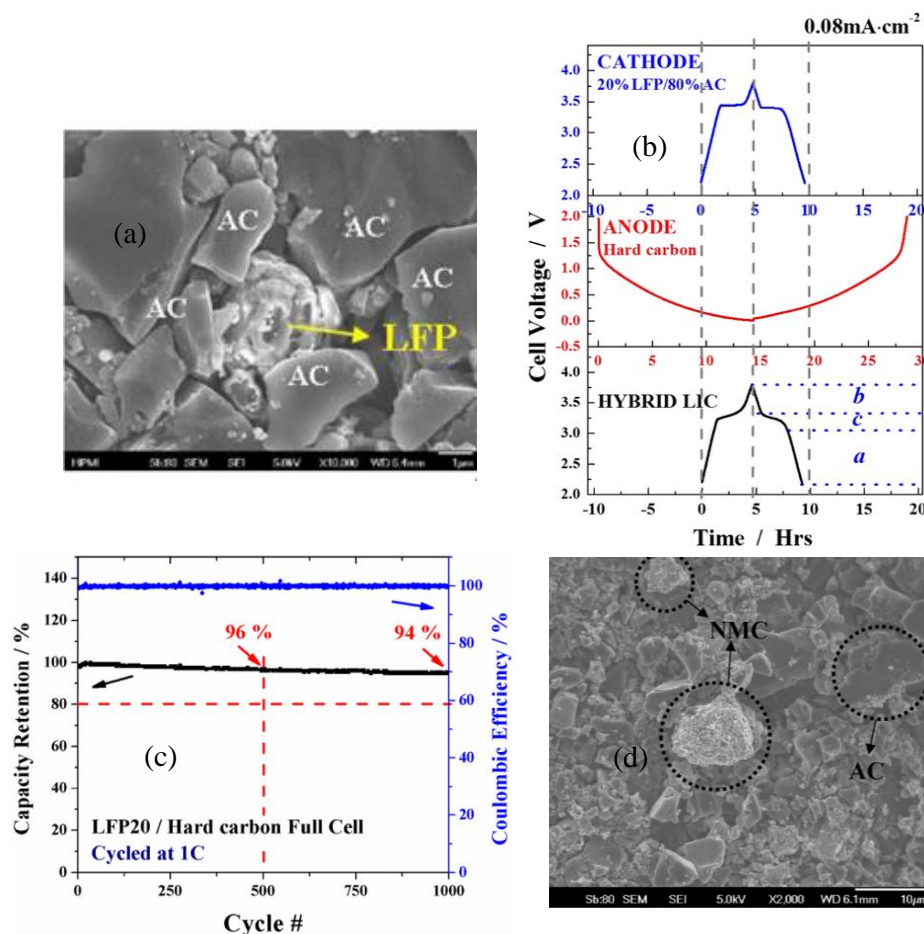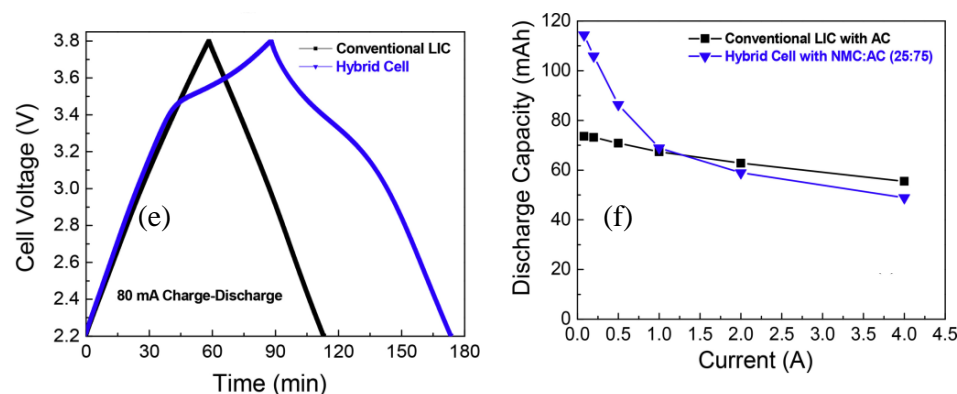

Figure 5. *Cont.*

Figure 5. (**a**) SEM images obtained from a hybrid LFP/AC electrode composite. (**b**) Capacity contribution for the individual electrodes in the hybrid cell. (**c**) Capacity retention of the hybrid LFP/AC LiC, retrieved from [93], copyright (2018), with permission from Elsevier. (**d**) SEM images obtained from the hybrid AC/NMC cell. Comparison of the (**e**) charge and discharge curves and (**f**) discharge capacity at different currents of the hybrid AC/NMC cell and conventional LiC cell, reprinted from [94], copyright (2018), with permission from Elsevier.

A capacity retention of 94% was obtained for the hybrid cathode after 1000 cycles at 1C while the pure LFP cathode realized 76% capacity retention after a similar duration. In the high C-rate cycling using 43C, a capacity retention of 76% after 20,000 cycles was obtained using the hybrid cathode; in contrast with 47% obtained by pure LFP after a similar duration. Therefore, the hybrid LFP and AC composite synergistically enhanced the energy and power density of the LiC compared to using singular AC or LFP as cathode materials. Furthermore, the beneficial effect of the hybrid cathode was more noticeable at high C-rates where the $FePO_4$ (FP) phase plagued by low conductivity cannot be discharged entirely due to increased concentration gradient from Li salt deficiency. The AC in the composite delayed the overpotential of the LFP, improved the conductivity of the FP phase, and enhanced Li-ion transport at high current densities. Granados-Moreno et al. [95] adopted a similar bifunctional blend of AC/LFP using a 60 wt.% AC and 40 wt.% LFP composite. This composite blend achieved a specific capacity of 102 mAh g^{-1} at 0.25 A g^{-1} and 80 mAh g^{-1} at 30 A g^{-1}. A similar work using AC/LFP composites by Bockenfeld et al. [96] further highlighted the positive synergy between the AC and LFP. Diluting the LFP with the AC yielded higher specific capacity than pure LFP at high C-rates. The authors attributed to the improvement to the favorable ratio of Li-ions in the electrolyte within the pores and in the active material when the LFP was mixed with the AC. Moreover, the AC/LFP composites had improved conductivity and favorable morphology because the LFP particles, which were smaller and less porous, could occupy the spaces between the AC particles, enabling adequate contact between the two active materials. Sun et al. [97] investigated the effect of different ratios of $LiNi_{0.5}Co_{0.2}Mn_{0.3}O_2$ powders (NMC) blended with the AC as bifunctional cathodes for LiC. A 25 wt.% NMC content was determined as the optimum blend which yielded a higher specific capacity than the pure AC (60.5 vs. 38.6 mAh g^{-1}) in the potential window 2.5–4.1 V. The hybrid AC/NMC blend enabled a 36% increase in the volumetric energy density without sacrificing the power density or cycle life compared to the pure AC cathode. Hagen et al. [94] used a similar AC/NCM (75/25 wt.%) ratio in laminate pouch cells and compared the performance to a conventional LiC using the AC as a cathode. SEM images obtained from the hybrid AC/NMC cathode are presented in Figure 5d. The NMC particles are dispersed around the AC which enables a good composite blend that would promote superior volumetric performance. The charge and discharge profiles of the conventional LiC and hybrid LiC with the AC/NCM cathode are shown in Figure 5e while the discharge capacities at various currents are compared in Figure 5f. The hybrid LiC electrode had a capacity of 74 mAh g^{-1} which was 57% higher than the capacity of the conventional AC cathode. This resulted in a 50.5% increase in specific energy. However, the power performance was marginally impacted due to the limitations of the

battery type electrode. Yu et al. [98] adopted lithium nickel cobalt aluminum oxides (NCA) as the battery-type cathode for bifunctional cathode composite blends with the AC.

The bi-functional hybrid electrode composite fabrication method can likewise affect the performance. A layer-by-layer spray printing approach was applied in developing smart multi-layer architecture electrodes incorporating dual composite materials in both the anode and cathode with an excellent energy density of 110 Wh kg^{-1} and power density of 15 kW kg^{-1} [99]. The LiC anode consisted of a spray-painted thin layer of discrete high-capacity Si (5 wt.%) at the lithium titanate (LTO) electrode surface. The same technique was applied in the cathode, which consisted of the AC and a thin spray-painted layer of LFP, but in a sandwich configuration of multi-stacked layers of spray-painted LFP and AC. The achieved high power density was enabled by optimizing the applied Si layer thickness and LFP layer thickness in the AC electrode composite sandwich. Hence, active materials with faster kinetics can be sandwiched between others with slower kinetics to improve the energy and power density.

3.2. Hybrid Composite with Other Carbon Materials

To achieve sufficient surface area and porosity in the synthesized AC, the precursors are often subjected to harsh gasification in the activation process, distorting the carbon structure and producing disjointed pores. Pores of varying dimensions are often created without sufficient interconnectivity when the activation methods do not include templating for tailored micropore formation. The presence of randomly created pores with insufficient interconnectivity can result in poor conductivity of the AC and inaccessibility of electrolyte ions into the pores. Moreover, while aiming to further increase the surface area, the existing micropores may collapse into mesopores and macropores from over-activation, consequentially reducing the electrode density and volumetric performance. Therefore, hybrid compositing with other carbon materials has been explored to increase the conductivity of the AC electrode and electrode density and improve the volumetric performance. Commonly incorporated carbon materials include carbon black, carbon nanotubes (CNTs), carbon nanofibers (CNFs), and carbon nanoonions (CNOs).

CNTs are widely renowned for their peculiar aspect ratios and extended graphitic layers, enabling increased conductivity and exceptional mechanical strength [100,101]. These properties facilitate improved percolation compared to typical carbon blacks when incorporated as nanotexturing composites in electrodes. Moreover, the entanglement of CNTs in the electrode composite can create open mesoporous networks, promoting the easy access of electrolyte ions to the active material. Incorporating CNTs as nanotexturing composites with the AC has yielded more superior performance than the typical carbon black often utilized [102].

CNOs in the family of carbon nanomaterials possess a very large external surface area consisting of circular stacks of carbon spheres resembling multi-walled fullerenes [103,104]. Compared to conventional carbon blacks, they possess smaller particle sizes (10 vs. 30–40 nm) and lower electrical conductivity (~3 vs. 8–50 S m^{-1}) [105–107]. This smaller particle size can facilitate improved performance through easier homogenous distribution in the AC electrode, filling the interparticle voids and enhancing the conductivity. However, the ease of large aggregate formation (up to 100 nm) may present a challenge while using such materials [105].

Overall, compositing the AC with other carbon materials can result in a carbon electrode sheet with decreased interparticle void spaces. The nanoparticles filling the void spaces must be efficiently distributed with optimized percentages (2–5%) to avoid incessant agglomeration and electrode inhomogeneity. Efficiently distributed nanoparticles enable increased conductivity for the electrodes. However, a decrease in surface area with increased nanoparticles is expected. Therefore, the benefits of compositing become obvious at high current densities where the effect of electrode resistance is magnified and the capacity retention is enhanced. In contrast, no noticeable impact is expected at low current densities, and a slight decrease in capacity may occur with a reduced AC percentage in the composite.

3.3. Binders

Binders perform an essential role in the electrode fabrication and proper functioning of electrodes for LiC. They serve as the holding agent, securing the active materials together while simultaneously providing a conductive pathway for ionic species. The appropriate selection of binders can influence the AC electrode's mechanical strength, electrode stability, self-discharge, and ionic and electrical conductivity. Typical binders used in AC electrode fabrication include polyvinylidene difluoride (PVDF), carboxymethyl cellulose/styrene-butadiene rubber (CMC)/SBR, polytetrafluoroethylene (PTFE), polyacrylic acid (PAA), and sodium alginate. The impact of these binders on the performance of AC has been investigated by several researchers. Chen et al. [108] compared the performance of electrodes fabricated using three binders AC/PTFE, AC/PVDF, and AC/CMC/SBR, using the organic electrolyte 1M TEABF$_4$ in PC and symmetric supercapacitor configuration. It was revealed that CMC/SBR possessed the best wettability and lowest contact angle in the electrolyte. The fluoropolymers, PTFE and PVDF, had lower wettabilities due to high surface energy. Furthermore, nitrogen physisorption analysis of the AC powder and AC electrode with different binders revealed decreased porosity and surface area due to the binders. The physisorption isotherms are presented in Figure 6a. The lowest surface area was obtained from the PVDF binder while the CMC/SBR had only a minor decrease compared to the pristine AC. These microstructural differences influenced the rate performance and interfacial impedance, especially at high charge and discharge rates. The compared electrochemical impedance spectroscopy (EIS) spectra and rate performance of the different binders are presented in Figure 6b,c. The AC with CMC/SBR exhibited superior performance compared to the rest, having the lowest interfacial impedance and best capacity retention. Moreover, the CMC/SBR had the lowest self-discharge among the binders, attributed to the ease of mass transport within the macropores/mesopores favoring homogenously adsorbed ions during charging. The homogeneously charged surface reduced the self-discharge caused by ion redistribution in the electrode.
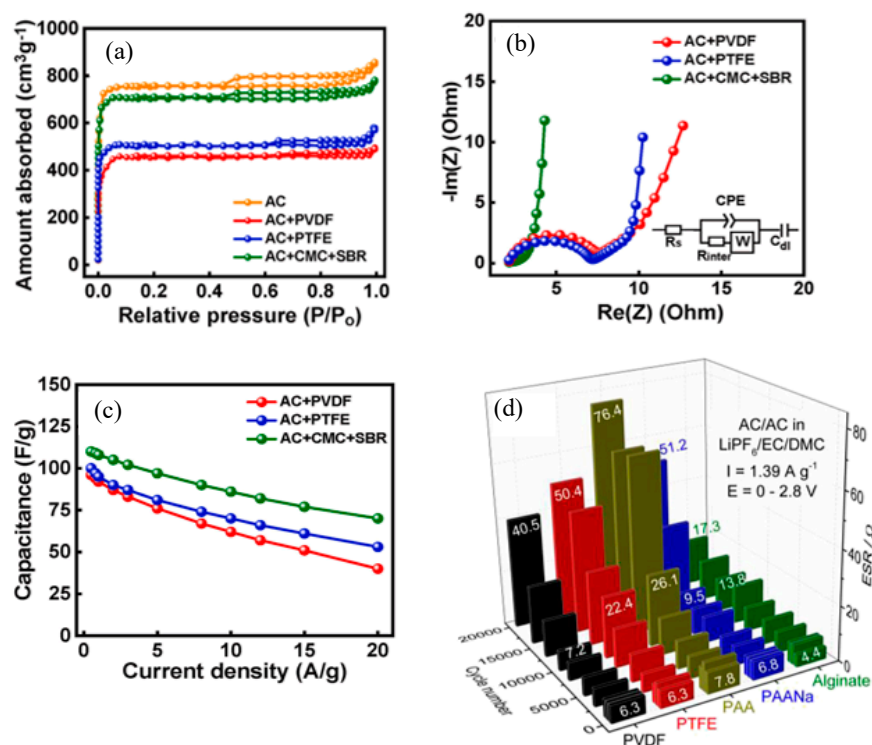
Figure 6. (**a**) N$_2$ physisorption isotherms of various samples. (**b**) EIS Nyquist plots, (**c**) Specific capacitances at various current densities for cells cycled in 1 M TEABF$_4$/PC electrolyte, reprinted from [108], copyright (2023), with permission from Elsevier. (**d**) Evolution of the ESR for the corresponding cells cycling between 0 V and 2.8 V at a specific current I = 1.39 A g^{-1} in 1 M LiPF$_6$/EC/DMC. Reprinted from [109], copyright (2017), with permission from Elsevier.

Tran et al. [109] investigated the influence of the binders PTFE, PVDF, PAA, alginate, and PAANa (sodium polyacrylate) on the performance and cycle life of AC electrodes used in LiC. The exceptional performance of the green alginate was highlighted. Stress relaxation tests conducted during the investigation of the rheological properties revealed that the alginate based slurry remained stable whereas the PVDF/NMP slurry viscosity decreased with time. Although the authors did not disclose the reason for the unstable viscosity of the PVDF/NMP binder, we infer that certain factors related to the ability to withstand mass or phase segregation could have affected the stability of the slurry over time [110]. Since similar active materials (activated carbon) were used and the only difference was the binder, the binder interaction with the particle and ability to flocculate into larger and heavier viscoelastic masses may have caused some sedimentation, which led to a decrease in the slurry viscosity [110]. Changes in slurry viscosity are significant problems encountered while upscaling electrode slurry formulation. Hence, alginate-based binders are advantageous over typical PVDF/NMP slurries. Additionally, the water-based nature eliminates the need for adapting special process operating conditions, such as those required for PVDF while using NMP solvent. Regarding cycling performance, the alginate binder AC electrode was more stable than the PVDF. Figure 6d shows the compared equivalent series resistance (ESR) as a function of cycle number. The lowest ESR was obtained using the alginate binder. Therefore, appropriate binder selection is essential for improved electrochemical performance.

The dissolving solvents for the selected binder also play a critical role in the active material–binder interactions and the surface chemistry of the resulting electrode. Generally, electrodes could be manufactured using dissolving solvents such as water and NMP or without dissolving solvents in dry electrodes. The environmental concerns regarding using NMP have encouraged the adoption of water-based electrode formulations. In large-scale manufacturing, a solvent recovery system must be installed for NMP recovery, which increases process costs and requires high temperature for its removal. Water-based slurries, on the other hand, do not face such restrictions. However, the drying process consumes about 40% of the energy requirements in the process line [111,112]. Electrodes manufactured using the water-based process are also plagued by the changes in surface chemistry related to the oxidization of the AC upon contact with moisture. Therefore, hydrophilic groups are formed on the high surface area alongside confined moisture in the pores that are difficult to remove without extensive drying procedures. When using organic electrolytes such as the widely utilized $LiPF_6$ salt, the tendency for hydrolysis is increased, which consequently causes the electrolyte degradation and cell capacity to fade if optimized formation procedures are not conducted.

Moreover, lots of gas generation is expected during the formation step as the electrolyte hydrolysis reactions are accelerated. On the contrary, the surface of the AC electrode with NMP is more hydrophobic; issues regarding confined moisture in the pores are minimal. However, NMP has a high boiling point of 202 °C [111] which means that some of the NMP may remain in the AC pores if extensive drying procedures are not incorporated. Remnant solvents in the pores can cause increased pressure buildup in cells since they diffuse and affect the device's operation. Given these limitations, dry electrodes involving no dispersing solvents are promising alternatives that eliminate drying and solvent recovery costs. Moreover, the dry electrode method can enable the realization of high areal capacity electrodes which are often difficult to attain using the slurry methods due to viscosity and flowability issues. Furthermore, the hydrophobic surface chemistry inherited from the polymer binder is preserved and the surface chemistry remains unmodified without any solvent, thus improving the wettability in organic electrolytes.

4. Electrolyte Optimization

Electrolytes are indispensable components in energy storage devices. Electrolytes enable the operation of energy storage devices by performing diverse roles, such as facilitating ion transfer between cathodes and anodes, stabilizing electrode surfaces, and

promoting electrochemical stability and device performance [113,114]. The electrolytes used in LiC consist of a salt of the corresponding metal ion dissolved in a solvent or solvent combination, with or without additives. These electrolyte constituents are optimized to influence the conductivity, viscosity, density, operating potential window, and operating temperature. Factors such as the metal ion transport between the cathode and anode, cathode and anode interfacial stability, device cycle life, energy, and power density are hence affected by the nature of the electrolyte.

4.1. Electrolyte Solvents

Electrolyte solvents dissolve the electrolyte salt to enable dissociation into mobile conducting ions enclosed by a solvation shell. The nature of the dissolving solvent affects the electrolyte classification, which could be aqueous or nonaqueous, an ionic liquid, or solid-state electrolytes without any dissolving liquid solvent. The latter two are not widely applied in LiC due to the rigorous preparation conditions, high costs for the ionic liquids, and poor conductivity of the solid-state polymer electrolytes at low temperatures. Meanwhile, the aqueous electrolytes are limited by the decomposition potential of water at 1.2 V which restricts the operating potential window. Even though very high conductivity and high capacitances can be obtained using such electrolytes, the resulting energy density remains constrained due to the low operating potential window. Nonaqueous electrolytes, on the other hand, yield lower capacitance from the bulkier solvated ions dimensions but higher energy densities due to the wider operating potential window. Hence, the solvent choice can significantly affect the performance of the device. Additionally, other benefits such as the formation of ternary graphite intercalation compounds in graphite anodes used in sodium-ion capacitors have been achieved through optimized glyme-solvated electrolytes [115]. In the absence of such ternary graphite compounds, the binary counterparts would intercalate between the graphene layers, thereby resulting in exfoliation, instability, and, consequently, negligible energy storage capacity in the graphite anode.

Among the nonaqueous electrolytes, carbonate solvent-based electrolytes are widely adopted in LiC due to their ability to operate at higher maximum potentials (>4 V) compared to conventional supercapacitor solvents such as acetonitrile (~2.7 V). The latter solvent is unstable at potentials below 0.5 V vs. Li but possesses higher conductivity and superior low-temperature performance than the former. However, the ion–solvent interaction can influence the AC's rate performance, especially at high C-rates. Carbonate solvents, such as EC, possess significantly larger dipole moments and bind more strongly to the Li cation than acetonitrile. Therefore, the strong coordination of EC to Li impacts the difficulty in the desolvation process by the surrounding electric field. This can interfere with the specific capacitance at high C-rates since the optimum pore size for the maximum power density is affected. The pore size of the AC must accommodate the dimensions of the solvated ion and allow for free diffusion of charges without affecting the double layer. Decaux et al. [116] investigated the influence of these two solvents on the performance of AC electrodes. It was revealed that larger pore dimensions in the range of 1.1 to 1.3 nm are needed to achieve increased capacity when using carbonate solvents. On the contrary, the easily de-solvated acetonitrile solvent required smaller pore dimensions (0.7–0.8 nm) to achieve the maximum specific capacitance.

Although high conductivity in electrolytes is required for high-power and high-rate cycling, the electrochemical stability at the electrode surface is equally important. Surface functionalities introduced deliberately or inadvertently during the AC production can affect the electrochemical stability.

The choice of solvent can also promote ion adsorption on the AC surface by optimizing the initial electrode potential. ho Lee et al. [117] reported on the effect of tetrahydrofuran (THF) on the AC capacity. The authors showed that adding THF to the electrolyte (1M LiBF$_4$ in EC:DEC(3:7)vol%) resulted in a shift in the electrolyte electrostatic potential, increased ionic mobility, and easier adsorption of the BF$_4$ anion on the AC electrode surface. ho Lee et al. [118] also reported enhanced rate performance of an AC/Li LiC

achieved via the addition of 1,3,5-trifluoro benzene (TFB) in the electrolyte (1M LiBF$_4$ in EC:DEC(3:7)vol%).

The electrochemical stability of the chosen solvent can influence the stability of the electrolytes. Aqueous solvents are limited by the decomposition of water at 1.2 V, which causes severe gas evolutions when operating at these limits. On the contrary, organic solvents typically operate at wider potential windows and have varying oxidative and reductive stabilities depending on the solvent or solvent combinations. The oxidative and reductive stability of the solvents can be estimated from the density functional theory calculations of their respective highest occupied molecular orbital (HUMO), lowest unoccupied molecular orbital (LUMO), and experimental examinations using typical inert working electrodes like glassy carbon or platinum [119]. However, the actual stability on the carbonaceous AC electrode differs from such experiments due to the carbon electrode/electrolyte interactions which limit the operating potential window and stability following oxidation of the surface at high potentials. Since similar LiB electrolytes are used in LiC, various researchers have investigated the oxidative and reductive stabilities of different electrolyte solvents and solvent combinations [113,120,121]. Carbonate solvents such as cyclic and linear carbonates like ethylene carbonate (EC), propylene carbonate (PC), ethyl methyl carbonate (EMC), dimethyl carbonate (DMC), and di ethyl carbonate (DEC) are usually the preferred alternatives due to the relatively higher operating potential windows and the ability to form passivation films on the negative electrode. However, these solvents typically decompose on the high surface area of the AC and such reactions are exacerbated by surface oxygen functionalities and confined moisture in the pores [122]. The decomposition products affect the morphology of the AC and reduce the available surface area and pores for the charge storage [123]. Other solvent types, such as the sulfonated derivatives, sulfone, and dimethyl sulfide have been reported to exhibit higher oxidative stabilities than the carbonate solvents [114]. However, these classes of solvents typically have higher viscosities and necessitate mixtures with low-viscosity solvents to maximize the operating temperature window. Recently, very promising fluorinated solvents have demonstrated excellent oxidative and reductive stabilities due to the strong electronegativity of fluorine that influences the LUMO and HUMO [124,125]. Therefore, they exhibit higher oxidation stabilities than typical carbonate solvents and can form fluorine-rich and stable interfaces on the negative electrode that synergistically enhance the cycle life [125].

4.2. Electrolyte Salts

Several metal-ion salts have been investigated with different degrees of dissociating ability, capacity, and conductivity in carbonate solvent blends. Using Li-salts as an example, LiPF$_6$, LiTFSI, LiFSI, LiCF$_3$SO$_3$, LiClO$_4$, and LiBF$_4$ are some notable examples that have been explored. Amatucci et al. [3] emphasized the importance of optimizing the electrolyte salt capacity and molecular weight in hybrid ion capacitors. The electrolyte salts LiPF$_6$, LiCF$_3$SO$_3$, LiClO$_4$, and LiBF$_4$ were revealed to possess capacities of 176, 272, 252, and 286 mAh g^{-1}, respectively. Moreover, using electrolyte salts with a high molecular weight could decrease the energy density of the LiC. Furthermore, the anions, in particular, influence the obtainable capacity of the AC electrode. The variation in electrochemical performance of the AC electrode using different lithium salts in the electrolyte can also be correlated with the dimension of the de-solvated anions (Figure 7a). Kato et al. [126] examined the influence of Li-salts with various anions on the performance of AC/LTO LiC. The rate performance of the different electrolytes is presented in Figure 7b. As expected, the Li-salt with the largest de-solvated anion dimension had the lowest capacity. However, LiBF$_4$, with the smallest de-solvated anion dimension, did not possess the largest specific capacity. The authors emphasized that the discrepancy was due to the lower conductivity of the LiBF$_4$ electrolyte which was attributed to the lower dissociation constant observed for the BF$_4^-$ anion compared to the others. Therefore, the importance of selecting appropriate electrolyte salts with de-solvated anion dimensions suited to the AC pores and an optimum balance in conductivity is further demonstrated.
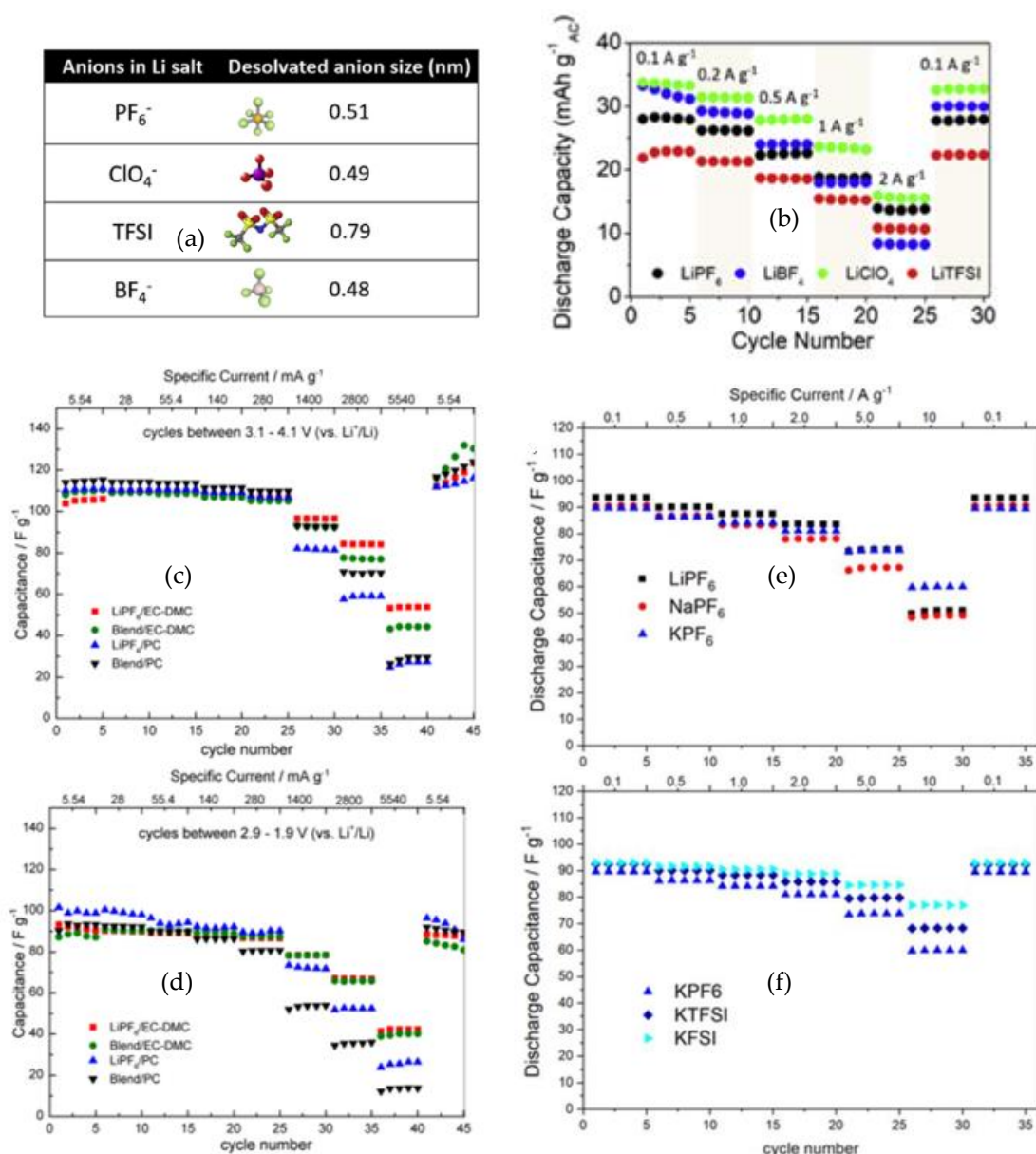
Figure 7. (**a**) De-solvated anion sizes and structures of some lithium salts. (**b**) Rate performance comparison of the different electrolytes, reprinted from [126], copyright (2019), with permission from Elsevier. Gravimetric specific capacitance of AC electrodes in different electrolytes. (**c**) Electrodes cycled between 3.1 V and 4.1 V vs. Li^+/Li. (**d**) Electrodes cycled between 2.9 V and 1.9 V vs. Li^+/Li, reprinted from [120], copyright (2016), with permission from Elsevier. (**e**,**f**) Rate capabilities of symmetric AC//AC capacitor cells in different electrolytes, reprinted from [127] (CC-BY).

Researchers have implemented dual anion salts to maximize the available capacity through the adsorption of ions of various dimensions. In a notable work, Zhang et al. [120] investigated the electrochemical performance of electrolyte salt blends consisting of NEt_4BF_4 and $LiPF_6$ dissolved in singular PC or EC:DMC (1:1) compared to singular $LiPF_6$ or $LiBF_4$. $LiBF_4$ exhibited inferior performance due to the highest equivalent series resistance and lowest conductivity, necessitating the substitution with NEt_4BF_4. The rate performance of the electrolytes in different potential windows covering anion and cation utilization is displayed in Figure 7c,d. It was interesting to observe that the capacitance of the electrolyte blend (NEt_4BF_4 and $LiPF_6$) was higher than the singular $LiPF_6$ at low current densities. However, at high current densities, the opposite occurred. This may have been caused

by increased competition between the dual anions at the AC pore entrance, creating a sieving effect and consequentially slightly lower capacity than singular $LiPF_6$. Moreover, the solvation shell contributed by the dissolving solvent also affected the performance and electrochemical stability.

The various alkali metal salts (derivatives of Li, Na, and K) possess different stabilities and distinct electrochemical performances when used as electrolyte salts with the same AC and organic solvents. Stpie et al. [127] investigated the electrochemical behavior of AC when exposed to different electrolytes based on Li, Na, and K salts containing the anions (PF_6, FSI, and TFSI) in similar solvents. The rate performance of the compared cations is presented in Figure 7e while the anions comparison with K is presented in Figure 7f. It was revealed that electrolytes based on the K-salts exhibited superior performance with higher ionic conductivity and faster ion diffusion within the AC micropores. Moreover, the larger K cation and "softer" character compared to Li facilitated less interaction with the electrolyte decomposition active sites on the AC and displayed a lower desolvation energy. Meanwhile, the strong acidic character of Li and binding energy to the solvent caused the increased presence of solvents in the AC pores where most decomposition reactions occur. The ease of desolvation of the K cation reduces the amount of solvent in the pores; thus, solvent decomposition occurs mostly at the external surface.

4.3. Electrolyte Dielectric and Viscosity

Properties of the electrolytes, such as dielectric, viscosity, and conductivity, have also been demonstrated to affect the self-discharge, rate performance, and electrochemical stability of the AC cathode. Eleri et al. [128] revealed that the electrolyte dielectric can influence the electrochemical stability of the AC cathode. Increasing the electrolyte dielectric improved the anion oxidative stability at the double layer region by modifying the solvation shell and increasing the resistance to oxidation during polarization at high energies. However, the increased dielectric leads to increased solvation energies and high viscosity [129,130]. Moreover, increased solvation energy results in high charge transfer resistance at the anodes due to high activation energy for desolvation, impacting the rate performance at high current densities [129,131]. Nevertheless, the cycling stability and coulombic efficiency of the cells with high dielectric solutions are superior to low dielectric electrolytes. The impacted rate performance at high current densities using high dielectric electrolytes could be mitigated by adequately tuning the AC pore size to enable the optimum adsorption of solvated and de-solvated ions and sufficient mass balancing on the anode.

Although a high dielectric is needed to achieve adequate salt dissociation, low dielectric electrolytes have also been optimized to reduce the solvation energies and improve the dissociation rate and conductivity through dual-cation systems. Chikaoka et al. [132] achieved a very high power density and improved stability in an AC/LTO LiC by using a dual-cation low-dielectric electrolyte. The electrolyte consisted of a mixture of spiro-(1,1)-bipyrrolidinium tetrafluoroborate ($SBPBF_4$) and $LiBF_4$ dissolved in DMC. The dual cation system eliminated the phase separation behavior and ion pairs caused by the single cation dissolution in the low dielectric DMC. Therefore, the low dielectric dual cation electrolyte had improved power density due to the low viscosity and improved conductivity.

5. Cell Design Optimization

The hybrid nature of LiC necessitates meticulous design to counter the imbalance of the capacitive AC cathode and the energy-dense intercalation type anode. The imbalance is due to the sluggish kinetics of the anode, in contrast with the rapid charge storage by ion physisorption occurring on the AC cathode. Consequentially, inadequate cell design can present issues such as underutilized potential windows, electrode potential encroachment into unsafe electrolyte decomposition regions, poor cycle life, and limited energy and power density. The following section discusses recent cell design strategies to improve the performance of the AC.

5.1. Capacity Balancing

Capacity balancing is a fundamental step required for the optimum performance of LiC due to the mismatch between the capacity of the AC cathode and the significantly larger anode material. High-power symmetric SC utilizes a 1:1 direct cathode: anode balance, which guarantees high power along with the rapid physisorption kinetics of the AC material [133,134]. However, if such ratios are utilized in LiC, for example, using the AC cathode (specific capacity <60 mAh g^{-1}) and the HC anode (specific capacity >360 mAh g^{-1}), the AC capacity would be completely charged before the anode. Moreover, the energy density is reduced since the anode potential is underutilized and may swing toward unstable regions where electrolyte degradation is accelerated [135].

It has been demonstrated in several works that a cathode:anode mass ratio >4 is required to achieve very high energy density in LiC [8,136]. Using such high mass ratios enables complete utilization of the anode capacity since an equal charge balance can be achieved between the AC cathode and the battery-type anode, improving the device capacity and energy density. Dsoke et al. [136] explicitly highlight the effect of the electrode mass ratio on the performance of AC/LTO LiC. The authors compared the performance of LiC of different electrode mass ratios, starting from the classically balanced mass ratio of 4.17:1 derived from the experimentally obtained AC electrode capacity of 38.36 mAh g^{-1} and LTO electrode capacity of 160 mAh g^{-1}. Therefore, the AC electrode thickness was increased to 4.17 times the initial mass while the LTO mass was kept constant. The schematics of the cells are presented in Figure 8a. Figure 8b,c shows the capacity retention and Ragone plots of AC/LTO LiCs assembled with different mass ratios and a symmetric AC/AC supercapacitor cell for comparison.
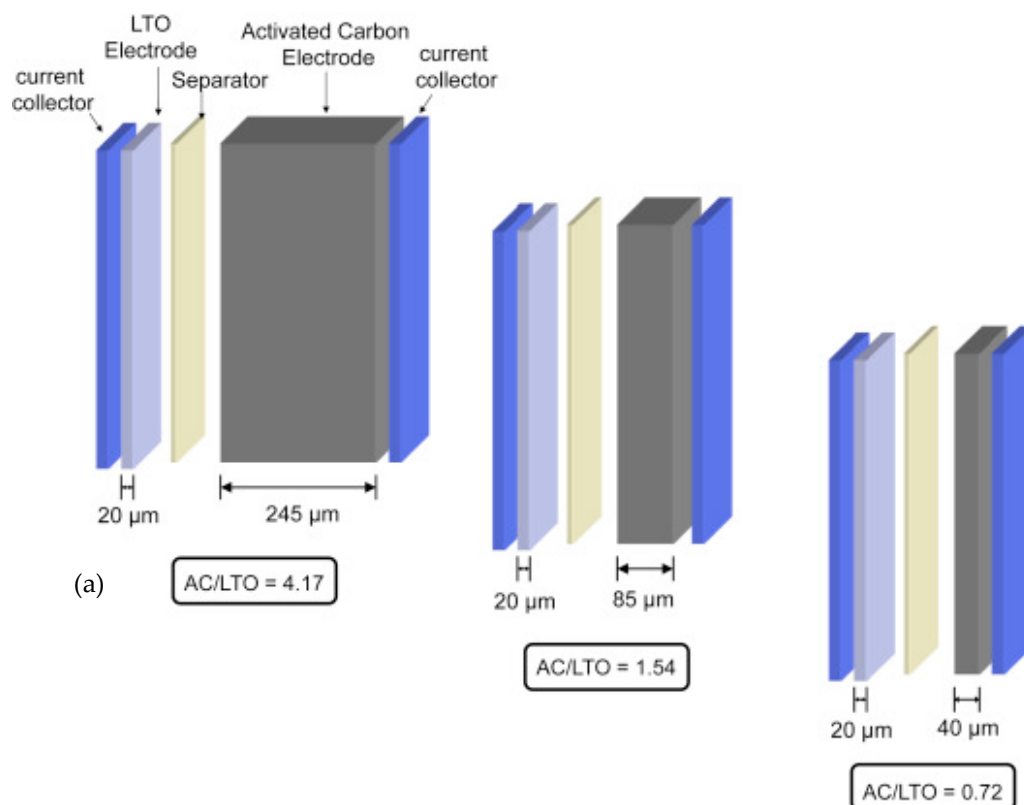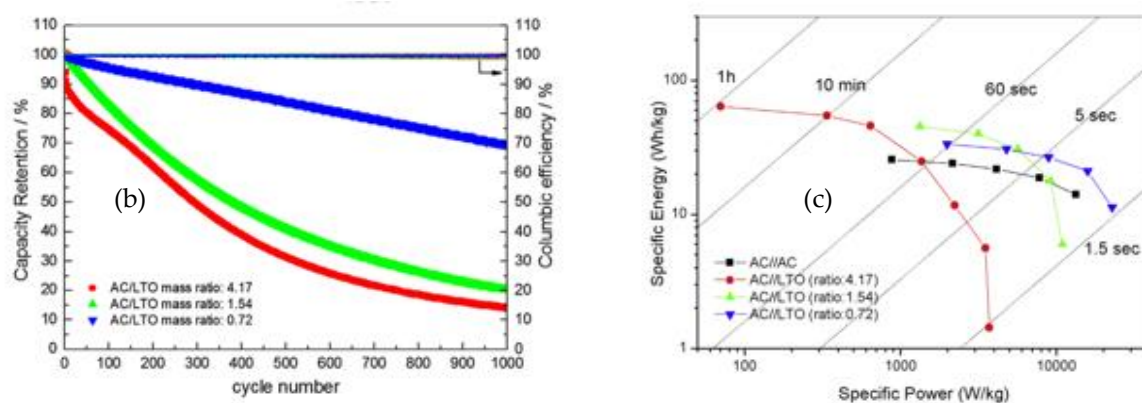

Figure 8. *Cont.*

Figure 8. (**a**) Schematic of AC/LTO systems balanced with an AC/LTO mass ratio of 4.17, 1.54, and 0.72. (**b**) Capacity retention of the cells after 1000 cycles at 10C. (**c**) Ragone plots of AC/LTO LiC assembled with different mass ratios. Reprinted from [136], copyright (2015), with permission from Elsevier.

As the AC/LTO mass ratio increased, the energy density increased while the capacity retention decreased. It is worth noting that the cycle life of LiC with a very high energy density deteriorates faster when such high mass ratios are utilized to achieve a similar capacity as the LiB counterparts. Moreover, the overall energy density of the cell is also significantly reduced after accounting for the weight of active materials which are mostly subjected to weight and thickness constraints.

5.2. Operating Potential Window Regulation

The operating potential window influences the capacity, electrode stability, and achievable energy and power density. Operating beyond stable limits can lead to encroachment into regions where electrolyte decomposition may be accelerated at the upper or lower vertex potentials. Furthermore, the anodes deliver distinct electrochemical performance depending on the potential window [137]. Therefore, investigating the operating potential window of the AC and selecting appropriate regions on the anode where kinetics mismatch can be alleviated is necessary. Jin et al. [137] demonstrated a practical matching approach for selecting an appropriate potential region during the design and fabrication of an AC/HC LiC. The authors first determined the appropriate operating potential region of the HC anode using a combination of galvanostatic charge and discharge analysis (GCD), galvanostatic intermittent titration technique (GITT), and electrochemical impedance spectroscopy (EIS) conducted at different potentials to observe the corresponding distinct electrochemical processes. After evaluating the appropriate region, the HC anode was pre-lithiated to enable operation within the chosen region and matched with the appropriate mass balance to the AC cathode and working potential. Incorporating these processes improved the energy density, power density, and life cycle.

Several operating potential limits for the AC cathodes have been utilized in various research, ranging from 1.5 to 4.6 V. Increasing the operating potential window enhances the capacity until a trade-off at these limits where further increased potential does not correspond to increased capacity. Moreover, electrolyte decomposition is accelerated at these limits and accompanied by severe passivation of the AC electrode surface by electrolyte decomposition products. The cycling stability is also affected by faradaic processes whose magnitude may vary based on the chosen potential window. Zhang et al. [138] investigated the capacity retention of AC/HC LiC cycled in different potential windows, namely 2.0–4.0 V and 2.2–3.8 V. The capacity retention was 73.8% after 80,000 cycles in the former and 94.5% of the initial value after 200,000 cycles in the latter. The selection of safe operating potential windows depends on the evaluation method, an objective widely explored by various researchers [139,140]. Sun et al. [141] reported a method for determining the operating potential of the AC cathode without the influence of the anode. The authors

established that the stable potential limits can be obtained using the energy efficiency and the criterion that the second derivative of the S value plotted against the vertex potential, $d^2S/dU^2 < 0.05$. The operating potential limit of the AC in their study was determined to be 2.2–3.9 V. However, these operating potential limits depend on the nature of the electrolyte (organic solvent and salt) and operating temperature. Other parameters such as the presence of oxygenated functional groups on the AC surface, binder type (CMC/SBR vs. PTFE), and aluminum current collector (etched vs. carbon coated) can significantly influence the operating potential window of the AC. Compared to the alternatives, superior stabilities are obtained using coated collectors and PTFE binders [141].

Although the AC-specific capacity can be increased by utilizing more expansive potential windows, the oxidative stability is adversely affected at too high potentials. At the same time, the reversibility is impacted at low potentials. The impacted oxidative stability is associated with the oxygen functionalities discussed earlier that are responsible for increased capacitance through pseudocapacitance but impact cycling stabilities. Zhang et al. [142] deduced the following mechanism via which the oxidative stability is affected by oxygen functionalities when operating at high potentials. When the AC electrode is cycled at high potentials, the oxygen functionalities likely present in the form of ketones, ethers, lactones, carboxyls, etc., and are oxidized at such high potentials to form CO_2 and H_2O. The H_2O hydrolyses the $LiPF_6$ salt and further reacts with the lithiated negative electrode to form Li_2O and H_2. Therefore, large amounts of gases are generated together with the detrimental HF that causes interfacial instabilities and further depletes the active Li^+ ions. At lower potentials, increased Li^+ trapping occurs on the micropores due to the poor Li reversibility caused by the reactions with oxygen functionalities on the AC. These limitations have consequently led to manufacturers adopting the operating potential window 2.2–3.8 V as the recommended limit in dual carbon LiC, whereby appreciable capacity is maintained without compromising the cycling stability of the cell. By retaining this limit, oxidation reactions on the AC surface and lithium trapping at too low potentials by the reduced surface functionalities are minimized.

5.3. Pre-Lithiation

In contrast with the battery counterparts, LiC possesses no metal-ion source other than the metal ions in the electrolyte. However, during the initial cycling process, the formation of SEI on the anode and cathode can rapidly deplete the already-limited metal ions in the cell. Therefore, a pre-lithiation step is necessary to increase the availability of metal ions for charge storage. The pre-lithiation also mitigates against metal-ion depletion after the SEI formation on the anodes, resulting in enhanced cycling performance without a change in the materials or device structure [143]. Moreover, sufficient metal ions allow the AC cathode to operate at a widened potential window through the adsorption of metal cations below the OCP and anions above the OCP. As a result, the capacity of the AC cathode is increased and the resulting energy density for the LiC is enhanced. Pre-lithiation also facilitates safe anode utilization within the typical electrolyte decomposition limits <0.8 V by forming an initial SEI with the excess metal ions.

The process of pre-lithiation is commonly achieved using various electrochemical or direct contact pre-metalation techniques [143,144]. Central to each method is a sacrificial metal cation source where cations migrate from and to the anode either under the influence of an externally applied electrochemical driving force or by internal or external short-circuiting after direct contact. The pre-lithiation step could also be conducted as a pre-assembly procedure where the anode is pre-cycled with the metal cation source and the potential is regulated to the desired pre-lithiation degree before disassembly and reassembly of the final full cell with the intended cathode. In this case, two cell assembly steps are needed, which may complicate assembly line procedure in full-scale manufacturing and present additional contamination risks. Moreover, the direct contact method is usually conducted with the corresponding pure metal as the metal cation source. Consequently, the direct contact method is often uncontrollable, with a nonuniform degree of pre-lithiation

since the strategy relies on direct contact between the metal and anode with no external controlling force. Moreover, the risk of thermal runways, fire hazards, and others associated with handling the highly reactive pure metal is significant and may pose serious concerns during large-scale assembly.

In response to the above concerns, a new pre-lithiation technique was developed which involves incorporating inorganic or organic sacrificial compounds containing the metal cations as an alternative to using the highly reactive pure metal during pre-lithiation [144–146]. These sacrificial compounds are composited in the AC cathode during the electrode fabrication process. The selection of sacrificial cathode pre-lithiation additives is based on the ability to irreversibly de-lithiate in the working potential window of the cathode and exhibit high volumetric or gravimetric capacity while remaining electrochemically, chemically, and thermally stable under electrode processing conditions and after the de-lithiation. Examples of such additives include Li_2MoO_3 [147], Li_5FeO_4 [148], Li_2DHBN [149], Li_3N [150], Na_2S [151], NaCN [152], $NaNH_2$ [153], $Na_2C_4O_4$ [154], $Li_2C_4O_4$ [146], and $Li_2C_4O_6$ [155].

Park et al. [147,148] used Li_2MoO_3 and Li_5FeO_4 as sacrificial pre-lithiation additives mixed with the AC electrode during the fabrication of LiC. However, the oxidation of these materials occurred at high potentials (4.7 V) which are in regions where electrolyte oxidation is prominent; the AC surface can easily be passivated at the detriment of the surface charge storage capacity. Moreover, there is a remnant inactive mass in the cell which subsequently decreases the specific energy of the LiC. The sacrificial salts, therefore, show more promise because they produce no residues after de-metalation. The listed ternary salts only produce N_2 and CO_2 gases which can be removed during the formation step. This is particularly important when using capacitive materials since any residue after the de-lithiation can block the pores or contribute to inactive masses in the cell. Arnaiz et al. [146] demonstrated an effective pre-metalation strategy using $Li_2C_4O_4$ and the K and Na derivatives as sacrificial pre-metalation additives mixed with the AC cathode and paired with an HC anode. Cyclic voltammetry (CV) and galvanostatic charge and discharge analysis conducted on the composite $Li_2C_4O_4$, conductive additive, and binder (65:30:5 mass ratio) are presented in Figure 9a,b. The results revealed the irreversible capacity (375 mAh g^{-1}) provided by the composite during the first cycle, as further evidenced by the broad peaks which diminished severely in subsequent cycles. Hence, confirming that the $Li_2C_4O_4$ is able to irreversibly oxidize in the first cycle and is completely consumed after the 10th cycle. The AC/$Li_2C_4O_4$ composite CV curves are displayed in Figure 9c. Similar first-cycle broad peaks are observed, attributed to the irreversible oxidation of the $Li_2C_4O_4$. These broad peaks were absent in the 10th cycle, with the CV profile exhibiting the typical regular box-like characteristics of the AC.

Furthermore, it was revealed in this work that the pre-lithiation process did not affect the performance of the AC. On the contrary, the rate performance of the recovered AC after the de-lithiation of the $Li_2C_4O_4$ agent was superior to the AC without the pre-lithiation, as shown in Figure 9d. Post-mortem electrode examinations revealed void spaces in the AC after the pre-lithiation attributed to the oxidation of $Li_2C_4O_4$ in the electrode. The cycled pre-lithiated electrode further exhibited microstructural changes, evidenced by the creation of additional meso and macroporosity in the AC. These microstructural changes on the AC electrode were beneficial for improved electrolyte accessibility and superior rate performance.

Although the sacrificial salts show more promise, it is desirable in production lines to avoid extra gas formation after the pre-lithiation process. Recently, Pan et al. [152] effectively pre-sodiated the anode in a sodium ion capacitor by mixing the AC cathode with sodium cyanide (NaCN) as a pre-sodiation additive. The oxidation of the NaCN occurred at 2.9 V vs. Na/Na+ with a capacity of 547 mAh g^{-1} without any gas evolution.
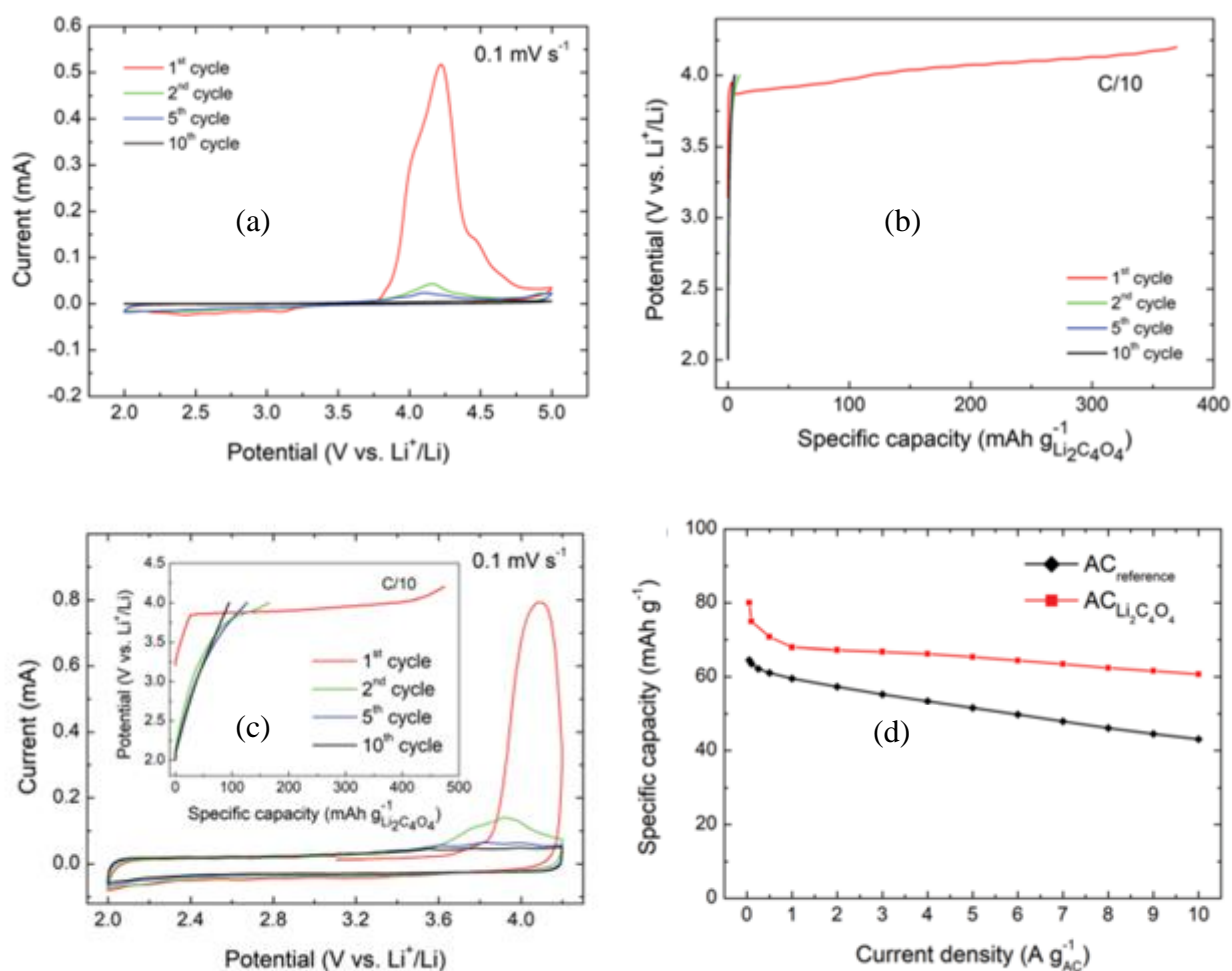
Figure 9. Electrochemical characterization of the as-prepared $Li_2C_4O_4$ salt mixed with conductive carbon and binder in a 65:30:5 mass ratio. (**a**) Cyclic voltammetry (CV) at 0.1 mV s^{-1} and (**b**) galvanostatic charges at C/10. Electrochemical characterization of the as-prepared $AC_{Li2C4O4}$ electrode: (**c**) CV at 0.1 mV s^{-1}, inset: galvanostatic charge at C/10, and (**d**) specific capacity values at different current densities for the $AC_{Li2C4O4}$ and the $AC_{reference}$ electrodes. Retrieved from [146], copyright (2020), with permission from Royal Society of Chemistry (RSC).

Some sacrificial pre-lithiation additives can serve as dual-functioning additives to pre-metalate the anode while increasing the capacitance of the AC through pseudocapacitance. Zhang et al. [156] demonstrated the use of Li-rich Li_2CuO_2 as a cathode prelithiation additive during the fabrication of AC/graphite LiC. The AC/Li_2CuO_2 cathode composite was revealed to behave as a pure capacitor when cycled between 2.8 and 4.2 V, yielding similar capacitance and capacity as the AC/Li half-cell. However, when the operating potential window was changed to 2.0–4.0 V, the remnant Li_2CuO_2 provided extra capacitance through pseudocapacitive behavior (increased from 150 F g^{-1} to 189 F g^{-1}) after irreversible delithiation in the first cycle (342 mAh g^{-1}).

6. Outlook and Perspectives

Different strategies enabling the increased performance of the AC cathode, when used in LiC, have been discussed. These strategies encompassed material, electrode, electrolyte, and cell design optimization techniques which enabled increased capacity, operating potential window, and stability of the AC cathode. Among the precursors, self-activating precursors present an opportunity to create high-performance AC with optimized pore size distribution by a simple controlled carbonization step. However, they

are often plagued by heterogeneously distributed concentrations of atomically dispersed alkali metals. We propose an approach adapted from the self-activating biomass precursors whereby synthetic precursors are developed with nanoscale/atomically dispersed alkali metals. Using such synthetic precursors and controlled percentages of the dispersed alkali metals will enable the production of high-quality AC with controlled pore size distribution and high purity.

Introducing some degree of graphitization in the AC presents another approach for enhancing the capacity. However, care should be taken to optimize the graphitization degree to improve the capacity without affecting the rate performance. The implementation of this technique will enable a hybrid charge storage mechanism consisting of shallow intercalation and the typical ion adsorption/desorption in the AC pores.

The beneficial effects of functionalization, particularly the oxygen functional groups, were demonstrated by many studies. Oxygen functionalization can be beneficial and likewise detrimental to the performance. However, a critical understanding of these redox processes occurring on the electrode surface following reactions with the electrolyte at different potentials is needed. This could be achieved via in situ studies by analyzing reaction products generated during electrochemical cycling and relating such products with the performance of the AC.

On the electrode level, compositing with bi-functional electrodes presents a rational strategy to improve the AC's capacity but with slight decrease in the rate performance. However, nanostructuring during active material synthesis can improve the rate performance of the composites. The high-capacity battery-type cathode could be nanosized and coated with a carbon precursor, which can later be activated. Hence, creating a bi-functional active material consisting of an inner core of high-capacity battery-type cathode and an outer shell of AC will enhance the charge storage kinetics.

Lastly, a fundamental understanding of the AC and battery-type electrode interaction is lacking, especially at the electrode–electrolyte interface. The influence of chemical cross-talks between the reaction by-products formed after reactions between the AC surface functionalities and the electrolyte needs to be investigated. These by-products can possibly migrate to the battery-type anode and negatively affect the SEI properties. Similarly, the SEI film forming additives introduced to influence the anode SEI may likewise affect the AC performance due to chemical cross-talks. Although it is widely accepted that the AC stores charge through ion adsorption in the double layer, the passivation film forming abilities of carbonate solvents may alter the performance. Hence, the broad question is whether the AC electrode–electrolyte interface can be influenced by film forming additives to delay electrolyte degradation or increase the operating potential window. If so, the consequences of such film-forming additives on the capacity/capacitance and the effect on the charge storage mechanism need to be understood.

In this review, we have outlined several strategies by which the performance of the AC cathode can be enhanced beyond the typical activation method optimization. These techniques mentioned, together with the future research directions, can facilitate improved performance of the AC cathode and subsequential energy and power density of the LiC.

absence of any commercial or financial relationships that could be construed as a potential conflict of interest.

References

1. Simon, P.; Gogotsi, Y. Materials for electrochemical capacitors. *Nat. Mater.* **2008**, *7*, 845. [CrossRef]
2. Simon, P.; Gogotsi, Y.; Dunn, B. Where do batteries end and supercapacitors begin? *Science* **2014**, *343*, 1210–1211. [CrossRef]
3. Amatucci, G.G.; Badway, F.; Du Pasquier, A.; Zheng, T. An asymmetric hybrid nonaqueous energy storage cell. *J. Electrochem. Soc.* **2001**, *148*, A930. [CrossRef]
4. Li, B.; Zheng, J.; Zhang, H.; Jin, L.; Yang, D.; Lv, H.; Shen, C.; Shellikeri, A.; Zheng, Y.; Gong, R. Electrode materials, electrolytes, and challenges in nonaqueous lithium-ion capacitors. *Adv. Mater.* **2018**, *30*, 1705670. [CrossRef]
5. Smith, P.H.; Tran, T.N.; Jiang, T.L.; Chung, J. Lithium-ion capacitors: Electrochemical performance and thermal behavior. *J. Power Sources* **2013**, *243*, 982–992. [CrossRef]
6. Ding, J.; Hu, W.; Paek, E.; Mitlin, D. Review of hybrid ion capacitors: From aqueous to lithium to sodium. *Chem. Rev.* **2018**, *118*, 6457–6498. [CrossRef] [PubMed]
7. Wang, H.; Zhu, C.; Chao, D.; Yan, Q.; Fan, H.J. Nonaqueous hybrid lithium-ion and sodium-ion capacitors. *Adv. Mater.* **2017**, *29*, 1702093. [CrossRef]
8. Shi, Z.; Zhang, J.; Wang, J.; Shi, J.; Wang, C. Effect of the capacity design of activated carbon cathode on the electrochemical performance of lithium-ion capacitors. *Electrochim. Acta* **2015**, *153*, 476–483. [CrossRef]
9. Sivakkumar, S.R.; Pandolfo, A. Evaluation of lithium-ion capacitors assembled with pre-lithiated graphite anode and activated carbon cathode. *Electrochim. Acta* **2012**, *65*, 280–287. [CrossRef]
10. Zhu, B.; Liu, B.; Qu, C.; Zhang, H.; Guo, W.; Liang, Z.; Chen, F.; Zou, R. Tailoring biomass-derived carbon for high-performance supercapacitors from controllably cultivated algae microspheres. *J. Mater. Chem. A* **2018**, *6*, 1523–1530. [CrossRef]
11. Magar, S.D.; Leibing, C.; Gómez-Urbano, J.L.; Cid, R.; Carriazo, D.; Balducci, A. Brewery waste derived activated carbon for high performance electrochemical capacitors and lithium-ion capacitors. *Electrochim. Acta* **2023**, *446*, 142104. [CrossRef]
12. Falco, C.; Sieben, J.M.; Brun, N.; Sevilla, M.; Van der Mauelen, T.; Morallón, E.; Cazorla-Amorós, D.; Titirici, M.M. Hydrothermal carbons from hemicellulose-derived aqueous hydrolysis products as electrode materials for supercapacitors. *ChemSusChem* **2013**, *6*, 374–382. [CrossRef] [PubMed]
13. Kleszyk, P.; Ratajczak, P.; Skowron, P.; Jagiello, J.; Abbas, Q.; Frąckowiak, E.; Béguin, F. Carbons with narrow pore size distribution prepared by simultaneous carbonization and self-activation of tobacco stems and their application to supercapacitors. *Carbon* **2015**, *81*, 148–157. [CrossRef]
14. Xue, B.; Jin, L.; Chen, Z.; Zhu, Y.; Wang, Z.; Liu, X.; Wang, X. The template effect of silica in rice husk for efficient synthesis of the activated carbon based electrode material. *J. Alloys Compd.* **2019**, *789*, 777–784. [CrossRef]
15. Tong, Y.; Yang, J.; Li, J.; Cong, Z.; Wei, L.; Liu, M.; Zhai, S.; Wang, K.; An, Q. Lignin-derived electrode materials for supercapacitor applications: Progress and perspectives. *J. Mater. Chem. A* **2023**, *11*, 1061–1082. [CrossRef]
16. Dubey, P.; Shrivastav, V.; Maheshwari, P.H.; Sundriyal, S. Recent advances in biomass derived activated carbon electrodes for hybrid electrochemical capacitor applications: Challenges and opportunities. *Carbon* **2020**, *170*, 1–29. [CrossRef]
17. Zou, K.; Cai, P.; Cao, X.; Zou, G.; Hou, H.; Ji, X. Carbon materials for high-performance lithium-ion capacitor. *Curr. Opin. Electrochem.* **2020**, *21*, 31–39. [CrossRef]
18. Han, P.; Xu, G.; Han, X.; Zhao, J.; Zhou, X.; Cui, G. Lithium ion capacitors in organic electrolyte system: Scientific problems, material development, and key technologies. *Adv. Energy Mater.* **2018**, *8*, 1801243. [CrossRef]
19. Dos Reis, G.S.; Larsson, S.H.; de Oliveira, H.P.; Thyrel, M.; Claudio Lima, E. Sustainable biomass activated carbons as electrodes for battery and supercapacitors—A mini-review. *Nanomaterials* **2020**, *10*, 1398. [CrossRef]
20. Carrott, P.; Carrott, M.R. Lignin–from natural adsorbent to activated carbon: A review. *Bioresour. Technol.* **2007**, *98*, 2301–2312.
21. González-García, P. Activated carbon from lignocellulosics precursors: A review of the synthesis methods, characterization techniques and applications. *Renew. Sustain. Energy Rev.* **2018**, *82*, 1393–1414. [CrossRef]
22. Yahya, M.A.; Al-Qodah, Z.; Ngah, C.Z. Agricultural bio-waste materials as potential sustainable precursors used for activated carbon production: A review. *Renew. Sustain. Energy Rev.* **2015**, *46*, 218–235. [CrossRef]
23. Danish, M.; Ahmad, T. A review on utilization of wood biomass as a sustainable precursor for activated carbon production and application. *Renew. Sustain. Energy Rev.* **2018**, *87*, 1–21. [CrossRef]
24. Abioye, A.M.; Ani, F.N. Recent development in the production of activated carbon electrodes from agricultural waste biomass for supercapacitors: A review. *Renew. Sustain. Energy Rev.* **2015**, *52*, 1282–1293. [CrossRef]
25. Rashidi, N.A.; Yusup, S. A review on recent technological advancement in the activated carbon production from oil palm wastes. *Chem. Eng. J.* **2017**, *314*, 277–290. [CrossRef]
26. Conway, B.E. *Electrochemical Supercapacitors: Scientific Fundamentals and Technological Applications*; Springer Science & Business Media: Berlin/Heidelberg, Germany, 2013.
27. Helmholtz, H.V. Ueber einige Gesetze der Vertheilung elektrischer Ströme in körperlichen Leitern, mit Anwendung auf die thierisch-elektrischen Versuche (Schluss.). *Ann. Phys.* **1853**, *165*, 353–377. [CrossRef]
28. Gao, Y.; Yue, Q.; Gao, B.; Li, A. Insight into activated carbon from different kinds of chemical activating agents: A review. *Sci Total Environ.* **2020**, *746*, 141094. [CrossRef]

29. Ukanwa, K.; Patchigolla, K.; Sakrabani, R.; Anthony, E.; Mandavgane, S. A Review of Chemicals to Produce Activated Carbon from Agricultural Waste Biomass. *Sustainability* **2019**, *11*, 6204. [CrossRef]

30. Barbieri, O.; Hahn, M.; Herzog, A.; Kötz, R. Capacitance limits of high surface area activated carbons for double layer capacitors. *Carbon* **2005**, *43*, 1303–1310. [CrossRef]

31. Khomenko, V.; Raymundo-Piñero, E.; Béguin, F. High-energy density graphite/AC capacitor in organic electrolyte. *J. Power Sources* **2008**, *177*, 643–651. [CrossRef]

32. Eleri, O.E.; Azuatalam, K.U.; Minde, M.W.; Trindade, A.M.; Muthuswamy, N.; Lou, F.; Yu, Z. Towards high-energy-density supercapacitors via less-defects activated carbon from sawdust. *Electrochim. Acta* **2020**, *362*, 137152. [CrossRef]

33. Salitra, G.; Soffer, A.; Eliad, L.; Cohen, Y.; Aurbach, D. Carbon electrodes for double-layer capacitors I. Relations between ion and pore dimensions. *J. Electrochem. Soc.* **2000**, *147*, 2486. [CrossRef]

34. Salanne, M.; Rotenberg, B.; Naoi, K.; Kaneko, K.; Taberna, P.-L.; Grey, C.P.; Dunn, B.; Simon, P. Efficient storage mechanisms for building better supercapacitors. *Nat. Energy* **2016**, *1*, 16070. [CrossRef]

35. Zheng, W.; Li, Z.; Han, G.; Zhao, Q.; Lu, G.; Hu, X.; Sun, J.; Wang, R.; Xu, C. Nitrogen-doped activated porous carbon for 4.5 V lithium-ion capacitor with high energy and power density. *J. Energy Storage* **2022**, *47*, 103675. [CrossRef]

36. Sun, J.; Li, G.; Wang, Z.; Guo, H.; Li, X.; Yan, G.; Wang, J. Balancing the anions adsorption and intercalation in carbon cathode enables high energy density dual-carbon lithium-ion capacitors. *Carbon* **2022**, *200*, 28–37. [CrossRef]

37. Cho, M.-Y.; Kim, M.-H.; Kim, H.-K.; Kim, K.-B.; Yoon, J.R.; Roh, K.C. Electrochemical performance of hybrid supercapacitor fabricated using multi-structured activated carbon. *Electrochem. Commun.* **2014**, *47*, 5–8. [CrossRef]

38. Jain, A.; Jayaraman, S.; Ulaganathan, M.; Balasubramanian, R.; Aravindan, V.; Srinivasan, M.P.; Madhavi, S. Highly mesoporous carbon from Teak wood sawdust as prospective electrode for the construction of high energy Li-ion capacitors. *Electrochim. Acta* **2017**, *228*, 131–138. [CrossRef]

39. Li, G.; Yang, Z.; Yin, Z.; Guo, H.; Wang, Z.; Yan, G.; Liu, Y.; Li, L.; Wang, J. Non-aqueous dual-carbon lithium-ion capacitors: A review. *J. Mater. Chem. A* **2019**, *7*, 15541–15563. [CrossRef]

40. Dubal, D.P.; Ayyad, O.; Ruiz, V.; Gomez-Romero, P. Hybrid energy storage: The merging of battery and supercapacitor chemistries. *Chem. Soc. Rev.* **2015**, *44*, 1777–1790. [CrossRef]

41. Li, S.; Chen, J.; Cui, M.; Cai, G.; Wang, J.; Cui, P.; Gong, X.; Lee, P.S. A High-Performance Lithium-Ion Capacitor Based on 2D Nanosheet Materials. *Small* **2017**, *13*, 1602893. [CrossRef]

42. Laszlo, K.; Tombacz, E.; Josepovits, K. Effect of activation on the surface chemistry of carbons from polymer precursors. *Carbon* **2001**, *39*, 1217–1228. [CrossRef]

43. Lota, G.; Grzyb, B.; Machnikowska, H.; Machnikowski, J.; Frackowiak, E. Effect of nitrogen in carbon electrode on the supercapacitor performance. *Chem. Phys. Lett.* **2005**, *404*, 53–58. [CrossRef]

44. Lyu, L.; Seong, K.-d.; Ko, D.; Choi, J.; Lee, C.; Hwang, T.; Cho, Y.; Jin, X.; Zhang, W.; Pang, H. Recent development of biomass-derived carbons and composites as electrode materials for supercapacitors. *Mater. Chem. Front.* **2019**, *3*, 2543–2570. [CrossRef]

45. Li, B.; Dai, F.; Xiao, Q.; Yang, L.; Shen, J.; Zhang, C.; Cai, M. Nitrogen-doped activated carbon for a high energy hybrid supercapacitor. *Energy Environ. Sci.* **2016**, *9*, 102–106. [CrossRef]

46. Yang, M.; Zhong, Y.; Ren, J.; Zhou, X.; Wei, J.; Zhou, Z. Fabrication of high-power Li-ion hybrid supercapacitors by enhancing the exterior surface charge storage. *Adv. Energy Mater.* **2015**, *5*, 1500550. [CrossRef]

47. Ci, L.; Song, L.; Jin, C.; Jariwala, D.; Wu, D.; Li, Y.; Srivastava, A.; Wang, Z.; Storr, K.; Balicas, L. Atomic layers of hybridized boron nitride and graphene domains. *Nat. Mater.* **2010**, *9*, 430–435. [CrossRef] [PubMed]

48. Zhao, X.; Zhang, Q.; Zhang, B.; Chen, C.-M.; Xu, J.; Wang, A.; Su, D.S.; Zhang, T. Decorated resol derived mesoporous carbon: Highly ordered microstructure, rich boron incorporation, and excellent electrochemical capacitance. *RSC Adv.* **2013**, *3*, 3578–3584. [CrossRef]

49. Lee, Y.-J.; Uchiyama, Y.; Radovic, L.R. Effects of boron doping in low-and high-surface-area carbon powders. *Carbon* **2004**, *42*, 2233–2244. [CrossRef]

50. Kalijadis, A.; Đorđević, J.; Trtić-Petrović, T.; Vukčević, M.; Popović, M.; Maksimović, V.; Rakočević, Z.; Laušević, Z. Preparation of boron-doped hydrothermal carbon from glucose for carbon paste electrode. *Carbon* **2015**, *95*, 42–50. [CrossRef]

51. Enterría, M.; Pereira, M.; Martins, J.; Figueiredo, J. Hydrothermal functionalization of ordered mesoporous carbons: The effect of boron on supercapacitor performance. *Carbon* **2015**, *95*, 72–83. [CrossRef]

52. Hishiyama, Y.; Irumano, H.; Kaburagi, Y.; Soneda, Y. Structure, Raman scattering, and transport properties of boron-doped graphite. *Phys. Rev. B* **2001**, *63*, 245406. [CrossRef]

53. Jiang, H.; Shi, D.; Sun, X.; Wang, S.; Li, Y.; Chang, B.; Zhang, B.; Shao, Y.; Wu, Y.; Hao, X. Boron carbonitride lithium-ion capacitors with an electrostatically expanded operating voltage window. *ACS Appl. Mater. Interfaces* **2020**, *12*, 47425–47434. [CrossRef] [PubMed]

54. Zhu, C.-L.; Wang, H.-L.; Fan, W.-J.; Zhai, S.-L.; Wang, X.-J.; Shi, J.; Huang, M.-H.; Liu, S.; Li, Z.; Chen, J.-W. Large-scale doping-engineering enables boron/nitrogen dual-doped porous carbon for high-performance zinc ion capacitors. *Rare Met.* **2022**, *41*, 2505–2516. [CrossRef]

55. Liu, C.; Koyyalamudi, B.B.; Li, L.; Emani, S.; Wang, C.; Shaw, L.L. Improved capacitive energy storage via surface functionalization of activated carbon as cathodes for lithium ion capacitors. *Carbon* **2016**, *109*, 163–172. [CrossRef]

56. Li, X.-R.; Jiang, Y.-H.; Wang, P.-Z.; Mo, Y.; Li, Z.-J.; Yu, R.-J.; Du, Y.-T.; Zhang, X.-R.; Chen, Y. Effect of the oxygen functional groups of activated carbon on its electrochemical performance for supercapacitors. *New Carbon Mater.* **2020**, *35*, 232–243. [CrossRef]

57. Zhang, S.S. Effect of surface oxygen functionalities on capacitance of activated carbon in non-aqueous electrolyte. *J. Solid State Electrochem.* **2017**, *21*, 2029–2036. [CrossRef]

58. Ding, Z.; Trouillet, V.; Dsoke, S. Are functional groups beneficial or harmful on the electrochemical performance of activated carbon electrodes? *J. Electrochem. Soc.* **2019**, *166*, A1004. [CrossRef]

59. Zhou, H.; Peng, Y.; Wu, H.B.; Sun, F.; Yu, H.; Liu, F.; Xu, Q.; Lu, Y. Fluorine-rich nanoporous carbon with enhanced surface affinity in organic electrolyte for high-performance supercapacitors. *Nano Energy* **2016**, *21*, 80–89. [CrossRef]

60. Gao, Y.; Yang, Z.; Wang, Y.; Wang, X. Boosting capacitive storage of cathode for lithium-ion capacitors: Combining pore structure with P-doping. *Electrochim. Acta* **2021**, *368*, 137646. [CrossRef]

61. Hu, X.; Fan, M.; Zhu, Y.; Zhu, Q.; Song, Q.; Dong, Z. Biomass-derived phosphorus-doped carbon materials as efficient metal-free catalysts for selective aerobic oxidation of alcohols. *Green Chem.* **2019**, *21*, 5274–5283. [CrossRef]

62. Jiang, Z.-L.; Sun, H.; Shi, W.-K.; Cheng, J.-Y.; Hu, J.-Y.; Guo, H.-L.; Gao, M.-Y.; Zhou, H.; Sun, S.-G. P-Doped Hive-like Carbon Derived from Pinecone Biomass as Efficient Catalyst for Li–O2 Battery. *ACS Sustain. Chem. Eng.* **2019**, *7*, 14161–14169. [CrossRef]

63. Zhu, Y.; Huang, Y.; Chen, C.; Wang, M.; Liu, P. Phosphorus-doped porous biomass carbon with ultra-stable performance in sodium storage and lithium storage. *Electrochim. Acta* **2019**, *321*, 134698. [CrossRef]

64. Chen, C.; Huang, Y.; Meng, Z.; Lu, M.; Xu, Z.; Liu, P.; Li, T. Experimental design and theoretical evaluation of nitrogen and phosphorus dual-doped hierarchical porous carbon for high-performance sodium-ion storage. *J. Mater. Sci. Technol.* **2021**, *76*, 11–19. [CrossRef]

65. Thangavel, R.; Kannan, A.G.; Ponraj, R.; Thangavel, V.; Kim, D.-W.; Lee, Y.-S. Nitrogen-and sulfur-enriched porous carbon from waste watermelon seeds for high-energy, high-temperature green ultracapacitors. *J. Mater. Chem. A* **2018**, *6*, 17751–17762. [CrossRef]

66. Xu, G.; Han, J.; Ding, B.; Nie, P.; Pan, J.; Dou, H.; Li, H.; Zhang, X. Biomass-derived porous carbon materials with sulfur and nitrogen dual-doping for energy storage. *Green Chem.* **2015**, *17*, 1668–1674. [CrossRef]

67. Ren, Y.; Zhang, J.; Xu, Q.; Chen, Z.; Yang, D.; Wang, B.; Jiang, Z. Biomass-derived three-dimensional porous N-doped carbonaceous aerogel for efficient supercapacitor electrodes. *Rsc Adv.* **2014**, *4*, 23412–23419. [CrossRef]

68. Fang, B.; Binder, L. Enhanced surface hydrophobisation for improved performance of carbon aerogel electrochemical capacitor. *Electrochim. Acta* **2007**, *52*, 6916–6921. [CrossRef]

69. Fang, B.; Wei, Y.Z.; Maruyama, K.; Kumagai, M. High capacity supercapacitors based on modified activated carbon aerogel. *J. Appl. Electrochem.* **2005**, *35*, 229–233. [CrossRef]

70. Fang, B.; Binder, L. A modified activated carbon aerogel for high-energy storage in electric double layer capacitors. *J. Power Sources* **2006**, *163*, 616–622. [CrossRef]

71. Wei, Y.-Z.; Fang, B.; Iwasa, S.; Kumagai, M. A novel electrode material for electric double-layer capacitors. *J. Power Sources* **2005**, *141*, 386–391. [CrossRef]

72. Fang, B.; Wei, Y.-Z.; Kumagai, M. Modified carbon materials for high-rate EDLCs application. *J. Power Sources* **2006**, *155*, 487–491. [CrossRef]

73. Molina-Sabio, M.; Rodrıguez-Reinoso, F. Role of chemical activation in the development of carbon porosity. *Colloids Surf. A Physicochem. Eng. Asp.* **2004**, *241*, 15–25. [CrossRef]

74. Lua, A.C.; Lau, F.Y.; Guo, J. Influence of pyrolysis conditions on pore development of oil-palm-shell activated carbons. *J. Anal. Appl. Pyrolysis* **2006**, *76*, 96–102. [CrossRef]

75. Bóta, A.; László, K.; Nagy, L.G.; Copitzky, T. Comparative study of active carbons from different precursors. *Langmuir* **1997**, *13*, 6502–6509. [CrossRef]

76. Guo, C.-Y.; Wang, C.-y. Effects of microstructure of precursors on characteristics of pitch based activated carbons. *Microporous Mesoporous Mater.* **2007**, *102*, 337–340. [CrossRef]

77. Zhou, S.-Y.; Li, X.-H.; Wang, Z.-X.; Guo, H.-J.; Peng, W.-J. Effect of activated carbon and electrolyte on properties of supercapacitor. *Trans. Nonferrous Met. Soc. China* **2007**, *17*, 1328–1333. [CrossRef]

78. Aworn, A.; Thiravetyan, P.; Nakbanpote, W. Preparation and characteristics of agricultural waste activated carbon by physical activation having micro-and mesopores. *J. Anal. Appl. Pyrolysis* **2008**, *82*, 279–285. [CrossRef]

79. Li, Z.; Zhang, L.; Amirkhiz, B.S.; Tan, X.; Xu, Z.; Wang, H.; Olsen, B.C.; Holt, C.M.; Mitlin, D. Carbonized chicken eggshell membranes with 3D architectures as high-performance electrode materials for supercapacitors. *Adv. Energy Mater.* **2012**, *2*, 431–437. [CrossRef]

80. Kim, Y.J.; Abe, Y.; Yanagiura, T.; Park, K.C.; Shimizu, M.; Iwazaki, T.; Nakagawa, S.; Endo, M.; Dresselhaus, M.S. Easy preparation of nitrogen-enriched carbon materials from peptides of silk fibroins and their use to produce a high volumetric energy density in supercapacitors. *Carbon* **2007**, *45*, 2116–2125. [CrossRef]

81. Yun, Y.S.; Cho, S.Y.; Shim, J.; Kim, B.H.; Chang, S.J.; Baek, S.J.; Huh, Y.S.; Tak, Y.; Park, Y.W.; Park, S. Microporous carbon nanoplates from regenerated silk proteins for supercapacitors. *Adv. Mater.* **2013**, *25*, 1993–1998. [CrossRef]

82. Zhu, F.; Cao, W.; Song, W.; Peng, J.; Yang, N.; Niu, J.; Wang, F. Biomass-derived carbon prepared through a quadruple-functional-salt approach for application in K-ion capacitors. *Chem. Eng. J.* **2022**, *449*, 137561. [CrossRef]

83. White, R.J.; Antonietti, M.; Titirici, M.-M. Naturally inspired nitrogen doped porous carbon. *J. Mater. Chem.* **2009**, *19*, 8645–8650. [CrossRef]
84. Tarimo, D.J.; Oyedotun, K.O.; Sylla, N.F.; Mirghni, A.A.; Ndiaye, N.M.; Manyala, N. Waste chicken bone-derived porous carbon materials as high performance electrode for supercapacitor applications. *J. Energy Storage* **2022**, *51*, 104378. [CrossRef]
85. Fidelis, M.; de Moura, C.; Kabbas Junior, T.; Pap, N.; Mattila, P.; Mäkinen, S.; Putnik, P.; Bursać Kovačević, D.; Tian, Y.; Yang, B. Fruit seeds as sources of bioactive compounds: Sustainable production of high value-added ingredients from by-products within circular economy. *Molecules* **2019**, *24*, 3854. [CrossRef]
86. Raymundo-Piñero, E.; Cadek, M.; Béguin, F. Tuning carbon materials for supercapacitors by direct pyrolysis of seaweeds. *Adv. Funct. Mater.* **2009**, *19*, 1032–1039. [CrossRef]
87. Endo, M.; Kim, Y.; Ishii, K.; Inoue, T.; Nomura, T.; Miyashita, N.; Dresselhaus, M. Heat-treatment retention time dependence of polyvinylidenechloride-based carbons on their application to electric double-layer capacitors. *J. Mater. Res.* **2003**, *18*, 693–701. [CrossRef]
88. Niu, J.; Shao, R.; Liu, M.; Liang, J.; Zhang, Z.; Dou, M.; Huang, Y.; Wang, F. Porous carbon electrodes with battery-capacitive storage features for high performance Li-ion capacitors. *Energy Storage Mater.* **2018**, *12*, 145–152. [CrossRef]
89. Qian, T.; Huang, Y.; Zhang, M.; Xia, Z.; Liu, H.; Guan, L.; Hu, H.; Wu, M. Non-corrosive and low-cost synthesis of hierarchically porous carbon frameworks for high-performance lithium-ion capacitors. *Carbon* **2021**, *173*, 646–654. [CrossRef]
90. Yang, S.; Zhang, L.; Sun, J.; Li, K.; Zhao, S.; Zhao, D.; Wang, J.; Yang, C.; Wang, X.; Cao, B. Corncob-derived hierarchical porous activated carbon for high-performance lithium-ion capacitors. *Energy Fuels* **2020**, *34*, 16885–16892. [CrossRef]
91. Sennu, P.; Aravindan, V.; Ganesan, M.; Lee, Y.G.; Lee, Y.S. Biomass-derived electrode for next generation lithium-Ion Capacitors. *ChemSusChem* **2016**, *9*, 849–854. [CrossRef]
92. Chen, X.; Mu, Y.; Cao, G.; Qiu, J.; Zhang, W.; Zhang, Q.; Ming, H. Structure-activity relationship of carbon additives in cathodes for advanced capacitor batteries. *Electrochim. Acta* **2022**, *413*, 140165. [CrossRef]
93. Shellikeri, A.; Yturriaga, S.; Zheng, J.; Cao, W.; Hagen, M.; Read, J.; Jow, T.; Zheng, J. Hybrid lithium-ion capacitor with LiFePO4/AC composite cathode–long term cycle life study, rate effect and charge sharing analysis. *J. Power Sources* **2018**, *392*, 285–295. [CrossRef]
94. Hagen, M.; Cao, W.; Shellikeri, A.; Adams, D.; Chen, X.; Brandt, W.; Yturriaga, S.; Wu, Q.; Read, J.; Jow, T. Improving the specific energy of Li-Ion capacitor laminate cell using hybrid activated Carbon/$LiNi_{0.5}Co_{0.2}Mn_{0.3}O_2$ as positive electrodes. *J. Power Sources* **2018**, *379*, 212–218. [CrossRef]
95. Granados-Moreno, M.; Moreno-Fernández, G.; Mysyk, R.; Carriazo, D. A high-energy hybrid lithium-ion capacitor enabled by a mixed capacitive-battery storage $LiFePO_4$–AC cathode and a SnP_2O_7–rGO anode. *Sustain. Energy Fuels* **2023**, *7*, 965–976. [CrossRef]
96. Böckenfeld, N.; Placke, T.; Winter, M.; Passerini, S.; Balducci, A. The influence of activated carbon on the performance of lithium iron phosphate based electrodes. *Electrochim. Acta* **2012**, *76*, 130–136. [CrossRef]
97. Sun, X.; Zhang, X.; Zhang, H.; Xu, N.; Wang, K.; Ma, Y. High performance lithium-ion hybrid capacitors with pre-lithiated hard carbon anodes and bifunctional cathode electrodes. *J. Power Sources* **2014**, *270*, 318–325. [CrossRef]
98. Yu, J.; Wang, X.; Peng, J.; Jia, X.; Li, L.; Chuan, X. Porous activity of biomass-activated carbon enhanced by nitrogen-dopant towards high-performance lithium ion hybrid battery-supercapacitor. *J. Electrochem. Soc.* **2021**, *168*, 120537. [CrossRef]
99. Lee, S.H. Smart Multi-Layer Architecture Electrodes for High Energy Density Lithium-Ion Capacitors. *Batter. Supercaps* **2023**, *6*, e202200380. [CrossRef]
100. Frackowiak, E.; Beguin, F. Carbon materials for the electrochemical storage of energy in capacitors. *Carbon* **2001**, *39*, 937–950. [CrossRef]
101. Beguin, F.; Frackowiak, E. *Carbons for Electrochemical Energy Storage and Conversion Systems*; CRC Press: Boca Raton, FL, USA, 2009.
102. Raymundo-Piñero, E.; Cadek, M.; Wachtler, M.; Béguin, F. Carbon nanotubes as nanotexturing agents for high power supercapacitors based on seaweed carbons. *ChemSusChem* **2011**, *4*, 943–949. [CrossRef] [PubMed]
103. Jäckel, N.; Weingarth, D.; Zeiger, M.; Aslan, M.; Grobelsek, I.; Presser, V. Comparison of carbon onions and carbon blacks as conductive additives for carbon supercapacitors in organic electrolytes. *J. Power Sources* **2014**, *272*, 1122–1133. [CrossRef]
104. Suarez-Martinez, I.; Grobert, N.; Ewels, C. Nomenclature of sp2 carbon nanoforms. *Carbon* **2011**, *50*, 741–747. [CrossRef]
105. Hantel, M.; Presser, V.; McDonough, J.; Feng, G.; Cummings, P.T.; Gogotsi, Y.; Kötz, R. In situ electrochemical dilatometry of onion-like carbon and carbon black. *J. Electrochem. Soc.* **2012**, *159*, A1897. [CrossRef]
106. Spahr, M.E.; Goers, D.; Leone, A.; Stallone, S.; Grivei, E. Development of carbon conductive additives for advanced lithium ion batteries. *J. Power Sources* **2011**, *196*, 3404–3413. [CrossRef]
107. McDonough, J.K.; Frolov, A.I.; Presser, V.; Niu, J.; Miller, C.H.; Ubieto, T.; Fedorov, M.V.; Gogotsi, Y. Influence of the structure of carbon onions on their electrochemical performance in supercapacitor electrodes. *Carbon* **2012**, *50*, 3298–3309. [CrossRef]
108. Chen, C.-C.; Patra, J.; Wang, F.-M.; Lin, J.-Y.; Dong, Q.-F.; Su, Y.-S.; Chang, J.-K. Binder-controlled pore size distribution of carbon electrodes to mitigate self-discharge of supercapacitors. *Carbon* **2023**, *204*, 555–565. [CrossRef]
109. Tran, H.Y.; Wohlfahrt-Mehrens, M.; Dsoke, S. Influence of the binder nature on the performance and cycle life of activated carbon electrodes in electrolytes containing Li-salt. *J. Power Sources* **2017**, *342*, 301–312. [CrossRef]
110. Galek, P.; Różański, J.; Fic, K. Toward better porous carbon-based electrodes by investigation of the viscoelastic properties of carbon suspension. *Chem. Eng. J.* **2023**, *463*, 142476. [CrossRef]

111. Pettinger, K.-H.; Dong, W. When does the operation of a battery become environmentally positive? *J. Electrochem. Soc.* **2016**, *164*, A6274. [CrossRef]

112. Zhang, Y.S.; Courtier, N.E.; Zhang, Z.; Liu, K.; Bailey, J.J.; Boyce, A.M.; Richardson, G.; Shearing, P.R.; Kendrick, E.; Brett, D.J. A review of lithium-ion battery electrode drying: Mechanisms and metrology. *Adv. Energy Mater.* **2022**, *12*, 2102233. [CrossRef]

113. Jow, T.R.; Xu, K.; Borodin, O.; Ue, M. *Electrolytes for Lithium and Lithium-Ion Batteries*; Springer: Berlin/Heidelberg, Germany, 2014; Volume 58.

114. Zhong, C.; Deng, Y.; Hu, W.; Qiao, J.; Zhang, L.; Zhang, J. A review of electrolyte materials and compositions for electrochemical supercapacitors. *Chem. Soc. Rev.* **2015**, *44*, 7484–7539. [CrossRef]

115. Divya, M.L.; Lee, Y.-S.; Aravindan, V. Glyme solvated Na and Li-ion capacitors based on co-intercalation process using pencil graphite as battery type electrode. *J. Power Sources* **2022**, *543*, 231823. [CrossRef]

116. Decaux, C.; Ghimbeu, C.M.; Dahbi, M.; Anouti, M.; Lemordant, D.; Béguin, F.; Vix-Guterl, C.; Raymundo-Pinero, E. Influence of electrolyte ion–solvent interactions on the performances of supercapacitors porous carbon electrodes. *J. Power Sources* **2014**, *263*, 130–140. [CrossRef]

117. ho Lee, C.; Jung, C. Enhancement of Li+ ions mobility on activated carbon electrode for lithium ion capacitor. *Electrochim. Acta* **2017**, *232*, 596–600. [CrossRef]

118. ho Lee, C.; Xu, F.; Jung, C. Influence of the electrolyte distribution near the micropores of the activated carbon (AC) electrode on high rate performance of high voltage capacitors. *Electrochim. Acta* **2014**, *131*, 240–244. [CrossRef]

119. Peljo, P.; Girault, H.H. Electrochemical potential window of battery electrolytes: The HOMO–LUMO misconception. *Energy Environ. Sci.* **2018**, *11*, 2306–2309. [CrossRef]

120. Zhang, T.; Fuchs, B.; Secchiaroli, M.; Wohlfahrt-Mehrens, M.; Dsoke, S. Electrochemical behavior and stability of a commercial activated carbon in various organic electrolyte combinations containing Li-salts. *Electrochim. Acta* **2016**, *218*, 163–173. [CrossRef]

121. Borodin, O.; Behl, W.; Jow, T.R. Oxidative stability and initial decomposition reactions of carbonate, sulfone, and alkyl phosphate-based electrolytes. *J. Phys. Chem. C* **2013**, *117*, 8661–8682. [CrossRef]

122. Naoi, K. 'Nanohybrid capacitor': The next generation electrochemical capacitors. *Fuel Cells* **2010**, *10*, 825–833. [CrossRef]

123. Eleri, O.E.; Huld, F.; Pires, J.; Tucho, W.M.; Schweigart, P.; Svensson, A.M.; Lou, F.; Yu, Z. Revealing mechanisms of activated carbon capacity fade in lithium-ion capacitors. *Electrochim. Acta* **2023**, *453*, 142359. [CrossRef]

124. Guo, K.; Qi, S.; Wang, H.; Huang, J.; Wu, M.; Yang, Y.; Li, X.; Ren, Y.; Ma, J. High-Voltage Electrolyte Chemistry for Lithium Batteries. *Small Sci.* **2022**, *2*, 2100107. [CrossRef]

125. He, M.; Su, C.-C.; Peebles, C.; Zhang, Z. The impact of different substituents in fluorinated cyclic carbonates in the performance of high voltage lithium-ion battery electrolyte. *J. Electrochem. Soc.* **2021**, *168*, 010505. [CrossRef]

126. Kato, K.; Rodrigues, M.-T.F.; Babu, G.; Ajayan, P.M. Revealing anion chemistry above 3V in Li-ion capacitors. *Electrochim. Acta* **2019**, *324*, 134871. [CrossRef]

127. Stępień, D.; Zhao, Z.; Dsoke, S. Shift to post-li-ion capacitors: Electrochemical behavior of activated carbon electrodes in li-, na-and k-salt containing organic electrolytes. *J. Electrochem. Soc.* **2018**, *165*, A2807. [CrossRef]

128. Eleri, O.E.; Pires, J.; Huld, F.T.; Lu, S.; Schweigart, P.; Svensson, A.M.; Lou, F.; Yu, Z. Enhanced activated carbon lithium-ion capacitor electrochemical stability through electrolyte dielectric optimisation. *Sustain. Energy Fuels* **2023**, *7*, 1846–1854. [CrossRef]

129. Xu, K. "Charge-transfer" process at graphite/electrolyte interface and the solvation sheath structure of Li+ in nonaqueous electrolytes. *J. Electrochem. Soc.* **2007**, *154*, A162. [CrossRef]

130. Xu, K.; Lam, Y.; Zhang, S.S.; Jow, T.R.; Curtis, T.B. Solvation sheath of Li+ in nonaqueous electrolytes and its implication of graphite/electrolyte interface chemistry. *J. Phys. Chem. C* **2007**, *111*, 7411–7421. [CrossRef]

131. Xu, K.; von Wald Cresce, A. Li+-solvation/desolvation dictates interphasial processes on graphitic anode in Li ion cells. *J. Mater. Res.* **2012**, *27*, 2327–2341. [CrossRef]

132. Chikaoka, Y.; Ochi, R.; Fujii, K.; Ariga, T.; Sakurai, M.; Matsumoto, A.; Ueda, T.; Iwama, E.; Naoi, K. Controlling the Phase Separation of Dimethyl Carbonate Solvents Using a Dual-Cation System: Applications in High-Power Lithium Ion-Based Hybrid Capacitors. *J. Phys. Chem. C* **2022**, *126*, 14389–14398. [CrossRef]

133. Shan, X.Y.; Wang, Y.; Wang, D.W.; Li, F.; Cheng, H.M. Armoring graphene cathodes for high-rate and long-life lithium ion supercapacitors. *Adv. Energy Mater.* **2016**, *6*, 1502064. [CrossRef]

134. Han, D.; Weng, Z.; Li, P.; Tao, Y.; Cui, C.; Zhang, L.; Lin, W.; Gao, Y.; Kong, D.; Yang, Q.-H. Electrode thickness matching for achieving high-volumetric-performance lithium-ion capacitors. *Energy Storage Mater.* **2019**, *18*, 133–138. [CrossRef]

135. Qin, H.; Chao, H.; Zhang, M.; Huang, Y.; Liu, H.; Cheng, J.; Cao, L.; Xu, Q.; Guan, L.; Teng, X. Precious potential regulation of carbon cathode enabling high-performance lithium-ion capacitors. *Carbon* **2021**, *180*, 110–117. [CrossRef]

136. Dsoke, S.; Fuchs, B.; Gucciardi, E.; Wohlfahrt-Mehrens, M. The importance of the electrode mass ratio in a Li-ion capacitor based on activated carbon and $Li_4Ti_5O_{12}$. *J. Power Sources* **2015**, *282*, 385–393. [CrossRef]

137. Jin, L.; Guo, X.; Shen, C.; Qin, N.; Zheng, J.; Wu, Q.; Zhang, C.; Zheng, J.P. A universal matching approach for high power-density and high cycling-stability lithium ion capacitor. *J. Power Sources* **2019**, *441*, 227211. [CrossRef]

138. Zhang, X.; Zhang, X.; Sun, X.; An, Y.; Song, S.; Li, C.; Wang, K.; Su, F.; Chen, C.-M.; Liu, F. Electrochemical impedance spectroscopy study of lithium-ion capacitors: Modeling and capacity fading mechanism. *J. Power Sources* **2021**, *488*, 229454. [CrossRef]

139. Weingarth, D.; Foelske-Schmitz, A.; Kötz, R. Cycle versus voltage hold–Which is the better stability test for electrochemical double layer capacitors? *J. Power Sources* **2013**, *225*, 84–88. [CrossRef]

140. Weingarth, D.; Noh, H.; Foelske-Schmitz, A.; Wokaun, A.; Kötz, R. A reliable determination method of stability limits for electrochemical double layer capacitors. *Electrochim. Acta* **2013**, *103*, 119–124. [CrossRef]

141. Sun, X.; Zhang, X.; Wang, K.; An, Y.; Zhang, X.; Li, C.; Ma, Y. Determination strategy of stable electrochemical operating voltage window for practical lithium-ion capacitors. *Electrochim. Acta* **2022**, *428*, 140972. [CrossRef]

142. Zhang, S.S. Dual-carbon lithium-ion capacitors: Principle, materials, and technologies. *Batter. Supercaps* **2020**, *3*, 1137–1146. [CrossRef]

143. Huang, Z.; Deng, Z.; Zhong, Y.; Xu, M.; Li, S.; Liu, X.; Zhou, Y.; Huang, K.; Shen, Y.; Huang, Y. Progress and challenges of prelithiation technology for lithium-ion battery. *Carbon Energy* **2022**, *4*, 1107–1132. [CrossRef]

144. Holtstiege, F.; Bärmann, P.; Nölle, R.; Winter, M.; Placke, T. Pre-Lithiation Strategies for Rechargeable Energy Storage Technologies: Concepts, Promises and Challenges. *Batteries* **2018**, *4*, 4. [CrossRef]

145. Dose, W.M.; Johnson, C.S. Cathode pre-lithiation/sodiation for next-generation batteries. *Curr. Opin. Electrochem.* **2022**, *31*, 100827. [CrossRef]

146. Arnaiz, M.; Shanmukaraj, D.; Carriazo, D.; Bhattacharjya, D.; Villaverde, A.; Armand, M.; Ajuria, J. A transversal low-cost pre-metallation strategy enabling ultrafast and stable metal ion capacitor technologies. *Energy Environ. Sci.* **2020**, *13*, 2441–2449. [CrossRef]

147. Park, M.-S.; Lim, Y.-G.; Kim, J.-H.; Kim, Y.-J.; Cho, J.; Kim, J.-S. A novel lithium-doping approach for an advanced lithium ion capacitor. *Adv. Energy Mater.* **2011**, *1*, 1002–1006. [CrossRef]

148. Park, M.S.; Lim, Y.G.; Hwang, S.M.; Kim, J.H.; Kim, J.S.; Dou, S.X.; Cho, J.; Kim, Y.J. Scalable integration of Li5FeO4 towards robust, high-performance lithium-ion hybrid capacitors. *ChemSusChem* **2014**, *7*, 3138–3144. [CrossRef]

149. Jeżowski, P.; Crosnier, O.; Deunf, E.; Poizot, P.; Béguin, F.; Brousse, T. Safe and recyclable lithium-ion capacitors using sacrificial organic lithium salt. *Nat. Mater.* **2018**, *17*, 167–173. [CrossRef]

150. Sun, C.; Zhang, X.; Li, C.; Wang, K.; Sun, X.; Ma, Y. High-efficiency sacrificial prelithiation of lithium-ion capacitors with superior energy-storage performance. *Energy Storage Mater.* **2020**, *24*, 160–166. [CrossRef]

151. Pan, X.; Chojnacka, A.; Jeżowski, P.; Beguin, F. Na$_2$S sacrificial cathodic material for high performance sodium-ion capacitors. *Electrochim. Acta* **2019**, *318*, 471–478. [CrossRef]

152. Pan, X.; Chojnacka, A.; Béguin, F. Gas free oxidation of NaCN for presodiating and stabilizing the anodic host of sodium-ion capacitors. *J. Energy Chem.* **2022**, *72*, 33–40. [CrossRef]

153. Jeżowski, P.; Chojnacka, A.; Pan, X.; Beguin, F. Sodium amide as a "zero dead mass" sacrificial material for the pre-sodiation of the negative electrode in sodium-ion capacitors. *Electrochim. Acta* **2021**, *375*, 137980. [CrossRef]

154. Pan, X.; Chojnacka, A.; Béguin, F. Advantageous carbon deposition during the irreversible electrochemical oxidation of Na$_2$C$_4$O$_4$ used as a presodiation source for the anode of sodium-ion systems. *Energy Storage Mater.* **2021**, *40*, 22–30. [CrossRef]

155. Shanmukaraj, D.; Grugeon, S.; Laruelle, S.; Douglade, G.; Tarascon, J.-M.; Armand, M. Sacrificial salts: Compensating the initial charge irreversibility in lithium batteries. *Electrochem. Commun.* **2010**, *12*, 1344–1347. [CrossRef]

156. Zhang, S.S. Eliminating pre-lithiation step for making high energy density hybrid Li-ion capacitor. *J. Power Sources* **2017**, *343*, 322–328. [CrossRef]

Appendix B - Paper II and supplementary information

Revealing mechanisms of activated carbon capacity fade in lithium-ion capacitors.

O. E. Eleri, F. Huld, J. Pires, W. M. Tucho, P. Schweigart, A. M. Svensson, F. Lou, and Z. Yu.

Revealing mechanisms of activated carbon capacity fade in lithium-ion capacitors

Obinna Egwu Eleri [a,b], Frederik Huld [a,b], Julie Pires [a], Wakshum Mekonnen Tucho [c], Philipp Schweigart [d], Ann Mari Svensson [d], Fengliu Lou [a,*], Zhixin Yu [b,*]

[a] Beyonder AS, 4313 Sandnes, Norway
[b] Department of Energy and Petroleum Engineering, University of Stavanger, 4036 Stavanger, Norway
[c] Department of Machine, Building and Materials Technology Laboratory IMBM, University of Stavanger, 4036 Stavanger, Norway
[d] Department of Materials Science and Engineering, Norwegian University of Science and Technology, 7491 Trondheim, Norway

ARTICLE INFO

ABSTRACT

The capacity fade mechanism of activated carbon (AC) electrode in Li-ion electrolyte was studied via electrochemical impedance spectroscopy (EIS) and post-mortem electrode characterizations at different stages of electrochemical cycling. Electrochemical cycling was conducted in half cells incorporating the AC working electrode, Li metal counter electrode, and 1 M LiPF$_6$ in EC:DMC (1:1) electrolyte. Three phases were identified during the ageing process that corresponded with transformation of the passivation layer at the electrode surface and charge transfer impedance derived from the EIS analysis. Surface area and morphology analysis showed that the AC surface was progressively transformed by degradation products that reduced the available surface area and accessibility of electrolyte moieties into the pores. X-ray photoelectron spectroscopy suggested that the degradation products are from the LiPF$_6$ salt decomposition and carbonate solvent decomposition, while Raman analysis demonstrated increased defects in the electrode as cycling progressed. The capacity fade was therefore caused by the synergistic effect of electrolyte degradation and active material transformation.

1. Introduction

Global climate awareness on the adverse impact of fossil fuel powered energy sources has prompted the electrification of previously fossil dominated technologies such as automobiles and stationary power systems. Lithium-ion capacitors (LiC) are excellent in satisfying such operations due to the synergistic effect of combining conventionally high power capacitor cathode such as activated carbon (AC) and energy rich battery-type intercalation anode such as graphite in the LiC device architecture [1,2]. Consequently, charge storage in LiC occur via ion adsorption/desorption on the cathode and lithium intercalation/de-intercalation on the anode. As such, the LiC possesses higher power densities than lithium-ion batteries(LiB) but lower energy densities [2]. The lower energy densities are attributed to the low capacity of the AC cathode (<60 mAh/g) by virtue of its predominantly physical surface charge storage process, which limits the attainable specific energy especially when compared to intercalation type cathodes (e.g., lithium iron phosphate) used in LiB [3]. Many researchers have attempted to improve the energy density of the LiC while maintaining the high-power requirements by expanding the operating potential window of the AC cathode [4–6].

Typically, electrolytes consisting of lithium salts such as LiPF$_6$ dissolved in carbonate solvents such as ethylene carbonate (EC), dimethyl carbonate (DMC), ethyl methyl carbonate (EMC) and diethyl carbonate (DEC) are incorporated in LiC to realize wide operating potential window, good conductivity, and anode and Al current collector passivating abilities of EC and LiPF$_6$ salt [7,8]. However, the high specific surface area and often unavoidable presence of surface oxygenated species on the AC electrode can negatively affect the realisable operating potential window and device cycle life due to parasitic reactions with electrolyte constituents [9,10]. The EC solvent may continuously decompose and form a passivating solid porous layer on the surface [11,12]. Furthermore, the highly sensitive PF$_6^-$ anion is prone to hydrolysis and oxidation as it contacts the polarized AC cathode [13,14]. These could consequently lead to the formation of by-products such as PF$_5$ and HF that may catalyse other cellular component degradation and cause interfacial instabilities [13,15,16].

The electrolyte degradation process proceeds via PF$_6^-$ and EC

* Corresponding authors.

E-mail addresses: fengliu@beyonder.no (F. Lou), zhixin.yu@uis.no (Z. Yu).

oxidation by F-abstraction and H-abstraction, subsequent to the parasitic faradaic reactions with oxygenated functionalities and moisture trapped in the AC pores [13,17]. Eventually, the cycle life of the device is affected as the electrolyte solvents and ionic moieties become depleted, and the surface of the AC cathode is passivated by the precipitated degradation products. Other contributors to capacity fade include binder decomposition, active material pulverization and gas generation, which can increase resistance and accelerate cycle life deterioration [18]. Mitigating such processes require in-depth investigation into how they occur and correlation of physical changes on the electrode surface with electrochemical state of the cell. Post-mortem analysis and in-situ/ex-situ spectroscopic techniques are therefore vital towards unravelling the causes of capacity fade and device failure.

Most of the previous studies have been conducted on the AC electrodes in supercapacitors utilizing $TEABF_4$ salt dissolved in propylene carbonate or acetonitrile solvent [18–20]. However, the use of Li-ion salts ($LiPF_6$) with the reactive PF_5, and the passivation film forming abilities of carbonate-based solvents (EC) have necessitated that the capacity fade mechanisms need to be revisited. Moreover, although the capacity fade mechanisms are related to the loss of active surface area and AC electrode modification by degradation products, the products remain largely unknown. Revealing the capacity fade mechanisms can thus provide measures via which they can be mitigated. In this regard, the nature, quantity, and when the degradation products are formed are to be studied. In addition, detrimental physio-chemical changes on the electrodes can be controlled via the incorporation of additives to either solubilize the degradation products or delay their formation.

In this study, the AC was characterized at different stages spanning before and after electrochemical cycling, using nitrogen physisorption, x-ray photoelectron spectroscopy (XPS), scanning electron microscopy (SEM) and Raman spectroscopy. The capacity retention was investigated via sequential floating voltage holds at 4.2 V, with electrochemical impedance spectroscopy (EIS) measurement acquired intermittently. The capacity fade was correlated with the EIS spectra and results from the AC characterization.

2. Experimental

2.1. Materials

Commercial activated carbon (YEC-8B) was purchased from Fuzhou Yihuan Carbon Co., Ltd. Lithium hexafluorophosphate ($LiPF_6$) (purity 99.94%), lithium chips, EC and DMC (purity 99.9%), polytetrafluoroethylene (PTFE) (60 wt.%) were purchased from Sigma Aldrich. The electrolyte 1 M $LiPF_6$ in EC:DMC (1:1) vol/vol was prepared by mixing the components in an Argon glove box with moisture and oxygen levels less than 0.1 ppm.

2.2. Electrode fabrication

Self-standing electrodes were assembled by mixing 92 wt.% AC powder and 8 wt.% PTFE binder into a dough, and roll pressed at 80 °C. The self-standing electrode was thereafter laminated at 160 °C onto a double-sided carbon coated Al current collector, with the aid of a hot rolling press (MTI-Corp). 15 mm discs were punched from the laminated electrode, weighed, and dried overnight in a vacuum oven at 140 °C. The active material thickness and loading was 100 μm and 6.7 mg/cm^2, respectively. After drying, the discs were transferred to the Argon glove box for cell assembly.

2.3. Cell assembly and electrochemical cycling

Half cells incorporating AC as the working electrode and lithium metal as the counter/reference electrode in CR2032 type coin cells were assembled in the glove box. Cellulose TF4030 (19 mm Ø) was used as the separator and 100 μl of the prepared electrolyte was added in each cell.

The assembled cells were subjected to galvanostatic charge and discharge (GCD) cycling at different current densities (0.1C for 3 cycles, 0.5 C for 3 cycles, 1C, 2C, 5C, 10C, 20 C, 1C and 10C for 5 cycles; 1C = 42.6 mAh/g) in the potential range 3.0–4.2 V. The floating voltage ageing protocol consisted of a floating voltage hold (FVH) at 4.2 V for 10 h with consecutive capacity checks at 10C before and after each floating sequence to monitor the capacity fade. EIS was acquired after every cumulative 100 h of floating on the cycled cells. The EIS measurements were conducted in the frequency range 100 kHz to 0.01 Hz with an amplitude of 5 mV. The EIS spectra were fitted using the impedance.py package in PYTHON.

2.4. Sample characterization

Cell disassembly was carried out in the Argon glovebox. The cells were de-crimped using a custom type CR2032 de-crimper (Hohsen). The extracted AC electrodes were washed in a DMC solution to rinse off excess electrolyte and dried for 24 h under vacuum in the anti-chamber of the glove box.

Nitrogen physisorption analysis was performed using a Tristar II micromeritics surface and pore volume analyser. The specific surface area and pore volumes were determined using the Brunauer-Emmett-Teller (BET) and Nonlocal Density functional theory (NLDFT) methods. Samples were degassed for 24 h at 80 °C prior to measurements, while ensuring limited exposure to ambient atmosphere during handling. Surface morphology examination was conducted using Supra 35VP (ZEISS) field emission gun scanning electron microscope (FEG-SEM). Raman spectra were obtained using a Renishaw InVia Qontor Raman Microscope. The spectra were acquired using a 532 nm laser wavelength, x20 objective lens, exposure time of 20 s and 3 accumulations. XPS data were collected with a Thermo Scientific ESCALAB 250 spectrometer, using a focused monochromatized Al Kα radiation (hν = 1486.6 eV). The pressure was maintained at 10^{-8} mbar and charge neutralization was applied. The analysed area of the samples was an ellipse with a dimension of 450 × 900 μm. The XPS introduction chamber was directly connected to an argon glovebox to protect the sample from any contact with air and moisture during the transfer. Spectra deconvolution and peak fitting was performed using Origin software and Gaussian peak fits.

3. Results and discussion

3.1. Electrochemical analysis

The capacity retention during the floating voltage is presented in Fig. 1, while the rate performance and respective charge/discharge curves at different C-rates are displayed in Figure S1 in Supporting Information (SI). The AC electrode endured up to 950 h of floating voltage
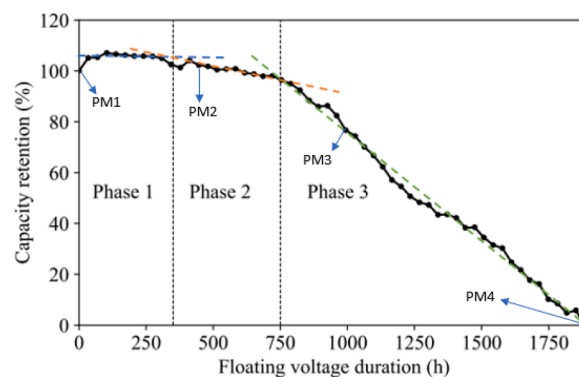

Fig. 1. Capacity retention during the floating voltage stability test; three distinct phases of capacity fade were identified. The arrows mark the FVH time points when the samples were obtained.

prior to reaching 80% capacity retention and approximately 1900 h before reaching 0% capacity retention. The ageing profile could be divided into three phases (denoted by the dashed lines) based on the distinct features and slope of the capacity retention profile. The exact position of the phases was determined by fitting the data to straight lines with varying slopes and marking the intersection of the lines. The phases corresponded to the capacity retention profile with three distinct features. Phase one is characterised by an initial increase in capacity, followed by a stable period which can be fitted to a horizontal straight line. After 350 h, the capacity retention decreases very slowly up to 750 h. The third phase is characterized by accelerated capacity fade in a steep slope until 0% capacity retention at 1900 h.

Samples for the post-mortem (PM) analysis were obtained at the respective positions denoted by PM in Fig. 1, to reveal the changes of the AC electrode surface. These points coincided with the state of the AC at different phases and was correlated with the capacity fade. The AC electrode after 450 h of FVH was without any visible capacity fade but was also studied to disclose possible surface transformations in phase two. The results from the post-mortem characterizations are presented in Section 3.2. All the characterized samples are summarized in Table 1.

The floating voltage stability test was complemented by EIS to reveal changes at the active material/electrolyte interfaces in relation to the state of capacity retention of the cell. The EIS spectra were acquired before floating (0 h) and after every 100 h of floating until 950 h when the cell was at 80% capacity retention, and periodically until 1900 h when the cell was at 0% capacity retention. The obtained EIS spectra are presented in Fig. 2a. The spectra were characterized by two semi circles at the high to medium frequency regions associated with the passivation layer impedance (Rp) and charge transfer impedance (Rct), a 45-degree sloping line at low frequencies attributed to Warburg diffusion (W) impedance, and a vertical straight line representing the capacitance (C). As the floating progressed, the spectra were gradually transformed at the high frequency region with the appearance of a conspicuous negatively sloped inverted line. The length and slope of this feature increased as the duration of ageing progressed. The origin of this feature was ambiguous and could be due to a capacitive behaviour/artefact which might have originated from the increasing active material and contact resistance usually obtained at high frequencies. To simplify the discussion, Rs was assigned to represent the bulk electrolyte resistance and active material/current collector contact resistance, which was the point at high frequency when the inverted sloping line intercepted with the real axis. The impedance spectra were fitted with similar circuits as reported in literature [21,22]. The evolution of the resistance Rs, Rp and Rct obtained from the fitting as the floating time progressed are presented in Fig. 2b. The deconvoluted R-CPE loops are illustrated in Figure S2 in SI, while the values of the fitting parameters are summarized in Table S1.

In Fig. 2b, Rs remained relatively constant in phase one as the floating voltage progressed, which implied that the bulk solution resistance and contact resistances were not altered in this phase and hence did not affect the capacity. On the contrary, Rp and Rct were 22 Ohm and 17 ohms before the floating but decreased significantly to around 5 ohms at the end of phase one. The trend for Rp and Rct in phase one

suggests a reformation of the passivating deposits at the electrode interfaces owing to electrochemical activation and improved accessibility of electrolyte ions at the surface [22]. The electrochemical activation may have opened more pores on the AC surface for adsorption of the PF_6^- anions during the floating voltage charge, which resulted in the slight capacity increase. In phase two, the increase in Rs signalled electrolyte decomposition and accumulation of degradation products that coincided with a steady decrease in capacity. Meanwhile, the relatively stable Rp and Rct suggested that the initially formed passivating deposits remained unchanged. However, the overlayed R-CPE loops in Figure S2b and e, indicated some slight increase in Rp and Rct, which implied some transformation of the passivating deposits and increased charge transfer resistance. The capacity fade in phase two could have therefore been instigated by reduced accessibility of electrolyte moieties into the electrode surface, together with the effect of diminished PF_6^- anions for charge storage following the electrolyte decomposition.

In phase three, the capacity retention progressively decreased with a 45-degree slope line to near zero. On the contrary, the Rs value began to rise in a 45-degree trend, which inferred that electrolyte resistance/electrolyte degradation and accumulation of degradation products was substantially accelerated in this phase. Also, Rp and Rct increased significantly to 16 ohm and 12 ohm after 1400 h of floating, which was almost 3 times the value at the end of phase one. In contrast, the Rs increased to 47.8 Ohm after 1400 h, which was almost 10 times greater than the value at the end of phase one. This further implied that the electrolyte could have been substantially decomposed after 750 h, while the growth of the inverted vertical sloping peak at high frequencies (Fig. 2a) suggested that the artefact was strongly related to the electrochemical ageing of the cell since it considerably increased towards the end of life.

The initial deterioration up to 80% capacity retention (950 h) could have been dominated by transformation of the AC electrode surface by the degradation products and gradual reduction of PF_6^- anions. Nevertheless, the contribution of the lithium counter electrode cannot be ignored, because the rapidly expanded Rp in phase three could be attributed to the deposition of irregular aggregates of dead lithium and pulverization of the initial formed surface passivating film on the lithium counter electrode [23]. More active sites might have been created upon which electrolyte degradation was accelerated as indicated by the exponential increase in Rs. Hence, electrolyte starvation in phase three may have significantly contributed to the capacity fade in this phase.

3.2. Degradation mechanism

The results from the electrochemical analysis using combined floating voltage and intermittent EIS analysis suggested transformations of the electrode surfaces as the capacity fade progressed. In this section, different characterization techniques are employed to reveal the nature of the surface changes and deposits on the electrodes at different stages, which contributed to the capacity fade.

SEM was used to probe the changes in surface morphology of the AC. From Fig. 3a and b, one can distinguish the effect of the PTFE binder as reflected by the fused and compacted nature of dry electrode, in contrast with the isolated grains of the AC powder. The compacted nature indicated a reduced surface area of the AC electrode when compared to the AC powder due to the PTFE binder penetration in the pores. Moreover, some aggregates of passivating deposited species were observed in the SEM image of the blank electrode (Fig. 3c). Therefore, by immersing the AC electrode in the electrolyte, though without cycling, the passivating deposits may have covered some of the available surface area or occupied the pores. The passivating deposits are likely formed from reactions between the electrolyte species and oxygen functionalities on the surface of the AC electrode [11,12,24].

The electrode at 0 h of FVH had undergone few GCD cycles but exhibited similar passivating deposits at the surface (Fig. 3d). However,

Table 1
Denotations and descriptions of the samples.

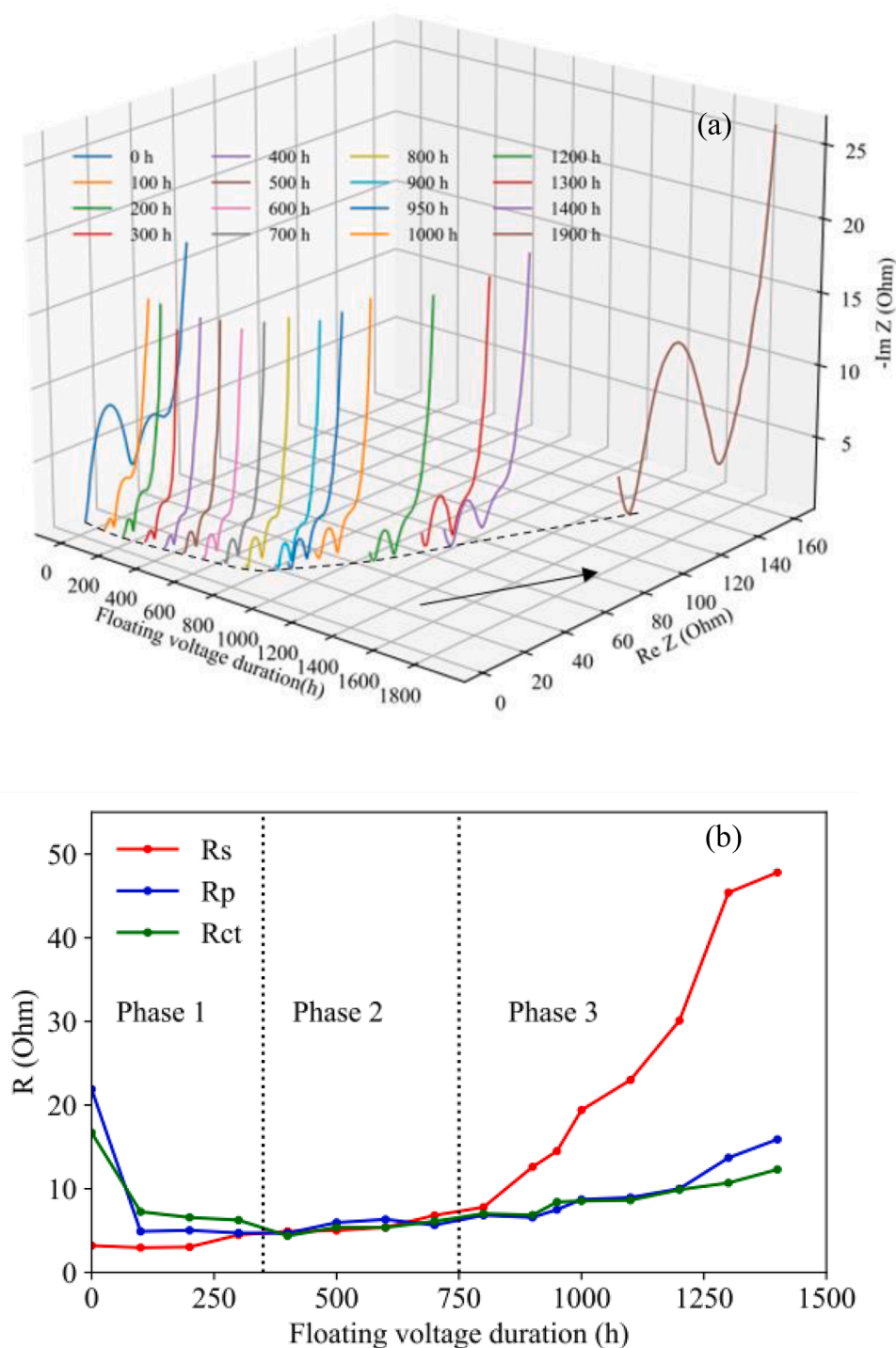| Denotations	Descriptions
AC powder	Dried AC powder
AC electrode	Dried AC electrode
Blank electrode	AC electrode immersed in electrolyte (uncycled)
0 h of FVH	AC electrode after GCD cycles but 0 h of FVH (cell at 100% capacity retention)
450 h of FVH	AC electrode after 450 h of FVH (cell at near 100% capacity retention)
950 h of FVH	AC electrode after 950 h of FVH (cell at 80% capacity retention)
1900 h of FVH	AC electrode after 1900 h of FVH (cell at 0% capacity retention)

Fig. 2. (a) 3D EIS spectra after different durations of floating; (b) Resistance parameters (Rs, Rp, Rct) after fitting.

the edges of the AC grains appeared to be etched, possibly from electrochemical activation due to the cycling [25]. As cycling progressed towards phase two (450 h of FVH) and three (950 h of FVH), the passivating deposits increased due to substantial deposition of insoluble electrolyte degradation products (Fig. 3e and f). Therefore, the capacity fade could be related to the loss of surface area and pores for ion adsorption.

At 1900 h of FVH (Fig. 3g) with 0% capacity retention, the AC electrode surface was completely covered by the aggregated decomposition products and appeared to be of a fused nature. In addition, some new spherical deposits were observed. EDX analysis of these spherical

spots (Figure S3) revealed that they were predominantly composed of carbon (69%), oxygen (8%), fluorine (20%) and phosphorus (2%), which are elemental constituents of the electrolyte and electrolyte degradation products.

Nitrogen physisorption analysis was used in probing the pore property transformation at different stages. The physisorption isotherms (Fig. 4a) display type I/IV characteristic according to the IUPAC classification, with predominantly micropores and some mesopores in the AC powder. The incorporation of the PTFE binder reduced the surface area and pore volume by around 20% and 7% (Fig. 4b). The reductions occurred mostly in the micropores where some of the PTFE binder was
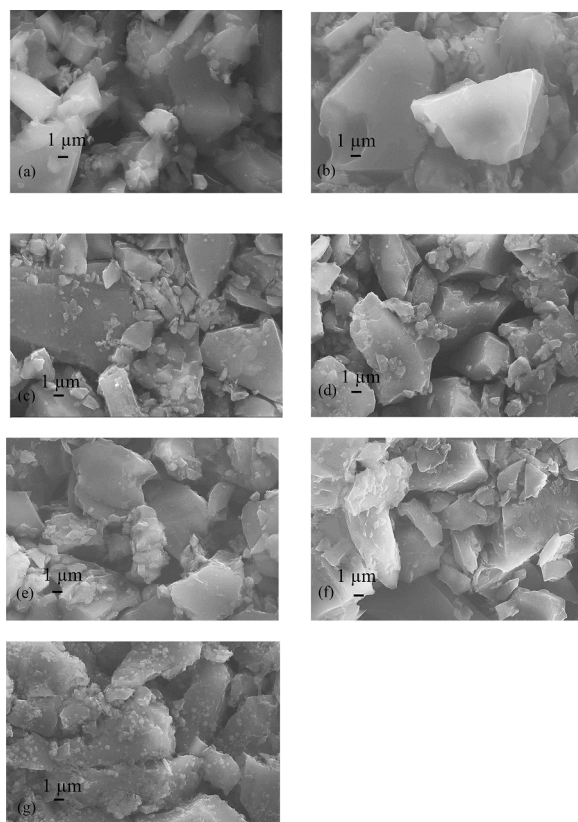
Fig. 3. SEM images of the (a) AC powder, (b) AC electrode, (c) Blank electrode, AC electrode at (d) 0 h of FVH, (e) 450 h of FVH, (f) 950 h of FVH, and (g) 1900 h of FVH. All images were taken at 10 000X magnification.

absorbed, while the slight reduction in the mesopores was due to compaction during the electrode fabrication process. The appearance of a hysteresis loop upon contact with the electrolyte (blank electrode) and further growth upon electrochemical cycling (0 h of FVH), inferred that the pore structure of the AC electrode was indeed modified by the electrochemical process.

Further reductions in surface area and pore volume were observed as the AC electrode (Blank electrode) was contacted with the electrolyte. The reductions are in accordance with the observed passivating deposits in SEM study. The AC electrode at 0 h of FVH had a remarkable increase in micropores compared to the blank electrode, although the total surface area and pore volume decreased. Therefore, the electrochemical activation process increased the micropores for charge storage and was responsible for the increased capacity retention beyond 100% in phase one [25–28]. The electrochemical activation may have opened pores that were blocked by the passivating deposits, although the decrease in total surface area and pore volume may be related to slight electrolyte degradation after the few GCD cycles. At 950 h of FVH, the surface area and pore volume decreased further, which inferred that electrolyte decomposition continued. The approximately 20% capacity loss was commensurate with the reduction in micropore volume after comparing the cumulative volume of micropores of the electrode (0.3491 cm^3/g) with the initial volume at 0 h of floating (0.4662 cm^3/g). This was expected, since the micropores were predominantly where ion adsorption and charge storage occurred. Moreover, the isotherm at 950 h of FVH was slightly modified, with a more pronounced hysteresis loop occurring within relative pressure of 0–0.4, in contrast with the barely visible hysteresis loop at 0 h of FVH. Hence, the pores were also modified by possible reactions with electrolyte degradation products such as HF and PF$_5$ that could erode active material and passivating deposits [13,29]. Furthermore, at 950 h of FVH, the electrode further broadened the pore

size distribution, with the presence of larger micropores around 1.4–1.6 nm and smaller micropores < 0.8 nm.

It was interesting to observe that the AC electrode at 1900 h of FVH still retained around 40–50% of the original surface area and pore volume. Thus, the failure in phase three could be certainly ascribed to the loss of ionic species from accelerated electrolyte degradation caused by electrode structural integrity alteration and eventual pulverization.

We further employed XPS to study the surface species evolution at different stages. The C1s spectra of the AC powder revealed the presence of six peaks at binding energies of 283.7, 284.2, 284.9, 285.5, 286.8 and 288.9 eV, corresponding to sp (C≡C), AC (C = C), CH$_x$ (C—C), C—OH, C—O and C = O surface groups (Fig. 5a). The C = C peak was characteristic of AC due to the abundant sp^2 like species and is correlated to the activation temperature [30]. The elemental composition of the AC powder was determined to be carbon (97.7%) and oxygen (2.3%). The C1s spectra of the AC electrode (Fig. 5b) revealed similar peaks as the AC powder but with a new peak at 291.9 eV, corresponding to the CF$_2$ group from the PTFE binder. The oxygenated functionalities on AC are responsible for electrolyte degradation and the passivating deposits observed at the surface of the blank electrode (Fig. 3c) [11,12,24].

The deconvoluted C1s, F1s and P2p spectra of electrodes after contact with the electrolyte are presented in Fig. 6. The C1s spectra of the blank electrode (Fig. 6a) showed peaks at 284.2, 286.5, 288.2, 290.1 and 291.9 eV, assigned to the C = C, C—O, C = O, CO$_3$ and CF$_2$ groups. The disappearance of the sp peak indicate that some carbon species were reacted. It is also interesting to see that the asymmetric conducting carbon shape was modified, and the PTFE intensity was increased in comparison to the C1s spectra of the AC electrode (Fig. 5b). The increased CF$_2$ intensity suggests that contact with the electrolyte exposed more PTFE at the surface after reacting with the oxygenated carbon species on the AC electrode. In the P2p spectra, Li$_x$PO$_y$F$_z$ and polyphosphates were identified at 133.7 and 235.5 eV, while LiF, Li$_x$PO$_y$F$_z$ and CF$_2$ species were identified at 685.1, 686.4 and 689.1 eV in the F1s spectra. These species together with the oxygenated carbon species are the products of LiPF$_6$ and the carbonate solvent decomposition after nucleophilic attack by surface oxygen species and moisture in the pores. Moreover, the LiF species could also come from the ion paired LiPF$_6$. LiF and PF$_5$ are the equilibrium decomposition products of ion paired LiPF$_6$, which is commonly present in incompletely dissociated LiPF$_6$ [13,17,31]. PF$_5$ is also responsible for inducing solvent degradation and other parasitic reactions that may form HF, which is detrimental to active material and interfacial stability [13,17,31].

The diminished AC peak in the C1s spectra for the electrode at 0 h of FVH (Fig. 6a) and the increase of the PTFE peak and oxygenated carbons are ascribed to surface passivation and continued electrolyte salt and carbonate solvent decomposition. Furthermore, the F1s and P2p spectra of the electrode at 0 h of FVH (Fig. 6b and c) showed increased intensities of LiF and phosphate species, confirming enhanced electrolyte degradation after the few GCD cycles. This correlates with the reduced surface area from the nitrogen physisorption analysis.

The C1s spectra of the electrodes after 450 h of FVH and at 950 h of FVH exhibited similar oxygenated carbon species. The further diminished AC peak signified intense surface coverage of the electrode, while the increased CF$_2$ band suggested exposed/exfoliated binder after surface restructuring. The P2p and F1s spectra showed increased presence of phosphates, Li$_x$PO$_y$F$_z$ and LiF, with the latter being the dominant specie. Thus, the capacity fade observed in phase three was caused by enhanced anion decomposition. This was in combination with restricted access of the already depleted ionic moieties to the pores of the AC electrode with decreased pore volumes.

At 1900 h of FVH, it was interesting to see that the intensity of AC was significantly increased, in comparison with the electrode after 950 h of FVH. We speculate that this may be related to the spherical amorphous specie observed in SEM (Fig. 3g) or caused by AC electrode pulverization from possible binder degradation. Moreover, the disappearance of the CF$_2$ band at 1900 h of FVH suggested that either
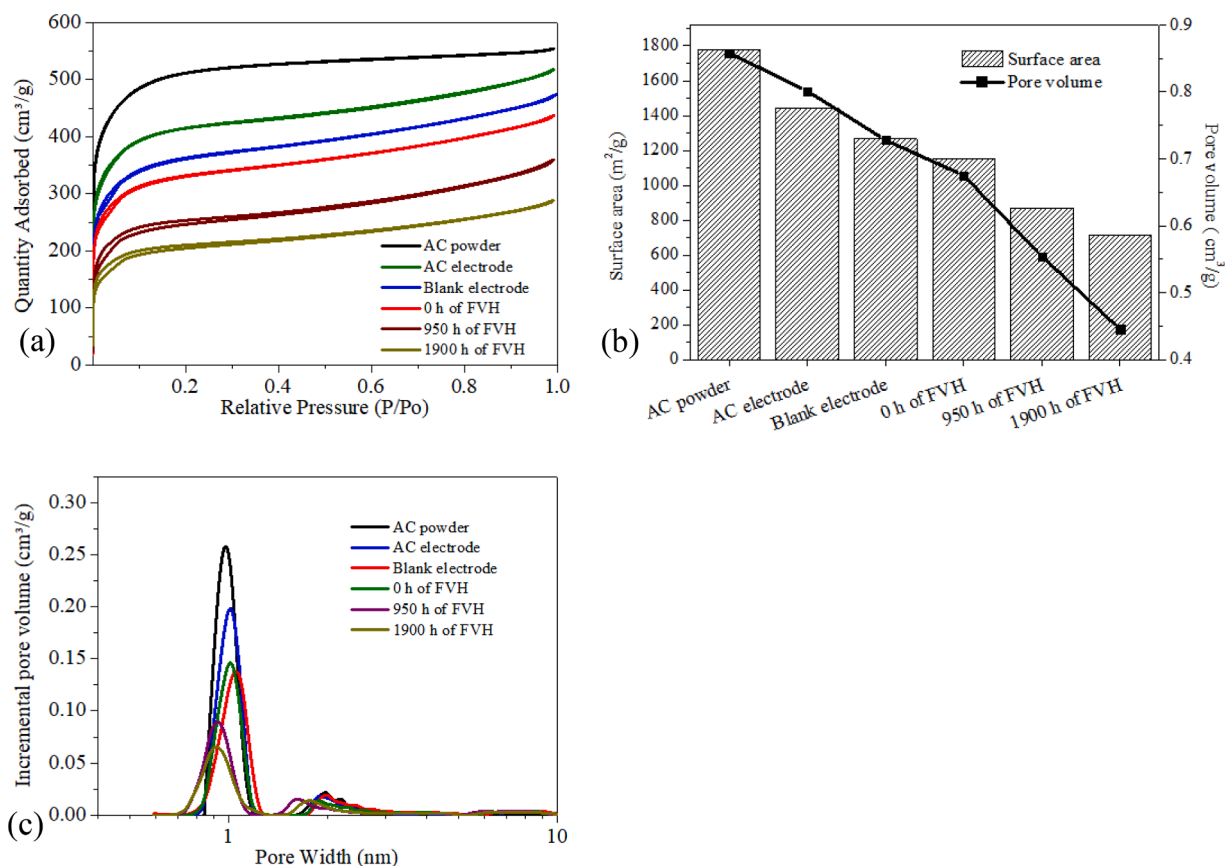
Fig. 4. (a) Nitrogen adsorption and desorption isotherms, (b) BET Surface area and pore volume, (c) Pore size distributions of AC powder and different AC electrodes.
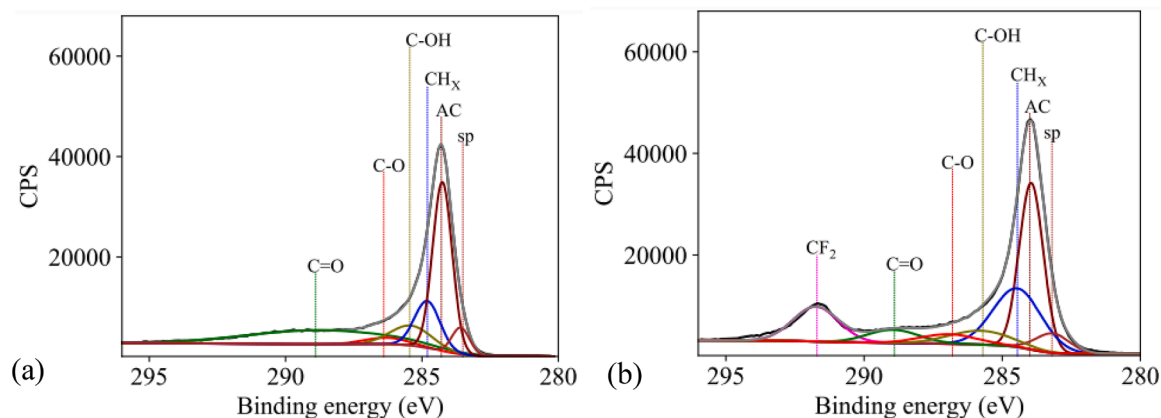

Fig. 5. Deconvoluted C1s spectra of (a)AC powder, (b) AC electrode.

the AC electrode surface was completely covered by this newly deposited amorphous carbon, or the PTFE binder reacted with adsorbed lithium on the surface of the electrode. Although PTFE is known to be very stable and unreactive, it could be reduced upon contact with lithium to form an amorphous carbon specie and LiF, as shown below [29]:

$$-(-CF_2-)_n- +2n\,Li \rightarrow n\,C\,(amorphous) + 2n\,LiF$$
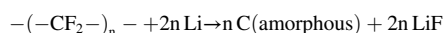
The presence of AlO_xF_y species in the F1s spectra at 1900 h of FVH (Fig. 6b) supports fluorinated attack of the current collector, which could indicate the pulverization of the AC electrode. Meanwhile, the increased $Li_xPO_yF_z$ and phosphates species signify total salt degradation at 1900 h of FVH (Fig. 6c).

Raman spectroscopy was conducted to investigate changes in graphitic order and defects during floating. The spectra were deconvoluted using origin software and exhibited five peaks as illustrated in Fig. 7a. The two prominent peaks at around 1350 and 1580 cm^{-1} are the characteristic D and G bands. The latter is attributed to the in-plane vibrations of sp^2 hybridized carbon, while the former is attributed to out of plane vibrations arising from structural defects and multiphases in the carbon structure [32]. The D_1 band at 1179 cm^{-1} is assigned to impurities in the graphitic lattice, while the D_2 band at 1493 cm^{-1} corresponds to the stacking defects in the graphene layer [32] and the presence of sp^2 amorphous carbon [33]. The D_3 band at 1653 cm^{-1} is assigned to disorder in the surface graphene layers [32,34,35].

The defect ratio was calculated from the intensities of the D and G band (Fig. 7b). The defect level increased as the AC powder was
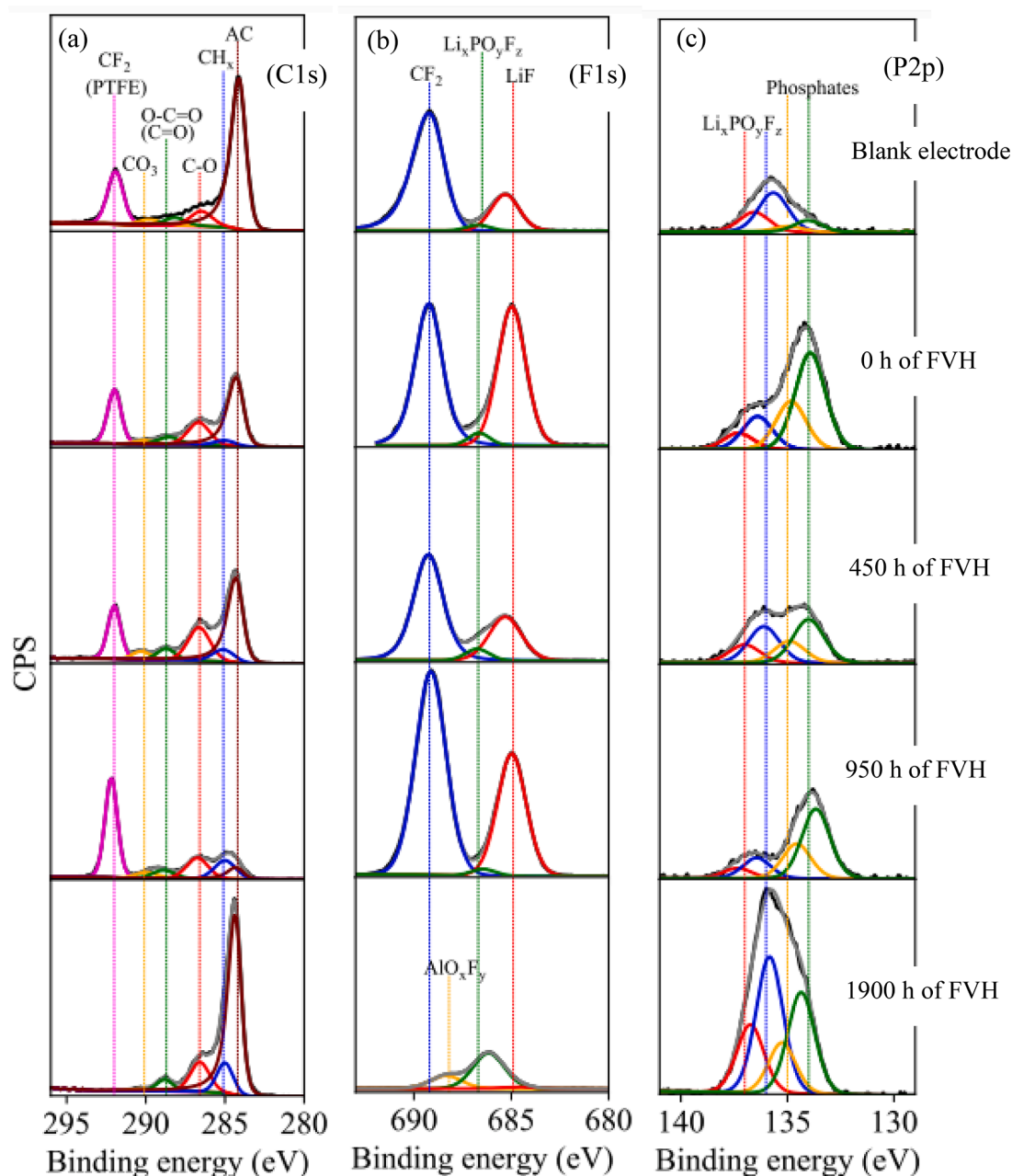
Fig. 6. Deconvoluted XPS spectra showing the (a) C1s, (b) P2p, and (c) F1s peaks of the AC electrode at different stages of FVH after contact with the electrolyte.

transformed to the AC electrode and subjected to electrochemical cycling. The defects originated from PTFE addition and deposits of electrolyte degradation products at the AC surface. Moreover, the decrease in the defect ratio after 450 h of FVH was caused by increased graphitization as evidenced by the band intensities (Fig. 7c). The band intensities in Fig. 7c showed that the D and G band increased in a continuous trend until the plateau at 450 h of FVH. Beyond this point, increased D_2 bands were responsible for the increased defects since the other defective bands (D_1 and D_3) remained relatively the same.

At 950 h of FVH, the defect ratio increased again and reached maximum after 1900 h of FVH. Hence, increased defects also contributed to the capacity fade. The increased defect level is synonymous with increased electrode resistance and reduced particle to particle conductivity [36]. Moreover, the continuously increasing D_2 band at 950 h and 1900 h of FVH meant that the stacking defects in the graphitized carbon structure was significant. Besides, it might also be related to the increased presence of sp^2 carbons formed after electrochemical

oxidization of the AC electrode by electrolyte species or binder exfoliation and electrode pulverization discussed earlier.

4. Conclusion

The causes of capacity fade in LiC have been investigated via a combination of intermittent EIS during floating voltage ageing and post-mortem characterization of the AC electrode at different electrochemical states. Three phases were identified during the floating voltage that corresponded to different electrochemical processes occurring in the cell in relation to the capacity fade. The first phase was assigned to the modification of the formed passivating deposits on the electrodes that permitted increased access of electrolyte species into the pores and the observed rise in capacity. The second phase marked the effect of electrolyte decomposition with gradual decrease in capacity, which was caused by PF_6 anion and other electrolyte species degradation. Here, the passivating deposits was built up progressively by the deposition of
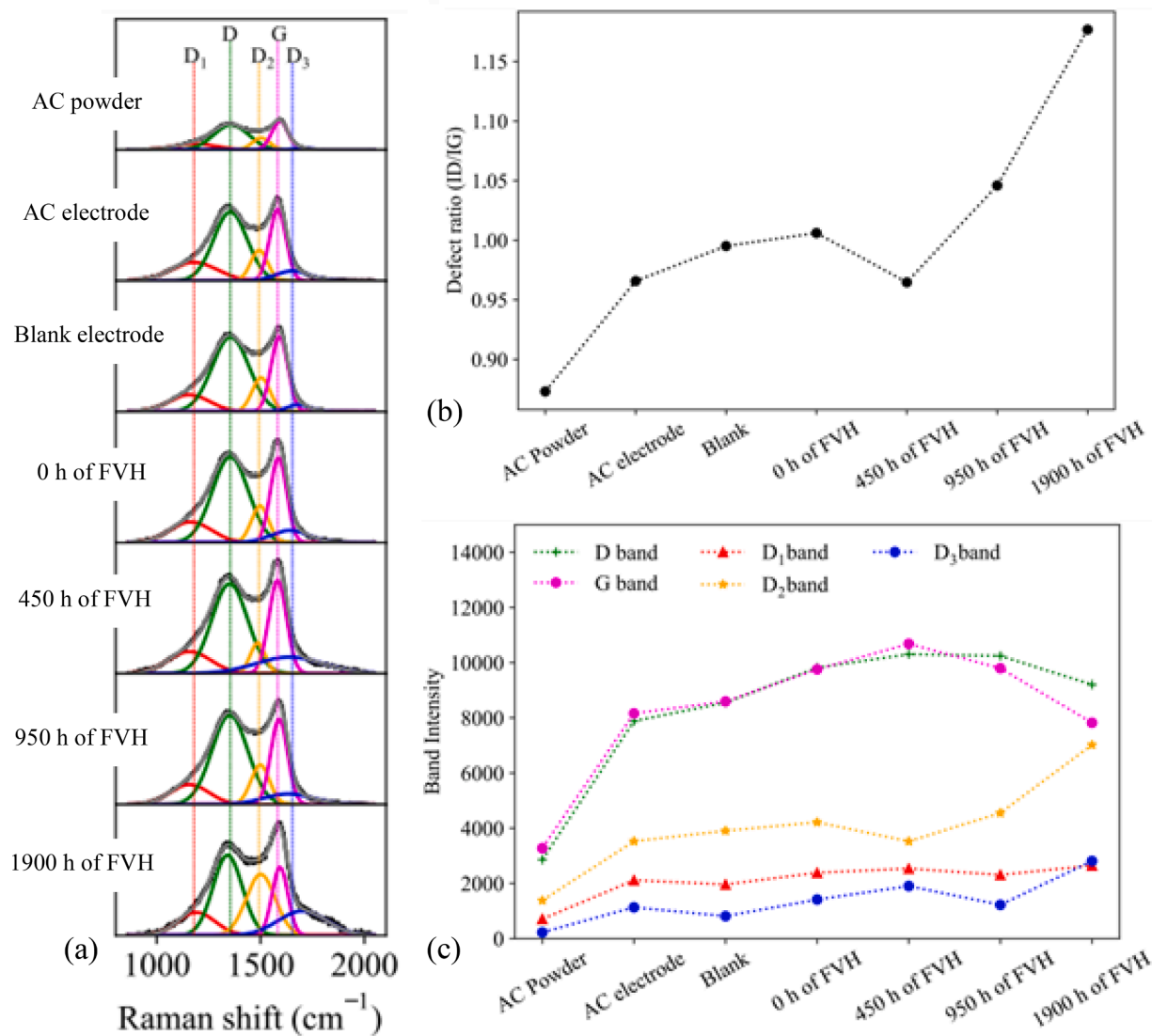
Fig. 7. (a) Deconvoluted Raman spectra, (b) Defect ratio, and (c) Comparison of band intensities of the activated carbon electrode at different stages. The I_d/I_g ratio was calculated from the intensity of the D and G bands.

degradation products. XPS study showed that the products consist of oxygenated carbon species, lithium fluorophosphates, lithium fluoride and polyphosphate species. Their presence resulted in the gradual reduction of available surface area of the AC electrode. In the third phase, electrolyte degradation was accelerated with a steep 45-degree slope in capacity reduction. We suppose that a combination of increased degradation products such as HF and PF_5 were responsible for catalysing solvent degradation and eventual depletion of the electrolyte moieties. Furthermore, the electrode at 80% capacity retention had increased phosphates and lithium fluoride as well as diminished AC peak, which suggested severe surface coverage by insoluble degradation products. Other factors such as increased defect ratio and growth of defective bands consisting of sp^2 hybridized species were possible contributors to the capacity fade via reduced conductivity.

We propose that strategies towards extending the cyclic stability and delaying the electrolyte degradation on AC cathodes should be targeted at improving the anion oxidation resistance. That would reduce the deposition of polyphosphates and other anion/$LiPF_6$ salt degradation products on the surface of the AC. Further measures could be the incorporation of additives to improve $LiPF_6$ dissociation and reduce ion pairing, additives for PF_5 and HF scavenging, incorporation of alternative anions with superior electrochemical stabilities, and solvent optimization to improve anion stability. These approaches could extend the phase one region in the capacity retention profile after engineering the passivation layer to be sufficiently resistive towards attack by degradations products. The added benefit of delaying the transition towards phase two where anion degradation commences in full could also be attained.

CRediT authorship contribution statement

Obinna Egwu Eleri: Conceptualization, Data curation, Formal analysis, Investigation, Visualization, Methodology, Writing – original draft, Writing – review & editing. **Frederik Huld:** Formal analysis, Investigation, Methodology, Writing – review & editing. **Julie Pires:** Formal analysis, Investigation, Methodology, Validation, Writing – review & editing. **Wakshum Mekonnen Tucho:** Investigation, Formal analysis, Resources, Methodology. **Philipp Schweigart:** Investigation, Validation, Writing – review & editing. **Ann Mari Svensson:** Resources, Validation, Writing – review & editing. **Fengliu Lou:** Conceptualization, Funding acquisition, Methodology, Validation, Resources, Project administration, Supervision, Writing – review & editing. **Zhixin Yu:** Validation, Funding acquisition, Resources, Project administration, Supervision, Writing – review & editing.

Declaration of Competing Interest

The authors declare that they have no known competing financial interests or personal relationships that could have appeared to influence the work reported in this paper.

Data availability

Data will be made available on request.

Acknowledgements

Supplementary materials

Supplementary material associated with this article can be found, in the online version, at doi:10.1016/j.electacta.2023.142359.

References

[1] G.G. Amatucci, F. Badway, A. Du Pasquier, T. Zheng, An asymmetric hybrid nonaqueous energy storage cell, J. Electrochem. Soc. 148 (8) (2001) A930.

[2] K. Naoi, S. Ishimoto, J.-i. Miyamoto, W. Naoi, Second generation 'nanohybrid supercapacitor': evolution of capacitive energy storage devices, Energy Environ. Sci. 5 (11) (2012) 9363–9373.

[3] S.R. Sivakkumar, A. Pandolfo, Evaluation of lithium-ion capacitors assembled with pre-lithiated graphite anode and activated carbon cathode, Electrochim. Acta 65 (2012) 280–287.

[4] S. Dsoke, Expanding the Cathodic Potential Window of Activated Carbon Electrodes in a Lithium-Salt Containing Electrolyte, Batteries Supercaps. 1 (6) (2018) 215–222.

[5] O.E. Eleri, K.U. Azuatalam, M.W. Minde, A.M. Trindade, N. Muthuswamy, F. Lou, Z. Yu, Towards high-energy-density supercapacitors via less-defects activated carbon from sawdust, Electrochim. Acta 362 (2020), 137152.

[6] H.-f. Xia, B. Zhang, C.-h. Wang, L. Cao, B. Luo, X.-m. Fan, J.-f. Zhang, X. Ou, Surface engineered carbon-cloth with broadening voltage window for boosted energy density aqueous supercapacitors, Carbon N Y 162 (2020) 136–146.

[7] L. Xing, X. Zheng, M. Schroeder, J. Alvarado, A. von Wald Cresce, K. Xu, Q. Li, W. Li, Deciphering the ethylene carbonate–propylene carbonate mystery in Li-ion batteries, Acc. Chem. Res. 51 (2) (2018) 282–289.

[8] S.-T. Myung, Y. Sasaki, S. Sakurada, Y.-K. Sun, H. Yashiro, Electrochemical behavior of current collectors for lithium batteries in non-aqueous alkyl carbonate solution and surface analysis by ToF-SIMS, Electrochim. Acta 55 (1) (2009) 288–297.

[9] M. Tokita, N. Yoshimoto, K. Fujii, M. Morita, Degradation characteristics of electric double-layer capacitors consisting of high surface area carbon electrodes with organic electrolyte solutions, Electrochim. Acta 209 (2016) 210–218.

[10] Z. Ding, V. Trouillet, S. Dsoke, Are functional groups beneficial or harmful on the electrochemical performance of activated carbon electrodes? J. Electrochem. Soc. 166 (6) (2019) A1004.

[11] F. Béguin, V. Presser, A. Balducci, E. Frackowiak, Carbons and electrolytes for advanced supercapacitors, Adv. Mater. 26 (14) (2014) 2219–2251.

[12] D. Stępień, Z. Zhao, S. Dsoke, Shift to post-li-ion capacitors: electrochemical behavior of activated carbon electrodes in li-, na-and k-salt containing organic electrolytes, J. Electrochem. Soc. 165 (12) (2018) A2807.

[13] J.G. Han, K. Kim, Y. Lee, N.S. Choi, Scavenging materials to stabilize LiPF6-containing carbonate-based electrolytes for Li-ion batteries, Adv. Mater. 31 (20) (2019), 1804822.

[14] C.L. Campion, W. Li, B.L. Lucht, Thermal decomposition of LiPF6-based electrolytes for lithium-ion batteries, J. Electrochem. Soc. 152 (12) (2005) A2327.

[15] H. Yang, G.V. Zhuang, P.N. Ross Jr, Thermal stability of LiPF6 salt and Li-ion battery electrolytes containing LiPF6, J. Power Sources 161 (1) (2006) 573–579.

[16] M.M. Thackeray, S.-.H. Kang, C.S. Johnson, J.T. Vaughey, R. Benedek, S. Hackney, Li 2 MnO 3-stabilized LiMO 2 (M= Mn, Ni, Co) electrodes for lithium-ion batteries, J. Mater. Chem. 17 (30) (2007) 3112–3125.

[17] O. Borodin, W. Behl, T.R. Jow, Oxidative stability and initial decomposition reactions of carbonate, sulfone, and alkyl phosphate-based electrolytes, J. Phys. Chem. C 117 (17) (2013) 8661–8682.

[18] P. Azaïs, L. Duclaux, P. Florian, D. Massiot, M.-.A. Lillo-Rodenas, A. Linares-Solano, J.-.P. Peres, C. Jehoulet, F. Béguin, Causes of supercapacitors ageing in organic electrolyte, J. Power Sources 171 (2) (2007) 1046–1053.

[19] P. Ruch, D. Cericola, A. Foelske, R. Kötz, A. Wokaun, A comparison of the aging of electrochemical double layer capacitors with acetonitrile and propylene carbonate-based electrolytes at elevated voltages, Electrochim. Acta 55 (7) (2010) 2352–2357.

[20] Y. Liu, B. Soucaze-Guillous, P.-.L. Taberna, P. Simon, Understanding of carbon-based supercapacitors ageing mechanisms by electrochemical and analytical methods, J. Power Sources 366 (2017) 123–130.

[21] Z. Shi, J. Zhang, J. Wang, J. Shi, C. Wang, Effect of the capacity design of activated carbon cathode on the electrochemical performance of lithium-ion capacitors, Electrochim. Acta 153 (2015) 476–483.

[22] X. Sun, X. Zhang, W. Liu, K. Wang, C. Li, Z. Li, Y. Ma, Electrochemical performances and capacity fading behaviors of activated carbon/hard carbon lithium ion capacitor, Electrochim. Acta 235 (2017) 158–166.

[23] K. Guo, S. Qi, H. Wang, J. Huang, M. Wu, Y. Yang, X. Li, Y. Ren, J. Ma, High-Voltage Electrolyte Chemistry for Lithium Batteries, Small Science 2 (5) (2022), 2100107.

[24] C. Tran, J. Kafle, X.-.Q. Yang, D. Qu, Increased discharge capacity of a Li-air activated carbon cathode produced by preventing carbon surface passivation, Carbon N Y 49 (4) (2011) 1266–1271.

[25] T. Zhang, B. Fuchs, M. Secchiaroli, M. Wohlfahrt-Mehrens, S. Dsoke, Electrochemical behavior and stability of a commercial activated carbon in various organic electrolyte combinations containing Li-salts, Electrochim. Acta 218 (2016) 163–173.

[26] M.M. Hantel, T. Kaspar, R. Nesper, A. Wokaun, R. Kötz, Partially reduced graphite oxide for supercapacitor electrodes: effect of graphene layer spacing and huge specific capacitance, Electrochem. Commun. 13 (1) (2011) 90–92.

[27] S. Mitani, S.-.I. Lee, K. Saito, S.-.H. Yoon, Y. Korai, I. Mochida, Activation of coal tar derived needle coke with K2CO3 into an active carbon of low surface area and its performance as unique electrode of electric double-layer capacitor, Carbon 43 (14) (2005) 2960–2967.

[28] T. Aida, I. Murayama, K. Yamada, M. Morita, High-energy-density hybrid electrochemical capacitor using graphitizable carbon activated with KOH for positive electrode, J. Power Sources 166 (2) (2007) 462–470.

[29] J. Kim, J.G. Lee, H.-s. Kim, T.J. Lee, H. Park, J.H. Ryu, S.M. Oh, Thermal degradation of solid electrolyte interphase (SEI) layers by phosphorus pentafluoride (PF5) attack, J. Electrochem. Soc. 164 (12) (2017) A2418.

[30] A. Lazzarini, A. Piovano, R. Pellegrini, G. Leofanti, G. Agostini, S. Rudić, M. R. Chierotti, R. Gobetto, A. Battiato, G. Spoto, A comprehensive approach to investigate the structural and surface properties of activated carbons and related Pd-based catalysts, Catal Sci Technol 6 (13) (2016) 4910–4922.

[31] D.M. Seo, O. Borodin, S.-.D. Han, Q. Ly, P.D. Boyle, W.A. Henderson, Electrolyte solvation and ionic association, J. Electrochem. Soc. 159 (5) (2012) A553.

[32] W. Chen, X. Zhou, S. Shi, N. Thiphuong, M. Chen, Synergistical enhancement of the electrochemical properties of lignin-based activated carbon using NH 3· H 2 O dielectric barrier discharge plasma, RSC Adv. 7 (12) (2017) 7392–7400.

[33] T. Jawhari, A. Roid, J. Casado, Raman spectroscopic characterization of some commercially available carbon black materials, Carbon N Y 33 (11) (1995) 1561–1565.

[34] A. Sadezky, H. Muckenhuber, H. Grothe, R. Niessner, U. Pöschl, Raman microspectroscopy of soot and related carbonaceous materials: spectral analysis and structural information, Carbon 43 (8) (2005) 1731–1742.

[35] M.A.d. Amaral, J.T. Matsushima, M.C. Rezende, E.S. Gonçalves, J.S. Marcuzzo, M. R. Baldan, Production and characterization of activated carbon fiber from textile PAN fiber, J. Aerospace Technol. Manag. 9 (2017) 423–430.

[36] P.T. Araujo, M. Terrones, M.S. Dresselhaus, Defects and impurities in graphene-like materials, Mater. Today 15 (3) (2012) 98–109.

Supporting information

Revealing mechanisms of activated carbon capacity fade in Lithium-ion capacitors

Obinna Egwu Eleri [a,b], Frederik Huld[a,b], Julie Pires[a], Wakshum Mekonnen Tucho[c], Philipp Schweigart[d], Ann Mari Svensson[d], Fengliu Lou[a*] and Zhixin Yu[b*]

[a] *Beyonder AS, 4313 Sandnes, Norway*

[b] *Department of Energy and Petroleum Engineering, University of Stavanger, 4036 Stavanger, Norway*

[c] *Department of Machine, Building and Materials Technology Laboratory IMBM, University of Stavanger, 4036 Stavanger, Norway*

[d] *Department of Materials Science and Engineering, Norwegian University of Science and Technology, 7491 Trondheim, Norway*

Corresponding authors[*]

ZY: zhixin.yu@uis.no

FL: fengliu@beyonder.no

Table S1: EIS fitting parameters from the AC/Li half-cell after different durations of floating voltage hold; CPE1 and CPE2 are the constant phase elements associated with the passivation layer and charge transfer ion diffusion.

| Time (h)	Rs (Ω)	Rp (Ω)	CPE1_0 (F)	CPE1_1	Rct (Ω)	CPE2_0 (F)	CPE2_1	W (Ω)	C (F)
0	3.2000	21.9000	0.0001	0.7810	16.7000	0.0135	0.6980	2.9500	3.2300
100	2.9600	4.9000	0.0008	0.5900	7.2500	0.0252	0.8290	2.7200	4.4900
200	3.0400	5.0300	0.0004	0.6780	6.5700	0.0292	0.7990	2.1600	2.5500
300	4.4900	4.7200	0.0007	0.6030	6.2500	0.0375	0.7740	1.5200	2.0900
400	4.9000	4.6900	0.0008	0.6020	4.3800	0.0320	0.8280	2.3700	3.3300
500	5.0100	5.9600	0.0005	0.6740	5.3900	0.0352	0.8290	1.9500	2.2000
600	5.3800	6.3300	0.0004	0.6940	5.3700	0.0380	0.8400	1.9700	2.2400
700	6.8200	5.6600	0.0002	0.8040	6.1000	0.0345	0.7940	1.9600	2.1300
800	7.7900	6.8300	0.0002	0.8080	7.0300	0.0336	0.8050	1.8400	1.8200
900	12.6000	6.5700	0.0003	0.7510	6.8500	0.0318	0.7510	2.0500	2.0800
950	14.5000	7.5100	0.0002	0.7850	8.4200	0.0292	0.7420	2.4400	2.4300
1000	19.4000	8.7200	0.0002	0.7710	8.5500	0.0322	0.7180	2.1600	2.2700
1100	23.0000	8.9500	0.0002	0.7600	8.6300	0.0330	0.7180	2.1100	1.9800
1200	30.1000	10.0000	0.0002	0.7300	9.8900	0.0302	0.6610	2.5200	2.4400
1300	45.4000	13.7000	0.0002	0.7540	10.7000	0.0349	0.6670	2.0400	1.5800
1400	47.8000	15.9000	0.0003	0.6820	12.3000	0.0263	0.6410	2.8900	2.2000
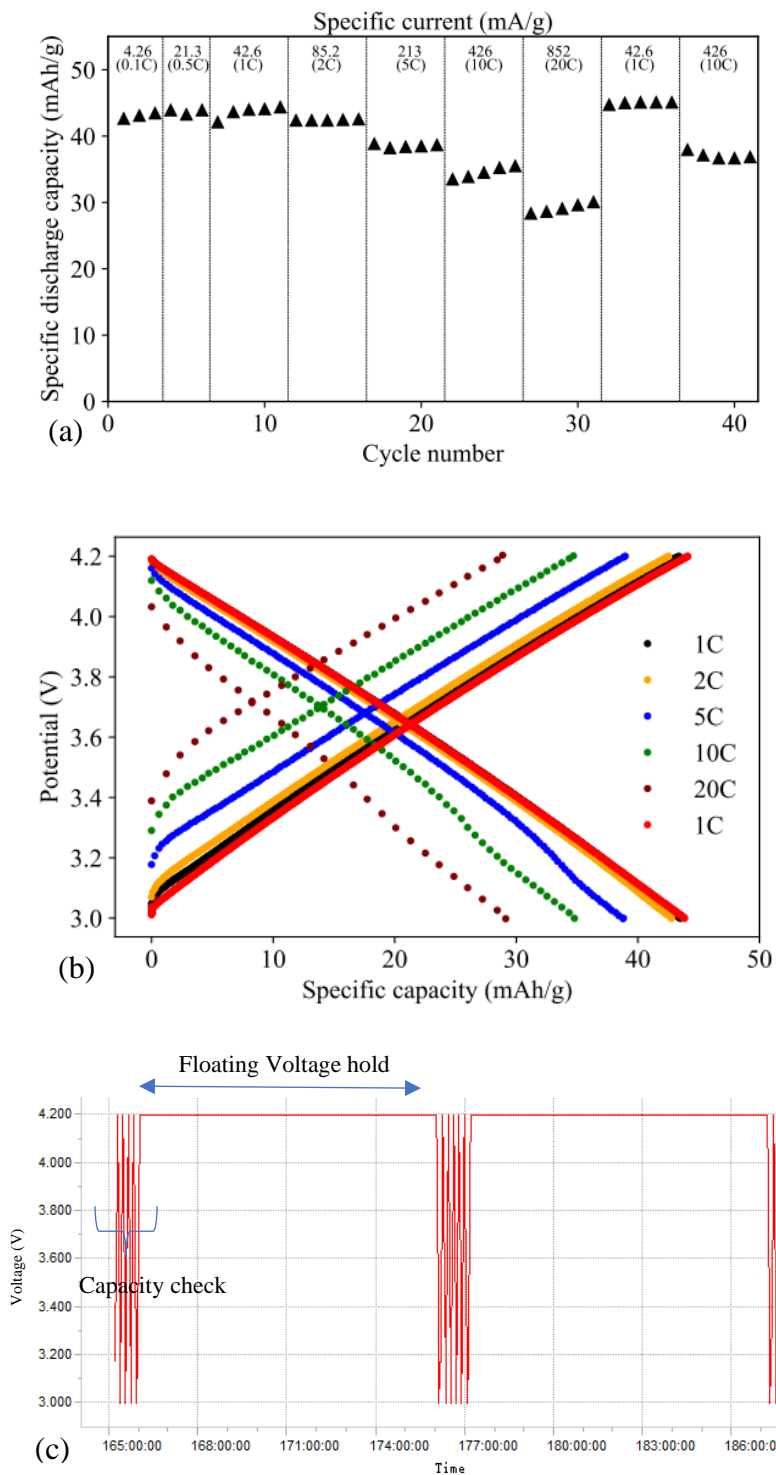
Figure S1: Results from the galvanostatic charge and discharge analysis (a) Rate performance at various C-rates, (b) Capacity plots at various C-rates, (c) Floating voltage protocol. The red 1C in Figure 1b represents the recovery cycles, after which the floating voltage hold sequence commenced from cycle 36 with the initial capacity checks at 10 C.
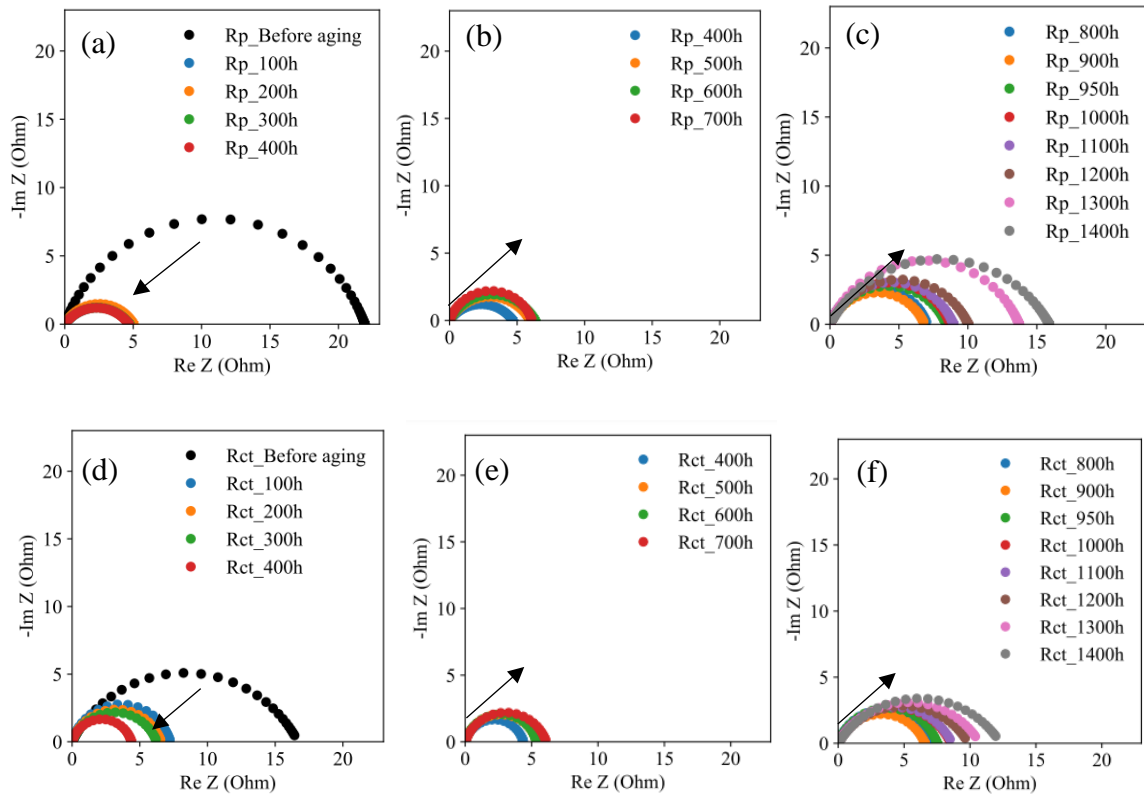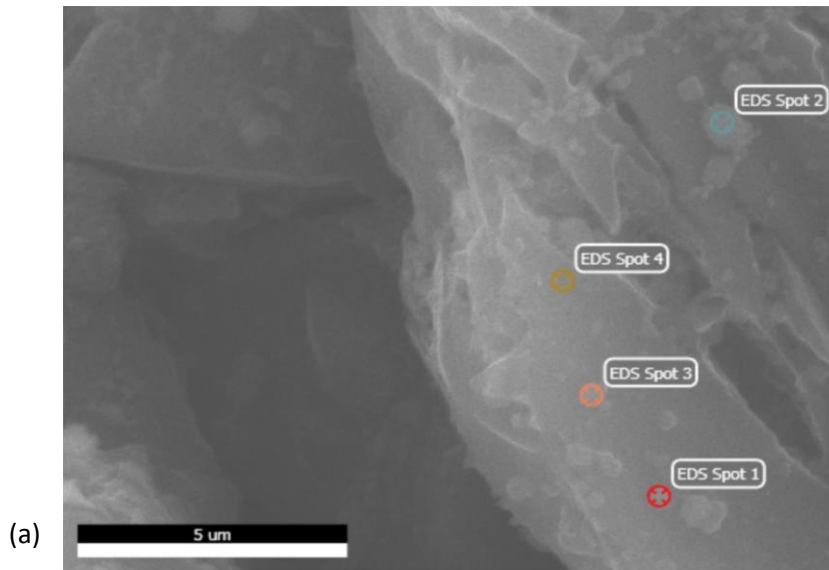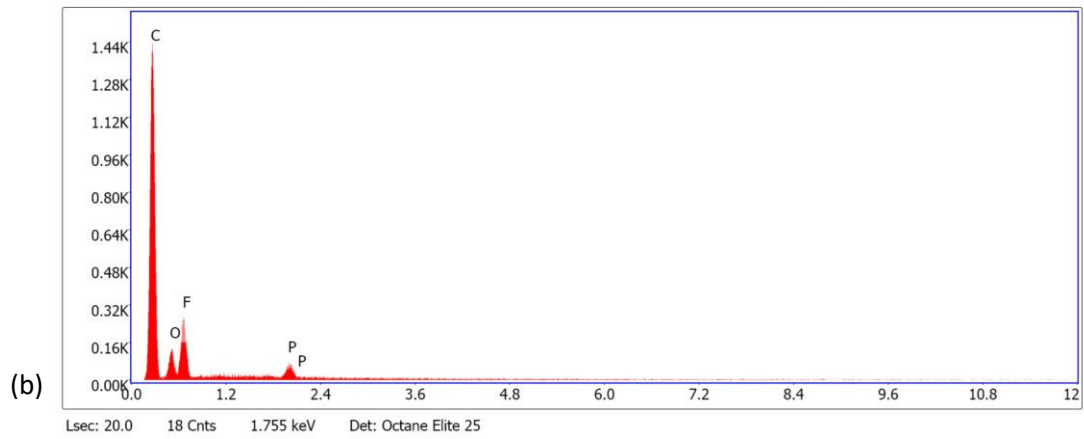
Figure S2: Deconvoluted R-CPE loops obtained after fitting. (a), (b) and (c) Passivation layer (Rp) impedance in Phase one, two and three; and (d), (e) and (f) Charge transfer impedance (Rct) in Phase one, two and three. "Before aging" represents 0 h of floating.

(a)

EDS Spot 1

(b)

Lsec: 20.0   18 Cnts   1.755 keV   Det: Octane Elite 25

eZAF Smart Quant Results

Element	Weight %	Atomic %	Net Int.	Error %	Kratio	Z	A	F
C K	74.91	81.93	1028.14	5.54	0.4959	1.0242	0.6465	1.0000
O K	9.35	7.68	73.86	15.54	0.0179	0.9732	0.1970	1.0000
F K	13.88	9.60	193.17	10.87	0.0383	0.9021	0.3058	1.0000
P K	1.86	0.79	51.22	11.10	0.0152	0.8376	0.9671	1.0073

(c)

EDS Spot 2

(d)

Lsec: 20.0   22 Cnts   1.755 keV   Det: Octane Elite 25
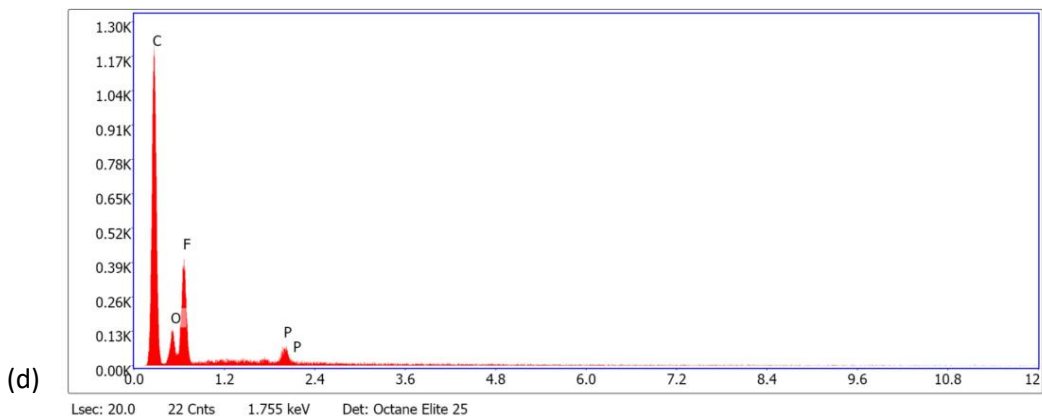
Element	Weight %	Atomic %	Net Int.	Error %	Kratio	Z	A	F
C K	69.34	77.72	868.34	6.24	0.4243	1.0318	0.5931	1.0000
O K	8.38	7.05	70.39	17.07	0.0173	0.9806	0.2107	1.0000
F K	20.24	14.35	299.67	10.04	0.0602	0.9090	0.3270	1.0000
P K	2.03	0.88	55.02	10.99	0.0165	0.8441	0.9569	1.0067

(e)

EDS Spot 3

(f)

Lsec: 20.0   22 Cnts   1.755 keV   Det: Octane Elite 25
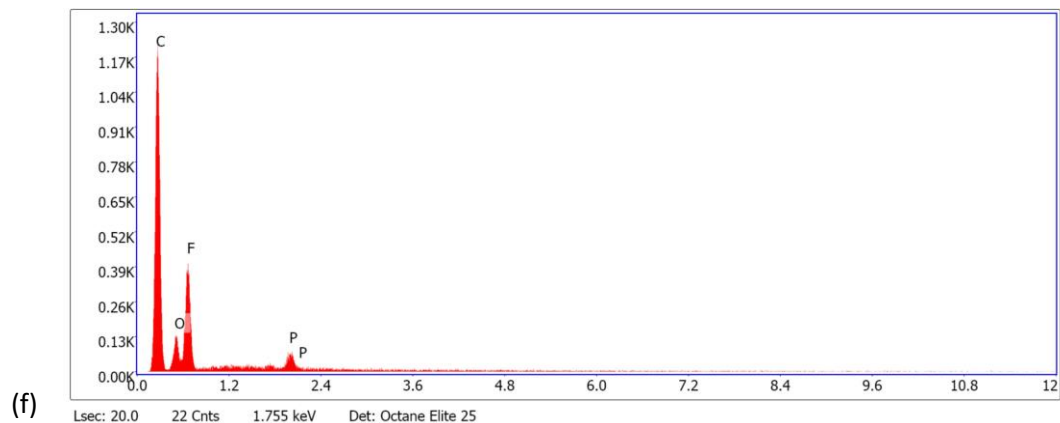
eZAF Smart Quant Results

Element	Weight %	Atomic %	Net Int.	Error %	Kratio	Z	A	F
C K	77.21	83.76	1063.66	5.41	0.5205	1.0218	0.6598	1.0000
O K	8.73	7.11	65.86	17.44	0.0162	0.9710	0.1914	1.0000
F K	12.11	8.30	164.20	11.23	0.0330	0.9000	0.3030	1.0000
P K	1.95	0.82	53.08	11.51	0.0160	0.8357	0.9709	1.0074

(g)

EDS Spot 4

(h)
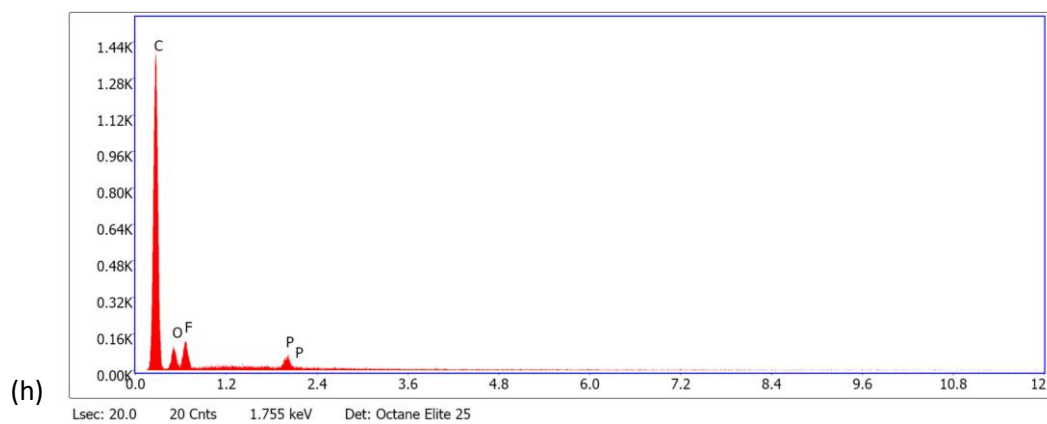
Element	Weight %	Atomic %	Net Int.	Error %	Kratio	Z	A	F
C K	81.35	86.84	997.72	5.11	0.5721	1.0169	0.6916	1.0000
O K	8.81	7.06	53.73	18.02	0.0155	0.9662	0.1823	1.0000
F K	7.76	5.24	86.12	13.39	0.0203	0.8955	0.2919	1.0000
P K	2.08	0.86	48.31	11.95	0.0170	0.8314	0.9786	1.0077

(i)

Figure S3(a-i): EDX quantification of the spherical spots observed in the electrode after 1900 h of FVH (at 0% capacity retention).

Appendix C - Paper III and supplementary information

Enhanced activated carbon lithium-ion capacitor electrochemical stability through electrolyte dielectric optimisation

O. E. Eleri, J. Pires, F. T. Huld, S. Lu, P. Schweigart, A. M. Svensson, F. Lou, and Z. Yu.

Sustainable Energy & Fuels, 2023, 7(8), 1846-1854.

DOI: 10.1039/D3SE00122A

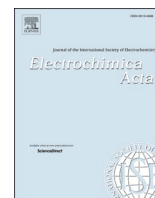**This paper is not included in the repository due to copyright restrictions**

Appendix D - Paper IV and supplementary information

Deciphering electrolyte dielectric extended electrochemical stability in lithium-ion capacitors.

O. E. Eleri, F. T. Huld, F. Lou, and Z. Yu.

Electrochimica Acta, 2023, 464, 142960.

DOI: 10.1016/j.electacta.2023.142960

Deciphering electrolyte dielectric extended electrochemical stability in lithium-ion capacitors

Obinna Egwu Eleri [a,b], Frederik T Huld [a,b], Fengliu Lou [b,*], Zhixin Yu [a,*]

[a] *Department of Energy and Petroleum Engineering, University of Stavanger, 4036 Stavanger, Norway*
[b] *Beyonder AS, Stokkamyrveien 30, 4313 Sandnes, Norway*

ARTICLE INFO

ABSTRACT

Solvent properties dominate the characteristics of electrode-electrolyte interfaces and hence influence the performance of lithium-ion capacitors (LiC). In this work, we demonstrate that the electrolyte dielectric influences the electrochemical stability of activated carbon(AC)/hard carbon(HC) LiC. Electrode interfaces from different 1 M $LiPF_6$ electrolyte formulations with varying dielectric are probed after stability tests using floating voltage holds (FVH) and galvanostatic charge and discharge (GCD) analysis. The electrode interfacial impedance was inversely proportional to electrolyte dielectric, with a more severe effect on the AC cathode than on the HC anode. Furthermore, surface morphology investigations and species characterisation with SEM and XPS revealed decreased degradation at the electrode surfaces as the electrolyte dielectric was increased. Overall, high electrolyte dielectric improved the electrolyte stability by delaying the PF_6^- anion degradation and detrimental byproduct formation through decreased ion-pairing and increased PF_6^- solvation shell resistance to oxidation. These findings are important for developing electrolytes for high-power and long-cycle life LiCs.

1. Introduction

LiC have received considerable attention in recent years due to their unique ability to possess superior energy densities than supercapacitors (SC) and higher power densities than lithium-ion batteries (LiB) [1,2]. These properties enable LiC to function as hybrid energy storage devices for applications requiring high power and energy density synergies.

The advantages of LiC arise from the device architecture, which involves cathodes from SC (such as activated carbon, AC), anodes from LiB (such as graphite and hard carbon, HC) and typical high-voltage organic LiB electrolytes to realise extended operating voltage windows [1–5]. The AC cathode enables high power, while the LiB anodes and the electrolyte contribute to the higher energy density [1,2]. Electrolytes for LiC typically consist of lithium salts ($LiPF_6$) dissolved in a mixture of cyclic and linear carbonate solvents such as ethylene carbonate (EC) and dimethyl carbonate (DMC) or ethyl methyl carbonate (EMC), and often with small amounts of additives [6]. The electrolyte constituents can influence the electrode interface stability, operating voltage window, operating temperature window, cellular components passivation, ion transport and active species population [7–10]. These factors determine the realisable specific energy, specific power, and cycle life of LiCs.

In most electrolyte formulations for different lithium-ion chemistries, EC has remained indispensable primarily due to the high dielectric ($\mathcal{E} = 89$) for salt dissociation, good conductivity and surface passivation ability of thermodynamically unstable electrodes [9]. However, the high viscosity of EC and relatively solid nature at room temperature necessitates that EC be dissolved with other linear carbonate solvents in different ratios. In this regard, different ratios of EC to linear carbonate solvents have been used in electrolyte formulations for LiCs, with the most common being the 1:1 and 3:7 binary solvent mixtures [11,12]. The ratios are dictated by the coordination number of Li in nonaqueous electrolytes (EC/Li 3- 4), corresponding to 30–50% EC content in the electrolyte [9,13]. Moreover, the choice of solvent and ratio of cyclic to linear carbonate solvents can significantly affect the electrolyte properties and cell performance. For example, the dielectric constants of EC: DMC and EC:EMC solvent mixtures with 30, 50 and 70% EC are approximately 18.1, 32.8 and 50, following an increasing trend with the EC% [14,15]. The dielectric constant influences ion conductivity, mobility, dissociation, electrochemical stability and reaction rates/mechanisms [14]. The EC to linear carbonate ratio affects the solvation structure of Li^+ and can likewise determine the nature of electrode/electrolyte interfaces and ion transport across such interfaces

---

[13]. Xu et al. investigated the influence of EC on the desolvation-dictated kinetic processes at the graphite electrode surface [13,16,17]. They revealed that high electrolyte dielectric promotes increased charge transfer resistances due to high desolvation energies at the electrode interfaces. However, such high desolvation energies may be beneficial for achieving long cycle life due to strengthened solvation shells and delayed anion degradation. Furthermore, Wang et al. revealed that EC binds tightly with PF_6^- anions in electrolyte solutions, thereby preventing detrimental anion intercalation in the interlayer spaces of graphite electrodes [18]. DFT studies have also supported the beneficial effect of high dielectric on the PF_6^- anion stability, as the anion oxidative stability is improved when the dielectric in the vicinity is increased [19]. Proatilova et al. demonstrated that EC-rich binary EC:EMC mixtures can facilitate improved electrochemical properties in silicon electrodes by forming efficient protective solid electrolyte interface (SEI) and high initial coulombic efficiencies [20].

The AC cathode used in LiCs is rich in surface functionalities and defects, which are invariably introduced during the activation process for high surface area and sufficient porosity. These functionalities and defective sites are conducive for accelerated electrolyte degradation [21]. The sensitive PF_6^- anion is consequently prone to hydrolysis and degradation when exposed to surface oxygen functionalities and confined moisture absorbed in the AC pores at high potentials. Therefore, several strategies have been employed to mitigate electrolyte decomposition on the AC surface through defect reduction [21], ZnO surface coating [22], heteroatom doping and surface treatment [23,24], though in very complex and expensive procedures. Recent studies have shown that the electrolyte dielectric can positively enhance the electrochemical stability of AC in symmetric cells and half cells with Li metal anodes [25]. The enhanced electrochemical stability was enabled by improved PF_6^- anion resistance to oxidation. This was achieved through a strengthened solvation shell caused by the high electrolyte dielectric, in addition to reduced ion pairs that could have formed PF_5 and HF. However, the mechanisms underlying the improvement seemed to impact the cathodes and anodes differently, as revealed by the AC/AC symmetric cell post-cycling impedance results. Therefore, a detailed examination of cathode and anode interfaces is needed to decipher the influence of the dielectric solvent separately.

In this work, we elucidate the distinct mechanisms of improved electrochemical stabilities with increased electrolyte dielectric using AC and pre-lithiated HC full cells. The electrolytes were 1 M LiPF$_6$ dissolved in different EC:DMC mixtures. Stability tests combining floating voltage holds (FVH) and galvanostatic cycling were performed on cells containing the different electrolytes, after which the AC and HC electrodes were analysed separately. Finally, the cathode electrolyte interface (CEI) and SEI formed on the AC cathode and HC anode were probed using electrochemical impedance spectroscopy (EIS) and post-mortem electrode characterisation. The positive effect of the electrolyte dielectric was more significant on the AC than on the HC electrodes.

2. Experimental

2.1. Materials

Commercial activated carbon (YEC-8B) was obtained from Fuzhou Yihuan Carbon Co., Ltd and used without purification. Polytetrafluoroethylene (PTFE, 20% vol), lithium chips, lithium hexafluorophosphate six salt (LiPF$_6$), EC and dimethyl carbonate (DMC) were purchased from Sigma Aldrich with battery grade purity. All electrolyte formulations were prepared by mixing the appropriate solvents and salts in a moisture and oxygen-free glove box. The solvents and prepared electrolytes were subjected to Karl Fishers' titration, and their water contents were determined to be less than 25 ppm.

2.2. Electrode preparation

AC electrodes were prepared by mixing the AC powder and PTFE binder in a ratio of 92:8 wt%, followed by kneading into a dough-like consistency using a mortar and pestle. Self-standing electrode sheets were fabricated by consistently passing the dough-like mixture through a hot rolling press at 80 °C until a thickness of 100 um was attained. The self-standing electrode sheets were laminated onto a double-sided carbon-coated current collector (MTI-Corp) using the hot rolling press at 160 °C. The active material loading was 5.7 mg cm^{-2}. Single-side coated commercial HC electrodes with active material loading of 2.7 mg cm^{-2} were obtained from Beyonder AS and used without further treatment. Electrode discs of 15 mm and 16 mm were punched from the AC and HC electrode sheets, respectively, and dried overnight in a vacuum oven at 140 °C or 120 °C. After drying, the electrode discs were transferred to the glove box, where the cell assembly was performed.

The electrolytes were prepared by dissolving 1 M LiPF$_6$ salt in binary solvent combinations of EC and DMC with increasing EC vol% (30, 50, and 70%). The electrolytes are denoted as EC:DMC(3:7), EC:DMC(1:1), and EC:DMC(7:3).

Electrochemical characterisations were conducted using type CR2032 coin cells (Holsen), with a cellulose TF4030 separator sandwiched between the electrodes and 100 μl electrolyte. Full cells were assembled with the AC as the cathode and pre-lithiated HC as the anode. The pre-lithiation of the HC was performed using HC/Li metal half cells. The pre-lithiation procedure was as follows: the cell was charged and discharged between 1.5–0.01 V for three cycles at 25 mA g^{-1}, upon which it was stopped at the last discharge with a targeted pre-lithiation capacity of 250 mAh g^{-1}. After the pre-lithiation, the cells were disassembled using a custom coin cell de-crimper (Holsen), and the electrodes were carefully extracted for full cell assembly.

Galvanostatic charge and discharge (GCD) analysis was performed on the cells using a Neware BTSD battery tester. Cycling studies were conducted in the potential window 3–4.2 V at different specific currents (1–1000 mA g^{-1}). For the FVH stability tests, three formation cycles at 4.26 mA g^{-1} were conducted on fresh cells in the potential window 3–4.2 V, after which five GCD capacity check cycles at 213 mA g^{-1} (based on the mass of the AC) were conducted before and after every 10 h voltage hold at 4.2 V. EIS measurements were obtained using a Metrohm Autolab potentiostat. The impedance spectra were acquired in the frequency range 10^5–10^{-2} Hz at an amplitude of 5 mV. Fitting and spectra analysis was conducted using the *impedance.py* package in PYTHON.

After cycling, the full cells were disassembled using a similar decrimper for post-mortem analysis. Two pairs of symmetric AC/AC and HC/HC electrodes from the cycled full cells were assembled into symmetric coin cells for the impedance studies. The extracted electrodes were carefully washed in DMC and dried for 24 h in the glovebox before post-mortem characterisation.

Surface morphology was examined using a Supra 35VP (ZEISS) field emission gun scanning electron microscope (FEG-SEM). Surface species characterisation was conducted by X-ray photoelectron spectroscopy (XPS) using a focused monochromatic Al Kα radiation acquired with a Thermo Scientific ESCALAB 250 spectrometer. The acquired spectra were deconvoluted and fitted using Origin software.

3. Results and discussion

3.1. GCD analysis

The GCD analysis of the AC—HC full cells was conducted in the operating potential window 3–4.2 V [25]. In this potential window, the PF_6^- is the adsorbed/desorbed specie on the AC electrode surface during charge/discharge. At the same time, Li$^+$ cations are intercalated/deintercalated in the HC electrode concurrently. Figure 1a, b and c show the 1st three charge and discharge cycles at 4.26 mA g^{-1}

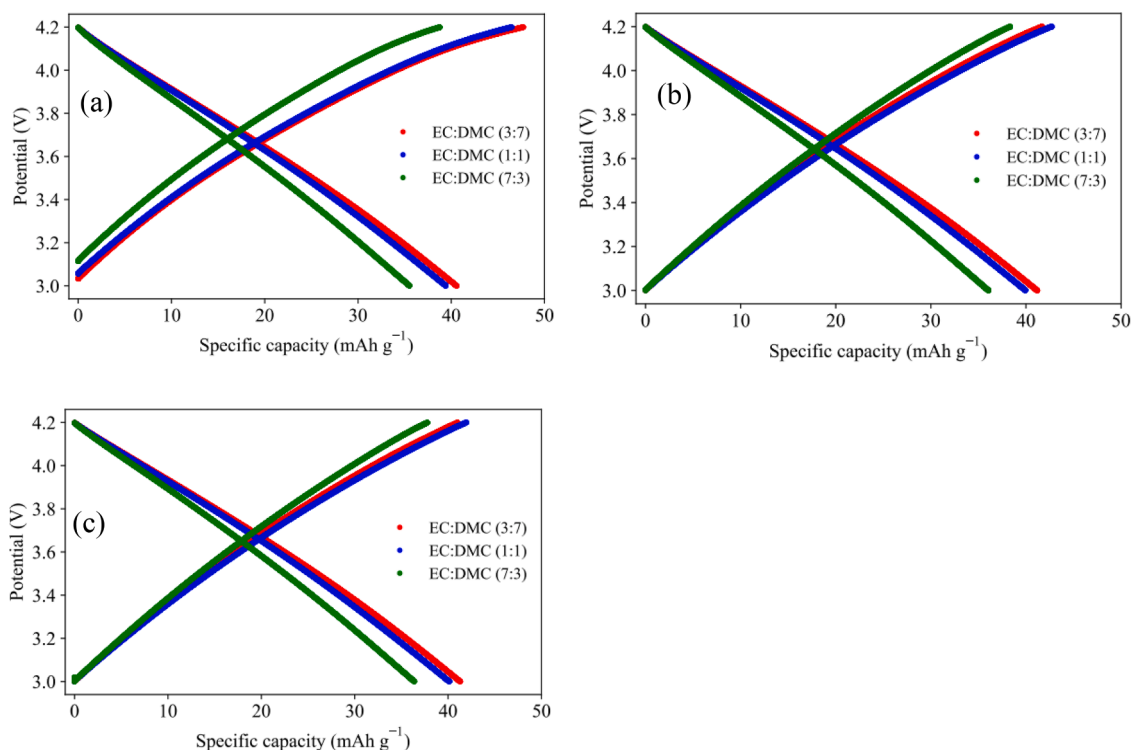**Fig. 1.** Charge and discharge profile of the different electrolytes at 4.26 mA g^{-1} (a) 1st cycle, (b) 2nd cycle, and (c) 3rd cycle.

obtained with the different electrolytes. Despite the pre-lithiation of the HC electrodes, all the electrolytes exhibit an initial coulombic efficiency (ICE) loss in the first cycle (Fig. 1a), attributed to CEI/SEI film formation on the AC and HC. The amount of CEI/SEI formed on the electrodes can be determined by the ICE, which gives a measure of the electrolyte ions trapped irreversibly in the CEI/SEI [26,27]. However, the CE loss is higher for EC:DMC(3:7) than for the other electrolytes, as summarised in Table 1. The higher CE obtained with increased EC% and electrolyte dielectric suggests that a thinner passivation film is formed, which suppresses further electrolyte degradation and consumption of active ionic species for charge storage. Low initial CE is a challenge encountered with HC anodes, for which losses of up to 20% of the initial capacity are expected due to SEI formation [28]. However, the pre-lithiation step enables the pre-SEI formation on the HC anode and reduces the capacity loss after full cell assembly. Therefore, the ICE loss may be related to the AC electrode, which possesses a high surface area and abundant oxygen surface functionalities [29]. Despite the high ICE of EC:DMC(7:3), the specific capacity is expectedly the lowest among the electrolytes due to the high viscosity.

3.2. Stability test

Figure 2a shows the capacity retention profile during the FVH stability test. After 900 h of FVH, EC:DMC(7:3) had the highest capacity retention of nearly 96%. On the other hand, EC:DMC(1:1) and EC:DMC(3:7) had a capacity retention of 90%. The charge and discharge capacity plots of the electrolytes after different durations of FVH are presented in Fig. 2b–d. The excellent capacity retention of EC:DMC(7:3)

Table 1
CE comparison of the electrolytes after the first three cycles.

| Electrolyte	1st cycle (%)	2nd cycle (%)	3rd cycle (%)
EC:DMC(3:7)	84.19	90.74	92.61
EC:DMC(1:1)	84.89	93.64	95.66
EC:DMC(7:3)	91.65	94.05	96.25

is demonstrated in Fig. 2d, where no significant change was observed. On the other hand, EC:DMC(1:1) and EC:DMC(3:7) exhibit slight deviations due to possible electrolyte decomposition and loss of ionic species for charge storage (Fig. 2b and c). The results from the floating voltage stability tests correspond with the previous study, where the effect of the electrolyte dielectric on AC electrochemical stability was examined in AC/Li half cells and AC/AC symmetric cells [25]. However, in this case, only marginal differences exist between the capacity retention of EC:DMC(3:7) and EC:DMC(1:1). Though, high EC% and electrolyte dielectric remain beneficial for enhanced electrochemical stability.

Since EC:DMC(1:1) and EC:DMC(3:7) barely showed any differences in capacity retention in the potential window 3–4.2 V, the upper vertex potential was extended to 4.6 V to further investigate the stability at stringent conditions. The same cells were retested in the potential window 3–4.6 V after reconditioning by three cycles of charge and discharge at 4.26 mA g^{-1}. GCD cycling was implemented instead of the previous FVH to prevent rapid electrolyte decomposition when the cells are subjected to sustained voltage holds at 4.6 V. The capacity retention during the GCD cycling is presented in Fig. 2e. Again, the superior stability of EC:DMC(7:3) is demonstrated, with 95% capacity retention after 1000 cycles. Moreover, there is a clear distinction between the capacity retentions of EC:DMC(1:1) and EC:DMC(3:7), with the former having a capacity retention of 88% and the latter 84% after the same duration.

3.3. EIS analysis

After the GCD analysis, EIS measurements were acquired from the cells and compared with the uncycled full cells to understand the mechanisms underlying the capacity fade. The EIS spectra from the uncycled cells display two prominent semi-circles: a small semi-circle at high-mid frequencies and a larger semi-circle deconvoluted into two additional semi-circles (Fig. 3a). The EIS spectra were deconvoluted using the Gaussian process distribution of relaxation time (GP-DRT) model to determine the number of processes and their assignment to
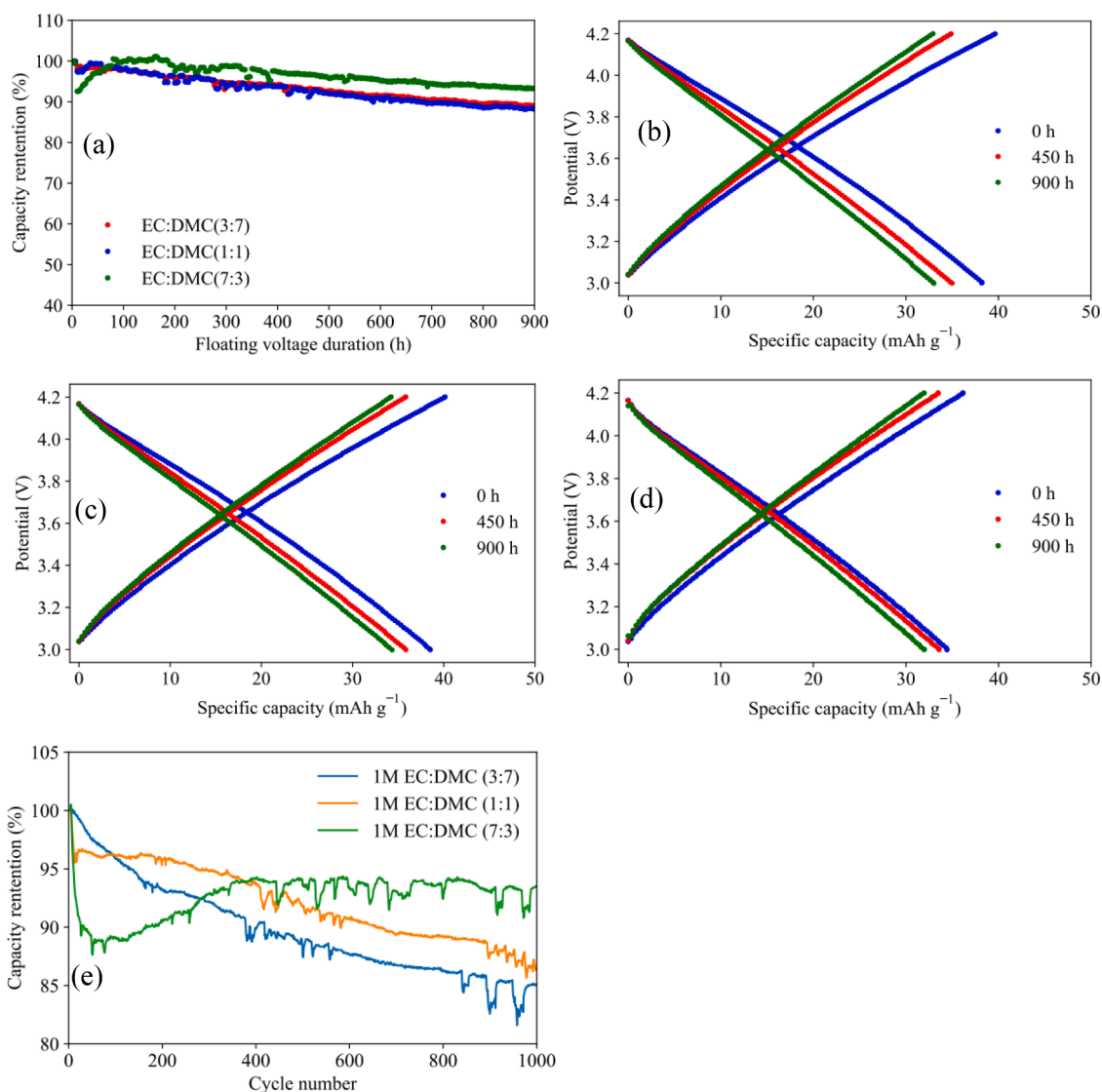
Fig. 2. (a) Capacity retention during floating voltage stability tests; Charge and discharge profile after different durations of floating voltage for (b) EC:DMC(3:7), (c) EC:DMC (1:1), and (d) EC:DMC(7:3); (e) Capacity retention during GCD cycling in the potential window 3–4.6 V at 213 mA g^{-1}.
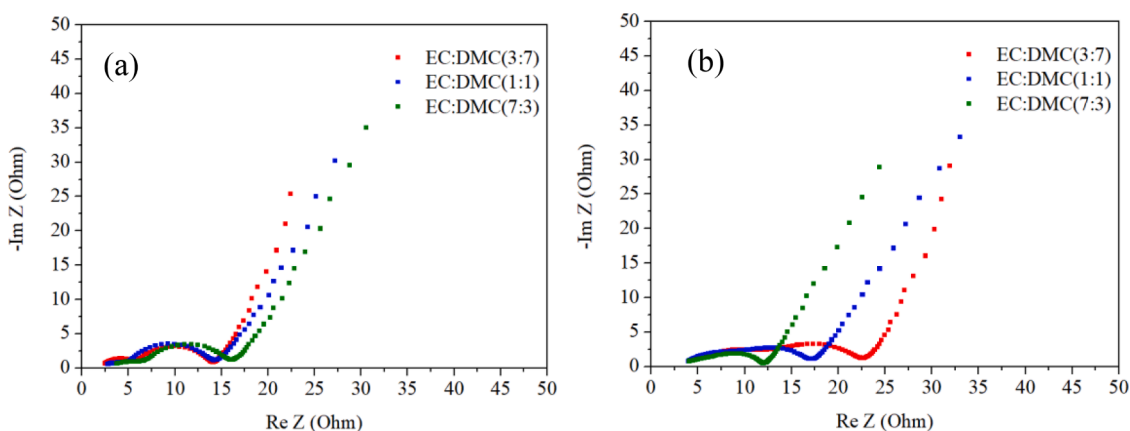
Fig. 3. EIS spectra obtained from different electrolytes (a) Uncycled AC-HC full cells, and (b) Cycled AC-HC full cells. EIS was acquired at open circuit potential (OCP) 3.06 V +/− 0.05 V.

individual electrodes [30]. Figure S1 in the Supporting Information (SI) shows the DRT analysis of EC:DMC(3:7) in different cell chemistries to separately match the peaks. Based on the peak positions and time constants, the three semi-circles in the uncycled AC—HC full cell EIS spectra are assigned to the active material and current collector contact resistance of AC and HC (predominantly AC), the resistance of the passivation layer formed on the electrodes (predominantly HC), and the charge transfer resistance, respectively [31,32]. The near 45-degree vertical sloping line at low frequencies is associated with the electrolyte Warburg diffusion coefficient (W).

The equivalent circuit used in the fitting is given by *R0-p(C1,R1)-p(CPE2,R2)-p(C3,R3)-W1-C4* [31]. Where *R0* represents the ohmic resistance (combined bulk electrolyte and active material resistance); *C1* and *R1* represent the capacitance, and active material/current collector contact resistance of the AC and HC electrode; *CPE2* and *R2* represent the capacitance and SEI resistance of the HC electrode; *C3* and *R3* represent the capacitance and charge transfer resistance; and *C4* the capacitance of the device. The constant phase element (CPE) was introduced to account for the surface roughness and heterogeneity of the SEI layer. Fitting without this element yielded significant errors and unsatisfactory results. However, using the respective circuits described and supported by the DRT analysis, x^2 values less than 10^{-4} were obtained. The obtained parameters after fitting are summarised in Table 2. For illustration purposes, different EIS spectra for EC:DMC(3:7) and their corresponding fitting are presented in Figure S1.

The *R1* values obtained from EC:DMC(3:7), EC:DMC(1:1) and EC:DMC(7:3) follow a decreasing trend as the electrolyte dielectric increases. The smaller *C1* value obtained in EC:DMC(3:7) indicates that the surface area is reduced to a large extent by the passivation film formed in this electrolyte compared to the others. The same trend of decreasing resistance with increased electrolyte dielectric was displayed for the *R2* values. Thus, the initial passivation layer impedance is more resistive in the AC and HC electrode with EC:DMC(3:7). It was interesting to see that *R3* increased proportionally with the electrolyte dielectric, in agreement with previous studies [13,17]. Therefore, the charge transfer resistance increases with the electrolyte dielectric due to higher desolvation energies at the HC anode interface [13,17]. Moreover, the largest *W* was obtained for EC:DMC(7:3), which can be attributed to the higher viscosity associated with increased EC%.

After the GCD cycling, the EIS spectra appeared to be depressed with a decreased imaginary impedance (Fig. 3b), which signified a reformed passivation layer at the electrode surfaces. The total cell impedance of EC:DMC(3:7) and EC:DMC(1:1) determined from the intercept on the real axis increased compared to the uncycled cells. However, the opposite trend is observed for EC:DMC(7:3). This was contrary to the expected growth in real impedance after cycling. Moreover, the two distinct semi-circles observed in the pristine cells are absent in the cycled cells. Instead, the semi-circles appear to be merged, further supporting significant electrode surface transformation after cycling. The spectra were fitted with the same equivalent circuit described previously. The obtained parameters after cycling are summarised in Table 3.

From the cycled cells EIS spectra fit, *R0* is increased in EC:DMC(3:7) and EC:DMC(1:1), consistent with increased electrolyte and active material resistance in the electrolytes. On the contrary, EC:DMC(7:3) exhibits a slightly decreased *R0*, signifying only marginal decomposition of the electrolyte, but the decreased *W* may imply decreased electrolyte

viscosity after cycling. Interestingly, *R1* decreased in all electrolytes while *R2* increased, although EC:DMC(3:7) had the highest value. EC:DMC(3:7) further exhibited a slight increase in *R3*, whereas the other electrolytes exhibited a decrease. This trend suggests a marginally increased charge transfer resistance in EC:DMC(3:7) as the capacity fade progressed. Meanwhile, the decreased charge transfer resistance of EC:DMC(1:1) and EC:DMC(7:3) may indicate that cycling induces significant reformations of the native passivation layer and electrode interfaces.

The full cell EIS analysis results indicate that EC:DMC(3:7) had the highest total resistance among the electrolytes, possibly due to increased electrolyte degradation and active material and surface passivation layer transformation. However, the interpretations of the resistance parameters to individual electrodes require further validation, given that the EIS measurement is obtained simultaneously across the various AC and HC interfaces, and the resistance parameters contain contributions from both electrodes [33].

To determine the transformations of the individual electrodes after cycling in relation to the electrolyte dielectric, symmetric cells were constructed from the cycled AC—HC full cells and subjected to EIS analysis. Two corresponding AC—AC and HC—HC electrodes were extracted and reassembled into symmetric cells with a new separator and electrolyte. Figure 4a and b show the spectra from the reassembled AC—AC and HC—HC symmetric cells. The EIS spectra of the symmetric cells were divided by two to account for the impedance of the single electrode.

Figure 4a shows that the AC-AC spectra display characteristics associated with symmetric AC cells. The semi-circle at high to mid-frequency corresponds to the particle-particle/particle-to-current collector contact resistance (R_p). The vertical line at low frequencies represents the double-layer capacitance. The spectra were fitted using similar equivalent circuits as Köps et al. [34]. The circuit consists of a resistor R_{el} representing the electrolyte solution resistance, an R_p/CPE loop representing the particle-to-particle/particle-to-current collector interface, a Warburg element W, and a capacitor C connected in series.

The *Rp* values after the fitting were 9.45, 4.85 and 3.37 Ohm for EC:DMC(3:7), EC:DMC(1:1) and EC:DMC(7:3), respectively. The symmetric AC—AC impedance results correspond with the trend in *R1* and *R2* values in the cycled full-cell EIS analysis. Furthermore, the increased electrolyte dielectric remarkably decreases the resistance of the AC electrode by a factor of three, implying decreased electrolyte decomposition products at the AC surface. Therefore, it confirms that the high electrolyte dielectric is beneficial for enhanced AC stability. Deposited electrolyte degradation products reduce the accessible surface area of the AC electrode and increase the resistance [29].
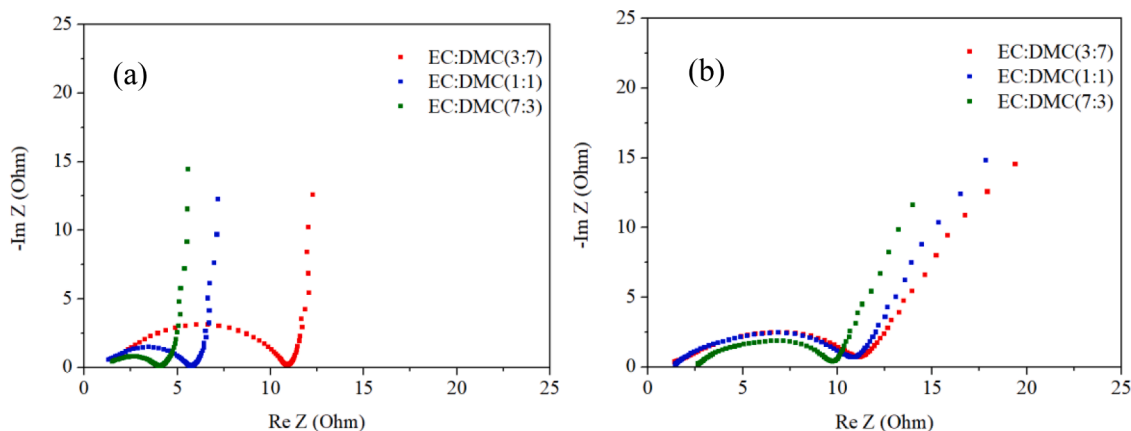
For the reassembled HC—HC symmetric cells (Fig. 4b), the semi-circle at high-mid frequencies is associated with the passivation layer and charge transfer impedance, while the vertical sloping line at low frequencies corresponds to the Warburg diffusion. It has been reported that the primary failure mechanism of graphite and HC anodes is due to the growth of the SEI and the loss of cyclable lithium ions [35]. Fitting the impedance spectra was challenging due to significant errors in some parameters. Hence, we directly compared the diameter of the semi-circle as a relative comparison of the total resistance due to the passivation layer and charge transfer. It turned out that the HC—HC anodes from EC:DMC(7:3) again present the smallest total resistance (~7.5 Ohm), attributed to a less resistive SEI or degradation products. Meanwhile, the

Table 2
Parameters of the uncycled AC-HC full cell spectra after fitting.

Electrolyte	R0 (Ohm)	C1 (F)	R1 (Ohm)	CPE2_0 (Ohm^{-1}s^a)	CPE2_1	R2 (Ohm)	C3 (F)	R3 (Ohm)	W1 Ohm s$^{-0.5}$	C4 (F)
EC:DMC(3:7)	1.81	0.00042	4.56	0.00721	0.345	7.64	0.000007	1.58	1.20	0.930
EC:DMC(1:1)	1.70	0.00186	2.74	0.00011	0.481	4.25	0.000310	4.75	3.27	0.950
EC:DMC(7:3)	2.97	0.00161	2.63	0.00039	0.563	4.64	0.000480	4.94	3.62	0.771

Table 3
Parameters of the cycled AC-HC full cell EIS spectra after fitting.

Electrolyte	R0 (Ohm)	C1 (F)	R1 (Ohm)	CPE2_0 (Ohm^{-1}s^a)	CPE2_1	R2 (Ohm)	C3 (F)	R3 (Ohm)	W1 Ohm s$^{-0.5}$	C4 (F)
EC:DMC(3:7)	3.20	0.000510	3.84	0.00060	0.477	12.8	0.00045	2.26	2.39	0.826
EC:DMC(1:1)	3.32	0.000232	2.21	0.00018	0.648	6.97	0.00078	3.57	3.89	0.867
EC:DMC(7:3)	2.63	0.000480	1.88	0.00054	0.557	5.28	0.00078	2.46	2.57	0.937

Fig. 4. EIS spectra for the reassembled (a) AC-AC, and (b) HC-HC symmetric cells.

resistance of EC:DMC(1:1) and EC:DMC(3:7) are similar at 9 Ohms. The total resistance values in the AC—AC and HC—HC symmetric cells correspond with the sum of *R1* and *R2*, and *R2* and *R3* obtained from the cycled AC—HC full cells. Hence, follows a decreasing trend with the increase of the electrolyte dielectric. Therefore, increased electrolyte dielectric is also beneficial for enhanced cycling stability of the HC anode, though to a lesser extent than the AC electrode.

3.4. Post-mortem electrode analysis

Post-mortem electrode examinations were then conducted on the cycled electrodes to reveal the constituents at the surface. The SEM images obtained from the AC and HC electrodes are presented in Fig. 5.

The SEM images show features of deposits of electrolyte degradation products on the cycled electrodes, which are absent in the uncycled reference electrode for both the AC and HC. The deposits on the surface of the cycled AC electrode (Fig. 5c, e and g) resembled aggregates, with varying degrees of visible binder among the samples. The cross-sectional SEM images in Figure S2 further confirm increased binder visibility in EC:DMC(3:7), which may be attributed to the AC electrode bulk and binder restructuring from exfoliation. We conjecture that the exfoliation may be linked to PF$_6^-$ intercalation within the graphitic layers, which reportedly reduces as the PF$_6^-$ anion is increasingly solvated [18]. This explains the reduced binder visibility in EC:DMC(1:1) and EC:DMC(7:3). Moreover, EC:DMC (3:7) had the highest surface deposits covering the AC grains. However, the aggregated deposits were reduced on the AC electrode surface as the electrolyte dielectric was increased, with EC:DMC(7:3) having less deposits at the surface. This is consistent with the EIS measurements (Fig. 4a). Therefore, the high resistance of EC:DMC (3:7) could be related to increased deposits of electrolyte degradation products at the AC surface and increased active material resistance caused by electrode transformations after exfoliation.

For the cycled HC electrodes (Fig. 5d, f and h), a layer with increased SEI formation is observed. However, the surface of EC:DMC(7:3) appeared relatively smoother than EC:DMC(1:1) and EC:DMC(3:7), with the latter showing the roughest and highest magnitude of deposits (Figure S3). Again, this is consistent with the HC—HC symmetric cell EIS analysis (Fig. 4b), corroborating a greater extent of electrolyte

decomposition with lower EC%.

The nature of surface passivating species on the AC and HC electrodes was probed using XPS. The C1s XPS spectra of the reference AC and HC electrodes are presented in Fig. 6a and b. The C1s spectra of the uncycled AC electrode display six peaks at binding energies of 283.5, 284.1, 284.7, 286.1, 288.1 and 291.7, corresponding to the presence of sp (C≡C), sp2 (C=C), sp3 (C—C), C—O, O—C—O groups and CF$_2$ from the PTFE binder [29,36]. The relative elemental composition of the AC surface is 69% carbon, 5% oxygen and 26% fluorine. For the uncycled HC electrode, the peaks are present at binding energies of 283.1, 284.1, 284.8, 286.1, 288.1 and 290.5 eV, corresponding to sp (C≡C), sp2 (C=C), sp3 (C—C), C—O, O—C—O and CO$_3$ groups. The different oxygenated carbon environments of the AC and HC electrodes are possible contributors to the low ICE after reactions with the electrolyte [37]. The uncycled HC electrode surface presents 86% carbon and 14% oxygen.

The C1s, P2p and F1s spectra of the cycled AC electrodes from EC:DMC (3:7), EC:DMC(1:1) and EC:DMC (7:3) are compared in Fig. 7, while the relative elemental composition is presented in Table 4. Notably, the C1s spectra of the cycled AC electrodes display six peaks at binding energies of 284.2, 285.3, 286.3, 287.2, 288.7 and 291.7 eV, corresponding to sp^2 (C=C), CH$_x$, C—O, C=O, O—C—O and CF$_2$ groups arising from the PTFE binder (Fig. 7a) [29,36]. The disappearance of the sp (C≡C) peak suggests that some carbon species were reacted or may be covered by the passivating layer. Moreover, the decreased C% and increased O% are evidence of passivation of the surface of the AC electrode and marginal CEI formation. However, the CEI is somewhat limited, as revealed by the SEM images, which do not resemble the clear layer of SEI formed on the HC anode. Nevertheless, the composition of the surface species in the C1s spectra resembles typical CEI products (lithium alkyl carbonates) found on cathodes cycled in carbonate solvents [38]. However, these products arise from ring-opening reactions of EC with PF$_5$ (from PF$_6^-$ or ion-paired LiPF$_6$ decomposition). Therefore, the diminished C—O content in the CEI of EC:DMC(1:1) and EC:DMC (7:3) suggests less carbonate solvent decomposition, possibly related to sufficiently solvated PF$_6^-$ and delayed PF$_6^-$ degradation at the surface [39].

In the P2p spectra, phosphates and LixPOyFz species are identified at
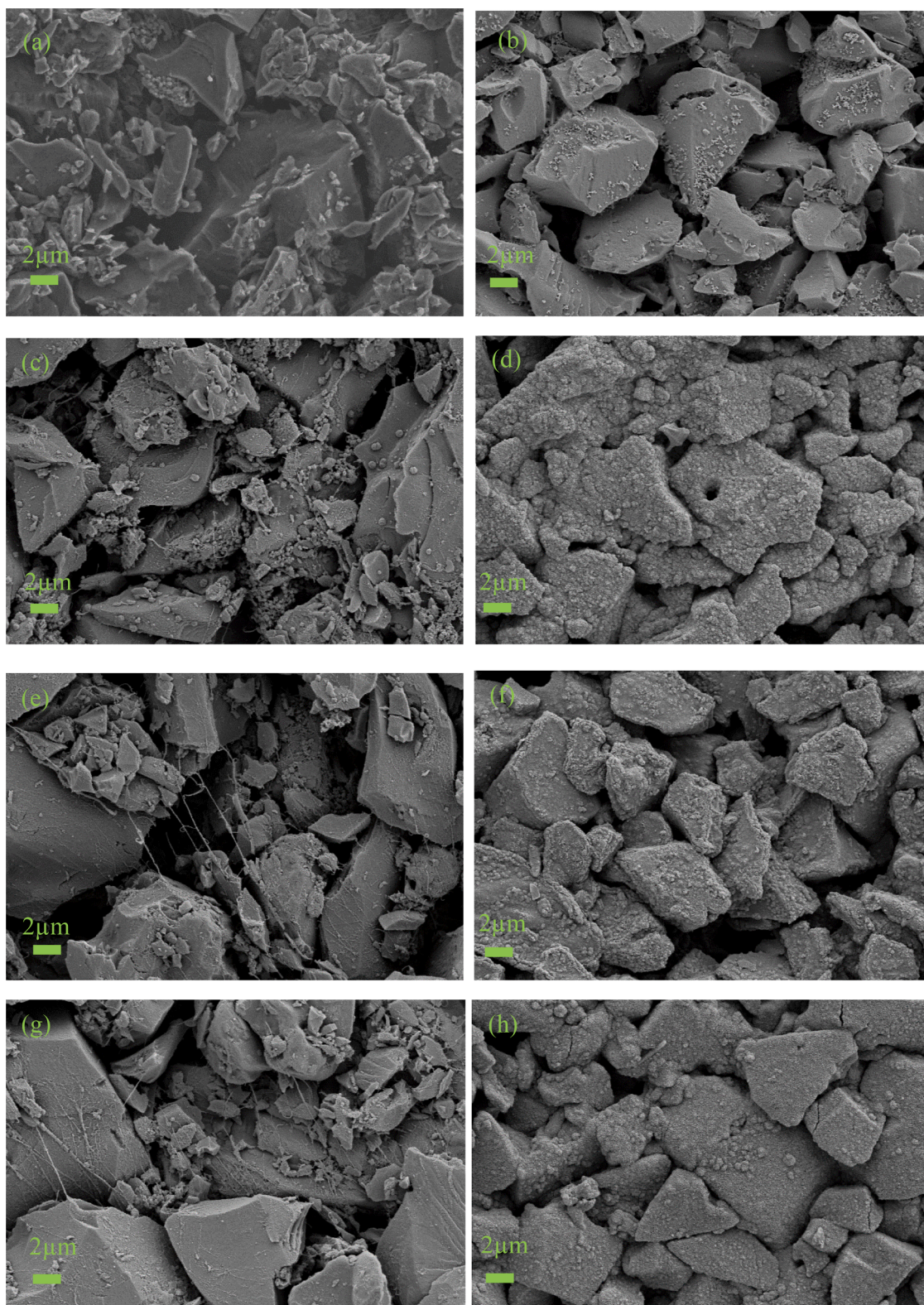
Fig. 5. SEM micrographs of (a, b) the reference AC and HC electrode; (c, d) cycled AC and HC electrode from EC:DMC(3:7); (e, f) cycled AC and HC electrode from EC:DMC(1:1); (g, h) cycled AC and HC electrodes from EC:DMC(7:3).

binding energies of 133.7, 134.57, 135.7 and 136.6 eV. These products are associated with the PF_6^- anion decomposition and remnant salts on the AC surface. This is more apparent on the AC electrode from EC:DMC (3:7), suggesting more PF_6^- decomposition products.

In the F1s spectra, LiF, $Li_xPO_yF_z$ and CF_2 were identified at binding

energies of 685.5, 686.7 and 689 eV. However, the immense presence of CF_2 peak from the PTFE binder diminishes the LiF peak and may be ascribed to more binder exposure at the surface as cycling progresses. Moreover, a slightly reduced ratio of LiF to CF_2 binder was observed for EC:DMC(7:3), in comparison with EC:DMC(3:7). This further supports
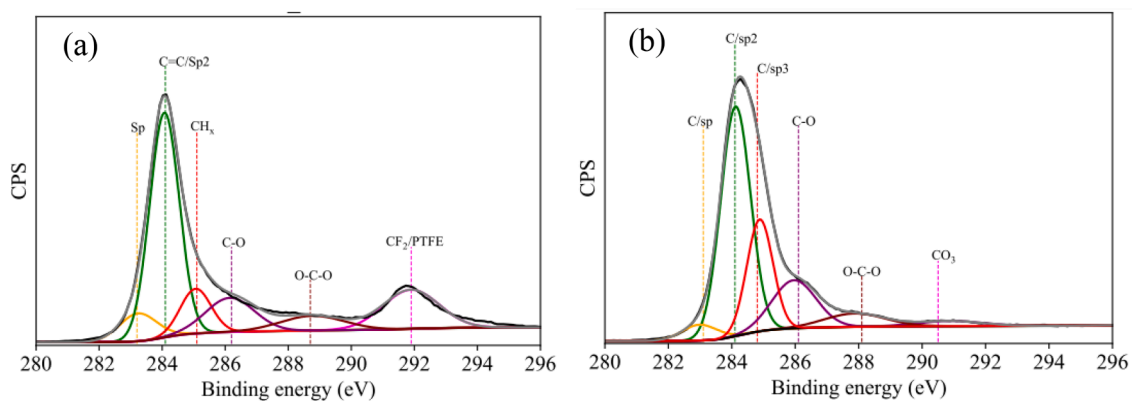
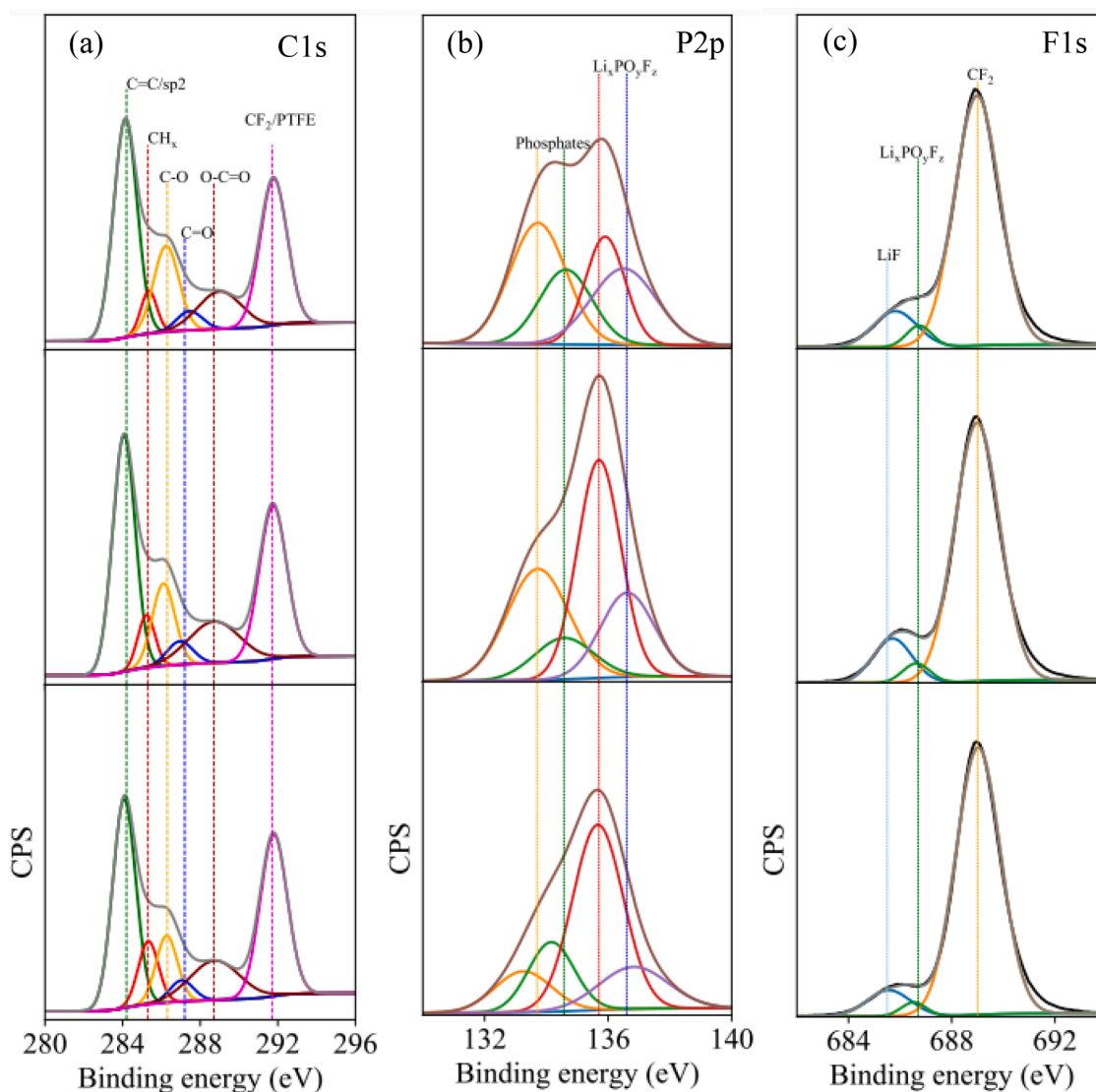**Fig. 6.** C1s XPS spectra of the uncycled (a) AC, (b) HC electrode.

Fig. 7. Deconvoluted XPS spectra of the cycled AC electrode (a) C1s, (b) P2p, and (c) F1s. Top EC:DMC(3:7), middle EC:DMC(1:1), and bottom EC:DMC(7:3).

that there is less PF_6^- degradation products at the AC surface with increased EC%. Increased phosphate species and LiF on the AC surface correlate with the capacity fade and are attributed to more passivating species with the capacity fade [29].

The C1s spectra of the cycled HC electrodes display a clearer trend

(Fig. 8a). In EC:DMC(3:7), six peaks are identified at binding energies of 283.8, 284.8, 285.5, 286.3, 288.7 and 290.1 eV, corresponding to LiCx/ spC, sp2 (C=C), CHx, C—O, C=O, O—C=O and CO$_3$ species [36,40, 41]. In EC:DMC(1:1) and EC:DMC(7:3), the CH$_x$ peak is absent, and the intensity of the LiCx/ spC peak is low.

Table 4

Relative concentrations of the C, O, F, P and Li on the surface of the cycled AC cathode in different electrolytes.

Elements	C%	O%	F%	P%	L%
Reference	69	5	26		
EC:DMC(3:7)	44	10	40	1	5
EC:DMC(1:1)	45	10	39	1	4
EC:DMC(7:3)	45	10	40	1	4

The disappearance of the CH_x peak in EC:DMC(1:1) and EC:DMC(7:3) may be related to less linear carbonate in the solvation shell and dominance of EC-derived SEI products at the HC electrode surface [41]. Additionally, the $C-O/OCH_3$ peak at binding energies of 287.1 eV is ascribed to DMC derived SEI products and decreases with the DMC% in the electrolyte [40]. The $O-C=O$ and CO_3 peaks at 288.7 and 290.1 eV are ascribed to $-CH_2OCO_2$ and Li_2CO_3, derived from EC [40,41]. Therefore, in EC:DMC(3:7), more DMC derived products are present, while in EC:DMC(1:1) and EC:DMC(7:3), more EC derived products are present. However, the SEI with more Li_2CO_3 is more stable than the DMC derived SEI, given the decreased intensity of the LiC_x peak. The presence of the LiC_x peak may indicate broken SEI at the surface. Hence the electrode in EC:DMC(3:7) possesses an unstable SEI, which does not

effectively protect against further electrolyte degradation. This is additionally confirmed by the elemental composition in Table 5, which shows more F% in EC:DMC(3:7) from $LiPF_6$ decomposition. The smoother surface of EC:DMC(1:1) and EC:DMC(7:3) may therefore indicate uniform SEI coverage at the surface, in contrast with the rough and otherwise broken SEI of EC:DMC(3:7) (Fig. 5d, f and h).

The O1s spectra revealed three peaks at binding energies of 530.5, 531.7 and 533.1 eV, corresponding to $ROLi/CO$, $C-O$ and $O-C=O$ (Fig. 8b) [40]. In the F1s spectra (Fig. 8c), LiF and $Li_xPO_yF_z$ species are present at binding energies of 685 and 687 eV. However, the intensity of LiF species is the highest in EC:DMC(3:7), which might be the cause of the high impedance. Furthermore, it has been reported that degradation

Table 5

Relative concentrations of C, O, F, P and Li on the surface of the cycled HC anode in different electrolytes.

Elements	C%	O%	F%	P%	L%
Reference	86	14			
EC:DMC(3:7)	38	31	4	1	25
EC:DMC(1:1)	31	39	2		28
EC:DMC(7:3)	31	39	2		28
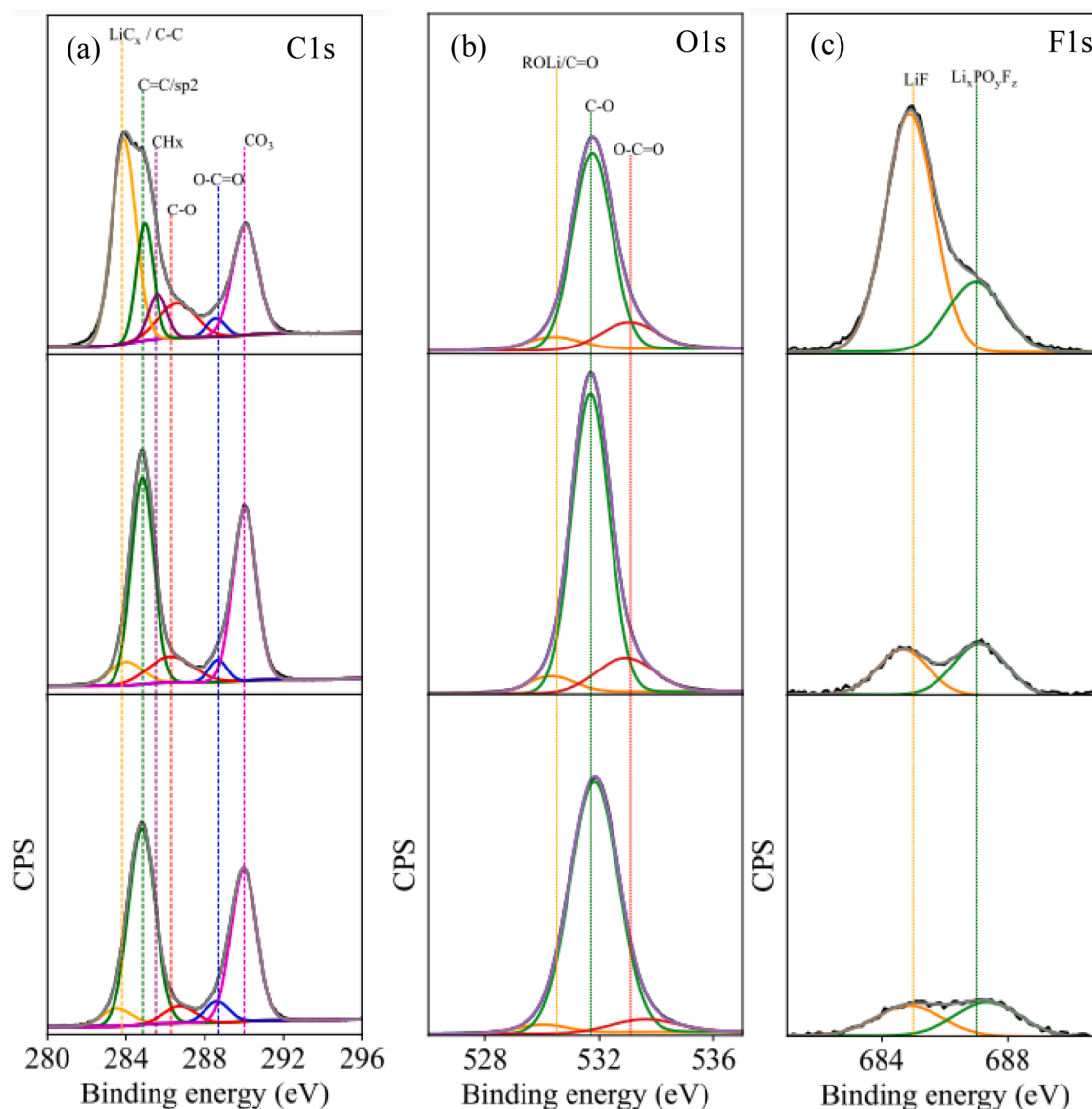
Fig. 8. Deconvoluted XPS spectra of the cycled HC electrode (a) C1s, (b) O1s, and (c) F1s. Top EC:DMC(3:7), middle EC:DMC(1:1), and bottom EC:DMC(7:3).

products from the cathode can migrate to the anode and get deposited [42]. Therefore, the increased LiF presence in EC:DMC(3:7) could also be related to ion-paired $LiPF_6$ and PF_6^- decomposition at the cathode.

The XPS results have thus revealed that the HC anode surface in EC: DMC(3:7) is likely enriched in LiF and LiCx/spC peak, compared to the other electrolytes. The presence of the latter suggested SEI attack since these peaks are supposed to be covered by the native passivation films. Although LiF is mostly a favourable SEI component due to its impressive stability, our results have shown that this alone does not translate to improved stabilities. Specifically, the increased LiF intensity and polyphosphates would result from PF_6^- degradation. PF_6^- degradation has been linked to the incomplete dissociation of $LiPF_6$, which depends on the solvating ability/electrolyte dielectric of the solvents [43]. Low solvating ability/electrolyte dielectric in EC:DMC(3:7) would lead to increased ion-paired $LiPF_6$ and propensity for dissociation into LiF and PF_5. While PF_5 may react with moisture in the AC pores and oxygen radicals at the surface, producing HF and POF_3. POF_3 could further react with DMC to produce POF_2OCH_3 and polyphosphates, which may also react with PF_5, to generate more POF_2OCH_3 in a continuous destructive cycle [44]. POF_3 can also catalyse further ring-opening reactions of the EC, thereby depleting EC and resulting in capacity fade.

Moreover, electrodes with well-formed SEIs are also prone to HF and PF_5 attacks. The former is responsible for SEI thickening, where Li_2CO_3 is converted to LiF and leads to more SEI formation [45]. This corroborates the XPS results for the HC anode, with EC:DMC(3:7) having the lowest intensity of Li_2CO_3 and the highest intensity of LiF. Therefore, the lower dielectric solvents are more prone to electrolyte degradation. High electrolyte dielectric is beneficial for enhanced stability, which is particularly suited for applications requiring high-powered devices with long cycle life.

4. Conclusion

We examined the influence of solvent composition/electrolyte dielectric on the electrochemical stability of AC/HC LiC. Electrolytes with increased EC% and solution dielectric demonstrated improved ICE and high stability during floating voltage hold tests and galvanostatic cycling. The electrode/electrolyte interface characteristics and the reasons for the improved stability were disclosed by EIS and XPS. The EIS measurements revealed decreased impedances as the EC% was increased, with a more significant effect on the AC electrode. Furthermore, surface chemical species analysis revealed the increased presence of anion degradation products in the electrolyte with the lowest dielectric, thereby confirming that anion degradation is responsible for the low stability. Although the cyclic carbonate to linear carbonate ratio at 3:7 is the base electrolyte solvent combination commonly used, increasing the dielectric presents a more effective way of enhancing the stability of the PF_6^- anion. This is particularly suited for AC electrodes, where the PF_6^- anion is used as a charge storage species, whose depletion may facilitate capacity fade and cycle life deterioration.

CRediT authorship contribution statement

Obinna Egwu Eleri: Conceptualization, Investigation, Formal analysis, Methodology, Data curation, Visualization, Writing – original draft, Writing – review & editing. **Frederik T Huld:** Formal analysis, Investigation, Methodology, Writing – review & editing. **Fengliu Lou:** Conceptualization, Validation, Funding acquisition, Methodology, Resources, Project administration, Supervision, Writing – review & editing. **Zhixin Yu:** Validation, Funding acquisition, Resources, Project administration, Supervision, Writing – review & editing.

Declaration of Competing Interest

The authors declare that they have no known competing financial interests or personal relationships that could have appeared to influence the work reported in this paper.

Data availability

Data will be made available on request.

Acknowledgements

Supplementary materials

Supplementary material associated with this article can be found, in the online version, at doi:10.1016/j.electacta.2023.142960.

Reference

[1] S.R. Sivakkumar, A. Pandolfo, Evaluation of lithium-ion capacitors assembled with pre-lithiated graphite anode and activated carbon cathode, Electrochim. Acta 65 (2012) 280–287.

[2] G.G. Amatucci, F. Badway, A. Du Pasquier, T. Zheng, An asymmetric hybrid nonaqueous energy storage cell, J. Electrochem. Soc. 148 (8) (2001) A930.

[3] Z. Shi, J. Zhang, J. Wang, J. Shi, C. Wang, Effect of the capacity design of activated carbon cathode on the electrochemical performance of lithium-ion capacitors, Electrochim. Acta 153 (2015) 476–483.

[4] H. Wang, C. Zhu, D. Chao, Q. Yan, H.J. Fan, Nonaqueous hybrid lithium-ion and sodium-ion capacitors, Adv. Mater. 29 (46) (2017), 1702093.

[5] J. Ding, W. Hu, E. Paek, D. Mitlin, Review of hybrid ion capacitors: from aqueous to lithium to sodium, Chem. Rev. 118 (14) (2018) 6457–6498.

[6] B. Li, J. Zheng, H. Zhang, L. Jin, D. Yang, H. Lv, C. Shen, A. Shellikeri, Y. Zheng, R. Gong, Electrode materials, electrolytes, and challenges in nonaqueous lithium-ion capacitors, Adv. Mater. 30 (17) (2018), 1705670.

[7] T.R. Jow, K. Xu, O. Borodin, M. Ue, Electrolytes for Lithium and Lithium-Ion Batteries, Springer, 2014.

[8] G.E. Blomgren, Liquid electrolytes for lithium and lithium-ion batteries, J. Power Sources 119 (2003) 326–329.

[9] K. Xu, Nonaqueous liquid electrolytes for lithium-based rechargeable batteries, Chem. Rev. 104 (10) (2004) 4303–4418.

[10] S.S. Zhang, A review on electrolyte additives for lithium-ion batteries, J. Power Sources 162 (2) (2006) 1379–1394.

[11] C. Decaux, G. Lota, E. Raymundo-Piñero, E. Frackowiak, F. Béguin, Electrochemical performance of a hybrid lithium-ion capacitor with a graphite anode preloaded from lithium bis (trifluoromethane) sulfonimide-based electrolyte, Electrochim. Acta 86 (2012) 282–286.

[12] J.-H. Kim, J.-S. Kim, Y.-G. Lim, J.-G. Lee, Y.-J. Kim, Effect of carbon types on the electrochemical properties of negative electrodes for Li-ion capacitors, J. Power Sources 196 (23) (2011) 10490–10495.

[13] K. Xu, ``Charge-transfer'' process at graphite/electrolyte interface and the solvation sheath structure of Li+ in nonaqueous electrolytes, J. Electrochem. Soc. 154 (3) (2007) A162.

[14] D.S. Hall, J. Self, J. Dahn, Dielectric constants for quantum chemistry and Li-ion batteries: solvent blends of ethylene carbonate and ethyl methyl carbonate, J. Phys. Chem. C 119 (39) (2015) 22322–22330.

[15] I.N. Daniels, Z. Wang, B.B. Laird, Dielectric properties of organic solvents in an electric field, J. Phys. Chem. C 121 (2) (2017) 1025–1031.

[16] K. Xu, A. von Wald Cresce, Li+-solvation/desolvation dictates interphasial processes on graphitic anode in Li ion cells, J. Mater. Res. 27 (18) (2012) 2327–2341.

[17] K. Xu, Y. Lam, S.S. Zhang, T.R. Jow, T.B. Curtis, Solvation sheath of Li+ in nonaqueous electrolytes and its implication of graphite/electrolyte interface chemistry, J. Phys. Chem. C 111 (20) (2007) 7411–7421.

[18] H. Wang, M. Yoshio, Suppression of PF 6− intercalation into graphite by small amounts of ethylene carbonate in activated carbon/graphite capacitors, Chem. Commun. 46 (9) (2010) 1544–1546.

[19] O. Borodin, W. Behl, T.R. Jow, Oxidative stability and initial decomposition reactions of carbonate, sulfone, and alkyl phosphate-based electrolytes, J. Phys. Chem. C 117 (17) (2013) 8661–8682.

[20] I. Profatilova, N.-S. Choi, K.H. Yew, W.-U. Choi, The effect of ethylene carbonate on the cycling performance of a Si electrode, Solid State Ionics 179 (40) (2008) 2399–2405.

[21] O.E. Eleri, K.U. Azuatalam, M.W. Minde, A.M. Trindade, N. Muthuswamy, F. Lou, Z. Yu, Towards high-energy-density supercapacitors via less-defects activated carbon from sawdust, Electrochim. Acta 362 (2020), 137152.

[22] C. Wu, F. Zhang, X. Xiao, J. Chen, J. Sun, D. Gandla, Y. Ein-Eli, D.Q. Tan, Enhanced electrochemical performance of supercapacitors via atomic layer deposition of ZnO on the activated carbon electrode material, Molecules 26 (14) (2021) 4188.

[23] C. Liu, B.B. Koyyalamudi, L. Li, S. Emani, C. Wang, L.L. Shaw, Improved capacitive energy storage via surface functionalisation of activated carbon as cathodes for lithium ion capacitors, Carbon N Y 109 (2016) 163–172.

[24] B. Fang, L. Binder, Enhanced surface hydrophobisation for improved performance of carbon aerogel electrochemical capacitor, Electrochim. Acta 52 (24) (2007) 6916–6921.

[25] O.E. Eleri, J. Pires, F.T. Huld, S. Lu, P. Schweigart, A.M. Svensson, F. Lou, Z. Yu, Enhanced activated carbon lithium-ion capacitor electrochemical stability through electrolyte dielectric optimisation, Sustain. Energy Fuels (2023).

[26] Y. Rangom, R.R. Gaddam, T.T. Duignan, X. Zhao, Improvement of hard carbon electrode performance by manipulating SEI formation at high charging rates, ACS Appl. Mater. Interfaces 11 (38) (2019) 34796–34804.

[27] X. Zhang, C. Fan, S. Han, Improving the initial Coulombic efficiency of hard carbon-based anode for rechargeable batteries with high energy density, J. Mater. Sci. 52 (2017) 10418–10430.

[28] X. Li, X. Sun, X. Hu, F. Fan, S. Cai, C. Zheng, G.D. Stucky, Review on comprehending and enhancing the initial Coulombic efficiency of anode materials in lithium-ion/sodium-ion batteries, Nano Energy 77 (2020), 105143.

[29] O.E. Eleri, F. Huld, J. Pires, W.M. Tucho, P. Schweigart, A.M. Svensson, F. Lou, Z. Yu, Revealing mechanisms of activated carbon capacity fade in lithium-ion capacitors, Electrochim. Acta 453 (2023), 142359.

[30] J. Liu, F. Ciucci, The Gaussian process distribution of relaxation times: a machine learning tool for the analysis and prediction of electrochemical impedance spectroscopy data, Electrochim. Acta 331 (2020), 135316.

[31] J.P. Schmidt, T. Chrobak, M. Ender, J. Illig, D. Klotz, E. Ivers-Tiffée, Studies on LiFePO4 as cathode material using impedance spectroscopy, J. Power Sources 196 (12) (2011) 5342–5348.

[32] W. Cao, M. Greenleaf, Y. Li, D. Adams, M. Hagen, T. Doung, J. Zheng, The effect of lithium loadings on anode to the voltage drop during charge and discharge of Li-ion capacitors, J. Power Sources 280 (2015) 600–605.

[33] M. Gaberšček, Understanding Li-based battery materials via electrochemical impedance spectroscopy, Nat. Commun. 12 (1) (2021) 6513.

[34] L. Köps, P. Ruschhaupt, C. Guhrenz, P. Schlee, S. Pohlmann, A. Varzi, S. Passerini, A. Balducci, Development of a high-energy electrical double-layer capacitor demonstrator with 5000 F in an industrial cell format, J. Power Sources 571 (2023), 233016.

[35] S. Frisco, A. Kumar, J.F. Whitacre, S. Litster, Understanding Li-ion battery anode degradation and pore morphological changes through nano-resolution X-ray computed tomography, J. Electrochem. Soc. 163 (13) (2016) A2636.

[36] M. Smith, L. Scudiero, J. Espinal, J.-S. McEwen, M. Garcia-Perez, Improving the deconvolution and interpretation of XPS spectra from chars by ab initio calculations, Carbon N Y 110 (2016) 155–171.

[37] R. Lundström, N. Gogoi, X. Hou, E.J. Berg, Competing ethylene carbonate reactions on carbon electrode in Li-ion batteries, J. Electrochem. Soc. 170 (4) (2023), 040516.

[38] H. Jia, L. Zou, P. Gao, X. Cao, W. Zhao, Y. He, M.H. Engelhard, S.D. Burton, H. Wang, X. Ren, High-performance silicon anodes enabled by nonflammable localised high-concentration electrolytes, Adv. Energy Mater. 9 (31) (2019), 1900784.

[39] Z. Piao, P. Xiao, R. Luo, J. Ma, R. Gao, C. Li, J. Tan, K. Yu, G. Zhou, H.M. Cheng, Constructing a stable interface layer by tailoring solvation chemistry in carbonate electrolytes for high-performance lithium-metal batteries, Adv. Mater. 34 (8) (2022), 2108400.

[40] Z.-Y. Wu, Y.-Q. Lu, J.-T. Li, S. Zanna, A. Seyeux, L. Huang, S.-G. Sun, P. Marcus, J. Światowska, Influence of carbonate solvents on solid electrolyte interphase composition over Si electrodes monitored by in situ and ex situ spectroscopies, ACS Omega 6 (41) (2021) 27335–27350.

[41] P. Verma, P. Maire, P. Novák, A review of the features and analyses of the solid electrolyte interphase in Li-ion batteries, Electrochim. Acta 55 (22) (2010) 6332–6341.

[42] O.C. Harris, S.E. Lee, C. Lees, M. Tang, Mechanisms and consequences of chemical cross-talk in advanced Li-ion batteries, J. Phys. Energy 2 (3) (2020), 032002.

[43] J.G. Han, K. Kim, Y. Lee, N.S. Choi, Scavenging materials to stabilise LiPF6-containing carbonate-based electrolytes for Li-ion batteries, Adv. Mater. 31 (20) (2019), 1804822.

[44] S. Wilken, M. Treskow, J. Scheers, P. Johansson, P. Jacobsson, Initial stages of thermal decomposition of LiPF 6-based lithium ion battery electrolytes by detailed Raman and NMR spectroscopy, RSC Adv. 3 (37) (2013) 16359–16364.

[45] A. Andersson, K. Edström, Chemical composition and morphology of the elevated temperature SEI on graphite, J. Electrochem. Soc. 148 (10) (2001) A1100.

Supporting Information

Deciphering electrolyte dielectric extended electrochemical stability in lithium-ion capacitors

Obinna Egwu Eleri[a,b], Frederik T Huld[a,b], Fengliu Lou[b*] and Zhixin Yu[a*]

[a] Department of Energy and Petroleum Engineering, University of Stavanger, 4036 Stavanger, Norway

[b] Beyonder AS, Stokkamyrveien 30, 4313 Sandnes, Norway

Corresponding authors[*]

ZY: zhixin.yu@uis.no
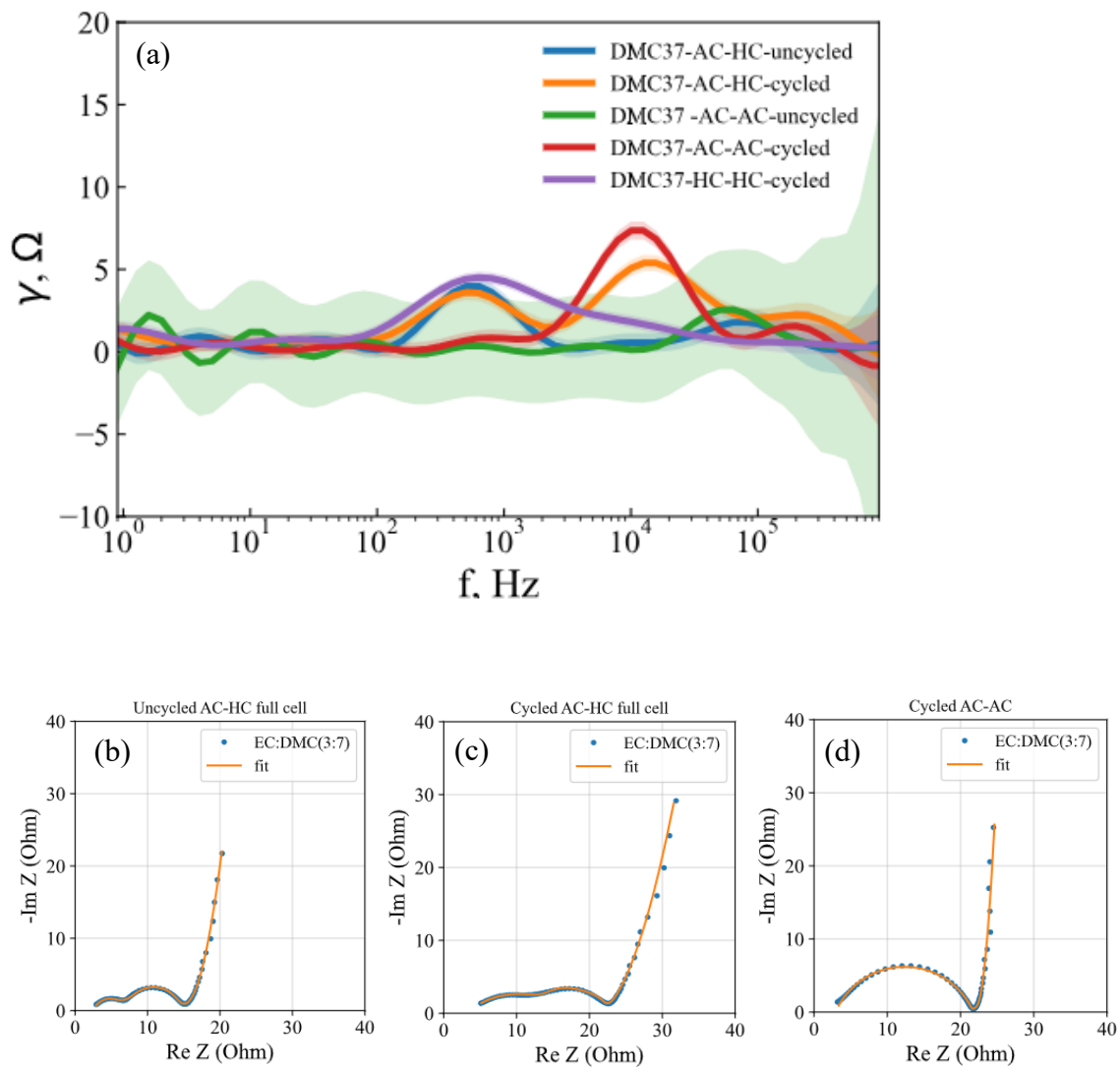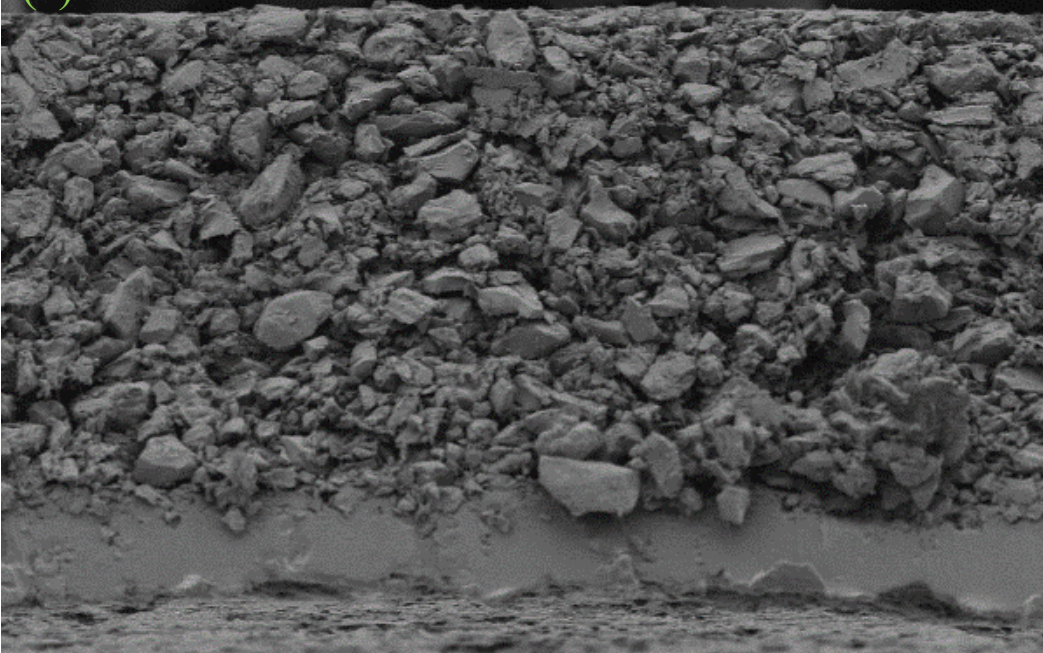FL: fengliu@beyonder.no

Figure S1: (a) Distribution of relaxation time analysis for different cells using EC:DMC(3:7) electrolyte; EIS spectra and fitting using EC:DMC(3:7) electrolyte in (b) uncycled AC/HC full cells, (c) cycled AC/HC full cells, and (d) cycled AC/AC symmetric cells.
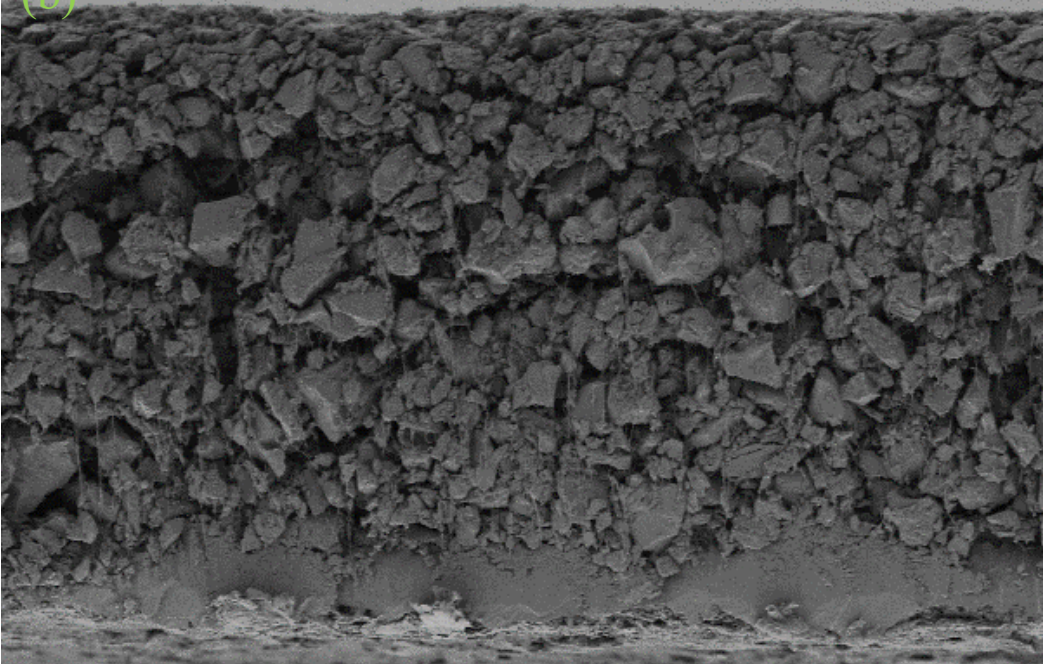
(a)

| 20 µm | EHT = 3.00 kV | Signal A = SE2 | Aperture Size = 30.00 µm | ZEISS |
| WD = 7.5 mm | Mag = 1.00 K X | Time: 1:32:52 |

(b)

| 20 µm | EHT = 3.00 kV | Signal A = SE2 | Aperture Size = 30.00 µm | ZEISS |
| WD = 7.4 mm | Mag = 1.00 K X | Time: 1:36:36 |

(c)

| 20 μm | EHT = 3.00 kV | Signal A = SE2 | Aperture Size = 30.00 μm | ZEISS |
| | WD = 7.5 mm | Mag = 1.00 K X | Time: 1:42:41 | |

(d)

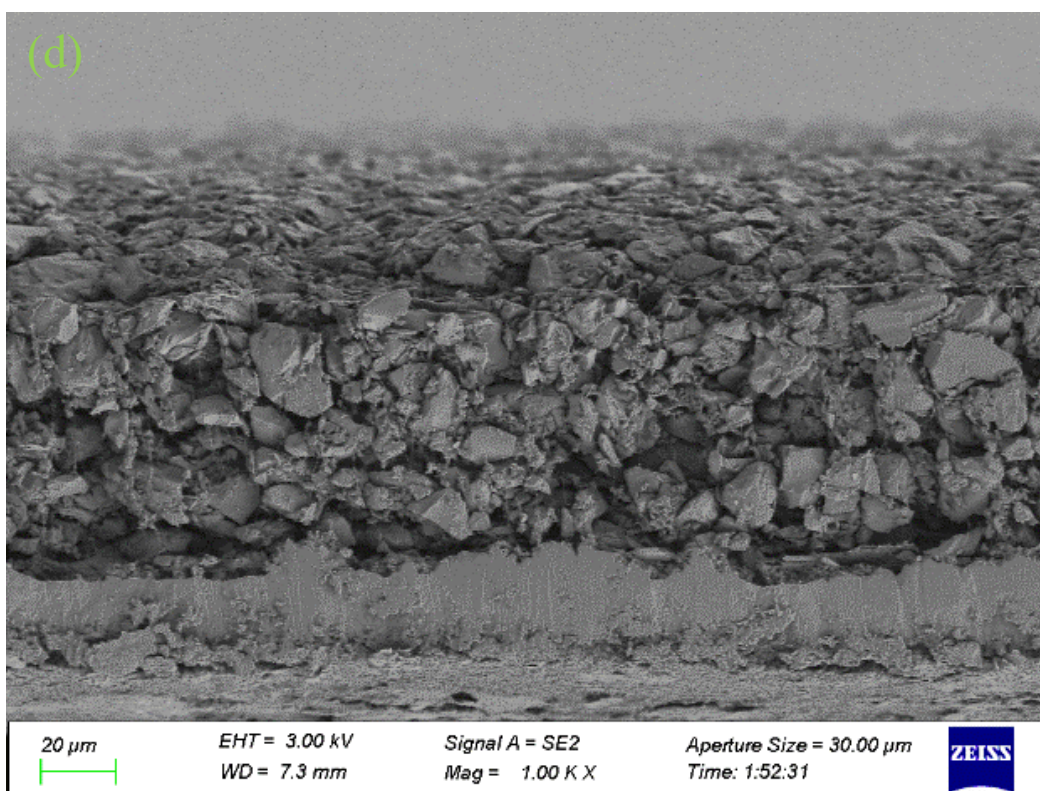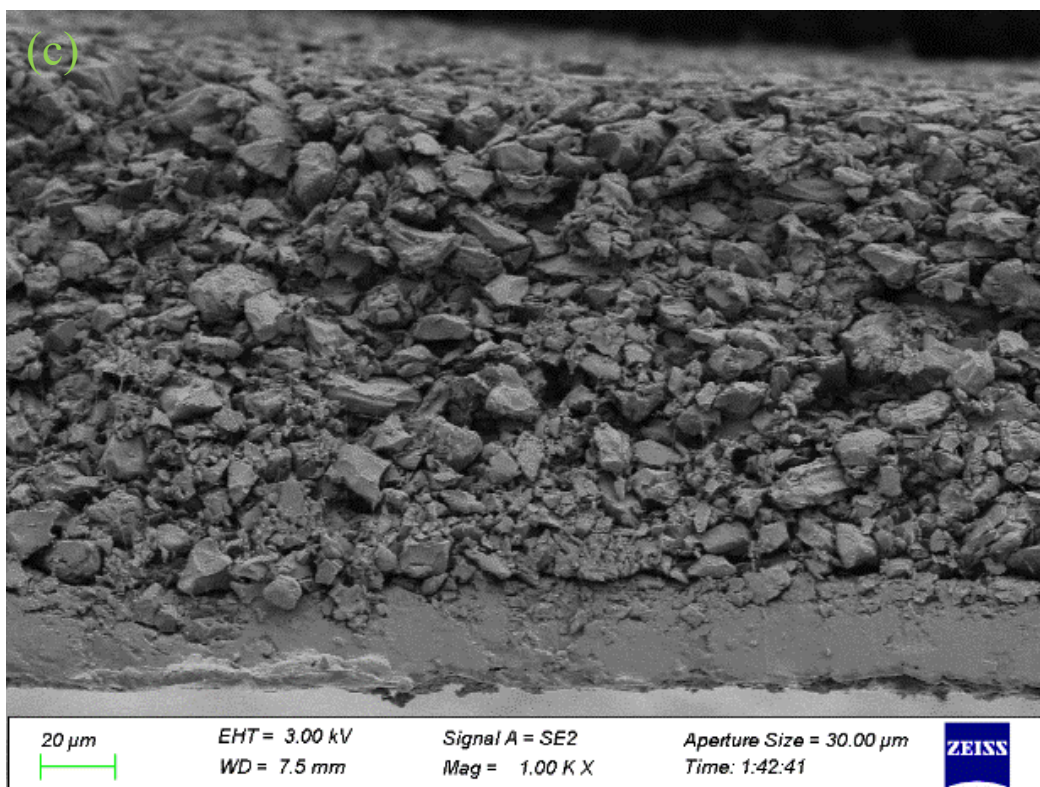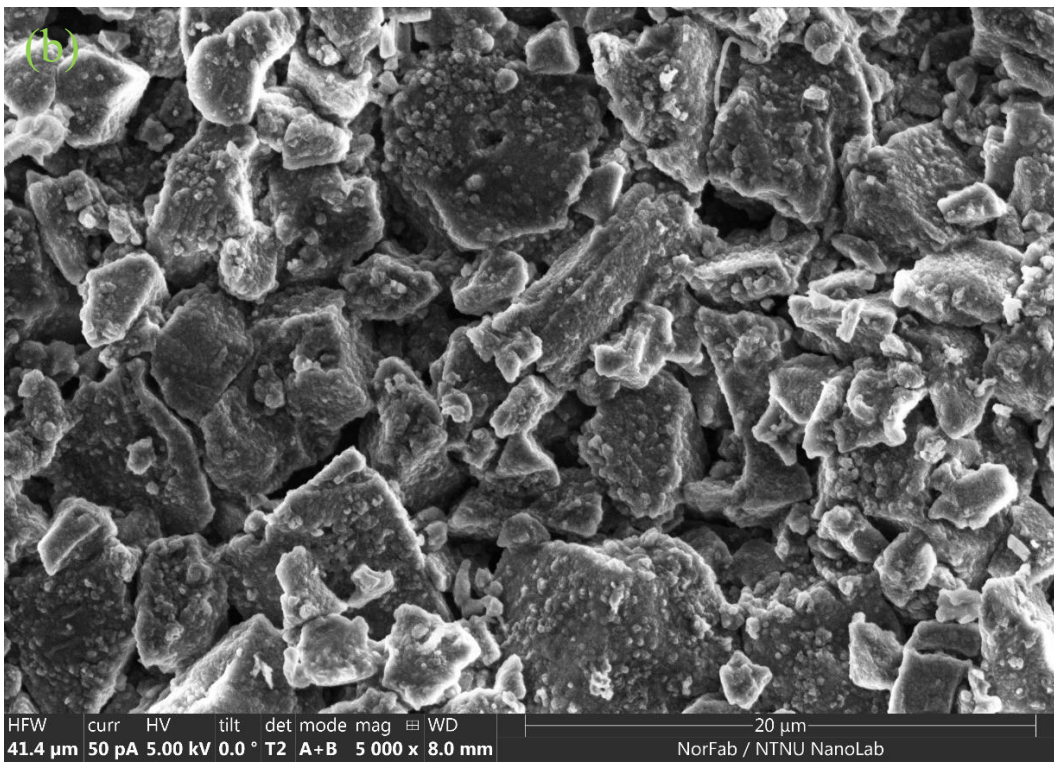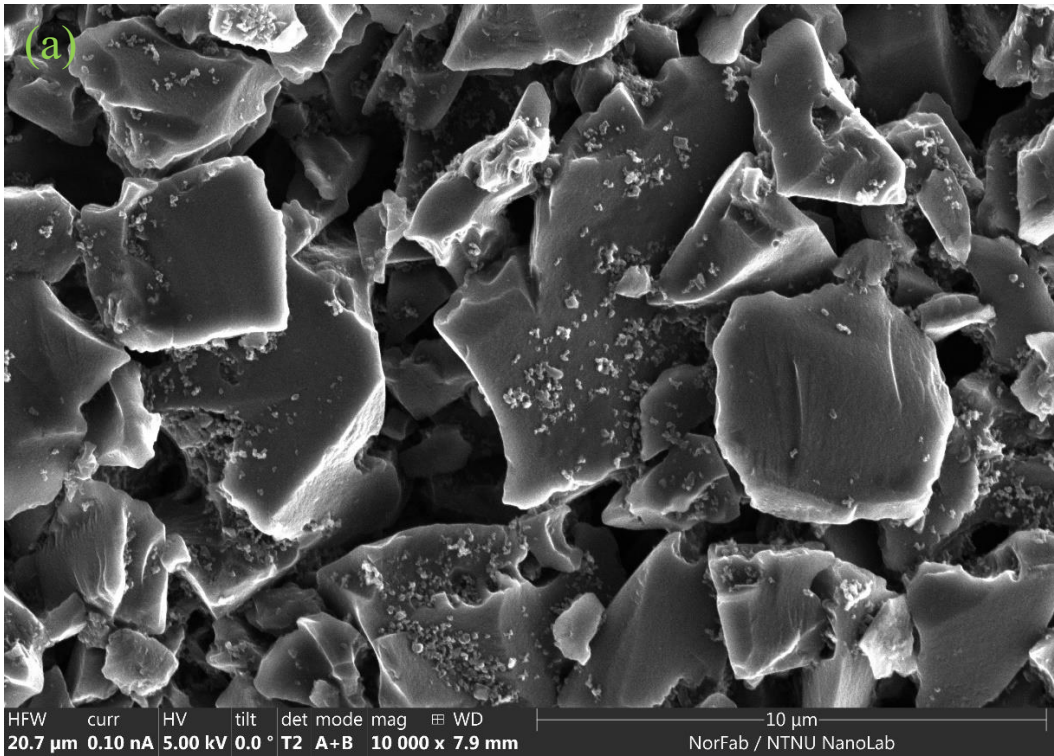| 20 μm | EHT = 3.00 kV | Signal A = SE2 | Aperture Size = 30.00 μm | ZEISS |
| | WD = 7.3 mm | Mag = 1.00 K X | Time: 1:52:31 | |

Figure S2: Cross-section SEM images of (a) reference AC electrode; cycled AC electrodes in (b) EC:DMC(3:7), (c) EC:DMC(1:1), and (d) EC:DMC(7:3).

(a)

HFW	curr	HV	tilt	det	mode	mag	⊞	WD	10 µm
20.7 µm	0.10 nA	5.00 kV	0.0 °	T2	A+B	10 000 x		7.9 mm	NorFab / NTNU NanoLab

(b)

HFW	curr	HV	tilt	det	mode	mag	⊞	WD	20 µm
41.4 µm	50 pA	5.00 kV	0.0 °	T2	A+B	5 000 x		8.0 mm	NorFab / NTNU NanoLab

(c)

| HFW | curr | HV | tilt | det | mode | mag ⊞ | WD | 20 μm |
| 41.4 μm | 50 pA | 5.00 kV | 0.0 ° | T2 | A+B | 5 000 x | 7.9 mm | NorFab / NTNU NanoLab |

(d)

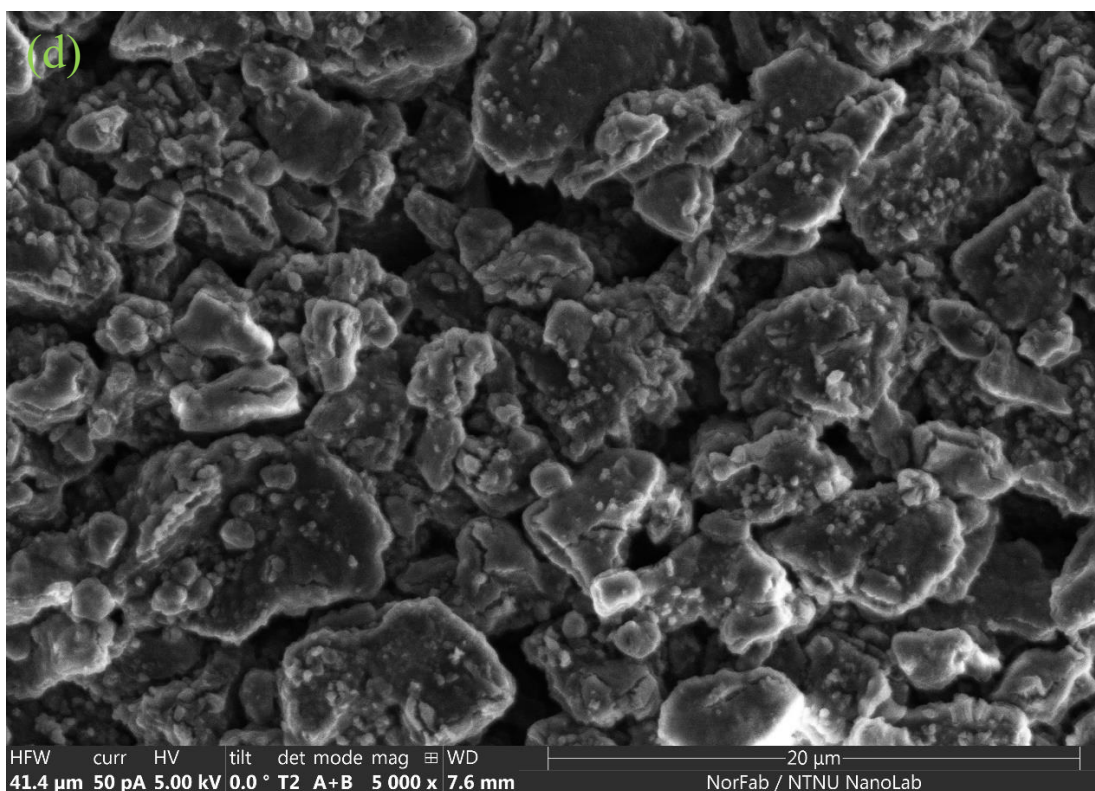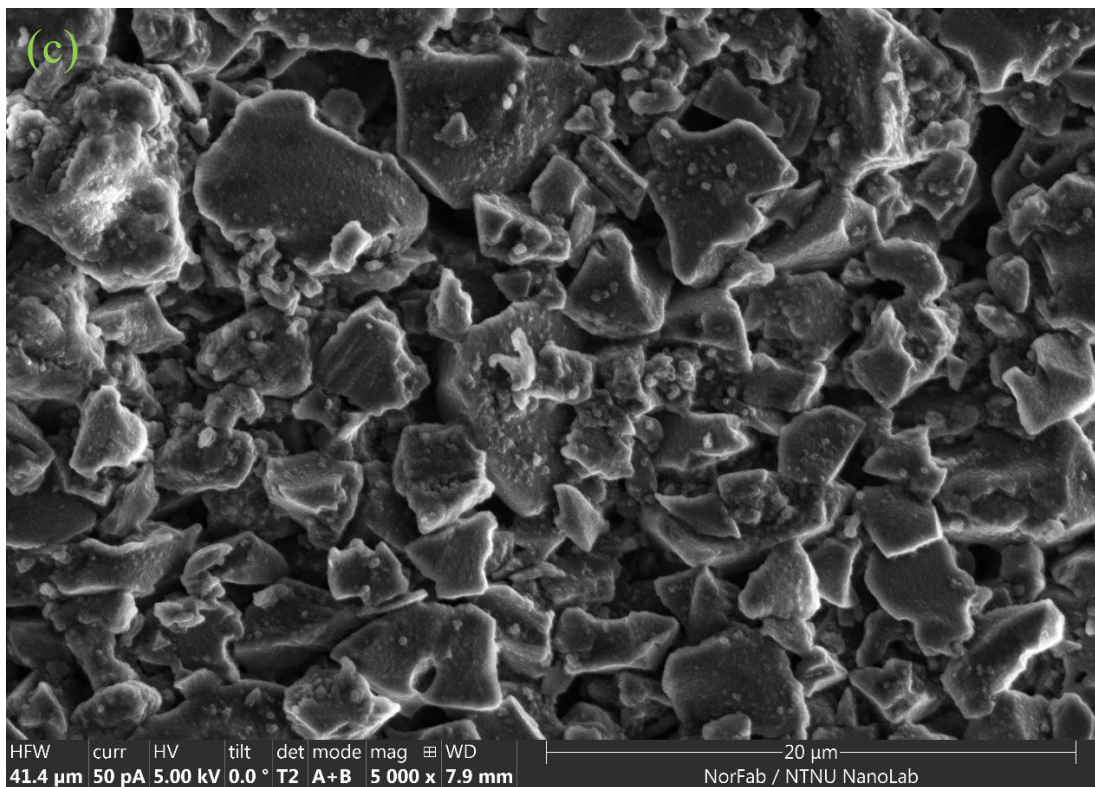| HFW | curr | HV | tilt | det | mode | mag ⊞ | WD | 20 μm |
| 41.4 μm | 50 pA | 5.00 kV | 0.0 ° | T2 | A+B | 5 000 x | 7.6 mm | NorFab / NTNU NanoLab |

Figure S3: SEM images of (a) reference HC electrode; cycled HC electrodes in (b) EC:DMC(3:7), (c) EC:DMC(1:1), and (d) EC:DMC(7:3).